AN INVESTIGATION INTO THE TORQUE DENSITY CAPABILITIES OF FLUX-FOCUSING MAGNETIC GEARBOXES

by

Krishna Kiran Uppalapati

A dissertation submitted to the faculty of
The University of North Carolina at Charlotte
in partial fulfillment of the requirements
for the degree of Doctor of Philosophy in
Electrical Engineering

Charlotte

2015

Approved by:

_____
Dr. Jonathan Z. Bird

_____
Dr. Sukumar Kamalasadan

_____
Dr. Ryan Adams

_____
Dr. Wesley B. Williams

ABSTRACT

KRISHNA KIRAN UPPALAPATI. An investigation into the torque density capabilities of flux-focusing magnetic gearboxes.
(Under the direction of DR. JONATHAN Z. BIRD)

Wind and many rotary based ocean energy conversion devices rely on a mechanical gearbox to increase their speed so as to match the requirements of the electromagnetic generator. However, mechanical gearboxes have a number of disadvantages such as the need for gear lubrication, no overload protection and the creation of acoustic noise. Frequently direct-drive generators are employed to overcome these issues, wherein the gearbox is removed and the shaft of the turbine is directly connected to the synchronous generator, either with an electrically excited or permanent magnet rotor. If the input speed to the generator is very low the torque must be very high in order to generate the necessary power. However, as the electrical loading of a synchronous generator is thermally limited, the size of the generator will become excessively large at high power levels.

An alternative to these technologies is to consider replacing the mechanical gearbox with a magnetic gear. A magnetic gear can create speed change without any physical contact. It has inherent overload protection, and its non-contact operation offers the potential for high reliability. Despite significant progress, existing magnetic gear designs do not achieve torque densities that are competitive with mechanical gearboxes.

This research has focused on designing a coaxial magnetic gear that can operate at a volumetric torque density that is comparable to a mechanical gearbox. A flux-focusing rotor topology also called spoke-type rotor magnet arrangement was adopted to improve

the air-gap magnetic flux density which in turn improves the torque transferred between the rotors. Finite element analysis was utilized to conduct a parameter sweep analysis of the different geometric parameters of the magnetic gear. A sub-scale magnetic gear with a diameter of 110 mm and a scaled-up magnetic gear with a diameter of 228 mm was designed, constructed and experimentally evaluated. The torque and torque density of sub-scale design was measured to be 115 Nm and 151.2 Nm/L respectively and that of the scaled-up model was measured to be 731 Nm and 239 Nm/L respectively.

An iterative magnetomechanical analysis technique was developed to study the deflection of the magnetic gear steel rotor bars due to the magnetic forces coming from the inner and outer rotor permanent magnets. The accuracy of the technique was validated by using an experimental test-stand. It was shown that the deflection is an important issue to consider especially if the air-gaps are small.

A 2-D analytical based model was derived for the flux-focusing coaxial magnetic gear by using the separation of variables method to solve the Laplace and Poisson equation in each region. After applying the applicable Dirchlet and Neumann boundary conditions a set of 16 equations with 16 unknown Fourier coefficients was obtained. The 16 unknowns were solved numerically by putting the equations in a matrix form. It was shown that the analytical based model immensely reduced the torque and field computational time when compared to using finite element analysis. However, the analytical model does not take into consideration the non-linear properties of the steel. The benefits of using the analytical model was demonstrated by conducting a radial scaling and gear-ratio analysis.

ACKNOWLEDGEMENTS

First of all I would like to dedicate this thesis to my parents Annapurna Uppalapati and Satyanarayana Raju Uppalapati and thank them for all the sacrifices they had to make so I can pursue my dreams. I should thank my wife Vijayshree Danthurthi for all the support, extreme patience and keeping up with me throughout the writing of this thesis. I should thank my sister Renuka, Brother-in-law Hari Krishnam Raju and my handsome nephew Harshith for all their support throughout my education.

I must thank my advisor and mentor Dr. Jonathan Bird for his constant support and advice. Apart from being a great advisor you have been a great mentor. I have learnt good work ethics from you. I must thank Dr. Ryan Adams, Dr. Sukumar Kamalasadan, Dr. Wesley Williams and Dr. Aixi Zhou for taking time to be a part of my committee and evaluating my work.

I must thank my fellow lab-mates Matthew Calvin, Joel Pritchard, Jason Wright, Walter Bomela for the invaluable help with the mechanical construction and test setup. I wouldn't have done this without your help. I must also thank all my lab-mates both past and present especially Paul Subhra, Nirmal Paudel, Vedanadam Acharya, Pavithra Padmanathan, Jia Dan, Bahrami Mojtaba, Debrupa Som and Kang Li. It was a delight to work with you guys.

Finally, I must thank and extend my gratitude to North Carolina Coastal Studies Institute for funding this research and Powersys, Inc for allowing me to use their FEA software JMAG for my analysis.

TABLE OF CONTENTS

LIST OF TABLES

LIST OF FIGURES

LIST OF ABBREVIATIONS

MHK	Marine Hydro Kinetic
DD	Direct Drive
SG	Synchronous Generator
WEC	Wave Energy Converter
OWC	Oscillating Water Column
MG	Magnetic Gear
PM	Permanent Magnet
FEA	Finite Element Analysis
FFMG	Flux-Focusing Magnetic Gear
OD	Outer Diameter

LIST OF SYMBOLS

p_1	Number of pole pairs on inner rotor
n_2	Number of cage rotor steel poles
p_3	Number of pole pairs on outer rotor
ω_1	Angular velocity of inner rotor (rad/s)
ω_2	Angular velocity of cage rotor (rad/s)
ω_3	Angular velocity of outer rotor (rad/s)
T_1	Torque on inner rotor (Nm)
T_2	Torque on cage rotor (Nm)
T_3	Torque on outer rotor (Nm)
l_m	Length of the magnet (m)
w_m	Width of the magnet (m)
B_m	Residual magnetic flux density (T)
c_f	Cogging factor
$C_{\varphi 1}$	Flux-concentration ratio of inner rotor
$C_{\varphi 3}$	Flux-concentration ratio of outer rotor
d	Axial length of the magnetic gear (m)
η	Efficiency (%)
g	Air-gap (m)
R_1	Inner radius of the inner rotor (m)
R_2	Outer radius of the inner rotor (m)

R_3	Inner radius of the cage rotor (m)
R_4	Outer radius of the cage rotor (m)
R_5	Inner radius of the outer rotor (m)
R_6	Outer radius of the outer rotor (m)
Ω^{I}	Inner rotor magnet region
Ω^{II}	Inner air-gap region
Ω^{III}	Cage rotor air region
Ω^{IV}	Outer air-gap region
Ω^{V}	Outer rotor magnet region
$\mathbf{B}$	Magnetic flux density (T)
$\mathbf{H}$	Magnetic field intensity (A/m)
$\mathbf{M}$	Magnetization vector (A/m)
$\mathbf{A}$	Magnetic vector potential (Wb/m)
μ_0	Permeability of free space (H/m)
μ	Relative permeability
B_r	Radial flux density (T)
B_θ	Azimuthal flux density (T)
i	Cage rotor pole position
j	inner rotor magnet position
k	Outer rotor magnet position
β_c	Angular span of cage rotor pole (rad/s)
β_h	Angular span of inner rotor magnet (rad/s)

β_l	Angular span of outer rotor magnet (rad/s)
θ_0	Initial position of cage rotor (rad/s)
θ_h	Initial position of inner rotor (rad/s)
θ_k	Initial position of outer rotor (rad/s)

CHAPTER 1 : INTRODUCTION

1.1. Motivation

The growing demand for energy across the world with ever increasing population and rapid industrialization is creating severe stress on the planet due to the depletion of natural resources like oil, natural gas and coal. The environmental effects like climate change due to carbon dioxide and green house gas emissions are threatening the bio-diversity of the planet [1]. These factors are leading to an increase in the demand for clean and sustainable energy. Renewable energy sources are not only providing alternative sources for power generation but also may be the only option for achieving a sustainable energy supply in the future.

Renewable energy sources like wind and marine hydrokinetic (MHK) energy are one of the fastest growing renewable energy technologies worldwide [2]. Typically in a wind turbine, power from the rotation of the wind turbine rotor is transferred to the generator through a main shaft, the mechanical gearbox and the generator. Such a configuration is shown in Figure 1-1. The mechanical gearbox is used to increase the speed from the input shaft to be able to generate power from the generator.

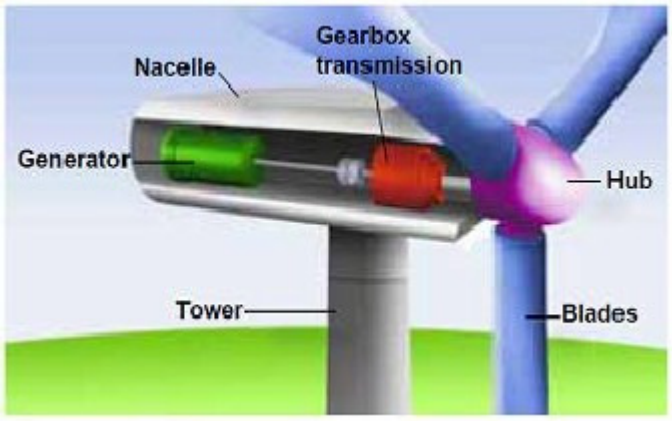

Figure 1-1: Typical wind turbine configuration [3]

However the mechanical gearbox tends to create many issues in the wind turbine. For instance, the wind speed is generally not constant and therefore this can result in frequent changes in the load applied to the gearbox [4]. This can create a lot of stress on the gearbox teeth and can result in the failure of the mechanical gearbox [5]. The frequent failure of wind turbine mechanical gearbox has resulted in an increase in maintenance costs, thereby affecting the levelized cost of power generation [6-7]. A wind turbine gearbox is typically designed for a life-span of 20 years but the frequent failures of the gearbox have resulted in a reduction in the gearbox life span to around 12 years [8].

In order to improve the reliability of wind turbines, direct-drive (DD) technology [9] can be utilized, where the gearbox is removed and the shaft of the wind turbine is directly connected to the synchronous generator (SG) either electrically excited or with permanent magnets (PM). An example of a direct-drive wind turbine generator is shown in Figure 1-2 [10]. Since the input speed to the generator is very low the torque should be very high in order to generate the required power [11]. As traditional electric machines have a much lower torque density than mechanical gearboxes the DD generator must be relatively large in size. Also since the generator is directly connected to the input

shaft, the converter has to be designed for the full range of input speed and hence the power electronics will be relatively costly [12] .

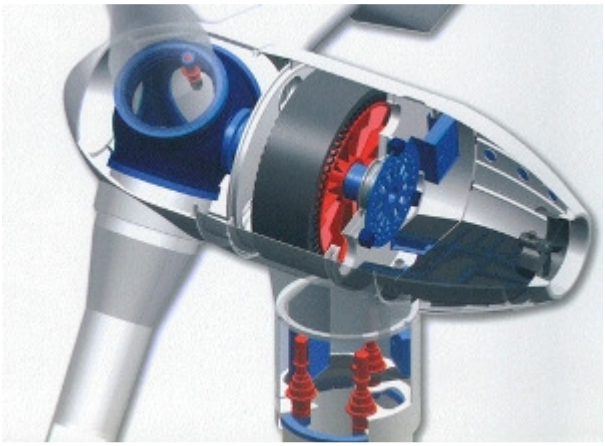

Figure 1-2: Direct-drive generator by Mtorres wind industries [10]

In MHK applications various wave energy converters (WEC), like oscillating water columns (OWC), overtopping converters, attenuators, point absorbers, axial-flow turbines are being used [13]. Figure 1-3 and Figure 1-4 illustrates some of the types of MHK converters that are being developed. Most MHK converters generally use a mechanical or a hydraulic gearing system to increase their speed [14]. Such devices have efficiency issues and the use of a mechanical gearbox with its acoustic noise and lubrication requirements may not be a good choice for use in remote off-shore and undersea locations.

(a) (b)

Figure 1-3: (a) Seagen, marine current turbine by Marine Current Turbines Limited [15], (b) oscillating water column by Oceanlinx [16]

Figure 1-4: AWS wave energy converter [17]

An effective solution to reliably converting low speed motion from renewable energy devices into high speed rotation suitable for power generation is to consider utilizing a contactless magnetic gear (MG) mechanism. This is the scope of this research, where many of the issues created by the mechanical gearboxes are addressed. A MG offers many advantages over a mechanical gearing system. Its contactless mechanism can solve a lot of issues with mechanical gearboxes like wear and tear, vibrations, lubrication requirements and high maintenance costs. A MG also provides inherent overload protection due to the contactless mechanism of operation. This makes the MG potentially highly valuable for wind turbine applications. However, not much attention had been paid to investigating MG's performance until the turn of the 21st century. Some of the reasons for this are the relative complexity of the MG and the shortcomings of earlier PMs. With the discovery of new PM materials with high energy densities it has become possible to obtain higher torque densities [18].

1.2. Literature Review

This section provides a survey of the various MG designs in the literature. The torque density and shear stress are calculated using the following equations.

The volumetric torque density of a MG can be calculated using

$$T_d = \frac{T}{\pi r_o^2 d} \tag{1.1}$$

where T = peak torque, r_o=outer radius and d = stack length.

The torque density at the air-gap of a rotary machine can be calculated from

$$T_{gd} = \frac{T_g}{\pi r_g^2 d} \tag{1.2}$$

where T_g = torque at the air-gap, r_g=air-gap radius.

Shear stress is defined as the force per unit area acting parallel to the plane of the surface. The shear stress, σ_s, is calculated from

$$\sigma_s = \frac{F}{2\pi r_g d} \tag{1.3}$$

where F is the air-gap force and r_g is the air-gap radius

When designing PM machines with high torque, the shear stress in the air-gaps of the rotors tends to increase quite a bit. This can pose a significant risk of demagnetization to magnets [19].

Since the torque created within the air-gap is defined as T_g=Fr_g, the shear stress can be expressed as

$$\sigma_s = \frac{T_g}{2\pi r_g^2 d} \tag{1.4}$$

Substituting (1.2) into (1.4) gives:

$$\sigma_s = \frac{T_{gd}}{2} \tag{1.5}$$

Thus the air-gap torque density and air-gap shear stress are related.

1.2.1. Mechanically Inspired MGs

Although MG technology existed for a long time, not much attention was given to the research due to the low torque density achieved from PMs.

C. Armstrong [20] was the first to obtain a patent in this field in 1901. The electromagnetic spur gear proposed by C. Armstrong consisted of two parts, one part had a gear with electromagnets as the gear teeth and the other had steel poles. This design is shown in Figure 1-5. The electromagnets present on one of the gears were turned on based on their position on the other gear and torque was transmitted.

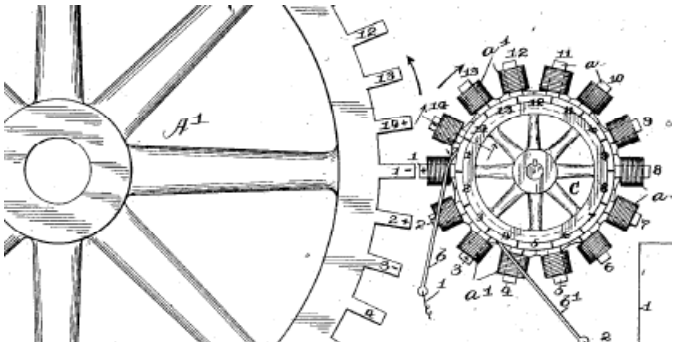

Figure 1-5: An electromagnetic spur gear proposed by C. Armstrong [20]

Although the gear had the advantage of contact-less torque transfer and noise-less operation, the amount of torque that could be transferred would be very low because at any given rotor position only 2 to 3 electromagnets transfer torque. As the electromagnets would need current go through them, this approach can result in a lot of losses and heating and would need lubrication and regular maintenance.

H. Faus [21] designed a permanent magnetic spur-type gear as shown in Figure 1-6 in 1941. The gear operated in the same manner as Armstrong's electromagnetic spur gear. The electromagnets and steel poles are replaced by permanent magnets in this design. All the magnets are placed in the same direction on the two rotors. This results in repulsion forces between the two rotors and the torque is transmitted. This design doesn't provide overload protection as the magnets can break when operating over maximum torque limit. Also the weak utilization of the PMs makes the design inefficient.

In 1993, S.Kikuchi [22] proposed the magnetic worm gear as shown in Figure 1-7. The magnetic worm gear was designed to have 1:33 gear ratio. Initial design had a very large air-gap and hence the maximum torque transferred as very low. In order to decrease the air-gap the worm gear is coupled with a wheel which increased the output torque by as much as 50%. Nevertheless the torque density capability would be significantly lower than its mechanical counterpart.

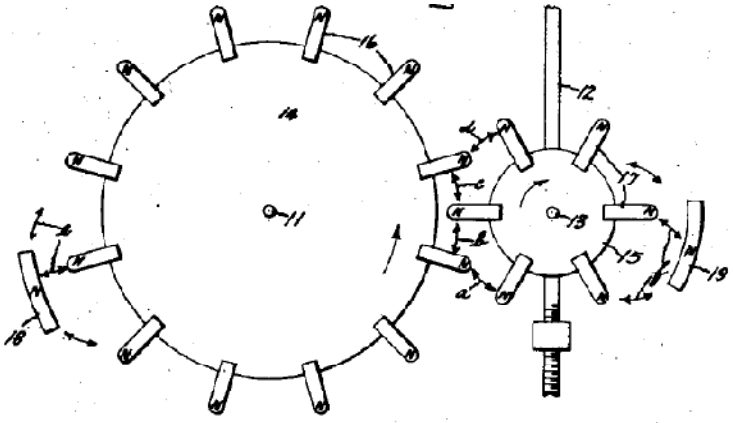

Figure 1-6: A magnetic spur gear proposed by Faus [21]

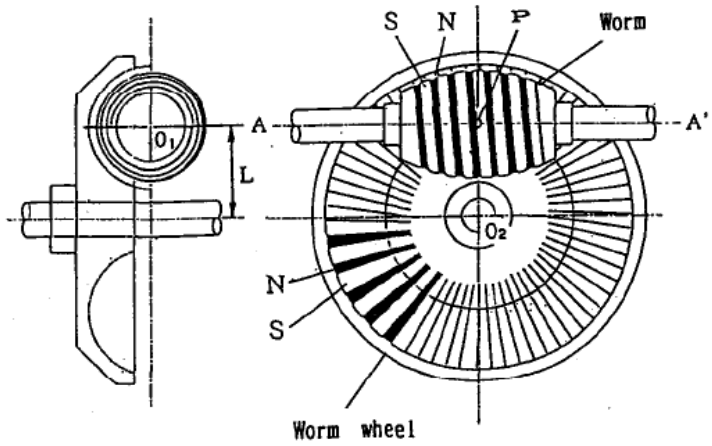

Figure 1-7: A magnetic worm gear proposed by S.Kikuchi [22]

In 1989 K. Tsurumoto [23-25] proposed the axial flux disk type spur MG as shown in Figure 1-8. Tsurumoto used samarium-cobalt as PM material. He attained a

gear ratio of 1:3 with a peak torque of 5.5 Nm. In [23] described a new design in which the PMs are directly mounted on the steel plate which improves the efficiency of the gear and increased the peak torque trnaferred by almost 300%.

M. Okano [26] described a superconducting version of the worm gear. Superconducting MGs could greatly improve the maximum torque that can be transferred when compared to normal permanent MGs. Superconducting magnets need to be continuously cooled as they conduct large currents. This means they should be continuously refrigerated. This increases the size and cost of the gear system. Two different spur gear configurations were designed, constructed and experimentally verified by Okano. The calculated torque density for the superconducting spur MGs was 4 Nm/L [26] which is high for the given size of the MG system.

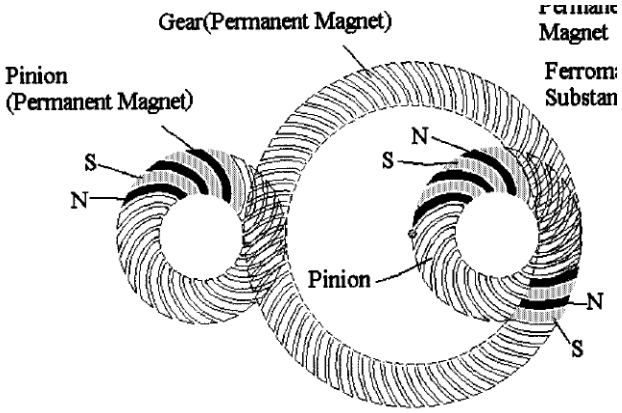

Figure 1-8: A spur magnetic gear proposed by M.Okano [26]

In 2008, Haung [27] proposed a magnetic planetary gear as shown in Figure 1-9. The gear arrangement had a sun gear, planet gears and a magnetic ring gear on back iron. The topology is analogous to a conventional mechanical planetary gear. The maximum torque transmitted depended on the number of planets surrounding the sun. As the

number of planets increased, the maximum torque that could be transmitted also increased. However, it was reported that increasing the number of planets would also increase the resulting cogging torque of the rotors. The simulated gearbox had a maximum torque density of 97.3 Nm/L but the measured torque density for the experimental setup was only 16 Nm/L.

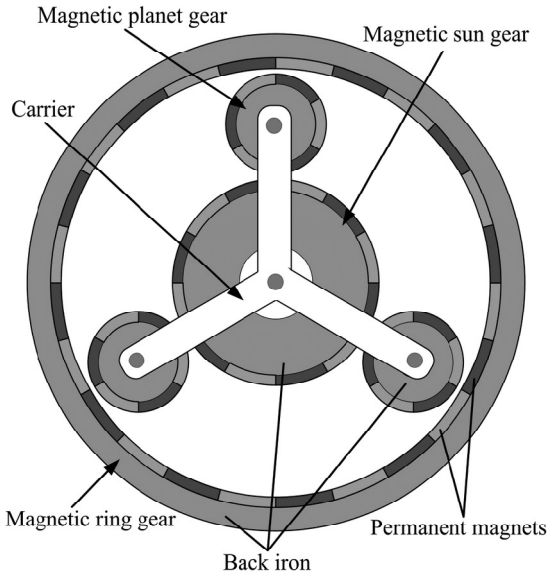

Figure 1-9: A magnetic planetary gear proposed by Huang [27]

All the MG designs described above use mechanical gear topologies with the teeth replaced by electromagnets or PMs. The torque transferred and the efficiency of these designs is very low due to low utilization of magnets as only a few magnets are transmitting torque at any given moment.

1.2.2. Coaxial MGs

In 1916 Neuland [28] proposed a unique MG as shown in Figure 1-10, which used three rotors to obtain an efficient torque transmitting mechanism. The gear consisted of three rotors of which one was held stationary, a laminated steel toothed outer

rotor, a central section with stationary cores with magnetizing windings and an inner rotor with laminated steel tooth.

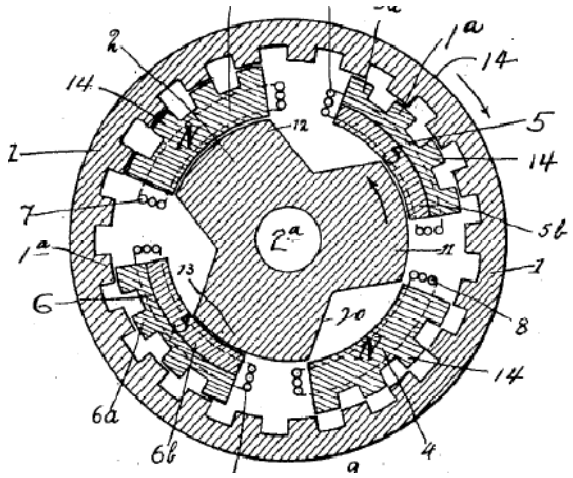

Figure 1-10: A coaxial MG topology proposed by Neuland [28]

The gear ratio is calculated by taking the number of steel tooth on the inner and outer rotors. The maximum torque that could be transmitted using this design would be much higher than the spur gear designs as almost all the magnets would aid in the transfer of torque between the rotors unlike the other designs. This greatly increases the torque density of the MG system. However the torque was not comparable to its mechanical counterpart since only one set of magnetizing windings were used in the design and the field created by the windings would be thermally limited.

In 1967, Reese [29] proposed a MG similar to the one described by Neuland. However, the inner rotor contained electromagnets instead of steel teeth as shown in Figure 1-11. The middle rotor and the outer rotor had steel poles and in this case the outer rotor was held stationary. The inner rotor was the input rotor and the middle rotor was the output rotor. When the inner rotor with electromagnets was rotated, the middle rotor with

steel poles tends to rotate with the inner rotor. This occurs because the magnetic field coming from the inner rotor will try to travel through the steel poles rather than air and this makes the steel poles on the middle rotor to rotate to align itself in least reluctance path for the field to travel. The gear ratio is determined by the number of electromagnets on inner rotor and the steel teeth on the middle rotor.

Martin [30] designed a coaxial MG similar to the ones described in [28] and [29] . However, in this design the outer and inner rotors had PM's. The number of magnets on the inner and outer rotor was different and is used to measure the gear ratio. This design approach is shown in Figure 1-12. The middle rotor modulated the magnetic field between the outer and the inner rotor. The length of the steel poles on the middle rotor was a key factor in determining the amount of torque transmitted between the rotors. The number of PMs on the inner and outer rotor and the number of steel poles on the middle rotor determined the resulting gear ratio of MG.

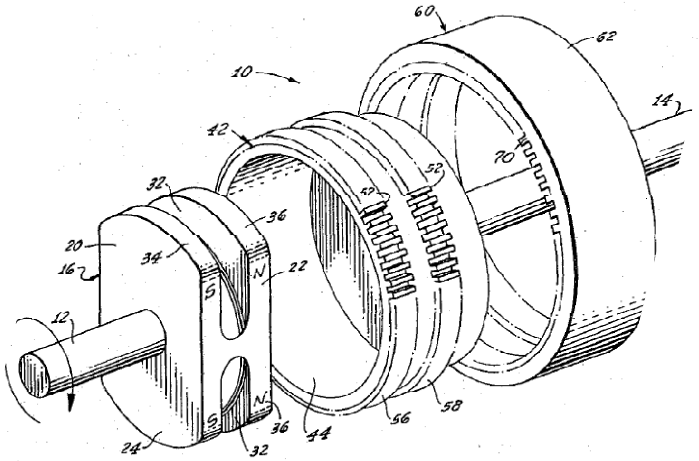

Figure 1-11: A coaxial MG proposed by Reese [29]

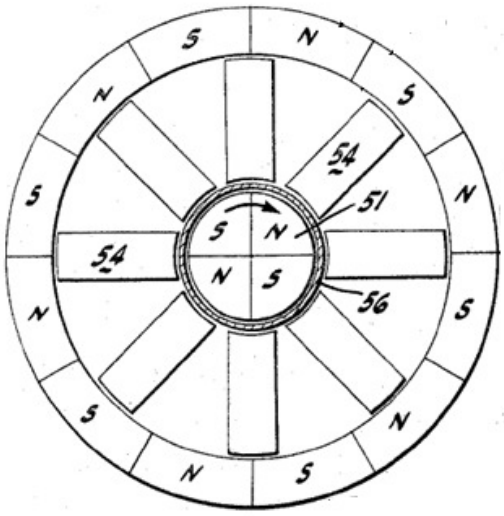

Figure 1-12: A coaxial MG proposed by Martin [30]

In 1997, B. Ackerman [31] obtained a patent for a coaxial MG. In this case the middle rotor had steel poles which were connected as shown in Figure 1-13. The operation of this design was similar to the one proposed by Martin [30]. Connecting the steel pieces in the middle rotor made the construction easier and robust. In 1999 Ackerman obtained another patent [32] for MG design where the steel poles on the middle rotor and the PMs on the outer rotor were interchanged.

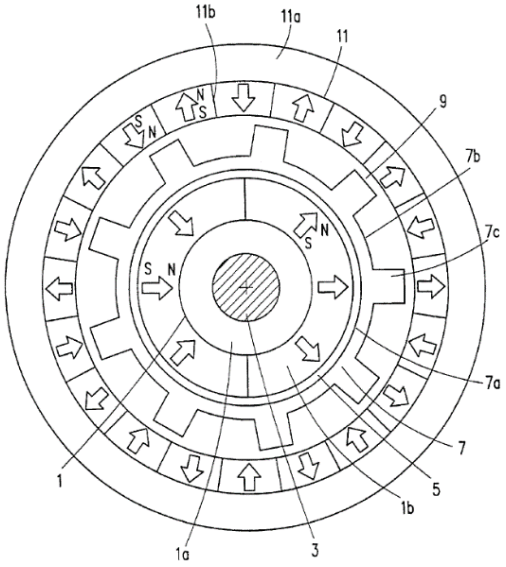

Figure 1-13: A coaxial MG proposed by Ackermann [31]

In 2001, K. Atallah [33] was the first to numerically calculate that a MG could achieve a torque density that is greater than a direct drive motor. The operating principle of the proposed MG design was similar to the one proposed by Ackerman [31] as shown in Figure 1-14. In [33] Atallah used harmonic analysis and Fourier series to derive the equations for relationship between the number of PMs on the inner and outer rotors and the steel poles on the middle rotor. Atallah used rare magnets in his design and numerically calculated a volumetric torque density of about 100 Nm/L. In 2004 Atallah experimentally demonstrated the MG design [34] with a gear ratio of 5.75:1 and achieved a volumetric torque density of 72 Nm/L.

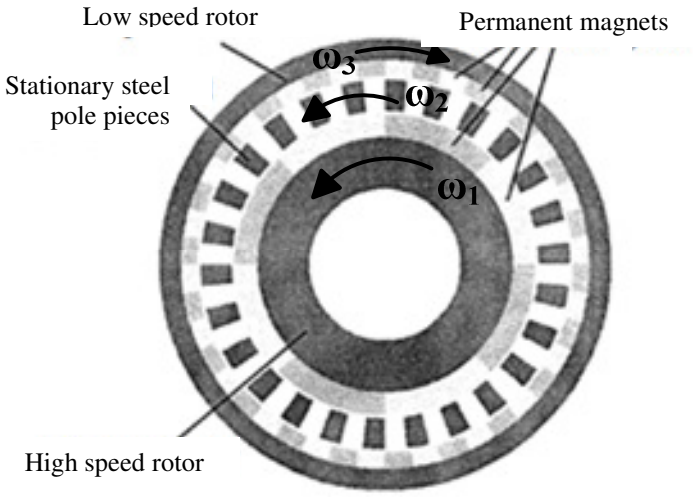

Figure 1-14: A coaxial MG proposed by K. Atallah [33]

P. Rasmussen [35] published a paper in 2003 on a coaxial MG that used an inner rotor spoke-type of magnet arrangement. This design is in Figure 1-15. The MG had a gear ratio of 1:5.5 and calculated a peak torque of 27 Nm. The design was constructed and tested. The measured torque was 16 Nm. This represents a torque density of 54 Nm/L. The difference in the calculated and actual measured peak torque values was

claimed to be due to the short axial length of the magnets and the 3D end effects. Rasmussen also compared the MG with conventional mechanical gears with the same gear ratio and maximum torque capabilities.

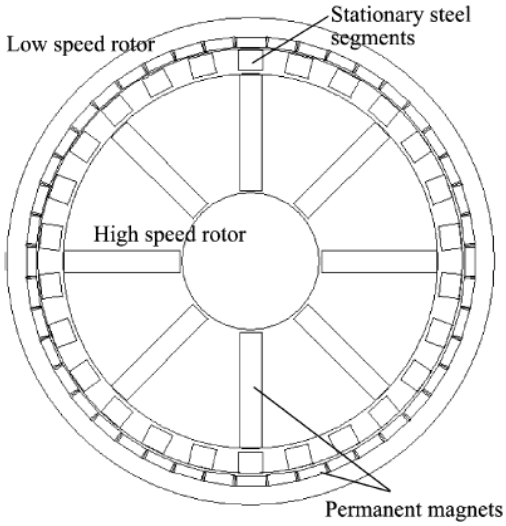

Figure 1-15: A coaxial MG proposed by P. Rasmussen, [35]

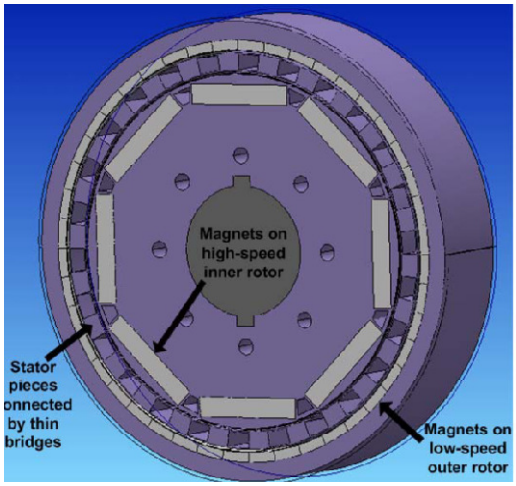

Figure 1-16: A coaxial MG proposed by Frank [36]

In 2011, N. Frank [36-38] studied an embedded magnet coaxial MG with a gear ratio of 5.5:1. This design is shown in Figure 1-16. The design presented in [36] by Frank had thin bridges connecting the steel poles in the middle rotor in order to improve the structural strength. The inner rotor had magnets embedded into the rotor to support the

magnets during operation. A torque density of 42 Nm/L was measured as opposed to 64 Nm/L calculated using FEA.

In 2014, Nakamura [39] designed a 10.33:1 coaxial MG in which the efficiency of the design was claimed to be 99% when calculated through FEA at a constant input speed of 300 RPM. The design is shown in Figure 1-17. The paper provides a comparison of torque on the outer rotors for different pole combinations and showed that a fractional gear ratio is crucial to designing a MG. The design utilized damper windings to reduce the oscillations and the transient time. A torque density of 60 Nm/L was predicted for this design.

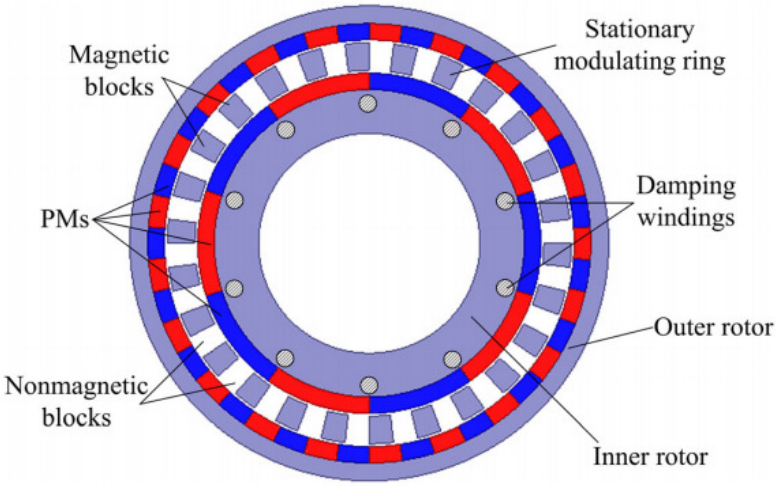

Figure 1-17: A coaxial MG with damper windings proposed by Nakamura [39]

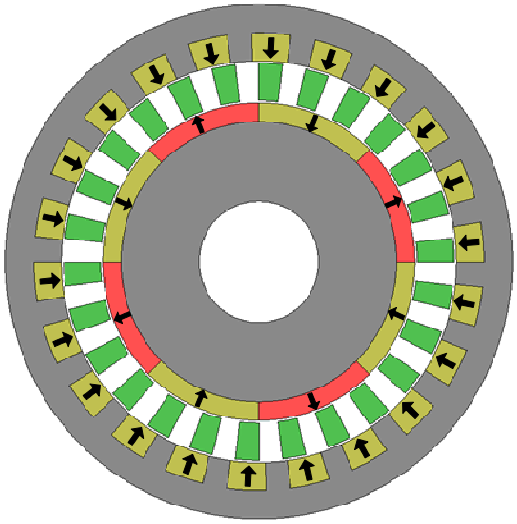

Figure 1-18: A coaxial MG with surface mounted inner rotor and buried outer rotor magnets by Liu [40]

In 2009, X. Liu [40] designed a 1:7.33 gear ratio MG with radially magnetized outer rotor buried magnets and surface mounted magnets on the inner rotor. This design is shown in Figure 1-18. The reason for using buried magnets was to give extra mechanical strength to the magnets and maintain the structural integrity of the outer rotor. The experimentally measured torque density was 53.3 Nm/L.

In 2009, J. Linni [41] compared the torque density and torque ripple performance of a radially magnetized MG and a Halbach rotor MG design. Both designs had a 1:4.25 gear ratio. The Halbach rotor magnet design is shown in Figure 1-19. The Halbach arrangement of magnets helped to achieve a near-sinusoidal field in the air-gap as well as a strong field intensity. Jian measured a torque density of 108 Nm/L and 95 Nm/L for the Halbach and radially magnetized magnet designs respectively.

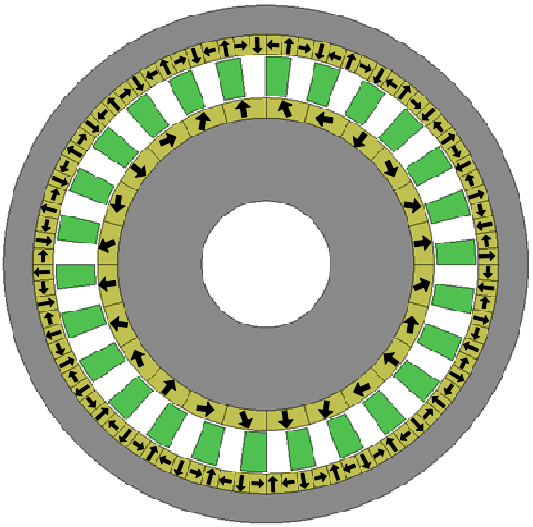

Figure 1-19: A MG with halbach arrangement of magnets proposed by Jian [41]

1.2.3. Other MG Topologies

In 2011, R. Holehouse [42] proposed a linear MG. The operating principle of the linear MG was same as that of a coaxial MG described before. Such a design is shown in Figure 1-20. The design had three rotors with PMs on the inner and outer rotors and steel poles on the middle rotor. It was shown that an active force density of up to 2 MN/L could be achieved [42]. It was shown that the higher force density values could be achieved if the output stroke was lower than the length of the high speed rotor. It was observed that the force capability of linear MG depends on the distance between the steel poles. A design with 1:3.25 gear ratio was constructed and experimentally verified.

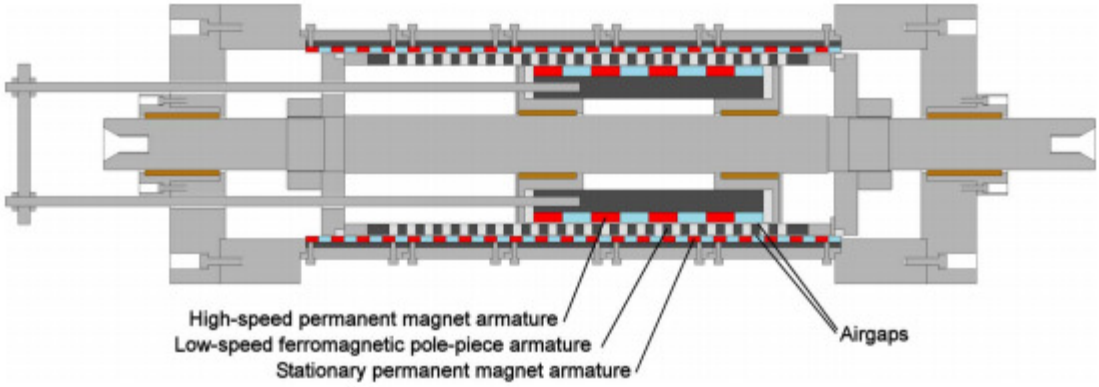

Figure 1-20: A linear MG proposed by Atallah [42]

In 2006, Mezani [43] published a paper on an axial MG as shown in Figure 1-21. The operating principle of this design was same as the coaxial MGs described before. In this design the rotors are placed in axial direction rather than in radial direction. The three rotors are separated axially from each other by a small air-gap. It was described that the axial MG can provide higher torque densities than coaxial MGs as the length of the three rotors could be same in case of axial MGs. Mezani calculated a torque density in excess of 70 Nm/L. More recently Acharya [44] proposed a flux focusing axial type MG, shown in Figure 1-22, it was calculated that an active region torque density of up to 289 Nm/L could be achieved. However such a design is difficult to construct due to the difficulty in maintaining a uniform axial air-gap.

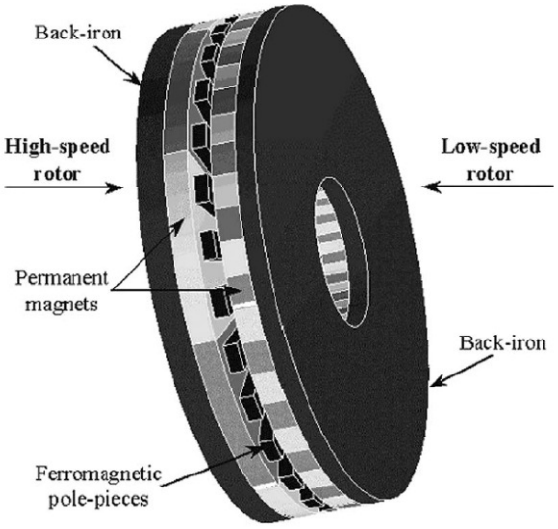

Figure 1-21: An axial MG proposed by Mezani [43]

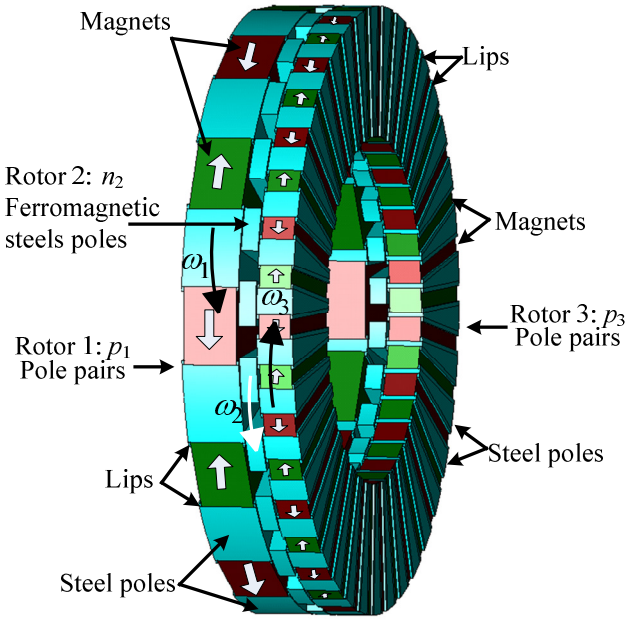

Figure 1-22: Flux focusing axial MG proposed by Acharya [44]

In 2010 J. Rens [45] proposed a harmonic MG as shown in Figure 1-23. The operating principle of a harmonic gear was producing a time varying air-gap between two rotors which have PMs installed on flexible cylinders. Outer rotor has a rigid stationary rotor with PMs and inner rotor has PMs installed on a flexible rotor. The time variation of the air-gap between the two rotors modulated the field produced by the magnets. Rens

derived equations using harmonic analysis to determine the gear ratio. A design with a gear ratio of 1:18 was designed which had a peak torque of 3756 Nm.

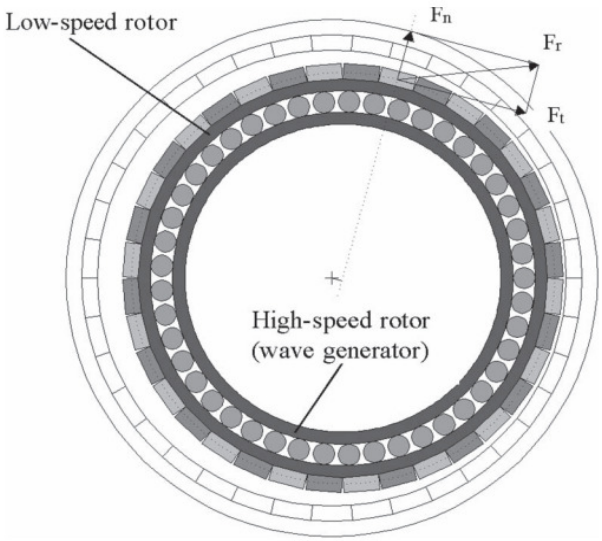

Figure 1-23: Magnetic harmonic gear proposed by Rens [45]

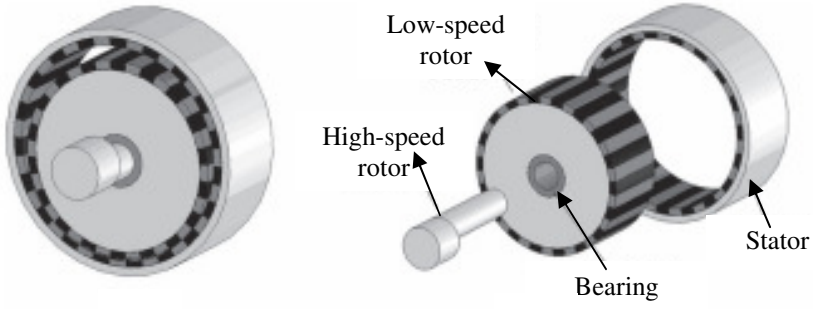

Figure 1-24: Magnetic harmonic gear without flexible rotor proposed by Rens [45]

The harmonic gear design practical implementation was pretty complicated due to the need for a flexible PM inner rotor and a flexible coupling to couple with a load. Rens proposed a way to avoid flexible shaft by using a conventional PM rotor connected using a bearing at an eccentricity with the outer rotor as shown in Figure 1-24. This cycloidal MG version was far easier to construct than a flexible harmonic gear. However it still needs a flexible coupling to be able to connect to the load as the output rotor is rotating eccentrically. This problem however was avoided by constructing a dual stage MG where

the output from the flexible shaft is connected as input to another harmonic gear with a rigid output shaft. This dual stage setup was constructed and experimentally verified. The calculated and experimentally measured torque density for the single stage harmonic MG was 158.5 Nm/L and 150 Nm/L respectively. A dual stage design had a torque density of 75 Nm/L. Although higher torque densities are achieved with this design, the need for a dual-stage MG design to make it simpler is not desired.

In 2008 F. Jorgensen [46] also published a paper demonstrating the capabilities of a cycloidal gearbox. The design is shown in Figure 1-25. Jorgensen experimentally tested a 1:21 gear ratio cycloidal gearbox with a torque density of 142 Nm/L. An optimized design was calculated to be able to reach 183 Nm/L. The cycloidal gearbox used 18 bearings and thus it is mechanically complex to build and it also creates unsymmetrical radial forces which will reduce the bearing life of the gearbox.

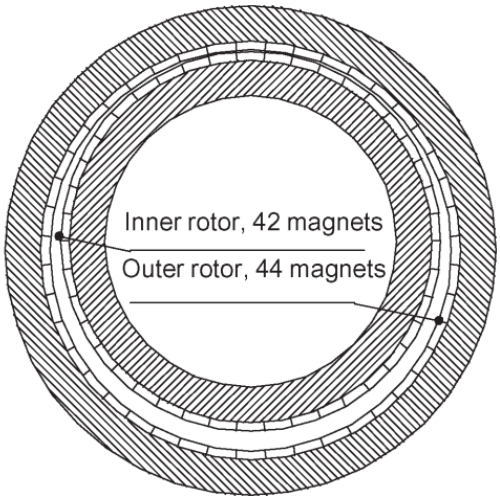

Figure 1-25: A cycloidal MG proposed by Jorgensen [46]

In 2014 Davey [47] published a paper on an axial flux cycloidal MG with a gear ratio of 30:1. This design has two magnet rings with the rotor rotating on an eccentric axis as shown in Figure 1-26. The stationary magnets are built on either side of the rotor

to balance the strong attractive axial magnetic forces. This design needed an orbital bearing plate and orbital bearings to transfer the eccentric rotation. It also needed an embedded counterweight on the shaft. The radius of the stator piece is increased significantly so that it always over shadows the rotor magnets. This design doesn't have the ferromagnetic pole pieces like other coaxial MG models. The disadvantage is that only one stator is available to generate output torque and strong double-taper bearings have to be used to prohibit flexure.

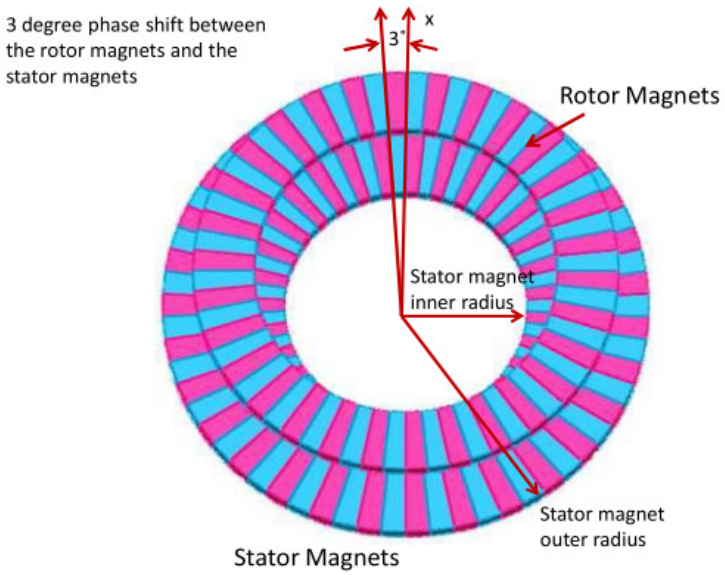

Figure 1-26: Cycloidal MG proposed by Davey [47]

1.2.4. Magnetically Geared Motors

In 2007, Atallah [48-50] patented a design in which a MG was integrated into a brushless PM machine. Atallah called the design a pseudo direct drive machine and it is shown in Figure 1-27. It was concluded that this magnetically geared machine could achieve a peak torque density in excess of 60 Nm/L while operating with a power factor of 0.9 or higher.

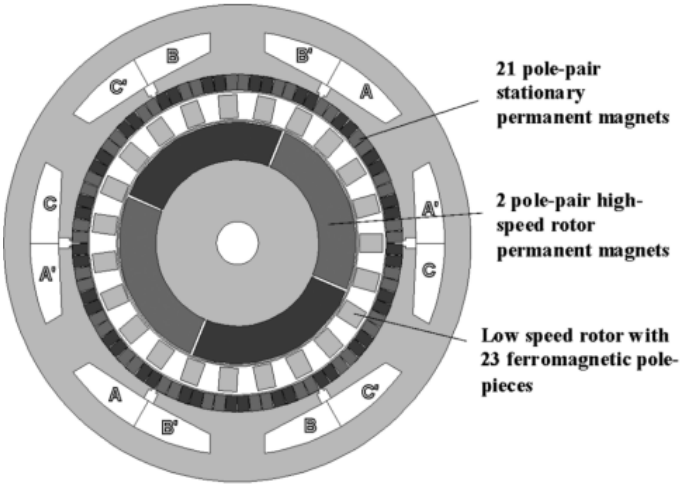

Figure 1-27: Pseudo direct drive machine patented by Atallah [49]

In 2009 Rasmussen [51] published a paper, on a motor integrated MG. In this design the stator windings interacted with the MG's inner high speed rotor. This design is shown in Figure 1-28. The paper described a scaling analysis which was used to optimize the design to achieve higher torques and torque densities. In an improved design it was calculated that a peak torque density of 130 Nm/L could be achieved [51]. However in the final design some changes were made due to practical issues and the measured torque density was 97 Nm/L [52].

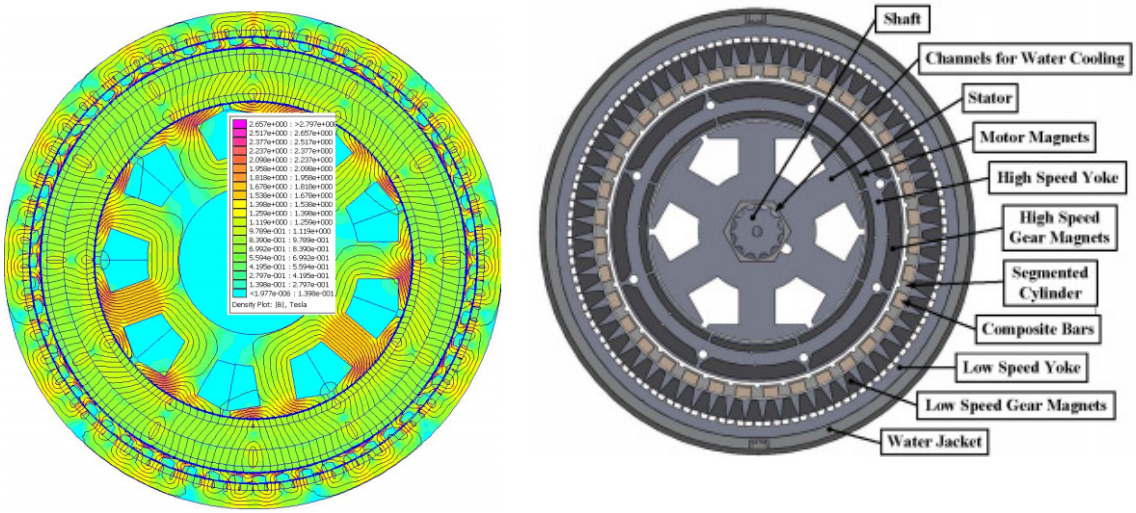

Figure 1-28: Motor integrated PM gear proposed by Rasmussen [51-52]

In 2007, Chau [53-55] proposed integrating an inner rotor with an outer MG via a coupling rotor, such a design is shown in Figure 1-29 designed to be used in electrical vehicle applications. A MG had to be used to increase the torque of the motor as it was not enough to launch the vehicle. When the proposed MG was connected to the motor the torque improved to 103 Nm. The torque density of the design was 87 Nm/L. Atallah's design differed from Rasmussen's and Chau's in that the outer stator winding interacted with the inner high speed MG rotor.

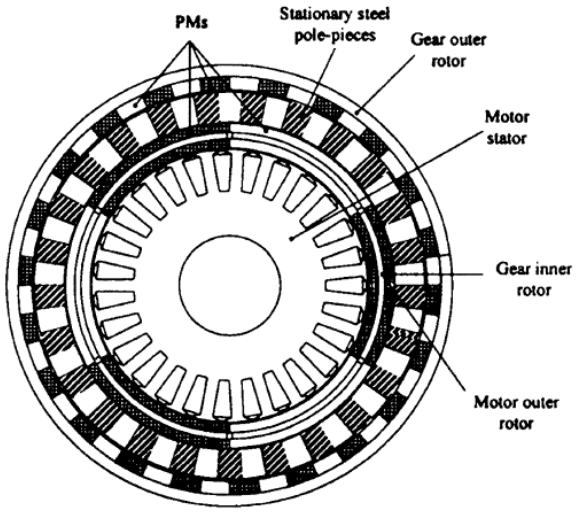

Figure 1-29: A coaxial MG with DC motor proposed by Chau [54]

P. Padmanathan [56] proposed a continuously variable MG as shown in Figure 1-30 which had a flux-focusing inner rotor. The continuously variable MG enabled a constant output speed to be created from a variable input speed fed from the input shaft. This was achieved by replacing the outer rotor of the MG with a stator. The electrical frequency of the stator was varied as the input speed varied to give a constant output speed.

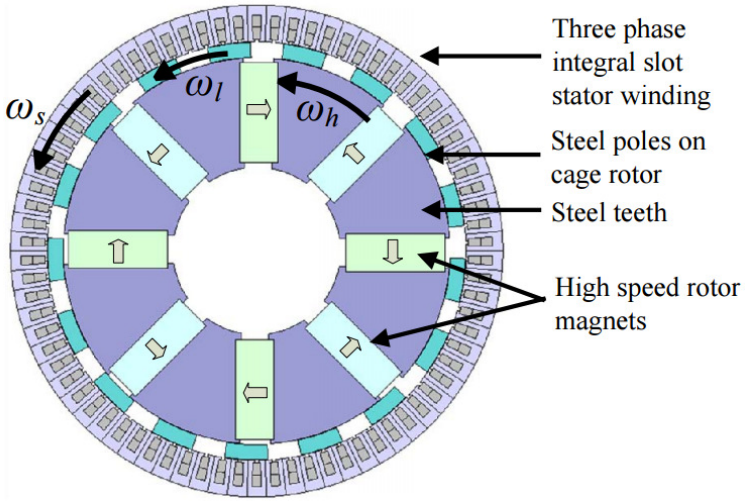

Figure 1-30: Continuously variable MG proposed by Padmanathan [56]

1.2.5. Summary of MG Performance

Figure 1-31 shows a summary of the volumetric torque densities of the experimentally verified MG designs published in the literature to-date.

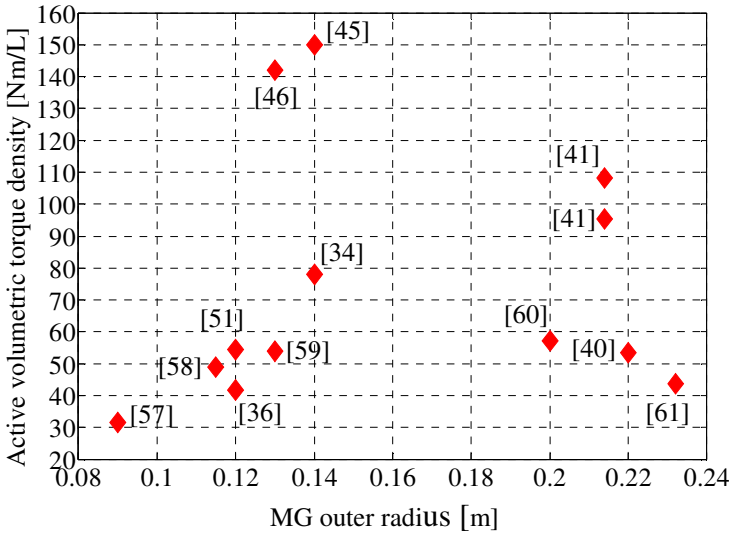

Figure 1-31: Torque density comparison with experimental MG research

A summary of the measured torque, torque density and shear stress on the inner and outer rotor is shown in Table 1-1 and their corresponding pole pair combinations are shown in Table 1-2. In Table 1-2, p_1 is the number of pole-pairs on the inner rotor, p_3 is the number of pole-pairs on the outer rotor and n_2 is the number of steel poles on the

middle rotor. All of the prior-art designs evaluated held the middle rotor stationary and rotated the inner and outer rotors. An alternative design would be to rotate the inner and middle rotors while holding the outer rotor stationary. Table 1-2 also shows the predicted torque values if the designs were to hold the outer rotor stationary. If the outer rotor is held stationary and middle rotor is rotated the input torque increased. The reason for this has been explained in chapter 2.

Table 1-1: Summary of prior art experimentally verified MG designs

Author	Calculated peak torque [Nm]	Measured torque [Nm]	Torque density [Nm/L]	Outer diameter [m]	Shear stress on inner rotor [kN/m^2]	Shear stress on outer rotor [kN/m^2]
Shah [59]	10.7	10.58	53.8	0.13	4.8	26.9
Atallah [34]	85.7	60	77.9	0.14	6.7	38.9
Rassmussen [51]	27	16	54.4	0.12	4.9	27.2
Frank [36]	16	12.3	41.8	0.12	3.8	20.9
L Brönn [58]	33	20	49	0.115	2.3	24.5
Liu [40]	76.3	73	53.3	0.22	3.6	26.6
Jian [41]	159.2	155.8	108.2	0.214	12.7	54.1
Jian [41]	139.7	137.2	95.3	.0214	11.2	47.6
Niguchi [57]	5.20	4.87	31.4	0.09	6.2	15.7
Jing [60]	168.7	168.1	57.1	0.2	6.7	28.5
Rens [45]	122	115	150	0.14	0.2	75
Jorgensen [46]	44	33	141.9	0.13	1.7	70.9
Huang [27]	4.7	4.4	15.8	0.094	1.3	7.9

Table 1-2: Summary of experimentally verified coaxial MG designs when one of the rotors is fixed

Author	p_1	p_3	n_2	Gear ratio	Calculated torque	
					when p_3 fixed	when n_2 fixed
Shah [59]	4	22	26	5.5	12.6	10.7
Atallah [34]	4	23	27	5.75	100.6	85.7
Rassmussen [51]	4	22	26	5.5	31.9	27
Frank [36]	4	22	26	5.5	18.9	16
L Brönn [58]	2	21	23	10.5	36.1	33
Liu [40]	3	22	25	7.33	86.7	76.3
Jian [41]	4	17	21	4.25	196.6	159.2
Jian [41]	4	17	21	4.25	172.5	139.7
Niguchi [57]	4	10	14	2.50	7.2	5.20
Jing [60]	4	17	21	4.25	208.3	168.7

The objective of this dissertation is to design a MG that can create a higher torque and greater volumetric torque density than prior designs published in the literature. The

intended applications for these designs are in low speed, high torque applications such as for wind and ocean energy generation.

1.3. Problem Statement

It can be seen from the literature review that although much research has been conducted in the last decade on MG designs, none of the devices to date have been shown to create torque densities that are sufficiently high to enable them to efficiently replace mechanical gearboxes. This research will try to address this shortcoming. Initially a suitable topology will be chosen for the design. A model will be designed and studied using finite element analysis (FEA) to obtain the maximum performance and then a prototype will be built to verify the results.

1.4. Thesis Layout

Chapter 1: Introduction

A literature review of the existing MG technology is presented. The problems with the current designs are discussed and the need for improvements are specified.

Chapter 2: Coaxial magnetic gears

The theory of a coaxial MG system is explained in detail in this chapter. The working principle is explained with derived equations. The design specifications are laid out for the design.

Chapter 3: Sub-scale flux focusing magnetic gear design

The electromagnetic design and scaling analysis of a sub-scale MG with a diameter of 110 mm is presented. The construction of the prototype is presented and the calculated results are experimentally verified.

Chapter 4: Scaled-up flux focusing magnetic gear design

The electromagnetic design and scaling analysis of the scaled-up MG with an outer diameter of 228 mm is presented. The construction of the prototype is presented and the experimental results are verified.

Chapter 5: Analytical modeling of the flux focusing magnetic gear

An analytical model is developed for the flux-focusing MG using the magnetic vector potential. The method of separation of variables is used to solve the Laplace and Poisson governing equations in each region. The torque and field results are compared with ideal (μ_r=100,000) and non-linear FEA results.

Chapter 6: Scaling analysis of flux focusing magnetic gear

The analytical model developed in chapter 5 is used to conduct a scaling analysis. The flux focusing magnetic gear is analyzed for different sizes of MG with different pole-pair combinations.

Chapter 7: Conclusions and future scope

This chapter provides a summary of this research and suggestions are made for future research in this area.

CHAPTER 2 : COAXIAL MAGNETIC GEARS

2.1. Introduction

In this chapter the principle of operation of a coaxial MG is discussed. The equations governing the design are discussed. Also the concept of a flux focusing magnetic gear (FFMG) is introduced. The finite element analysis used for designing and optimizing the models is described.

2.2. MG Principle of Operation

A MG as shown in Figure 2-1 typically consists of three rotors, an inner rotor with p_1 pole pairs, an outer rotor with p_3 pole pairs and a middle rotor consisting of n_2 number of pole-pairs.

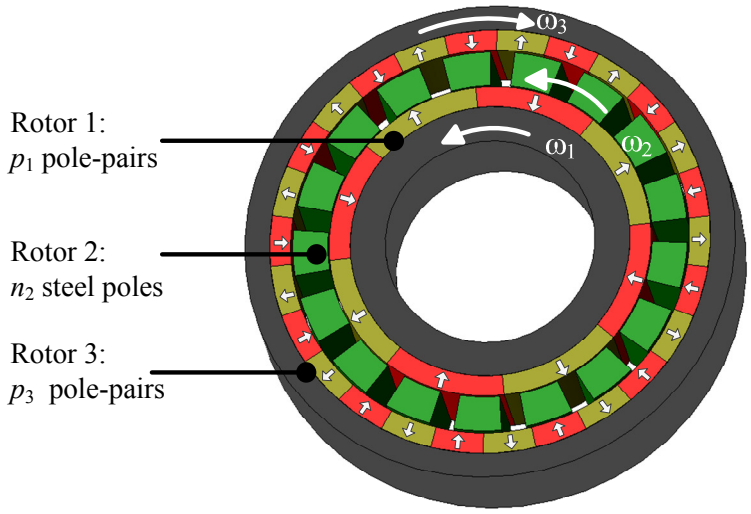

Figure 2-1: Magnetic gear with pole-pairs $p_1 = 4$, $n_2 = 17$ steel poles and $p_3 = 13$ pole-pairs.

The middle rotor henceforth called a cage rotor consists of ferromagnetic steel pole pieces which modulate the magnetic fields produced by the inner and outer rotor. The steel pieces on the cage rotor create space harmonics in the air-gaps between the inner and outer rotors. The magnetic fields created by the inner and outer rotors interact via the pole pieces and transfer torque. The working principle of a typical MG is explained using Figure 2-2. For clarity the design is represented as a linear model.

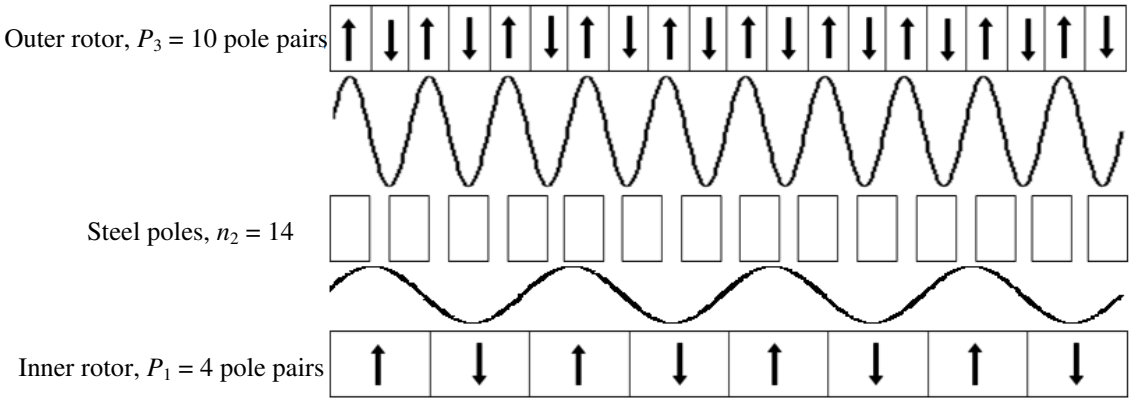

Figure 2-2: Typical MG modified into linear model

In this example, the model has 10 pole-pairs, p_3, on the outer rotor, 4 pole-pairs, p_1, on the inner rotor and 14 steel poles, n_2, on the cage rotor. The magnetic field created due to the inner rotor has a dominant 4^{th} harmonic due to the 4 pole-pairs. This field is modulated by the 14 steel poles on the cage rotor and this results in a field with a dominant 10^{th} harmonic being created. This field interacts with the 10^{th} harmonic of the outer rotor field which has 10 pole- pairs and consequently transfers torque.

The inner rotor with p_1 pole pairs, outer rotor with p_3 pole pairs and cage rotor with n_2 pole pieces are assumed to be rotating at ω_1, ω_3 and ω_2 rad/s respectively.

The flux density distribution at a radial distance r produced by the inner rotor when the cage rotor and outer rotor are absent can be represented as a function of radial distance r and angle θ and can be written as [33, 56]

$$B_{ri}(r,\theta) = \sum_{m=1,3,5,..,}^{\infty} b_{rm}(r)\cos[mp_1(\theta - \omega_1 t) + mp_1\theta_0] \tag{2.1}$$

where θ_0 is the initial angle of the inner rotor and $b_{rm}(r)$ is the Fourier coefficient for the radial component of the flux density.

When the steel poles of the cage rotor are included, the field from the inner rotor will be distributed along the steel pieces as they provide the better medium for the field to flow. The modulation function of the cage rotor bars can be represented in the Fourier form as

$$\lambda(r,\theta)=\lambda_{r0}(r)+\sum_{j=\pm1}^{\pm\infty} \lambda_{rj}(r)\cos[\,jn_2(\theta-\omega_2 t)] \tag{2.2}$$

Where λ_{r0} and λ_{rj} are the Fourier coefficients for the modulating functions.

The resultant field in the outer rotor air-gap can be obtained by multiplying equation (2.1) and (2.2)

$$B_{ro}(r,\theta) = B_{ri}(r,\theta)\lambda(r,\theta) \tag{2.3}$$

which can then be re-written as

$$\begin{aligned} B_{ro}(r,\theta) = & \sum_{m=1,3,5}^{\infty} \lambda_{r0}(r)b_{rm}(r)\cos[mp_1(\theta - \omega_1 t) + mp_1\theta_0] \\ & + \sum_{m=1,3,5}^{\infty}\sum_{j=\pm1}^{\pm\infty} \lambda_{rj}(r)b_{rm}(r)\cos[mp_1(\theta-\omega_1 t)+mp_1\theta_0]\cos[\,jn_2(\theta-\omega_2 t)] \end{aligned} \tag{2.4}$$

Using the trigonometric function given in (2.5)

$$\cos(A)\cos(B) = \frac{\cos(A-B)+\cos(A+B)}{2} \tag{2.5}$$

equation (2.4) can further be expanded and rearranged to

$$\begin{aligned} B_r(r,\theta) = & \sum_{m=1,3,5}^{\infty} \lambda_{r0}(r) b_{rm}(r)\cos[mp_1(\theta-\omega_1 t)+mp_1\theta_0] \\ & + \sum_{m=1,3,5}^{\infty}\sum_{j=\pm1}^{\pm\infty} \frac{\lambda_{rj}(r)b_{rm}(r)}{2}\Bigg(\cos[(mp_1+jn_2)(\theta-\frac{mp_1\omega_1+jn_2\omega_2}{mp_1+jn_2}t)+mp_1\theta_0] \\ & + \cos[(mp_1-jn_2)(\theta-\frac{mp_1\omega_1-jn_2\omega_2}{mp_1-jn_2}t)+mp_1\theta_0]\Bigg) \end{aligned} \tag{2.6}$$

Similarly the tangential component created by the inner rotor can be expressed as

$$B_{\theta i}(r,\theta) = \sum_{m=1,3,5,..,}^{\infty} b_{\theta m}(r)\sin[mp_1(\theta-\omega_1 t)+mp_1\theta_0] \tag{2.7}$$

where $b_{\theta m}(r)$ is the Fourier coefficient for the tangential component of the flux density.

The modulation function for tangential component of the flux density can be written similar to equation (2.3) as

$$\lambda(r,\theta)=\lambda_{r0}(r)+\sum_{j=\pm1}^{\pm\infty}\lambda_{\theta j}(r)\sin[jn_2(\theta-\omega_2 t)] \tag{2.8}$$

The resultant tangential field in the outer air gap after modulation can be obtained by multiplying equations (2.8) and (2.9) and this gives

$$\begin{aligned} B_\theta(r,\theta) = & \sum_{m=1,3,5}^{\infty} \lambda_{r0}(r) b_{rm}(r)\sin[mp_1(\theta-\omega_1 t)+mp_1\theta_0] \\ & + \sum_{m=1,3,5}^{\infty}\sum_{j=\pm1}^{\pm\infty} \frac{\lambda_{rj}(r)b_{\theta m}(r)}{2}\Bigg(\sin[(mp_1+jn_2)(\theta-\frac{mp_1\omega_1+jn_2\omega_2}{mp_1+jn_2}t)+mp_1\theta_0] \\ & + \sin[(mp_1-jn_2)(\theta-\frac{mp_1\omega_1-jn_2\omega_2}{mp_1-jn_2}t)+mp_1\theta_0]\Bigg) \end{aligned} \tag{2.9}$$

In order for the torque to be created the radial field harmonic component from the outer rotor must match the harmonic component created by the modulated inner rotor field. This will occur if [33, 56]

$$p_{m,j} = |mp_1 + jn_2|$$
$$\text{where} \quad m = 1,3,5,...,\infty \qquad (2.10)$$
$$j = 0,\pm1,\pm2,\pm,...,\pm\infty$$

and the angular rotational speed of the flux density harmonics is given by

$$\omega_{m,j} = \frac{mp_1}{mp_1 + jn_2}\omega_1 + \frac{jn_2}{mp_1 + jn_2}\omega_2 \qquad (2.11)$$

The velocity of the space harmonic in the outer air-gap is a combination of angular velocities of the harmonics from the inner and cage rotor. It can be seen from equation (2.11) that j=0 is not a valid choice as this will result in there being no inner and outer rotor speed change. It has been shown in [33, 56] that the highest asynchronous space harmonics can be obtained when $m = 1$ and $j = -1$. This means that in order to attain the highest torque density the number of pole pairs on the outer rotor should be equal to

$$p_3 = n_2 - p_1 \qquad (2.12)$$

The relation between the angular velocities of the three rotors can now be written as

$$\omega_{1,1} = \frac{p_1}{p_1 - n_2}\omega_1 - \frac{n_2}{p_1 - n_2}\omega_2 \qquad (2.13)$$

$\omega_{1,1}$ is the speed on rotor 3 (ω_3=$\omega_{1,1}$). The inner rotor has the least number of pole-pairs (as shown in Figure 2-1). Rearranging (2.13) one can therefore write

$$\omega_1 = \frac{n_2}{n_2 - p_3}\omega_2 - \frac{p_3}{n_2 - p_3}\omega_3 \qquad (2.14)$$

Assuming that there are no losses the torque relation between rotors can be derived from the conservation of power flow and is given by

$$T_1\omega_1 + T_2\omega_2 + T_3\omega_3 = 0 \tag{2.15}$$

where T_1, T_2, T_3 are the torques on the inner rotor, cage rotor and outer rotor respectively.

When the cage rotor is held stationary, i.e. ω_2=0, the speed ratio is given by

$$\omega_1 = \frac{-p_3}{n_2 - p_3}\omega_3 \tag{2.16}$$

Now substituting (2.16) into (2.15) gives the relation between the inner rotor and cage rotor torque as

$$T_2 = -\frac{n_2}{n_2 - p_3}T_1 \tag{2.17}$$

Similarly when the outer rotor is stationary, ω_3=0, (2.14) reduces to

$$\omega_1 = \frac{n_2}{n_2 - p_3}\omega_2 \tag{2.18}$$

Substituting (2.18) into (2.14) gives the torque relationship between the outer and inner rotors

$$T_3 = \frac{p_3}{n_2 - p_3}T_1 \tag{2.19}$$

By combining (2.15) and (2.19) the torque relationship between the cage rotor and outer rotor is

$$T_2 = -\frac{n_2}{p_3}T_3 \tag{2.20}$$

Equation (2.19) shows that if $n_2 > p_3$ then the torque on the cage rotor will be greater than on the outer rotor and will be the other way round if $n_2 < p_3$. It appears that no authors have investigated designs which have $p_3 > n_2$.

The relation between the torques on the three rotors is

$$T_1 + T_2 + T_3 = 0 \tag{2.21}$$

This relationship can be confirmed by substituting (2.16) and (2.18) into (2.20), this gives

$$T_1 - \left(\frac{n_2}{n_2 - p_3} \right) T_1 + \left(\frac{p_3}{n_2 - p_3} \right) T_1 = 0 \tag{2.22}$$

Further rearranging the left side of (2.21) becomes zero.

2.3. Flux Focusing Approach

The MG models designed in the literature have mostly used surface mounted magnets for torque transmission. The air-gap flux density in a ferrite magnet rotor can be substantially increased by arranging the magnets in a flux focusing arrangement also called a spoke-type [62-65] and axial flux concentration [66] arrangement. A Spoke type rotor magnet arrangement gives a natural flux concentration capability because two circumferentially magnetized PMs buried between the steel cores as shown in Figure 2-3 contribute to the air-gap flux for each rotor pole. The flux concentration of magnets onto the steel can be seen in Figure 2-4. This flux concentration capability allows the air-gap magnetic flux density to be higher than the flux density of each PM that contributes to the air-gap magnetic flux density. This results in higher specific torque output than normal rotors.

With this type of arrangement the PMs are less likely to become demagnetized [63]. Although the spoke-type arrangement of magnets has many advantages, the

technology is not used worldwide significantly. One disadvantage of this type of arrangement is the complicated construction required to reduce or eliminate the PM flux leakage from the radially inward portions of the PMs as shown in Figure 2-5. Another disadvantage is the complicated construction required to retain the PMs and the pole pieces in the rotor during normal operation.

Ignoring fringing the theoretical peak flux focusing capability of a spoke type rotor with rectangular magnets is related by [67] .

$$\frac{B_{gm}}{B_m} = \frac{2P_1}{\pi} \tag{2.23}$$

where B_m is the flux density within the magnet and B_{gm} is the specified magnet air-gap flux density. Equation (2.23) can be derived by considering the relationship between the magnet length and steel pole arc length.

The steel pole arc length, l_s, of the inner rotor, as shown in Figure 2-3, is defined as

$$l_s = \frac{2\pi r_{o1} - 2P_1 l_m}{2P_1} \tag{2.24}$$

where r_{o1} is the outer radius of the inner rotor, P_1 is the number of pole-pairs and l_m is the length of the rectangular magnet. The length of the inner rotor magnet is defined as

$$L_1 = r_{o1} - r_{i1} \tag{2.25}$$

where r_{i1} is the inner radius of the inner rotor.

Ignoring leakage through the inner rotor arc, the flux across the outer arc length l_s is equal to the flux produced by the two adjacent magnets across length w_m. This can then be written as

$$B_{gm}\left(\frac{2\pi r_{o1}-2P_1 l_m}{2P_1}\right)=2w_m B_m \tag{2.26}$$

The maximum width w_m of the magnet occurs when the magnets just touch at the nonmagnetic core inner radius r_{i1} such that

$$r_{i1}=\frac{2P_1 l_m}{2\pi} \tag{2.27}$$

Thus the length of the inner rotor magnet L_1 can be written as

$$L_1 = r_{o1} - r_{i1} = r_{o1} - \frac{2P_1 l_m}{2\pi} \tag{2.28}$$

Substituting equation (2.28) into (2.26) we get

$$B_{gm}\left(\frac{\pi r_{o1}-P_1 l_m}{P_1}\right)=2\left(r_{o1}-\frac{P_1 l_m}{\pi}\right)B_m \tag{2.29}$$

By rearranging the terms and simplifying we get equation (2.23).

Therefore, in order to take advantage of the flux focusing the rotor should have more than 2 pole pairs.

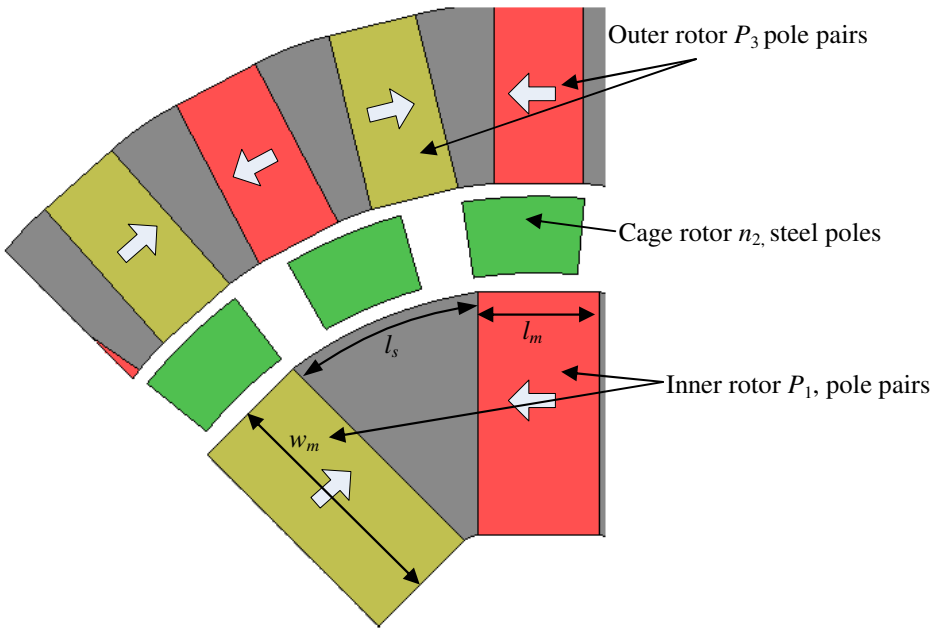

Figure 2-3: Flux focusing arrangement of magnets

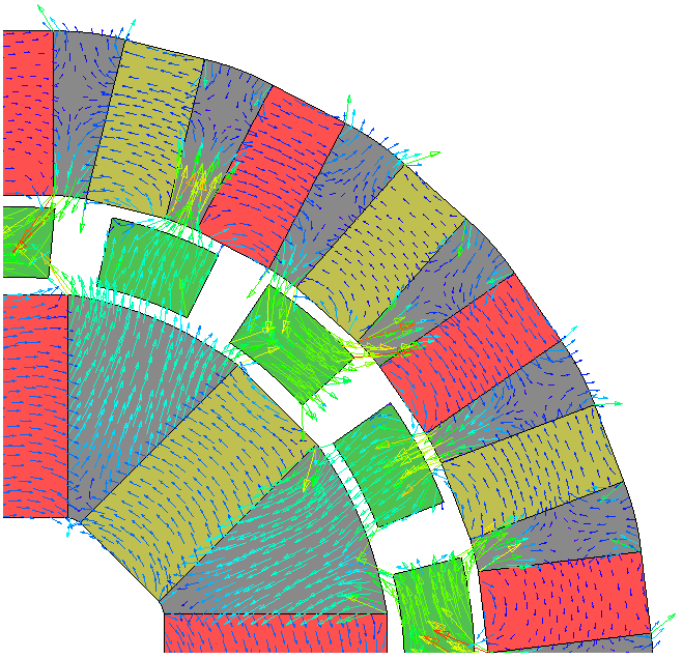

Figure 2-4: Magnetic flux concentrating on the steel

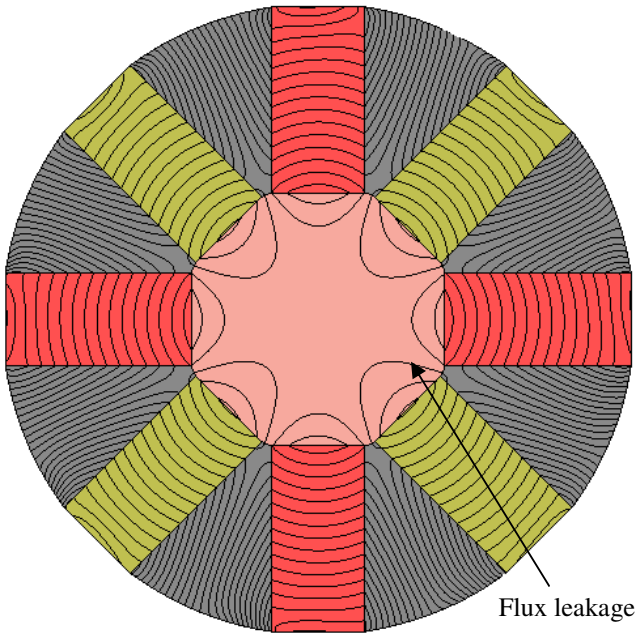

Figure 2-5: Flux leakage on the shaft of inner rotor

2.4. Finite Element Analysis

FEA is used for simulating the performance of the MG designs. FEA simulations have been run using the JMAG software package. It is used for 2-D and 3-D electromagnetic transient and static analysis. FEA involves dividing the geometry into elements called mesh. The field inside each element is represented by a polynomial and the set of equations for unknown coefficients are solved in order to obtain the final solution. In this thesis the design and analysis of the FFMG is accomplished by using the 2-D transient electromagnetic analysis module and the magnetostatic module of JMAG. The deflection analysis is performed using the 3-D electromagnetic and structural analysis modules of JMAG. Figure 2-6 shows the FFMG design using JMAG and Figure 2-7 shows the corresponding vector potential, radial and absolute values of the flux density as well as the mesh plot. It can be seen that the mesh elements are relatively fine. The size and the number of elements will determine the accuracy of the results. The greater the number of elements the better will be the accuracy. However, increasing the number of elements also increases the computation time and also the size of the result file.

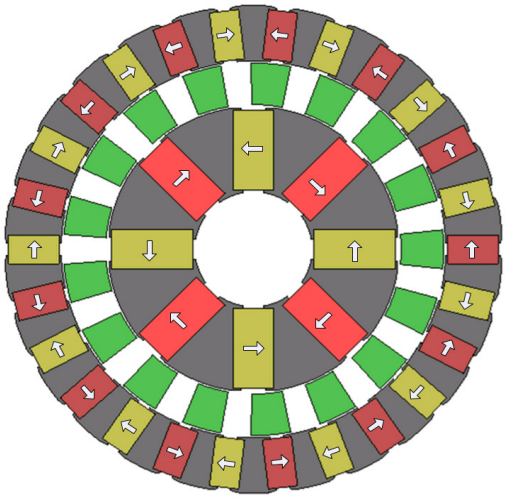

Figure 2-6: 2D model of FFMG using JMAG

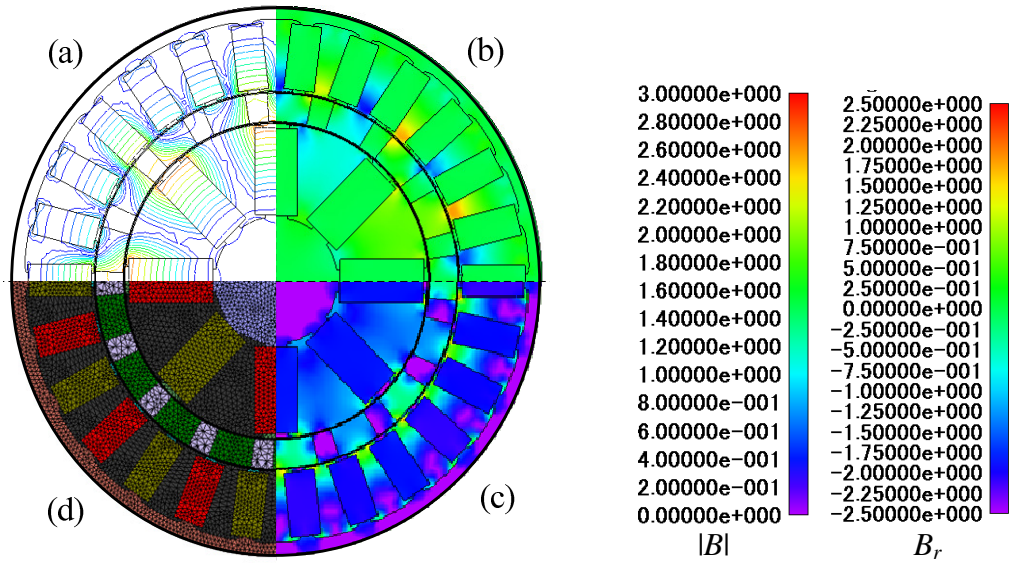

Figure 2-7: Mosaic plot, a) magnetic vector potential field lines, b) radial flux density B_r, c) flux density magnitude |**B**|, d) finite element analysis mesh plot

2-D transient electromagnetic analysis can output the results like magnetic fields, forces and electromagnetic torque on the rotors along with the eddy current and hystersis losses. Initially 2-D transient analysis is run by rotating one rotor. This will give the position of the rotor relative to other rotors which results in the transfer of the maximum torque between rotors. Once this position is determined the geometry is fixed in this position and magnetostatic analysis can be run instead of transient analysis. This will greatly reduce the computing time and size of the result file. For magnetomechanical analysis the 3 -D magnetostatic analysis is used and these results are used as the input to the 3-D structural analysis.

CHAPTER 3 : SUB-SCALE FLUX FOXUSING MAGNETIC GEAR DESIGN

3.1. Introduction

In this chapter the design, construction and experimental evaluation of a sub-scale coaxial FFMG is presented. Experimental and analysis results for the following three different designs will be presented.

I. Design with ferrite magnets on the inner and outer rotor

II. Design with NdFeB magnets on the inner rotor and ferrite magnets on the outer rotor

III. Design with NdFeB magnets on the inner and outer rotor

In Section 3.2 the design and topology of the MG is presented. In section 3.3 the parametric sweep analysis of the design is presented. Section 3.4 presents the deflection analysis of the cage rotor bars due to the radial magnetic forces created by inner and outer rotor, section 3.5 presents the final design after optimization and section 3.6 presents the experimental construction and results.

3.2. MG Design

The initial design parameters for the sub-scale FFMG are shown in Figure 3-1. The inner rotor with p_1=4 pole-pairs was initially designed using an existing Pacific Scientific F46 spoke-type rotor as shown in Figure 3-2. The FFMG cage rotor with n_2=17 iron segments and the outer rotor with p_3=13 pole-pairs were constructed around this rotor. However, in the final design the Pacific Scientific rotor was not used and a new rotor was

designed with the same dimensions but with shorter stack length. The reason for doing this is explained in section 3.4.

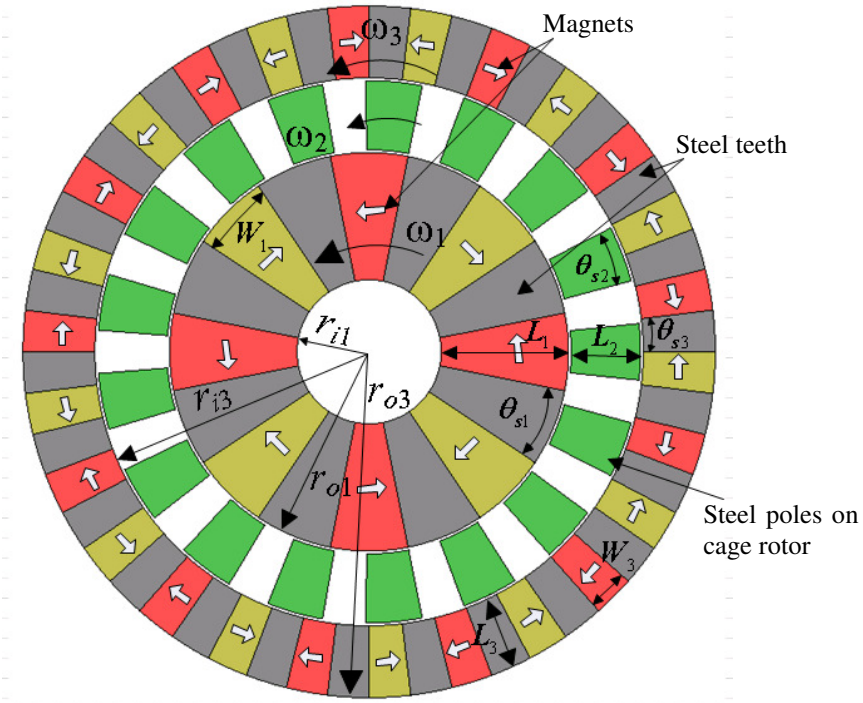

Figure 3-1: Magnet gear using surface PMs. p_1=4 pole-pairs, n_2=17 steel poles and p_3=13 pole-pairs on outer rotor.

Table 3-1: Initial MG parameters

	Description	Value	Units
Inner rotor	Pole pairs, p_1	4	
	Inner radius, r_{i1}	13	mm
	Outer radius, r_{o1}	33	mm
	Steel pole span, θ_{s1}	π/8	rad.
	Airgap, g	0.5	mm
Cage rotor	Steel poles, n_2	17	-
	Inner radius, r_{i2}	33.5	mm
	Outer radius, r_{o2}	46.5	mm
	Steel pole span, θ_{s2}	π/15	rad.
Outer cylinder	Pole pairs, p_3	13	-
	Inner radius , r_{i3}	47	mm
	Outer radius, r_{o3}	59	mm
	Steel pole span, θ_{s3}	π/26	rad.
	Airgap, g	0.5	mm
Material	Magnet, TDK FB3G	0.46	T
	Steel resistivity	$5.7\text{x}10^{-7}$	Ω-m
	Stack length, d	152.4	mm

Figure 3-2: Pacific Scientific F46 flux focusing rotor used as inner rotor

As can be seen from Figure 3-1, the magnets are arranged in a spoke-type arrangement embedded between the steel teeth. The air-gap flux density in a magnet rotor can be significantly improved by arranging the magnets in such a flux focusing arrangement also called a flux concentration arrangement as discussed in the previous chapter. Table 3-1 shows the initial MG parameters. An air-gap of g=0.5mm has been chosen between each rotor.

The relation between the angular velocities between the three rotors is

$$\omega_1 = \frac{p_3}{p_3 - n_2}\omega_3 + \frac{n_2}{n_2 - p_3}\omega_2 \tag{2.15}$$

In order to achieve the highest torque, the outer rotor is held stationary,ω_3=0. Since $p_3 - n_2 = p_1$, equation (2.15) becomes

$$\omega_1 = \frac{n_2}{p_1}\omega_2 = G_{12}\omega_2 \tag{3.1}$$

With p_1=4 pole pairs and n_2=17 steel poles a gear ratio of 4.25:1 is obtained. This gear ratio combination was chosen because Gouda's analysis [68] indicated that a maximum torque density is obtained when the gear ratio is between 3 and 5.

When designing the MG the torque ripple in the FFMG must also be considered. The torque ripple can be minimized by considering the cogging factor due to the PMs. The cogging factor is defined by [69]

$$C_f = \frac{2p_1 n_2}{LCM(2p_1, n_2)} \tag{3.2}$$

where *LCM*=lowest common multiple.

The pole combinations have been chosen so that all the conditions are satisfied. The cogging factor C_f =1 is obtained for the chosen pole combinations.

3.3. Parameter Optimization Analysis

In order to improve the performance of the FFMG, parametric optimization of the outer and cage rotor bars is performed by varying the radii and widths. The flux concentration between the rotors can be defined in terms of the ratio of the inner and outer radii of the three rotors. A parameter sweep analysis is performed to improve this flux concentration ratio.

3.3.1. Inner Rotor Flux Concentration Ratio

The flux focusing is achieved by changing the flux flowing through the width of the steel pole relative to the length of the magnets. Defining

$$L_1 = r_{o1} - r_{i1} \tag{3.3}$$

$$W_{s1} = r_{o1}\theta_{s1} \tag{3.4}$$

where r_{i1} = inner rotor radius, r_{o1} = outer rotor radius and θ_{s1} = steel pole span. Ignoring fringing and assuming that all the flux is flowing into the cage rotor poles, the magnet and air-gap flux relationship must be

$$B_{g1} W_{s1} d = B_{m1} 2 L_{m1} d \tag{3.5}$$

where B_{g1} = flux density from the inner rotor steel pole. B_{m1} = inner rotor magnet flux density, d = stack length. Therefore, a flux concentration ratio can be defined as

$$C_{\varphi 1} = \frac{B_{g1}}{B_{m1}} = \frac{2}{\theta_{s1}}\left[1 - \frac{r_{i1}}{r_{o1}}\right] \tag{3.6}$$

Using the values given in Table 3-1 the flux concentration ratio for the inner rotor is $C_{\varphi 1}$ = 3.09.

3.3.2. Outer Rotor Magnet Width, W_3 Optimization

As shown in Chapter 2 the dominant harmonic of the field is responsible for transferring maximum torque between rotors. Hence the maximization of the 13th radial flux density harmonic component is key to achieving maximum outer rotor torque transmission capability. Therefore, the outer rotor magnet width, W_3, cage rotor pole span, θ_{s2} and outer cylinder length were all varied and the 13th harmonic and torque values were studied. It was determined that the choice of the optimal magnet width was not changed by varying the pole span or outer cylinder length. For instance, Figure 3-3 shows that the peak 13th harmonic for different cage rotor span values is always at W_3=7mm. Similarly the peak torque value for different outer cylinder lengths, L_3, is always at W_3=7mm as shown in Figure 3-4. Consequently the magnet widths W_3 was chosen to be 7mm. This gives an outer rotor steel span θ_{s3} of $\pi/26 = \pi/(2p_3)$ radians.

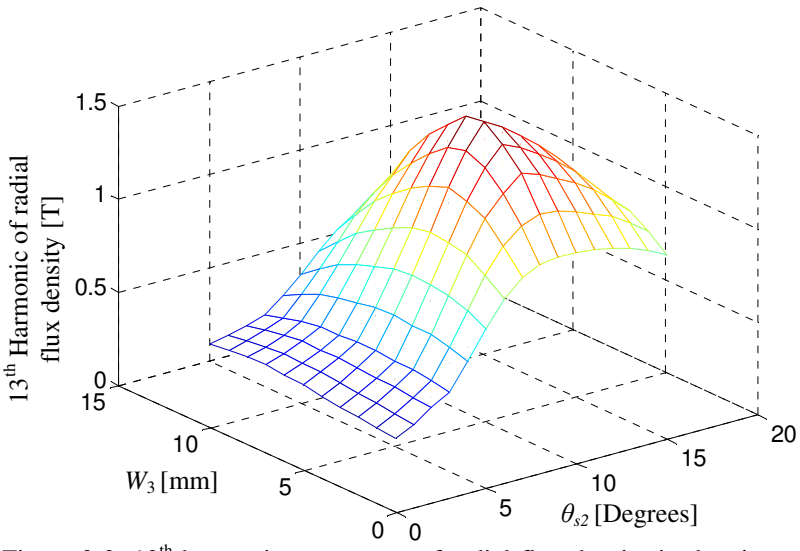

Figure 3-3: 13th harmonic component of radial flux density in the air-gap adjacent to outer rotor for varying widths of outer rotor magnets, W_3 and steel poles span θ_{s2}

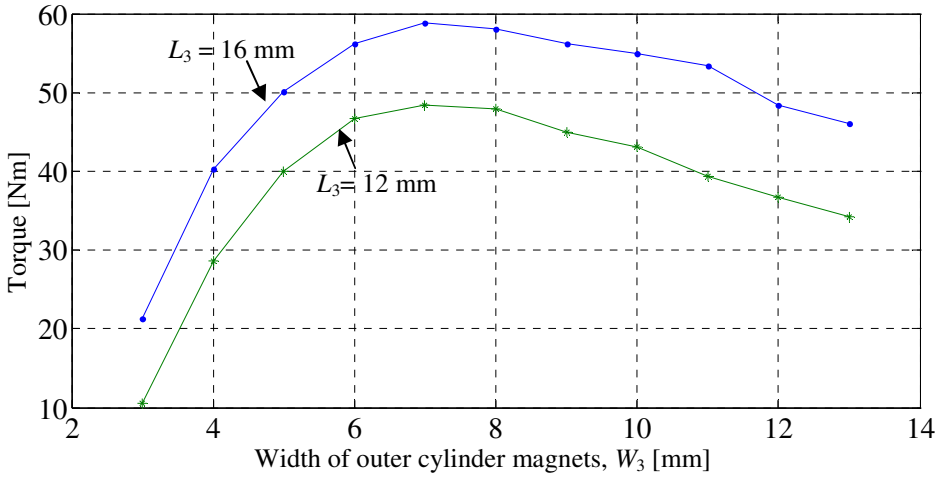

Figure 3-4: Torque comparison for two different outer cylinder magnet thicknesses, L_3

3.3.3. Outer Cylinder Magnet Length, L_3 Optimization

For the outer cylinder the flux is concentrated inwards. Defining

$$L_3 = r_{o3} - r_{i3} \tag{3.7}$$

$$W_{s3} = r_{i3}\theta_{s3} \tag{3.8}$$

Then the magnet and air-gap flux are related by

$$B_{g3}W_{s3}d = B_{m3}2L_3d \tag{3.9}$$

where B_{g3} = flux density from the outer cylinder steel pole and B_{m3} = outer cylinder magnet flux density. The outer cylinder flux concentration ratio is then

$$C_{\varphi 3} = \frac{B_{g3}}{B_{m3}} = \frac{2}{\theta_{s3}}\left[\frac{r_{o3}}{r_{i3}} - 1\right] \tag{3.10}$$

With θ_{s3}= π/(2p_3) radians and r_{i3}=47mm held fixed. The outer cylinder radius r_{o3} was varied from r_{o3}=55 to 65 mm. The other parameters determined from the previous analysis are kept constant. The resultant torque and torque density values as a function of the $C_{\varphi 3}$ is shown in Figure 3-5. Based on this analysis $C_{\varphi 3}$=5.28 gives the highest torque density. This corresponds to an outer radius r_{o3}=62mm**.**

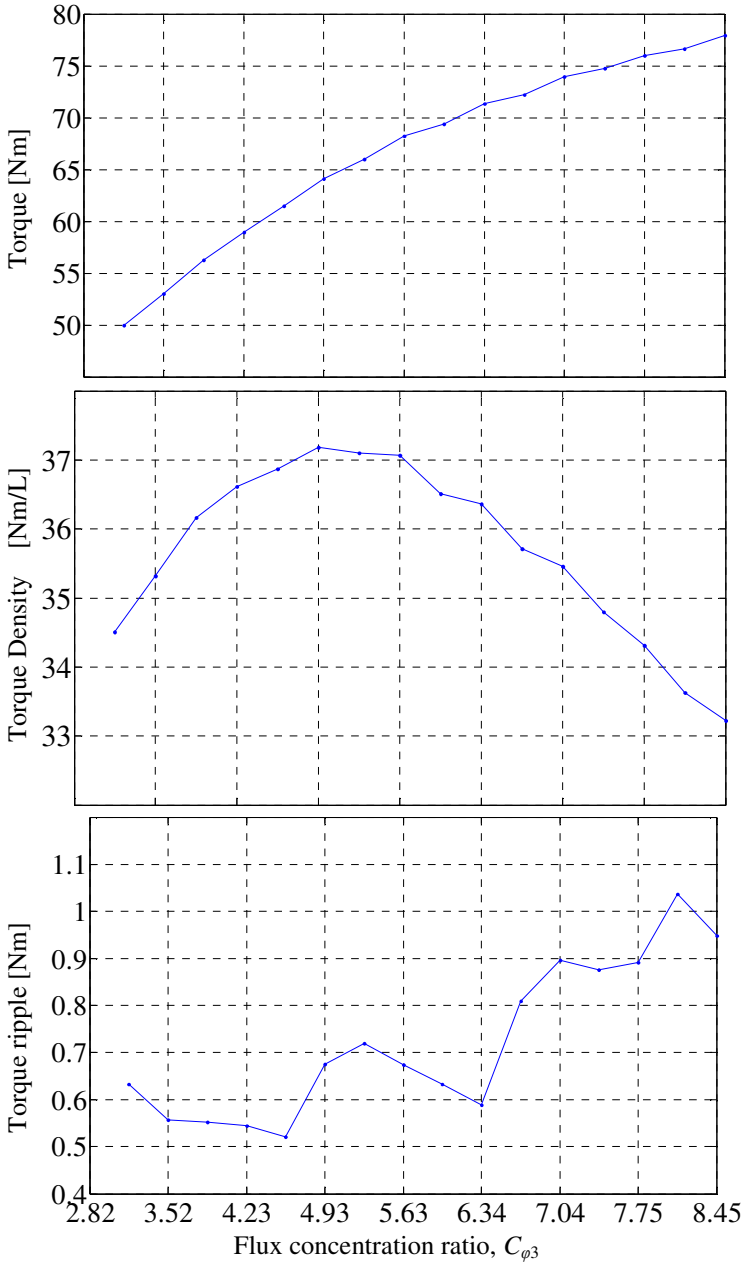

Figure 3-5: Torque, torque density and torque ripple comparison for varying flux concentration ratio, $C_{\varphi 3}$

3.3.4. Steel Rotor Cage length, $L_{2,}$ Optimization

With W_3=7mm and $L_{3.}$=15mm held constant the radial length of the cage rotor steel poles, L_2 was varied. The torque, torque density and torque ripple as a function of L_2 is shown in Figure 3-6.

The change in this length consequently also changed the outer cylinder dimensions; this resulted in the torque density decreasing with increasing L_2. Based on this analysis the radial length of the steel poles was chosen to be L_2=6mm.

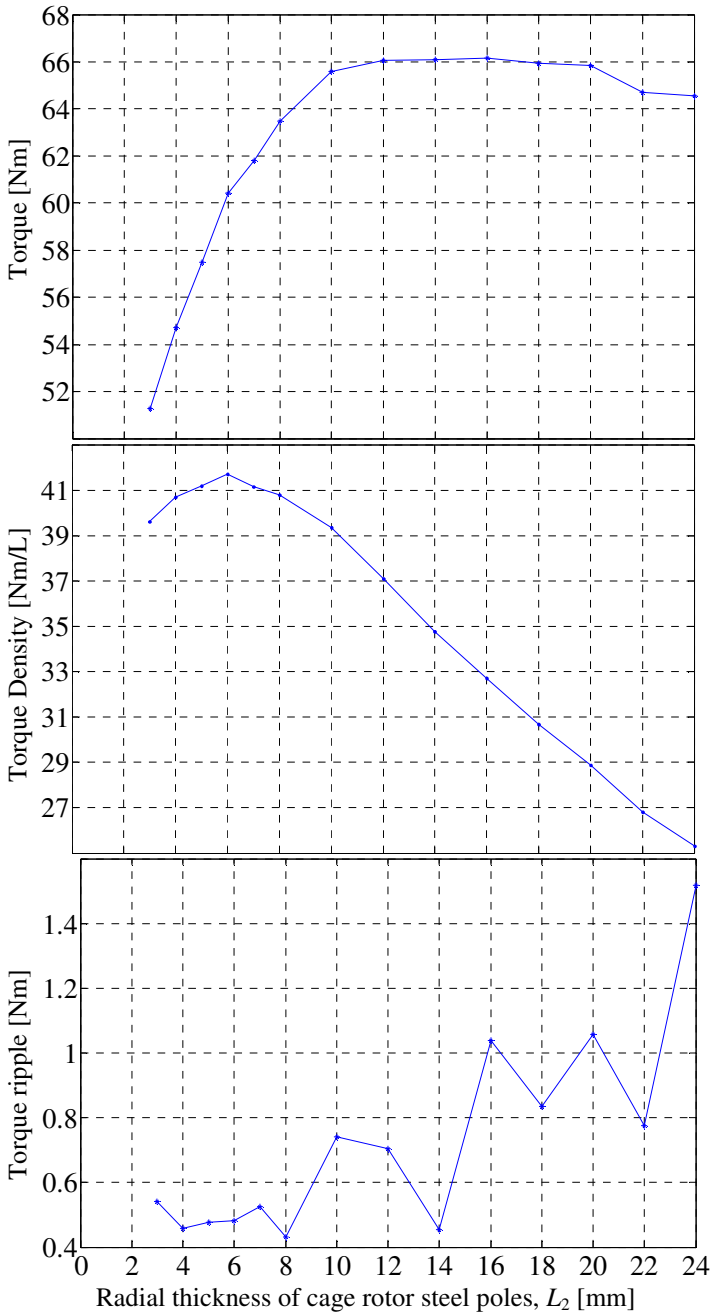

Figure 3-6: Torque, torque density and torque ripple comparison when the cage rotor steel thickness L_2 is varied.

3.3.5. Cage Rotor Steel Pole Width Span, $\theta_{s2,}$ Optimization

The ratio of the cage rotor steel pole span, θ_{s2}, with respect to the outer cylinder steel pole span, θ_{s3}, is defined as

$$W_{s23} = \frac{\theta_{s2}}{\theta_{s3}} \tag{3.11}$$

θ_{s2} was varied while θ_{s3} was held constant at π/26 radians, the variation of this angular span with respect to torque and torque density is shown Figure 3-7. The other parameters W_3=7mm, L_3=15mm and L_2=6mm obtained from the previous analysis were fixed. The analysis shows that the peak torque occurs when W_{s23}=2.02. This corresponds to an angular span, $\theta_{s2}=\pi/p_3$. The final parameters after optimization are shown in Table 3-2 and the final flux concentration ratios are shown in Table 3-3.

Table 3-2: Fixed geometric parameters and material properties

	Description	Value	Units
Inner rotor	Pole pairs, p_1	4	-
	Inner radius, r_{i1}	13	mm
	Outer radius, r_{o1}	33	mm
	Steel pole span, θ_{s1}	π/8	rad.
	Airgap, g	0.5	mm
Cage rotor	Steel poles, n_2	17	-
	Inner radius, r_{i2}	33.5	mm
	Outer radius, r_{o2}	39.5	mm
	Steel pole span, θ_{s2}	π/p_3	rad.
Outer cylinder	Pole pairs, p_3	13	-
	Inner radius , r_{i3}	40	mm
	Outer radius, r_{o3}	55	mm
	Steel pole span, θ_{s3}	π/26	rad.
	Airgap, g	0.5	mm
Material	Ferrite magnet, Hitachi NMF12F	0.46	T
	Magnet, NdFeB, N40H, B_r	1.25	T
	416 steel resistivity	0.570	μΩ-m
	1018 steel resistivity	0.159	μΩ-m
Active region stack length, d		76.2	mm

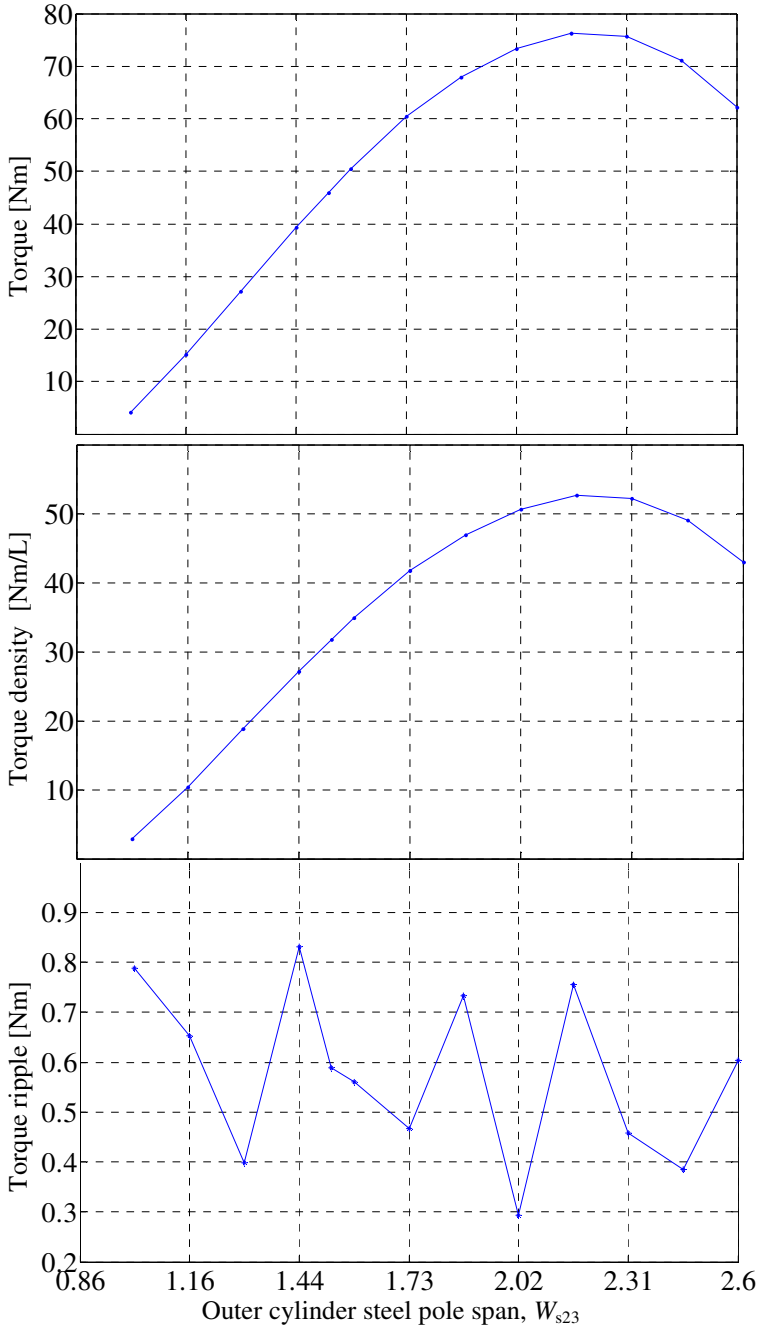

Figure 3-7: Torque ripple comparison for varying outer cylinder steel pole span values

Table 3-3: Key design parameters

Flux concentration ratio	$C_{\varphi 3}$	5.28
	$C_{\varphi 1}$	3.08
Angular span ratio	W_{s23}	2.02
Angular span [radians]	θ_{s1}	$\pi/(2p_1)$
	θ_{s2}	π/p_3
	θ_{s3}	$\pi/(2p_3)$

Figure 3-8 shows the final torque obtained when using ferrite magnets with residual flux density, B_r=0.38T. A maximum torque of 73 Nm is predicted giving an active region torque density of 50.4 Nm/L. Similarly, Figure 3-9 gives the corresponding torque values for B_r=0.46 T ferrite magnets.

Table 3-4 summarizes the torque and torque density values for different ferrite magnets with and without a magnetic steel inner shaft. It can be seen that a torque of 95.5Nm can be achieved by using the Hitachi NMF ferrite magnets with a corresponding remnant flux density value of 0.46 T. This corresponds to a torque density of 65.5Nm/L when using the Hitachi magnets. When a magnetic steel shaft is introduced on the inner rotor it is observed that the external field is significantly reduced due to the field leakage through the shaft. When these inner rotor changes are incorporated the predicted torque significantly decreases.

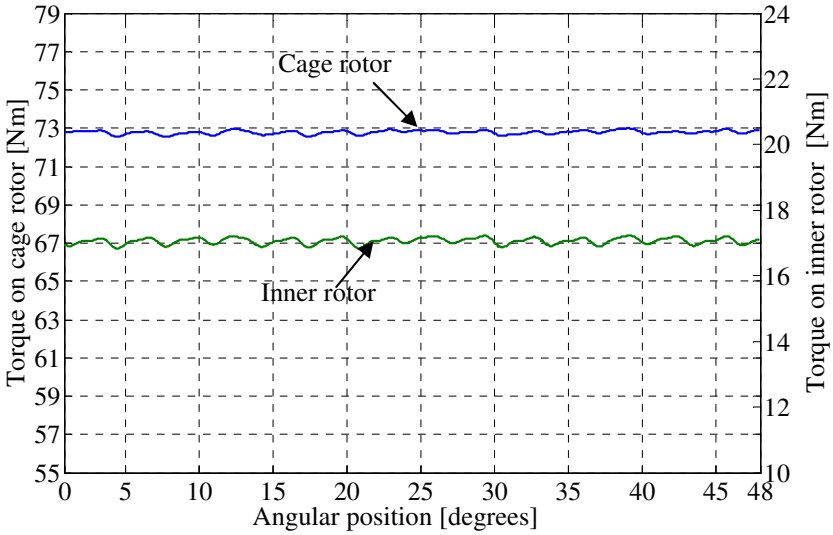

Figure 3-8: Torque when using ferrite magnets with B_r=0.38T.

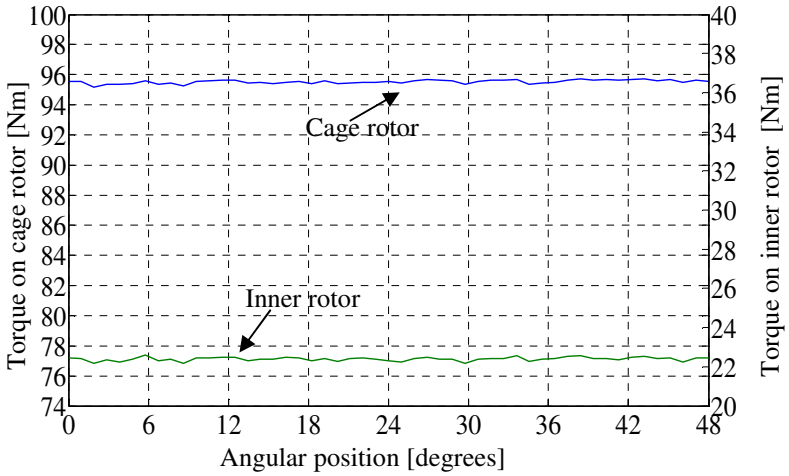

Figure 3-9: Torque when using ferrite magnets with B_r=0.46T

Table 3-4: Torque and torque density values for various ferrite magnets

Outer cylinder magnet, B_r	**Inner rotor magnet, B_r [T]**	**Shaft Diameter**	**Torque [Nm]**	**Torque Density [Nm/L]**
0.38	0.38	1in	58.5	40.5
0.43	0.31	1in	49	33.5
0.43	0.31	24mm	54.6	38
0.43	0.31	22mm	57.5	39.8
0.43	0.31	20mm	59	40.5
0.43	0.43	1in	75.6	52
0.43	0.43	No shaft	92.5	64
0.46	0.46	No shaft	95.5	65.5

3.4. Magnetomechanical Analysis

When a magnetically conducting plate such as a steel plate is placed near a stationary magnetic source, magnetic forces are created between the magnetic plates. When these forces are sufficiently high or the magnetic plate is sufficiently thin the plate will deflect. The forces can become so high that the plate can break. Moon and Pao [70-71] were the first to study the deflection of a cantilevered beam experimentally and analytically. In most electrical machines the elastic deformation due to these magnetic forces is negligibly small [69, 72] although it does play a role in creating vibration and acoustic noise [73-74]

Due to the small air-gaps and high forces created by the FFMG's inner and outer rotors, the cage rotor bars can significantly deflect. The deflection of the cage rotor steel poles will close the air-gap between the magnetic rotor and the steel bars leading to an increase in the magnetic force and consequently further deflection is seen on the steel poles. Therefore, the magnetic force and steel pole deflection is highly coupled and the deflection varies along the axial length of the steel poles.

In order to study the cage rotor steel pole deflection the magnetic forces were first calculated using JMAG 3-D nonlinear FEA with constant uniform air-gap along the axial length. The computed radial and tangential forces along the axial length on each FEA element were then imported into the JMAG 3-D mechanical FEA package to compute the resulting deflection values when the ends of the steel poles were held fixed. The new deflected steel pole position along the axial length was then again used to compute magnetic force on the cage bars and so on. This iterative process was continued until no further significant deflection of the bars was observed. Figure 3-10 summarizes the iterative procedure.

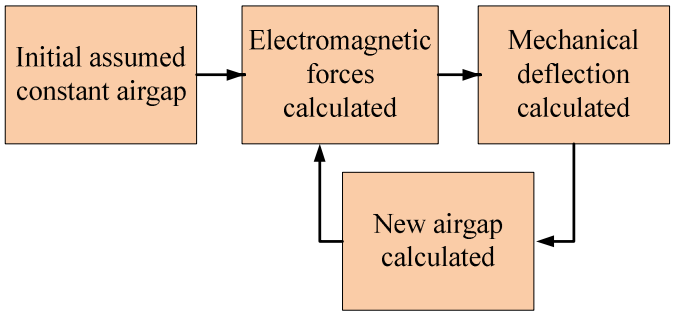

Figure 3-10: Iterative magnetomechanical deflection analysis procedure for the cage rotor bars

3.4.1. Deflection Analysis when using Pacific Scientific F46 rotor

The deflection of the cage rotor steel pole when using the Pacific Scientific F46 flux focusing rotor was verified following the procedure presented above. In order to

experimentally verify the deflection values obtained through FEA an experimental measurement of the deflection along the axial length of a single steel pole placed above the Pacific Scientific rotor was undertaken using an MDL400 TESA-Hite gauge (accurate to 0.00254mm) as shown in Figure 3-11 and Figure 3-12. An air-gap of 0.77 mm was used in this analysis.

Table 3-5 shows the properties of the steel used in the assembly. The 416 grade magnetic stainless steel was chosen to be used on the cage rotor as it has higher resistivity relative to the 1018 steel and therefore the induced eddy currents will be lower.

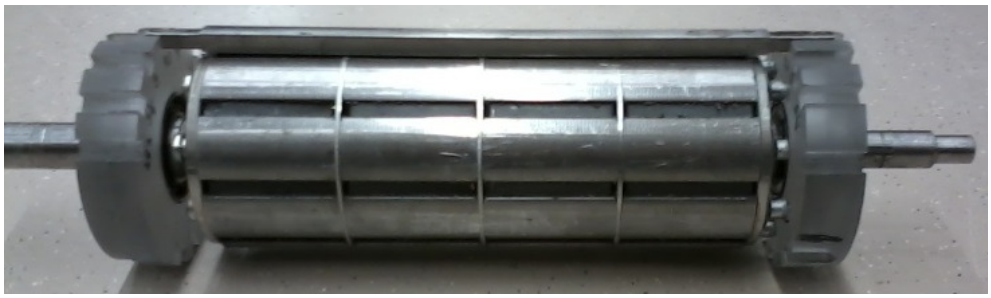

Figure 3-11: Pacific Scientific F46 rotor with a single cage bar. An air-gap of 0.77 mm was used

Table 3-5: Steel properties

	Description	Value	Units
Material Properties 1018 grade steel	Steel resistivity	1.59×10^{-7}	Ωm
	Poisson's ratio	0.3	-
	Density	7.85	g/cm^3
	Young's modulus	210000	Mpa
Material Properties 416 grade steel	Steel resistivity	5.7×10^{-7}	Ωm
	Poisson's ratio	0.29	-
	Density	7.75	g/cm^3
	Young's modulus	200000	MPa

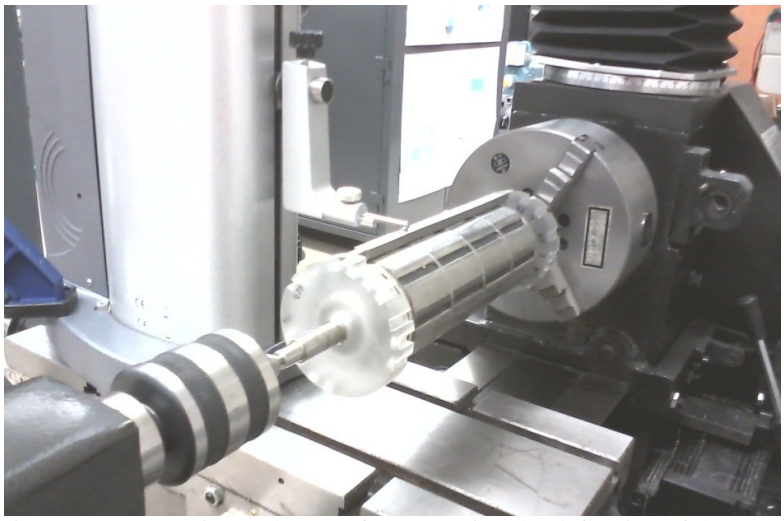

Figure 3-12: Experimental set up for measuring the deflection of the cage rotor bars using a TESA-Hite MDL 400 height gauge

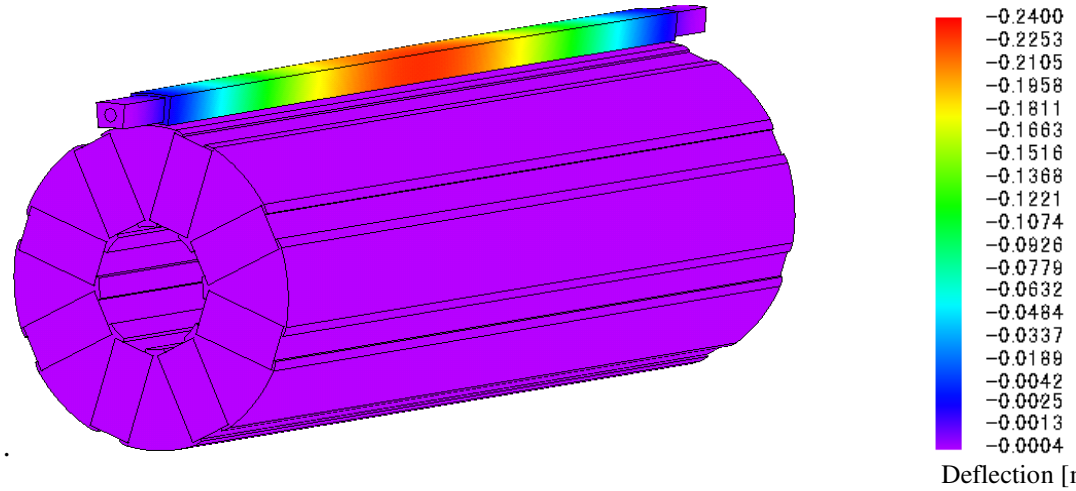

Figure 3-13: Deflection analysis of single cage rotor bar due to the inner rotor flux focusing rotor FEA magnetomechanical analysis results when the initial airgap is 0.77 mm.

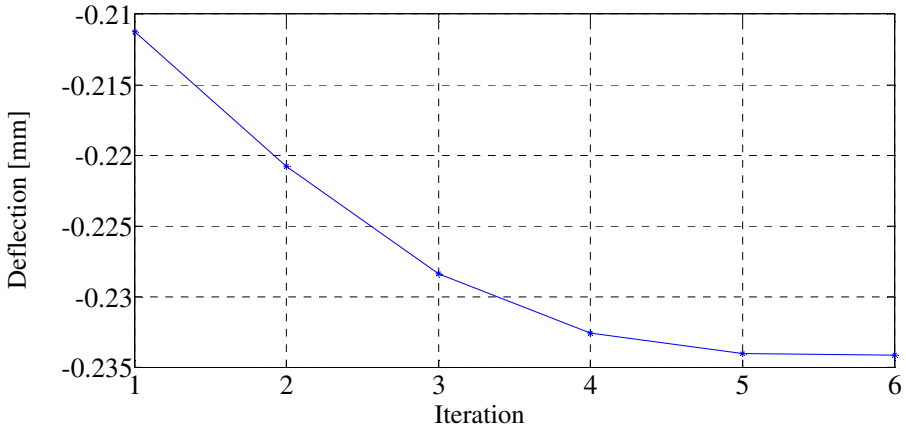

Figure 3-14: Net deflection amount as a function of FEA iteration at axial position z=3.5inches for a single cage rotor bar. The deflection results show the deflection amount from an initial air-gap of 0.77mm.

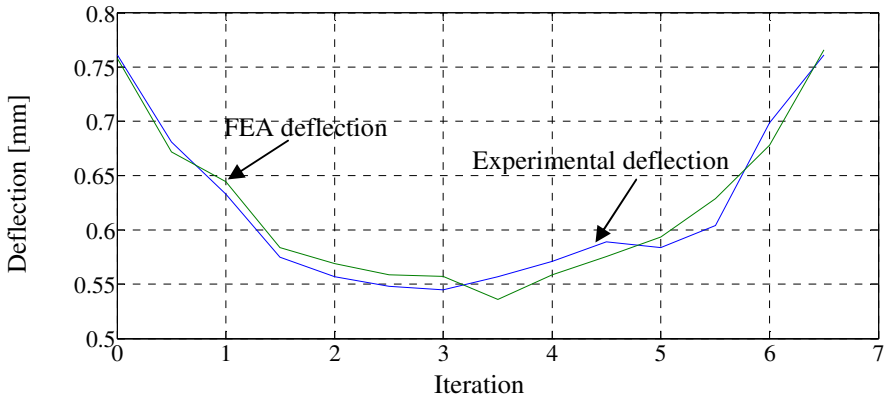

Figure 3-15: Air-gap reduction of a single cage rotor bar along its axial length due to the inner rotor magnetic force.

The deflection on the bar was studied by using the 3-D model shown in Figure 3-13. The calculated deflection as a function of iteration is shown in Figure 3-14. It can be seen that the iterations converge after 6 iterations and a maximum deflection of 0.24 mm is obtained. Figure 3-15 shows the measured and calculated air-gap reduction due to the deflection along the axial length of the cage rotor bar. It can be seen that there is a very close agreement between the calculated and experimental results. The experimental and calculated values are provided in Table 3-6.

Table 3-6: Deflection experimental and calculated data

Axial position (inches)	**FEA deflection [mm]**	**FEA air-gap change [mm]**	**Experimental deflection [mm]**	**Experimental air-gap change[mm]**
0	-0.009	0.761	-0.0120	0.7580
0.5	-0.089	0.681	-0.0982	0.6718
1	-0.137	0.633	-0.1256	0.6444
1.5	-0.195	0.575	-0.1861	0.5839
2	-0.213	0.557	-0.2011	0.5689
2.5	-0.222	0.548	-0.2115	0.5585
3	-0.225	0.545	-0.2126	0.5574
3.5	-0.213	0.557	-0.2341	0.5359
4	-0.199	0.571	-0.2114	0.5586
4.5	-0.181	0.589	-0.1947	0.5753
5	-0.186	0.584	-0.1764	0.5936
5.5	-0.166	0.604	-0.1412	0.6288
6	-0.071	0.699	-0.0920	0.6780
6.5	-0.009	0.761	-0.00393	0.76607

3.4.2. Magnetomechanical Analysis for a 6 Inch Axial length FFMG

The assembly of the FFMG is shown in the Figure 3-16. The air-gap between each rotor is 0.5 mm as previously mentioned. Figure 3-17 shows the calculated radial deflection of the cage rotor bars due to the inner and outer rotor magnets. It can be seen that the maximum deflection of 0.34 mm is predicted in the radial direction. Figure 3-18 shows the deflection of the cage rotor bars in the theta direction. A deflection of 0.1 mm is predicted in this direction. Figure 3-19 shows the iterative procedure followed for calculating the deflection. It can be seen that the iterations converge after four iterations and a maximum deflection of 0.34 mm is observed.

This level of deflection indicates that the deflection of the bars in a MG must be carefully designed in order to mitigate bending. With an initial air-gap of 0.5 mm it is not feasible to construct FFMG with such bending of the cage rotor bars. Hence based on this analysis the stack of the design has been reduced from 6 inches to 3 inches. This reduced the deflection of the cage rotor significantly as will be shown in the following section.

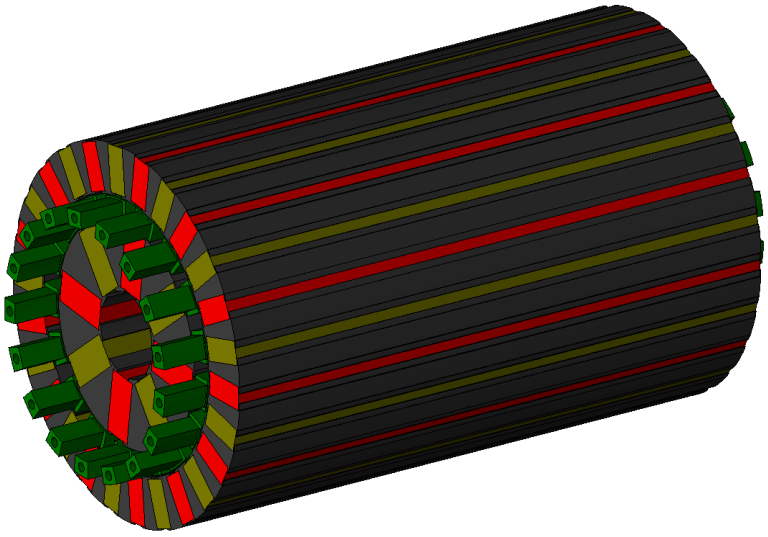

Figure 3-16: Assembly of MG with Pacific Scientific rotor as inner rotor

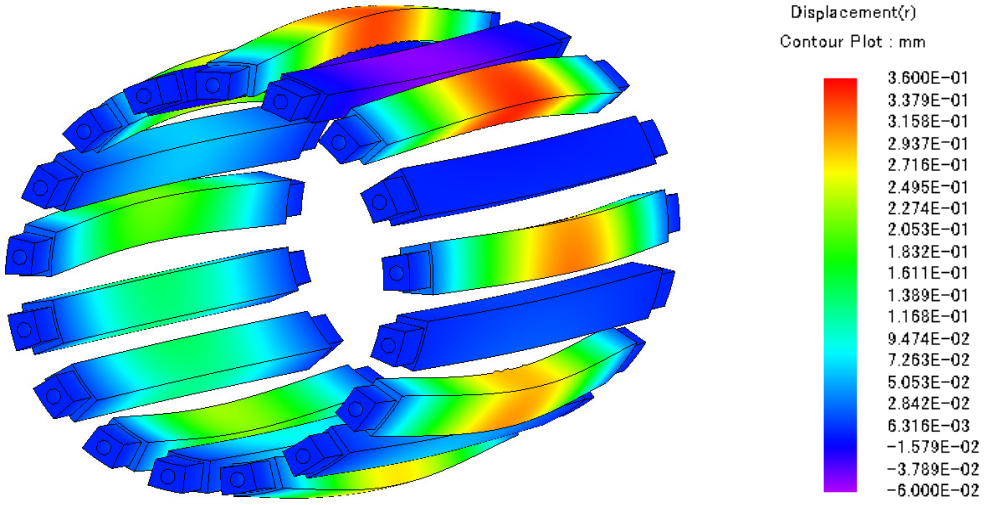

Figure 3-17: Radial deflection of the cage rotor bars due to the inner and outer rotor magnets

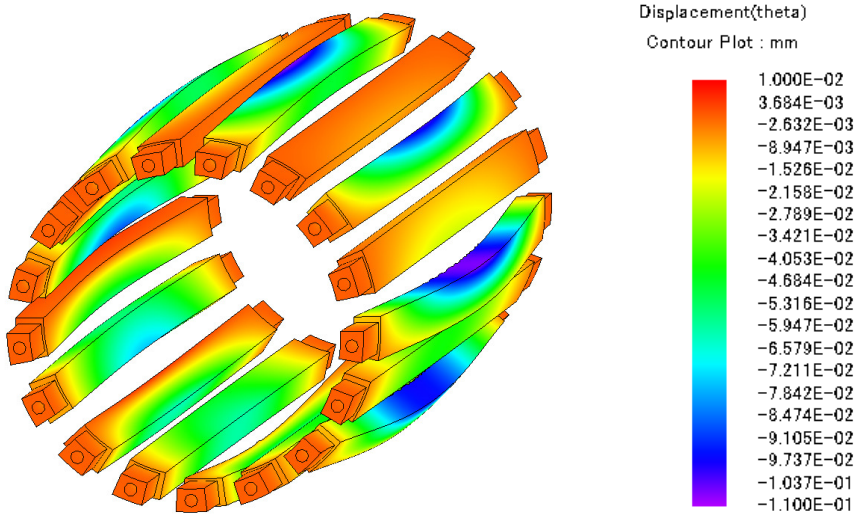

Figure 3-18: Deflection of the cage rotor bars in the theta direction due to the inner and outer rotor magnets

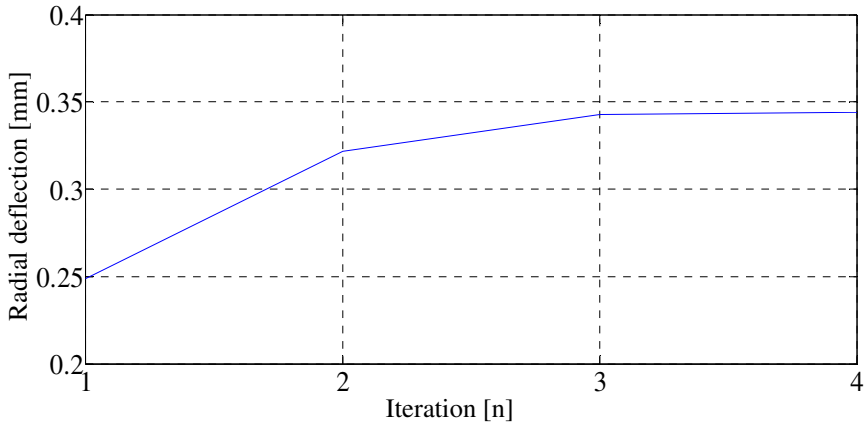

Figure 3-19: Maximum radial deflection of the cage rotor bars for the model for four iterations

3.4.3. Magnetomechanical analysis for 3 inch FFMG with ferrite magnets

Magnetomechanical analysis was performed on the FFMG with a 3 inch active stack length with ferrite magnets. Figure 3-20 shows the complete assembly of the 3 inch active stack length FFMG. The deflection in the radial direction and theta direction are shown in Figure 3-21 and Figure 3-22 respectively.

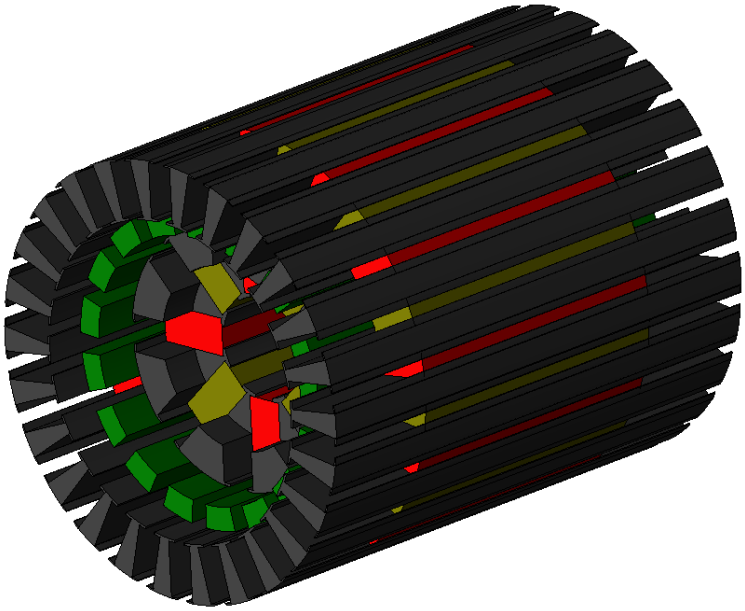

Figure 3-20: Sub-scale FFMG assembly with a 3 inch active stack length

A maximum deflection of 0.0178 mm is predicted as shown in Figure 3-23. The deflection values converge after 4 iterations.

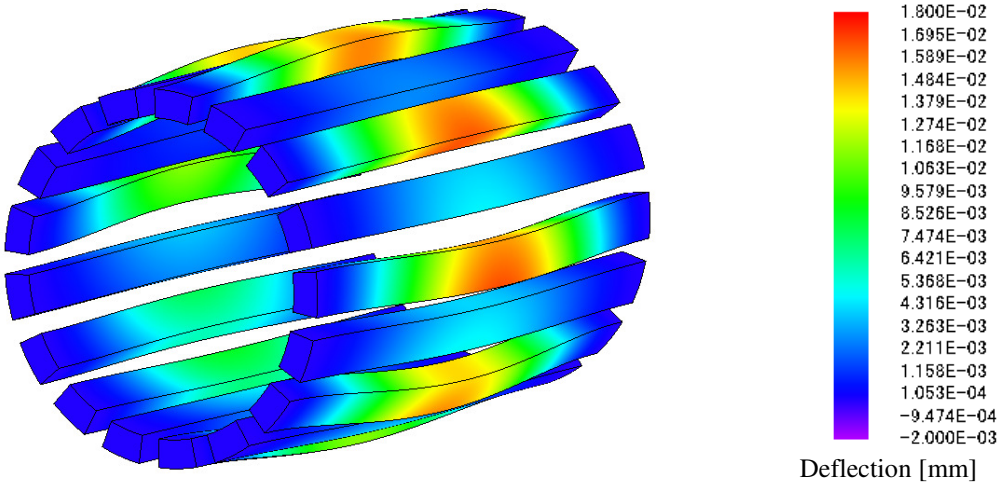

Figure 3-21: Radial deflection of the cage rotor bars with ferrite magnets on the inner and outer rotors

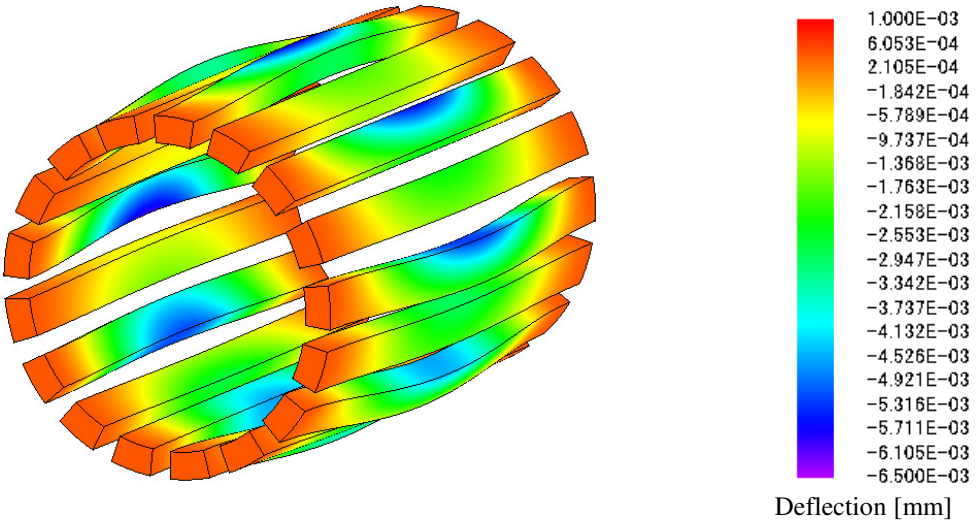

Figure 3-22: Deflection of cage rotor bars in the azimuthal direction with ferrite magnets on the inner and outer rotors

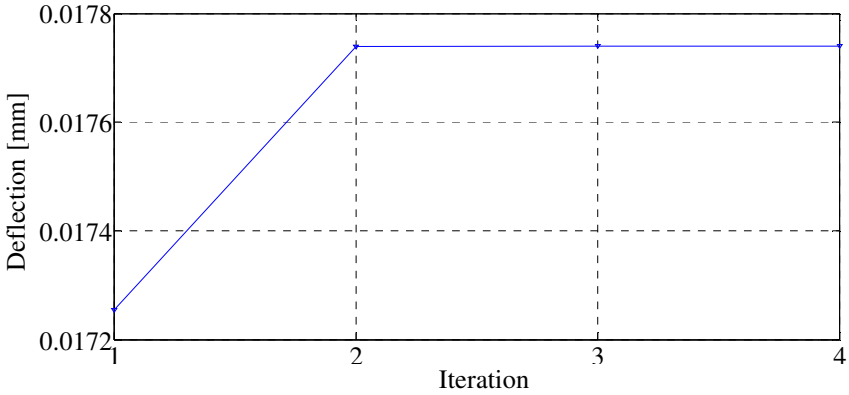

Figure 3-23: Maximum radial deflection of the cage rotor bars for the FFMG model without inner rotor

3.4.4. Magnetomechanical analysis for 3 inch model with NdFeB magnets

Magnetomechanical analysis is performed on the FFMG with a 3 inch active stack length with NdFeB magnets and B_r = 1.25 T. The ferrite magnets from the previous design are replaced with NdFeB magnets without otherwise changing the design. The deflection in the radial direction and azimuthal direction are shown in Figure 3-24 and Figure 3-25 respectively.

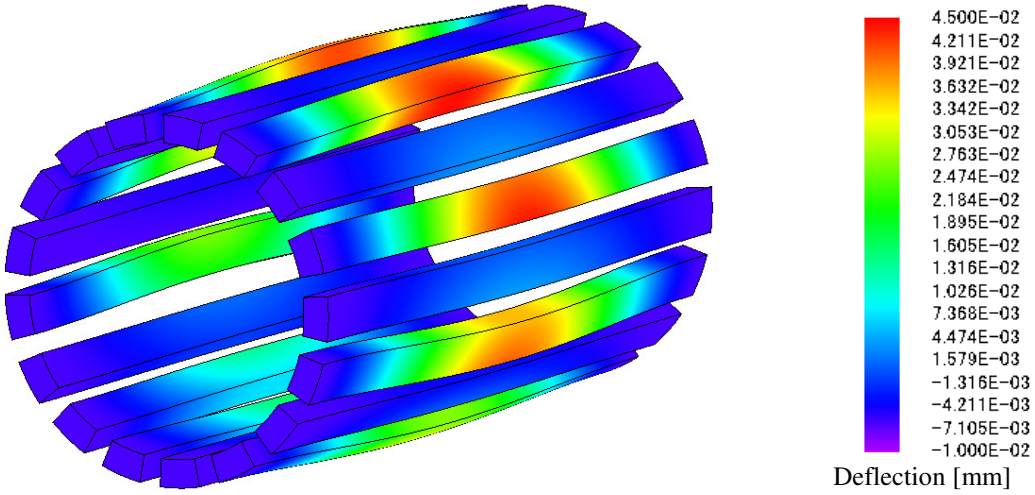

Figure 3-24: Radial deflection of cage rotor bars with NdFeB magnets on inner and outer rotors

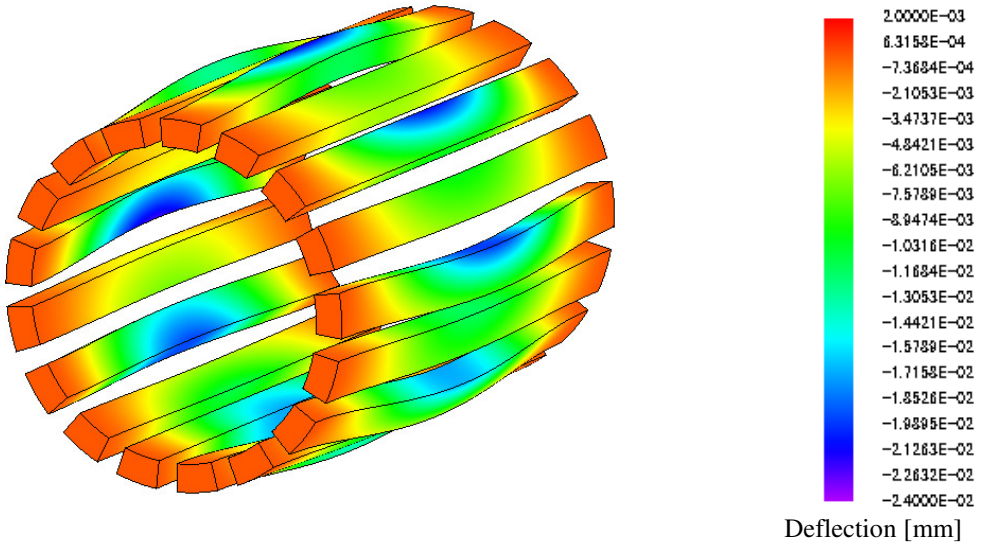

Figure 3-25: Deflection of cage rotor bars in the azimuthal direction with NdFeB magnets on inner and outer rotors

A maximum deflection of 0.044 mm is predicted as shown in Figure 3-26. The deflection values converge after 3 iterations.

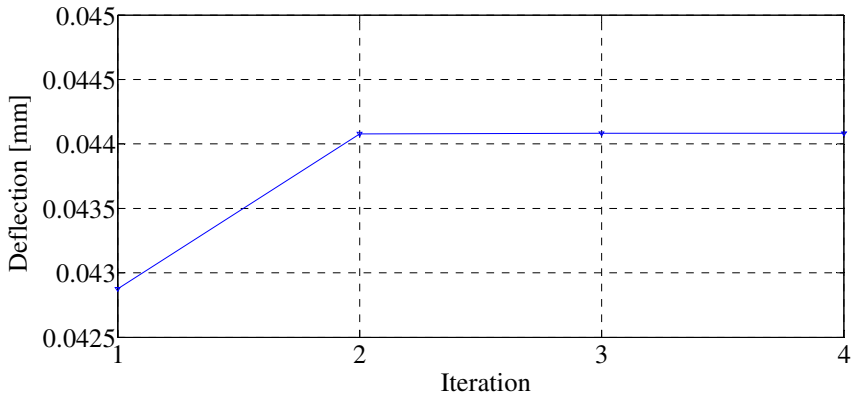

Figure 3-26: Maximum radial deflection of cage rotor bars for model without inner rotor for four iterations

It can be concluded from the analysis that the deflection for the 3 inch model with ferrite and NdFeB magnets is low and therefore will not pose any difficulties in construction.

3.5. Final Design

The final FFMG design is shown in Figure 3-27. In order to minimize cost the magnets are made rectangular in cross section. Also in order to retain the magnets in place and prevent them from moving out radially the inner and outer rotor steel teeth are provided with extensions that retain the magnets in place and give mechanical support to the design as shown in Figure 3-28.

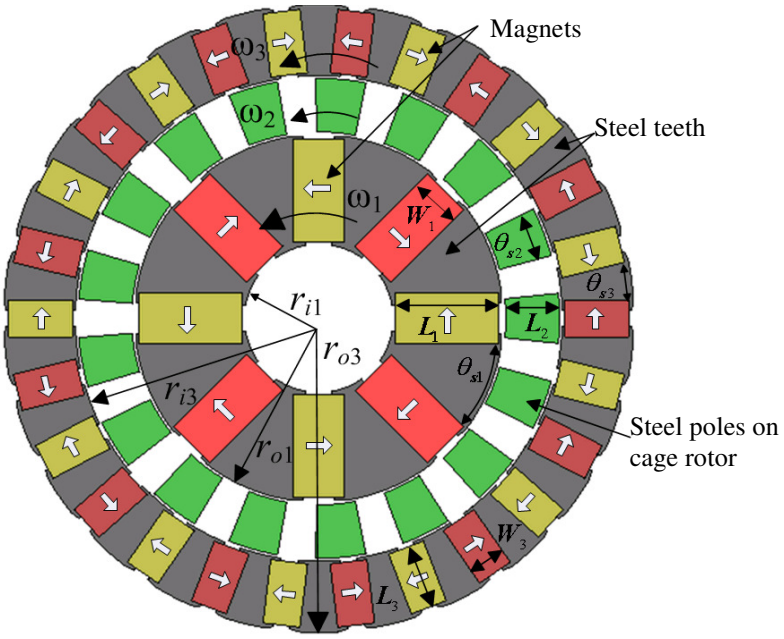

Figure 3-27: Final FFMG after optimization

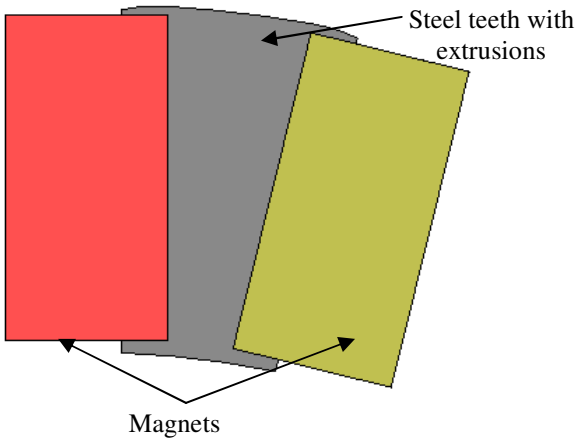

Figure 3-28: Final FFMG with steel teeth extrusion

Table 3-7 shows the material properties for the different steel grades. Grade 416 steel has been chosen for the cage rotor bars and 1018 grade steel is used for the inner and outer rotor cores.

Table 3-7: Material properties for different steel grades

	416 grade	**430 grade**	**1018 grade**	**M270-35A silicon steel**	**SMC**
Steel resistivity (μΩm)	0.51	0.6	0.16	520	150
Density (g/cm^3)	7.75	7.82	7.85	7.65	7.1
Tensile strength (MPa)	515	483	634	565	124

3.6. FFMG with Ferrite Magnets

The FFMG design with ferrite magnets was analyzed using FEA and the calculated torque and efficiency was experimentally verified. Figure 3-29 shows the predicted torque on the three rotors. A peak torque of 41 Nm on the cage rotor is predicted for this design. The torque is sinusoidal because only the inner rotor is rotated and all other rotors are held stationary. Figure 3-30 through Figure 3-33 shows the radial flux density curves in the inner and outer air-gaps of the FFMG. The figures clearly show the dominant 4th and 13th harmonics in the inner and outer air-gaps respectively.

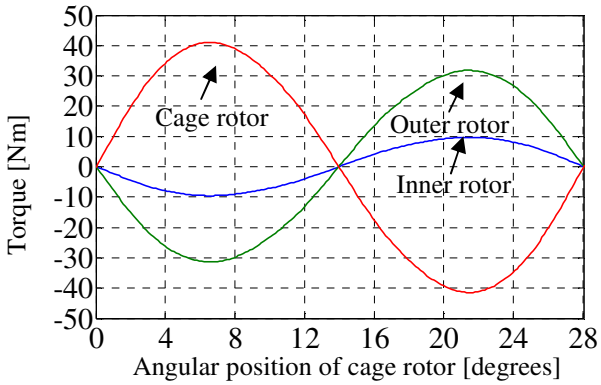

Figure 3-29: Predicted torque when using ferrite magnets and when only inner rotor is rotating.

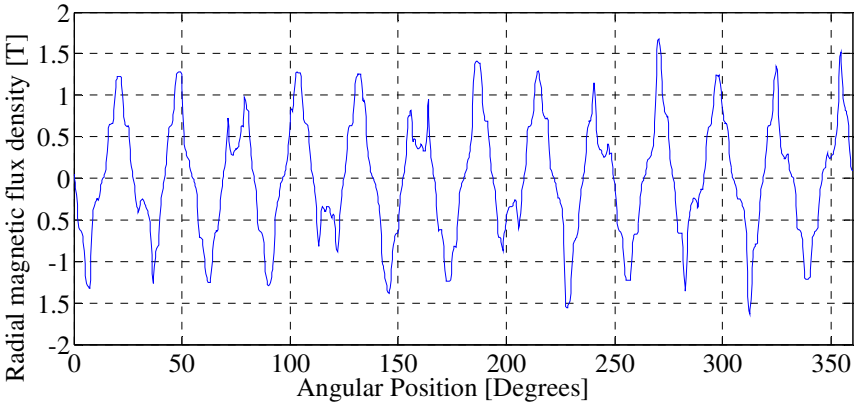

Figure 3-30: Radial flux density, B_r, in the outer rotor airgap adjacent to outer cylinder

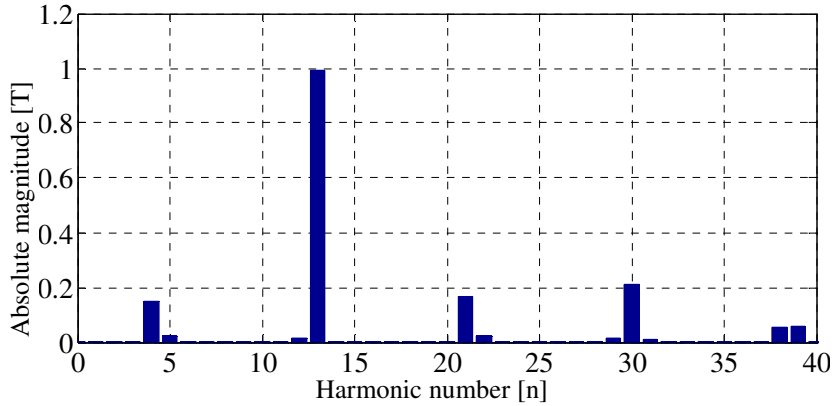

Figure 3-31: Spatial frequency analysis of radial flux density, B_r, in the outer rotor airgap adjacent to outer cylinder

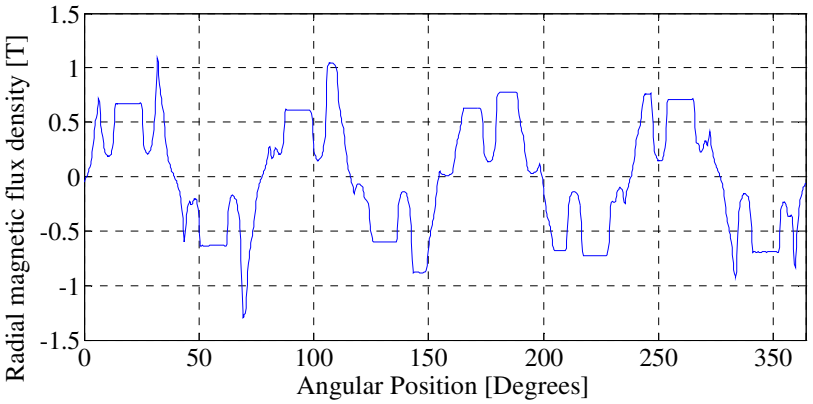

Figure 3-32: Radial flux density, B_r, in the inner rotor airgap adjacent to the inner rotor

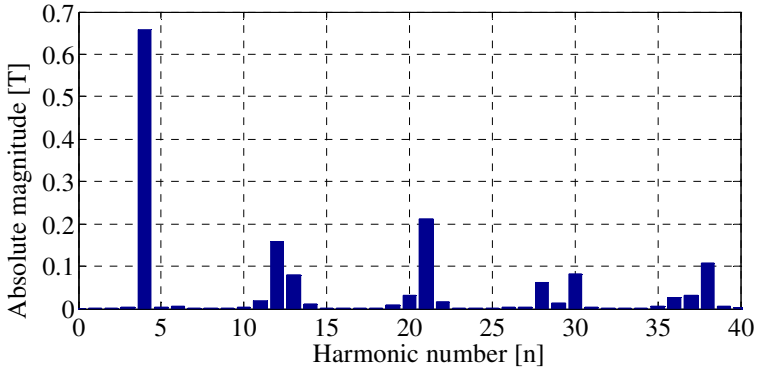

Figure 3-33: Spatial frequency analysis of the radial flux density, B_r, in the inner rotor airgap adjacent to the inner rotor

Figure 3-34(a) shows the inner rotor assembly with ferrite magnets. Figure 3-34(b) shows the assembly of the inner and cage rotor. Figure 3-35 shows the complete assembly of the FFMG with the outer rotor included and the mounting end plates. The outer rotor is held stationary where as the cage rotor is connected to the input shaft and inner rotor is connected to output shaft. Figure 3-36 shows the experimental setup on the test bed.

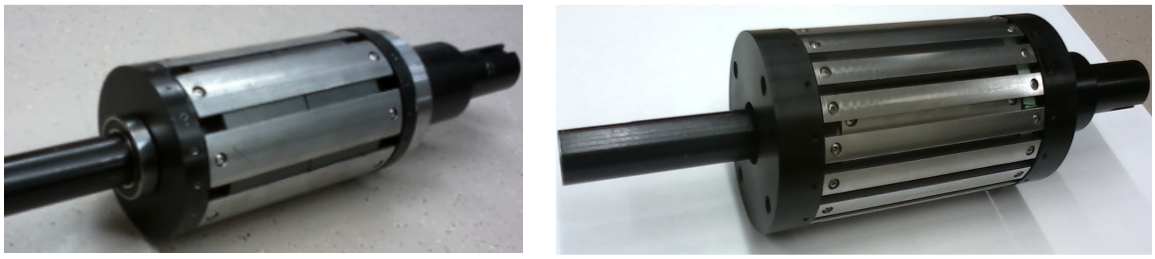

(a) (b)

Figure 3-34: FFMG assembly (a) inner rotor, (b) cage rotor

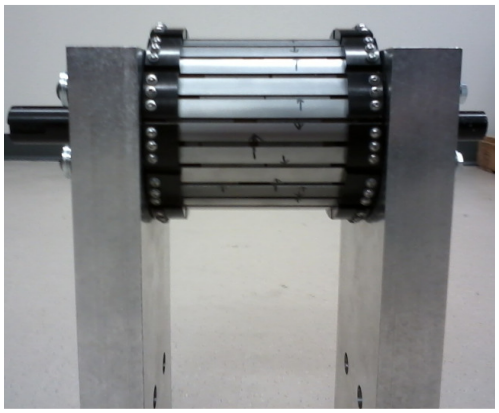

Figure 3-35: FFMG full assembly with end plates

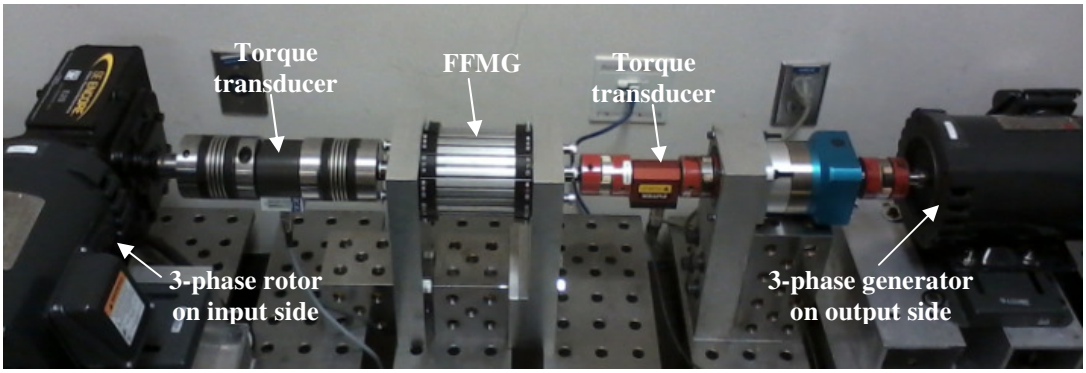

Figure 3-36: MG setup on the testbed

The experimental torque is measured on the cage and inner rotors. The torque obtained is shown in Figure 3-37. A maximum slip torque of 25Nm on the low-speed rotor was obtained. This value is only 58% of the torque predicted using FEA, it results in an active torque density of just 33 Nm/L. In order to understand the reason for the lower measured torque. The radial magnetic field created by the inner rotor and outer rotor when surrounded by air was measured. The results are shown in Figure 3-38 and Figure 3-40. The dominant harmonics that transmit torque within the inner and outer rotor air-gaps are the 4^{th} and 13^{th} harmonics respectively. These harmonic terms were extracted and plotted separately as shown in Figure 3-39 and Figure 3-41. It can be observed that the dominant harmonic fields obtained experimentally for the inner and outer rotors are 18 % and 24% lower than the FEA predictions. This lower field value has resulted in the experimental torque being significantly lower than expected.

In order to determine the cause of the discrepancy between the calculated and measured values a field comparison for a single inner rotor ferrite magnet was conducted. The resulting field comparison along one length of the magnet is shown in Figure 3-44 and Figure 3-45, the magnet dimensions are shown in Figure 3-43. It can be noted that a significant discrepancy exists. The discrepancy was close to 13%.

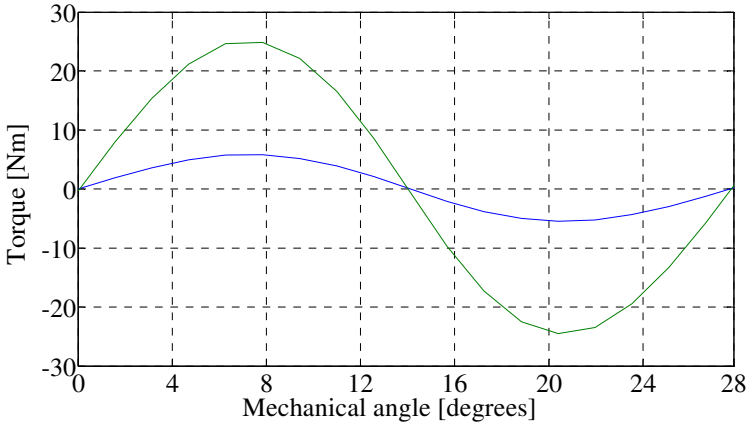

Figure 3-37: Experimentally measured torque on the inner and cage rotor under pole slipping condition

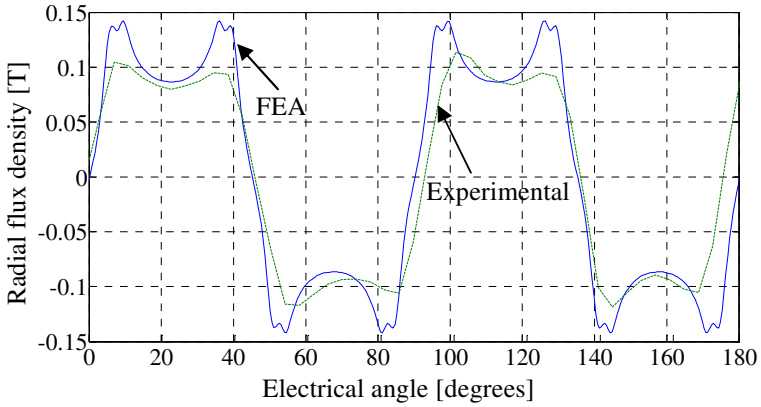

Figure 3-38: Radial magnetic flux density comparison 0.5 mm above the ferrite magnet inner rotor

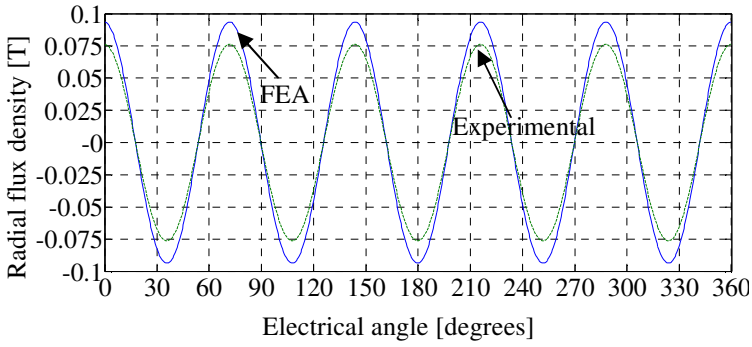

Figure 3-39: 4th harmonic comparison 0.5 mm above the ferrite magnet inner rotor

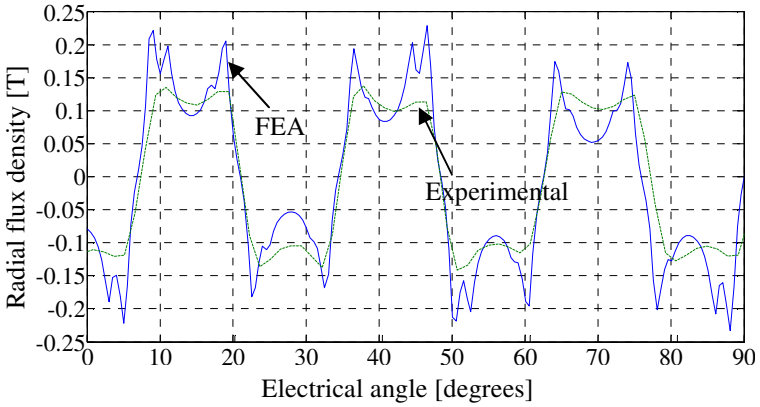

Figure 3-40: Radial flux density comparison 0.5 mm above the ferrite magnet outer rotor (when inner and cage rotor are absent)

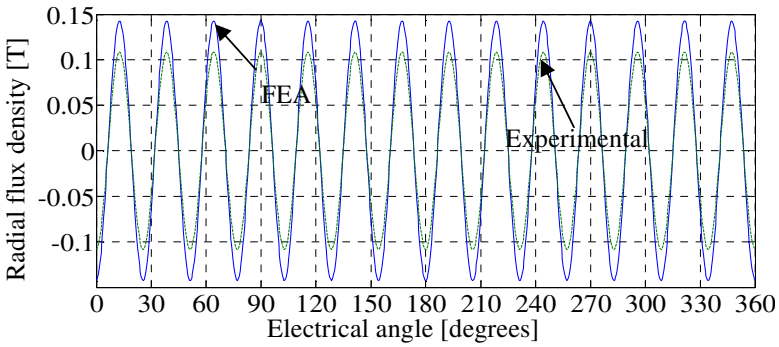

Figure 3-41: 13th harmonic comparison 0.5 mm above the ferrite magnet outer rotor when only the outer rotor is present

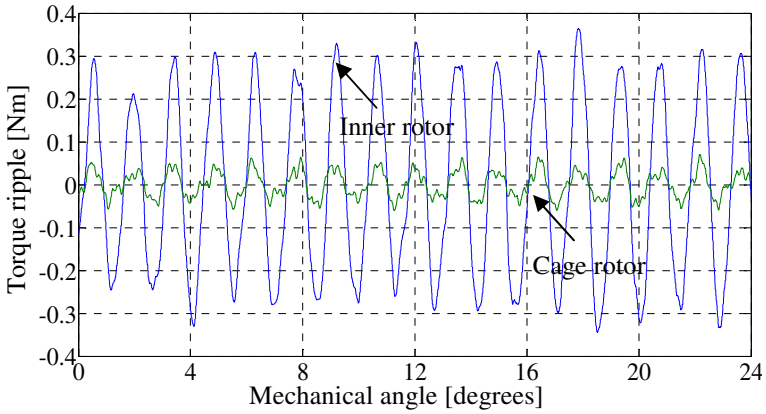

Figure 3-42: Torque ripple for the ferrite magnet MG

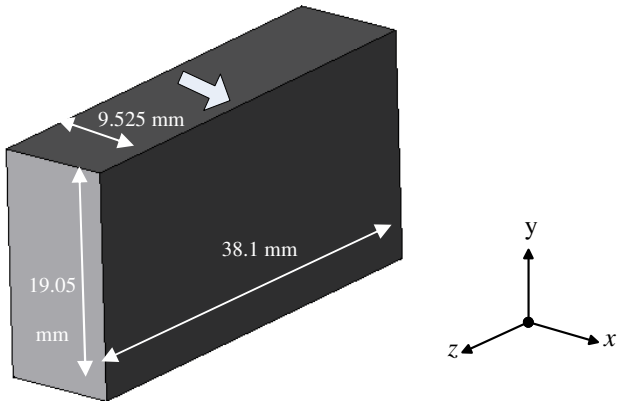

Figure 3-43: Inner rotor ferrite magnet dimensions

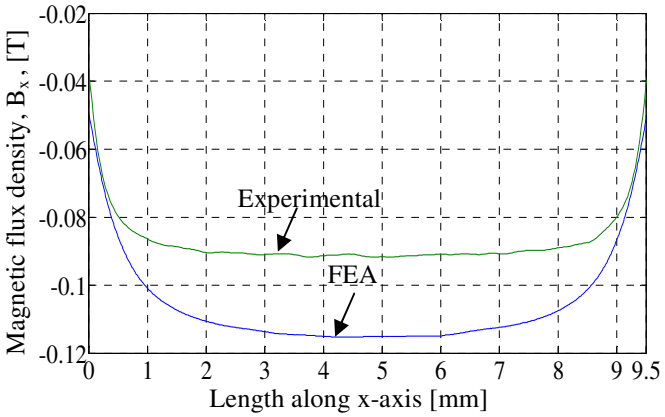

Figure 3-44: Comparison of *x*-component of magnetic flux density along the x-axis of magnet with 0.375" length with 0.46 T magnet.

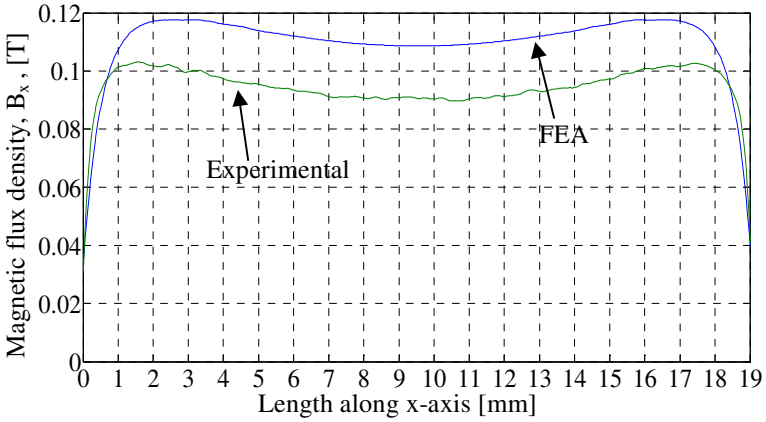

Figure 3-45: Comparison of *x*- component of magnetic flux density along the y-axis of magnet with 0.75" length with 0.46 T magnet.

When the magnet B_r field value was reduced down to obtain a match and then used in the FFMG FEA model a close agreement between the experimental and

calculated value was obtained. This confirmed that the ferrite magnets supplied did not meet the quoted specifications. Figure 3-46 and Figure 3-47 show the field comparison for the magnet with a residual magnet flux density of B_r = 0.413 T. The comparison of radial field and the corresponding dominant harmonic on the inner and outer rotor when using the new magnet field value are shown in Figure 3-48 through Figure 3-51. The torque obtained when using this magnet is compared with the experimental design and can be seen in Figure 3-52. A very close agreement is obtained with the new magnet design.

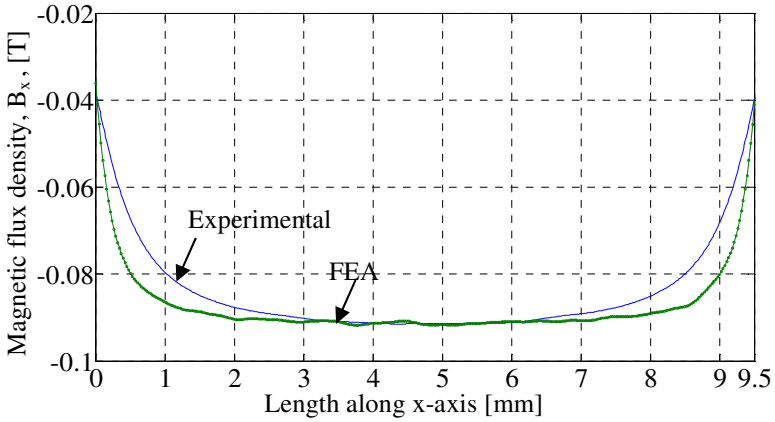

Figure 3-46: Comparison of *x*-component of magnetic flux density along the x-axis of magnet with 0.375" length with 0.413 T magnets.

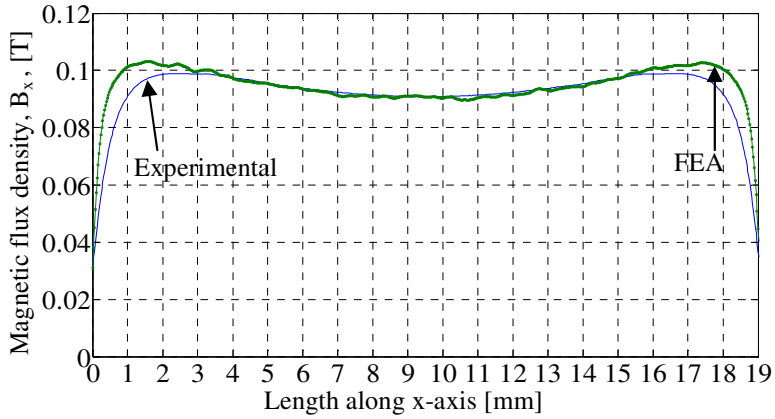

Figure 3-47: Comparison of *x*- component of magnetic flux density along the y-axis of magnet with 0.75" length with 0.413 T magnet.

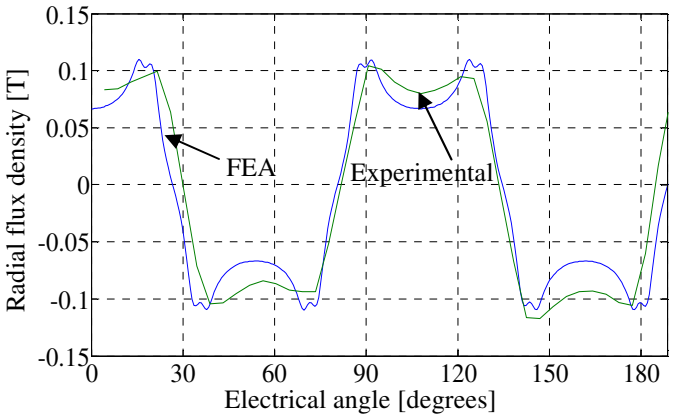

Figure 3-48: Radial flux density comparison in the inner rotor air-gap with just the inner rotor

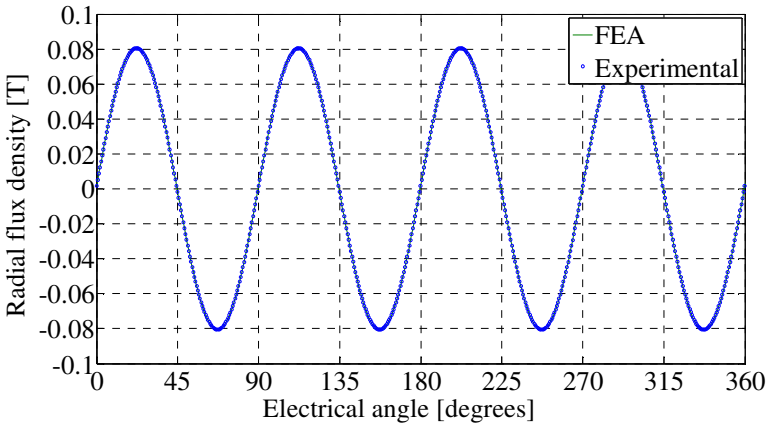

Figure 3-49: 4th harmonic comparison 0.5 mm above the ferrite magnet inner rotor

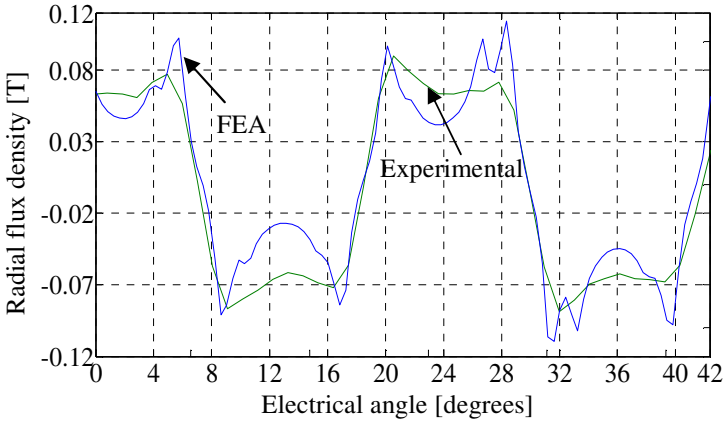

Figure 3-50: Radial flux density comparison on the outer rotor with ferrite magnets at a radius of r=56.5 mm.

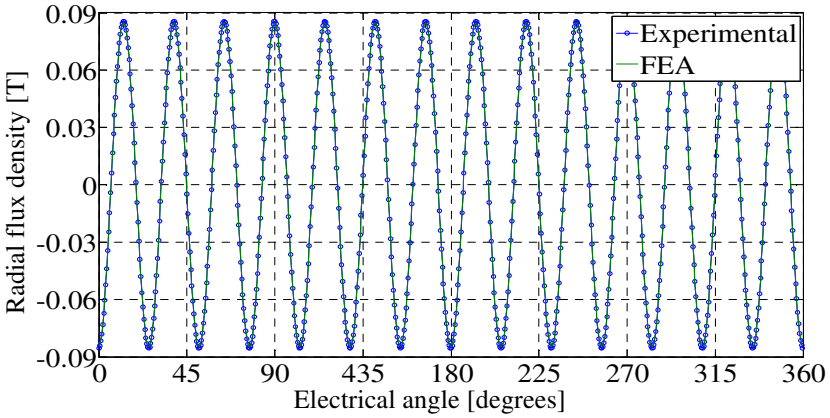

Figure 3-51: 13th harmonic comparison of radial flux density on the outer rotor at a radius of r=56.5 mm.

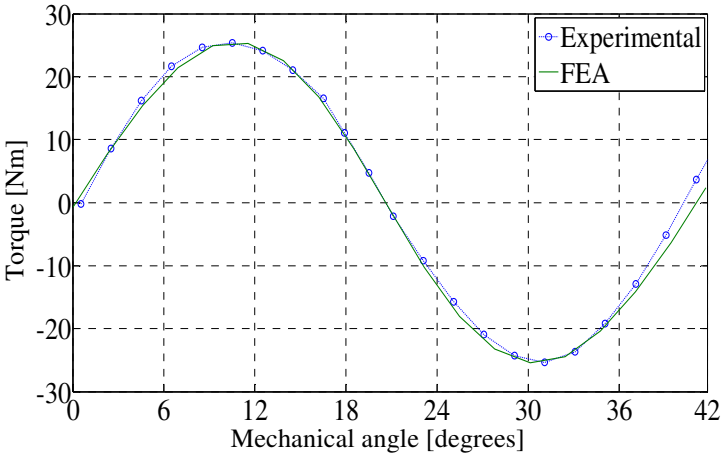

Figure 3-52: Torque comparison for ferrite MG with reduced magnet properties

The measured torque ripple is shown in Figure 3-42. A torque ripple of 0.7 Nm is obtained on the high speed rotor. This is 2.8% of the peak torque obtained which is 25 Nm.

The efficiency of the FFMG at various speeds is defined by

$$\eta = \frac{T_1 \omega_1}{T_2 \omega_2} \tag{3.12}$$

where T_1 and ω_1 are the torque and angular speed of the inner rotor and T_2 and ω_2 are the torque and angular speed of the cage rotor.

The efficiency comparison for the FFMG between the measured and FEA analysis is shown in Figure 3-53. An efficiency of 98.5% is obtained at the designed speed of 20RPM. The efficiency goes down rapidly as speed increases and this is predominately due to the induced eddy current losses in the cage rotor bars. This indicates that this design could only be used for the first stage of a MG.

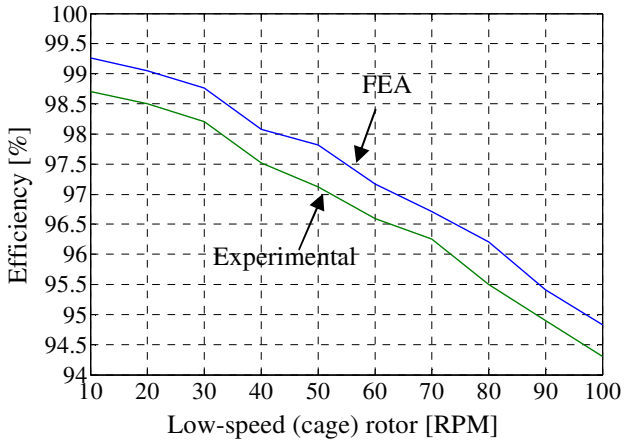

Figure 3-53: Comparison of efficiency of FFMG with ferrite magnets at various speeds.

3.7. Hybrid Magnet MG

A FFMG model with the same dimensions as the ferrite FFMG, but with NdFeB magnets inserted into the inner rotor, was also modeled and experimentally tested. Figure 3-54 shows the predicted torque on the three rotors for this hybrid FFMG.

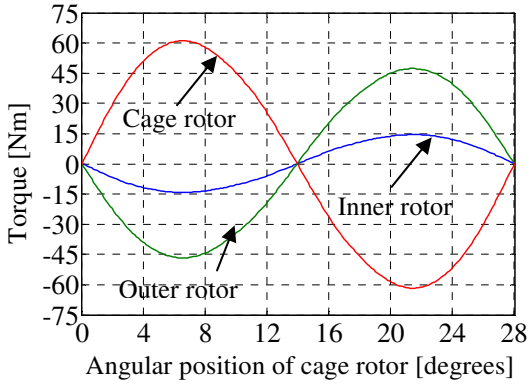

Figure 3-54: Predicted torque for the hybrid FFMG design where NdFeB magnets are in the inner rotor and ferrite magnets are in the outer rotor

This hybrid magnet MG's predicted peak torque is 61 Nm. Figure 3-55 shows the field comparison for the high-speed rotor in air and corresponding dominant harmonic in Figure 3-56. It is can be seen that the experimental and FEA values are very close. Figure 3-57 shows the experimental torque measured during pole slippage. A peak torque of 48 Nm was achieved which is only 78% of the predicted 61 Nm torque. This represents a measured torque density of 66.3 Nm/L while the predicted was 84.9 Nm/L. This discrepancy is again attributed to the Hitachi NMF-12F ferrite magnets having lower magnetic properties than expected. The efficiency for this hybrid magnet designed is shown in Figure 3-58. At the design speed of 20 RPM the measured efficiency is 97.7%.

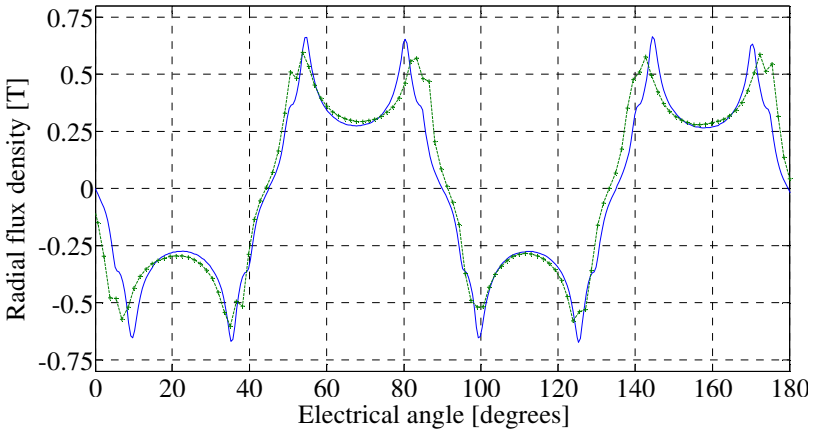

Figure 3-55: Radial flux density comparison in the inner rotor air-gap with just the inner rotor present

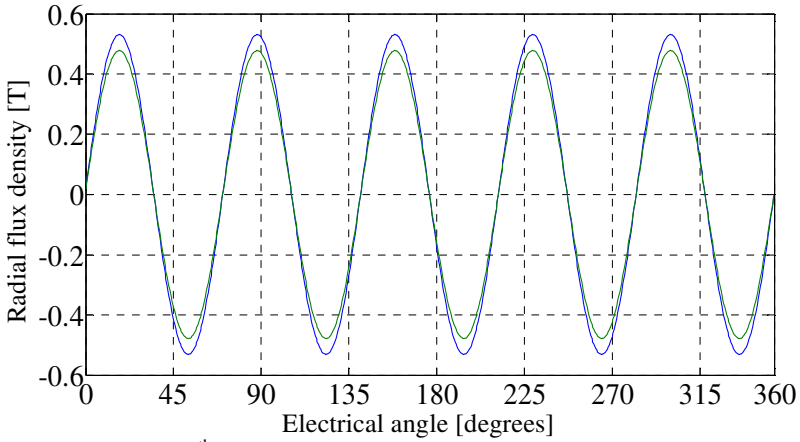

Figure 3-56: The 4th harmonic comparison of the radial flux density in the inner rotor air-gap with just the inner rotor present.

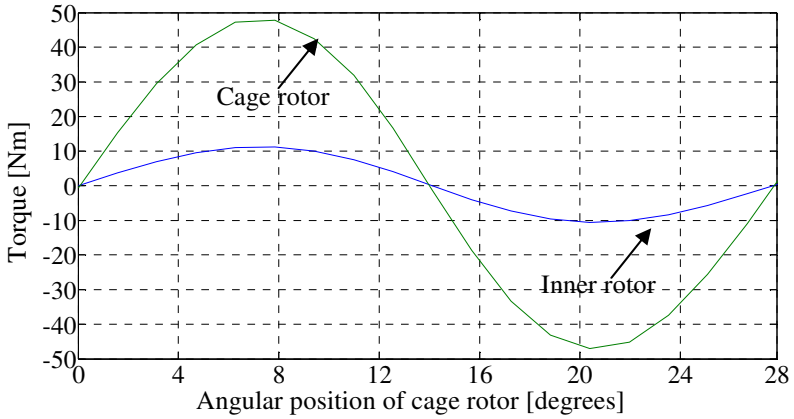

Figure 3-57: Measured torque for the hybrid FFMG design where NdFeB magnets are in the inner rotor and ferrite magnets are in the outer rotor

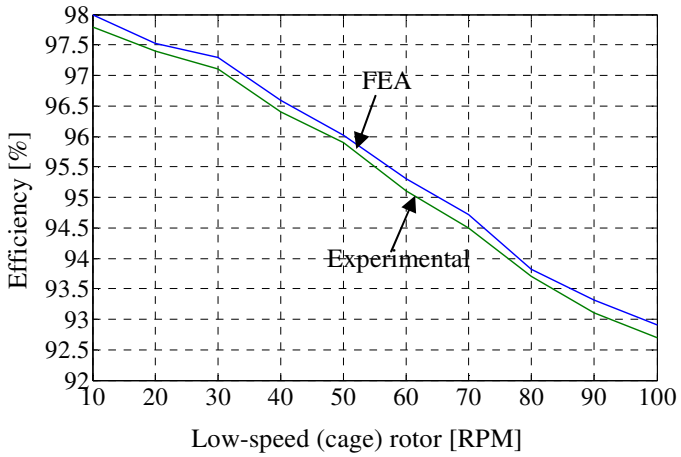

Figure 3-58: Comparison of efficiency for the hybrid FFMG at various speeds.

3.8. MG with Rare Earth Magnets

A FFMG with the same dimensions as the above with NdFeB magnets in both the inner and outer rotors was also experimentally tested. Figure 3-59 shows the calculated torque when using the NdFeB magnets. The calculated peak torque on the cage rotor is 115.7 Nm. This gives a volumetric torque density of 154.2 Nm/L. The radial flux densities in the inner and outer air-gaps and their corresponding harmonics are shown in Figure 3-62 to Figure 3-63.

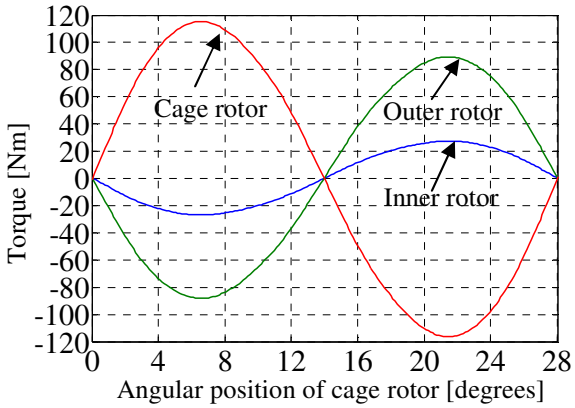

Figure 3-59: Predicted torque when using NdFeB magnets

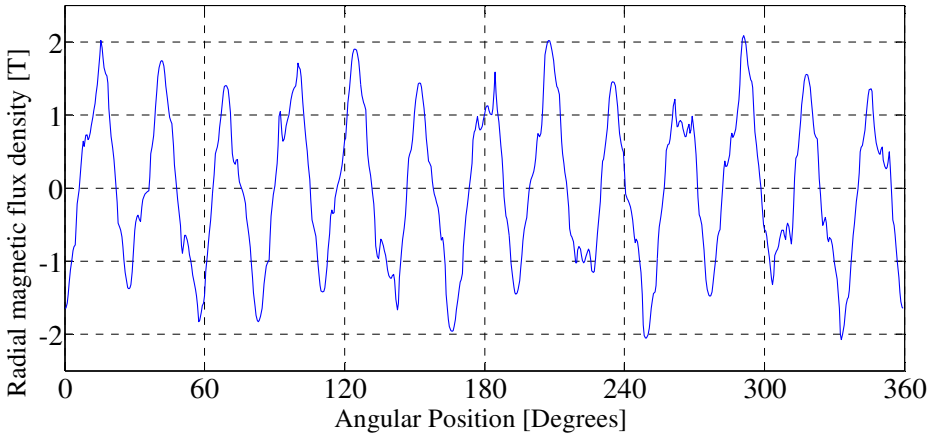

Figure 3-60: Radial flux density, B_r, in the outer rotor air-gap adjacent to outer cylinder at r=39.75 mm.

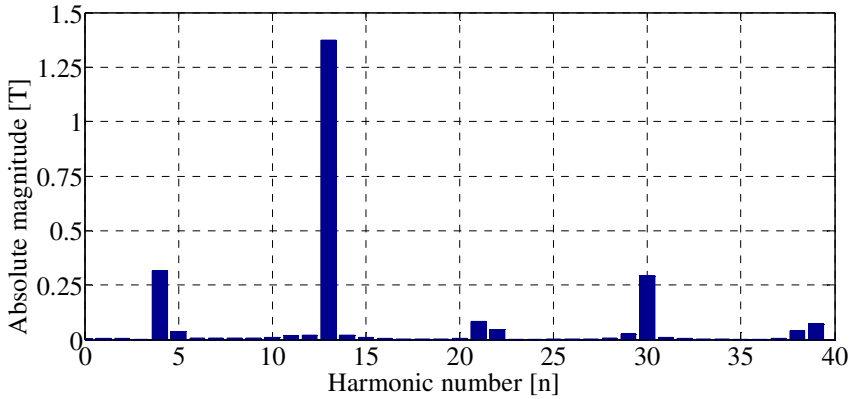

Figure 3-61: Spatial frequency analysis of radial flux density, B_r, in the outer rotor airgap adjacent to outer rotor

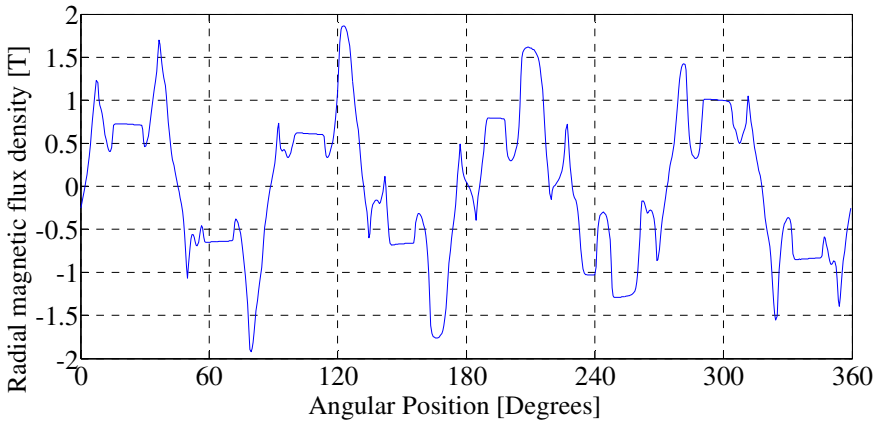

Figure 3-62: Radial flux density, B_r, in the inner rotor airgap adjacent to inner cylinder and corresponding spatial frequency analysis at r=33.25 mm.

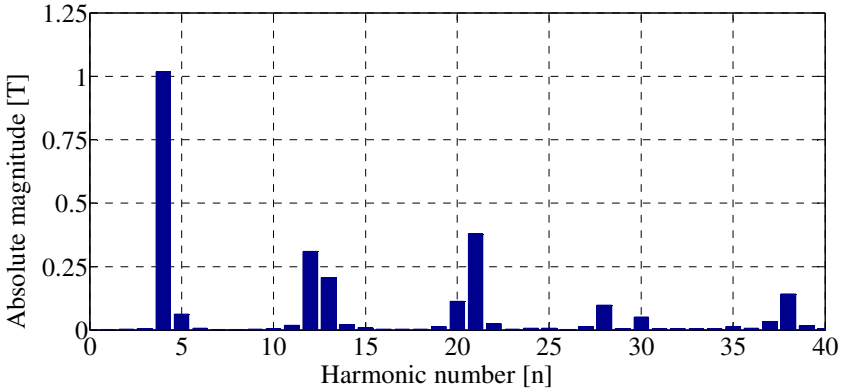

Figure 3-63: Spatial frequency analysis of radial flux density, B_r, in the inner rotor airgap adjacent to inner rotor

The predicted peak torque for this model is 115.7 Nm while the measured peak torque before pole slippage was determined to be 113.5 Nm. This represents a discrepancy of just 1.9%. This results in an active region torque density of 151.2 Nm/L. The radial flux density at a distance of 0.25 mm away from inner rotor when the inner rotor is surrounded by air, was measured experimentally and compared with FEA to validate the magnetic strength of the magnets. Figure 3-64 shows the comparison between the fields and it can be seen that a very close match was obtained between the two fields.

Figure 3-65 shows the torque under varying loads and Figure 3-66 shows the torque ripple measured on the inner and cage rotor respectively at maximum load condition while

Figure 3-67 shows the efficiency at different speed and load conditions. An efficiency of 97.4% is obtained at the speed of 20 RPM. It should be noted that the torque ripple shown in Figure 3-66 was measured using a helical beam coupling on both sides of the FFMG, however the torque ripple shown in Figure 3-67 was measured with a helical beam coupling on the low-speed side and a flexible spider coupling on the high-speed side of the FFMG. It was determined that the spider coupling introduced more oscillatory torque ripple than the flexible coupling and this is one of the reasons for the somewhat lower torque ripple measured for the NdFeB design. A performance summary for the three different FFMG constructed is provided in Table 3-8 and Table 3-9.

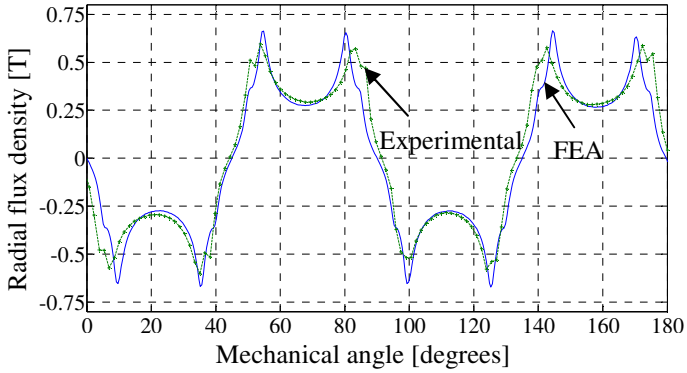

Figure 3-64: Radial flux density comparison in the inner rotor air-gap with just the inner rotor and NdFeB magnets

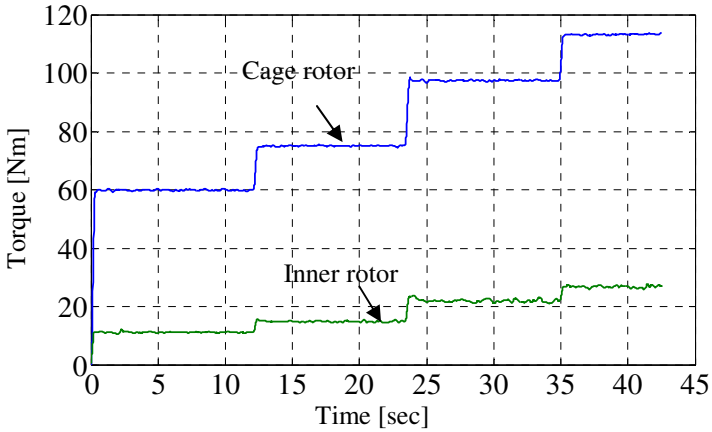

Figure 3-65: Torque on the cage and inner rotor of experimental setup with NdFeB magnets on both the rotors for various loads

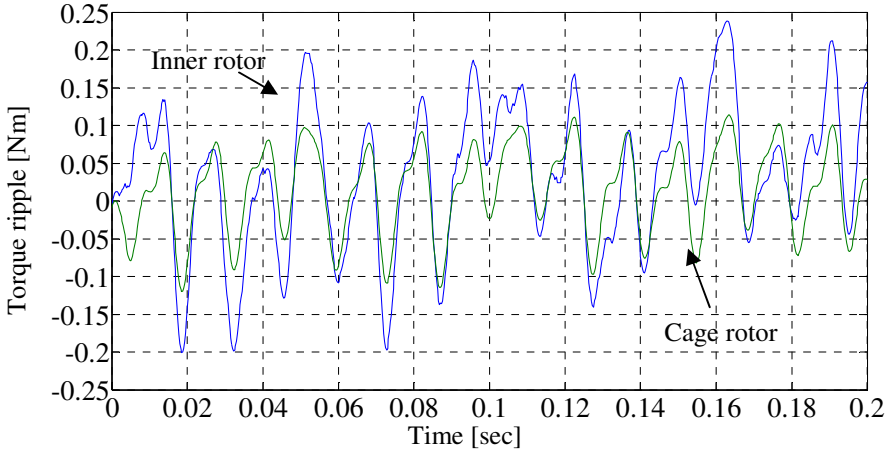

Figure 3-66: Experimental torque ripple on the cage rotor for MG model with NdFeB magnets at maximum load

Figure 3-67 shows the efficiency measured at various loads at different input speeds for FFMG with NdFeB magnets. The efficiency decreases as the load and speed increases. An efficiency of 97.4% is obtained at a design speed of 20 RPM at maximum load just before the FFMG pole slips.

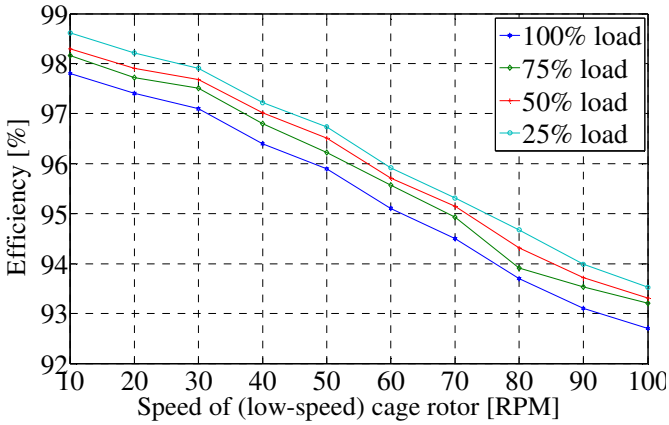

Figure 3-67: Efficiency of the FFMG at various speeds measured at peak load condition (just before pole slipping).

Table 3-8: Calculated and measured torque values

Type	**Torque [Nm]**	
	Calculated	**Measured**
Ferrite	42	25
Hybrid	61	48
NdFeB	115.7	113.5

Table 3-9: Summary of experimental performance metrics

Type	Torque density [Nm/L]		Mass density [Nm/kg]		Torque-per-kg of magnet [Nm/kg]
	Active region	Full assembly	Active region	Full assembly	
Ferrite	33 (56)	30.5	4.5	3.7	14.6
Hybrid	66.3 (81)	58.6	8	6.7	24.2
NdFeB	151.2 (154)	138.5	17.4	14.8	44.6

Table 3-10: Air-gap magnetic shear stress and torque density

Design	Air-gap	Radius [mm]	Torque [Nm]	Torque Density [Nm/L]	Shear Stress [kN/m^2]
Sub-scale	Outer	39.75	86.8	229.5	114.7
	Inner	33.25	26.7	100.9	50.4

3.9. Demagnetization Analysis

The magnets used in the design see a rotating magnetic field from the air-gap crossing the magnets at the corners, in the direction opposite to that of their orientation. This results in the magnetic material undergoing cyclic demagnetization around the tips. In order to investigate this phenomenon with angular rotor position two points within the magnet were selected, as shown in Figure 3-68. Point 2 is far from the air-gap and therefore does not see any local demagnetization. A demagnetization ratio was defined such that:

$$\text{Demagnetization ratio } (\%) = 100\left(1-\frac{|B_2|}{|B_1|}\right) \tag{3.13}$$

Where B_1 is the residual magnetic flux density of the specified step and B_2 is the residual magnetic flux density of the step that is displayed. Using this ratio a demagnetization surface plot was made at one rotor position as shown Figure 3-69. The local demagnetization around the corners of the ferrite magnets is clearly evident. Figure 3-70 shows the demagnetization path taken for the field at point 1 and point 2.

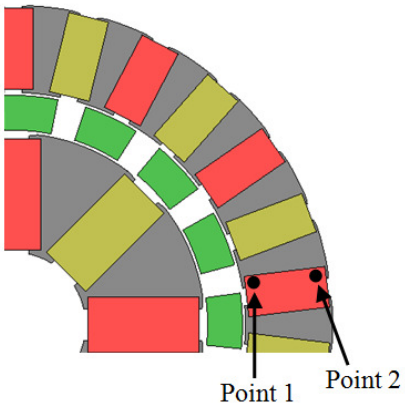

Figure 3-68: Demagnetization analysis at two points on the outer rotor magnets

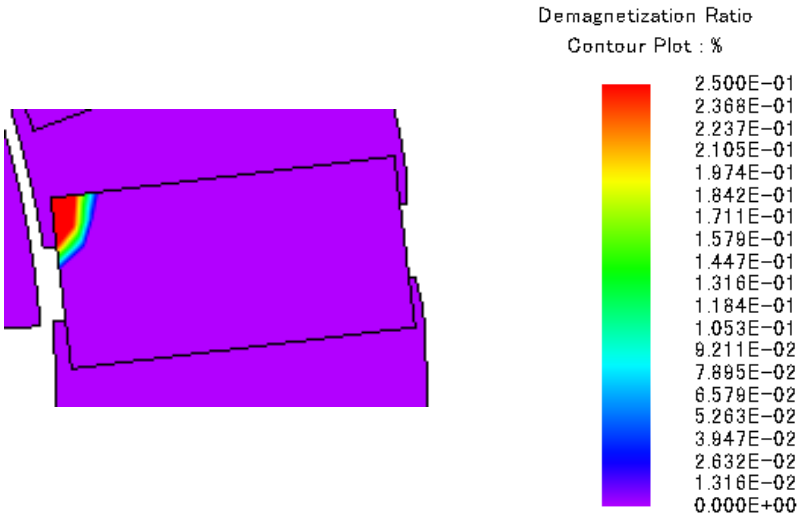

Figure 3-69: Demagnetization ratio of the magnets

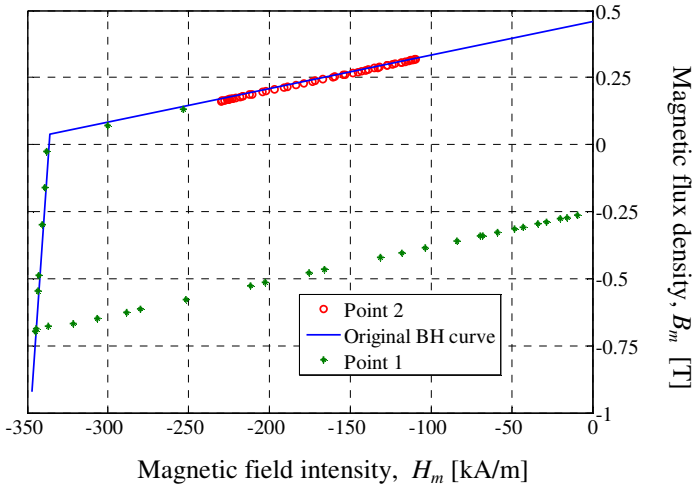

Figure 3-70: Demagnetization path at point 1 and point2 on the magnet as a function of rotor position.

It can be clearly seen from Figure 3-70 at point 1, the flux density once demagnetized follows a new path which is very different from the original path. The demagnetization of magnets on the tips can therefore have some effect on the output torque. However this effect is very localized.

CHAPTER 4 : SCALED-UP FLUX FOCUSING MAGNETIC GEAR DESIGN

4.1. Introduction

In this chapter the design, construction and experimental evaluation of a scaled-up coaxial FFMG is presented. In Section 4.2 the design and topology of the scaled-up FFMG is presented. In section 4.3 a judicious parameter sweep of the design is presented. Section 4.4 gives the harmonic analysis of the design and comparison with the sub-scale FFMG. Section 4.5 presents the deflection analysis of the cage rotor bars due to the magnetic forces from the inner and outer rotor, and Section 4.6 gives the experimental construction and results.

4.2. Magnetic gear design

The scaled-up FFMG is designed by doubling the number of poles and outer radius used by the sub-scale FFMG presented in chapter 3. The design has p_3=26 pole pairs on the outer rotor, p_1=8 pole pairs on the inner rotor and n_2=34 steel poles on the cage rotor. As all the poles are doubled the gear ratio for this design is 4.25:1, the same as the sub-scale design. The primary intention for designing the scaled-up FFMG is to investigate the possibility of achieving a higher volumetric torque density. The scaled-up FFMG design under investigation before optimization is shown in Figure 4-1(a) and the material properties and fixed geometric parameters are given in

Table 4-1, Table 4-2 and defined in Figure 4-1(b).

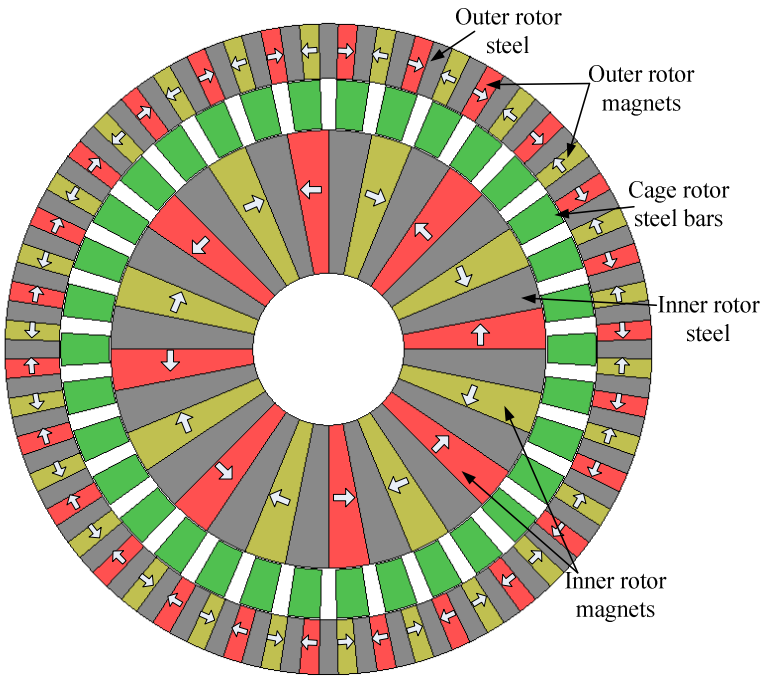

(a)

Figure 4-1: (a) Scaled-up FFMG MG using initial geometric values with p_1=8 pole-pairs on the inner high speed rotor, n_2=34 steel poles on the low-speed rotor and p_3=26 pole-pairs on the outer stationary rotor.

4.3. Parameter Sweep Analysis

It is assumed that the magnet and steel pole-spans are equal on the high-speed and stationary rotor such that $\theta_{1s}=\theta_{1m}=360^o/(4p_1)$ and $\theta_{3s}=\theta_{3m}=360^o/(4p_3)$. In addition, the outer radius of the stationary rotor and inner radius of the high-speed rotor are held fixed at r_{o3}=110 mm and r_{i1}=25 mm. As the objective of the parameter sweep is to maximize the volumetric torque density the inner rotor radius was kept small. The cage rotor bar span was initially held fixed at $\theta_{s2} = 180^o/p_3 \approx 7^o$ and the torque was calculated when varying the outer radius of the high-speed rotor, r_{o1}, and the length and width of the cage rotor bars, l_2 and θ_{s2}.

Table 4-1: Fixed geometric parameters and material properties

	Description	Value	Unit
Inner rotor (high speed)	Pole pairs, p_1	8	-
	Steel pole span, θ_{s1}	π/16	radians
	Air-gap, g	0.5	mm
Cage rotor	Steel poles, n_2	34	-
Outer rotor (stationary)	Pole pairs, p_3	26	-
	Inner radius, r_{i3}	77	mm
	Outer radius, r_{o3}	110	mm
	Steel pole span, θ_{s3}	π/52	radians
	Air-gap, g	0.5	mm
Material	Ferrite magnet, Hitachi NMF12F	0.46	T
	NdFeB magnet, N40H, B_r	1.25T	T
	416 steel resistivity (cage rotor)	57.0	μΩ-cm
	1018 steel resistivity (inner/outer rotor)	15.9	μΩ-cm
Active region stack length, d		75	mm

Table 4-2: Geometric parameters varied

	Description	Value	Unit
Inner rotor (high speed)	Inner radius, r_{i1}	25	mm
	Outer radius, r_{o1}	66	mm
Cage rotor	Cage bar length, l_2	10	mm
	Pole span, θ_{s2}	7	degrees

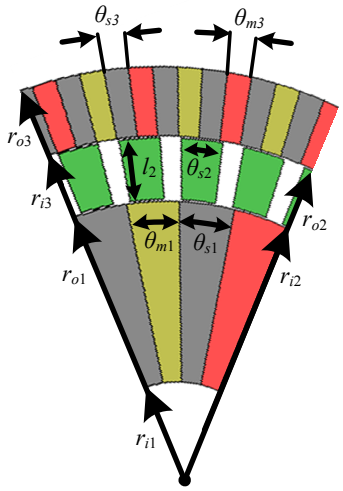

Figure 4-2: The geometric parameters.

The cage bar length is defined as $l_2 = r_{o2} - r_{i2}$. The resulting torque density plot is shown in Figure 4-3 for the case when ferrite magnets are used. It can be noted that the torque density is always maximum when the cage bar length is $l_2 = 5$ mm. At $l_2 = 5$ mm and $r_{o1} = 90$ mm the peak torque density when using ferrite magnets is calculated to be

92.2 Nm/L. Figure 4-4 shows that θ_{s2}=7° gives the highest torque density and is not affected by changes in high-speed outer rotor radius values.

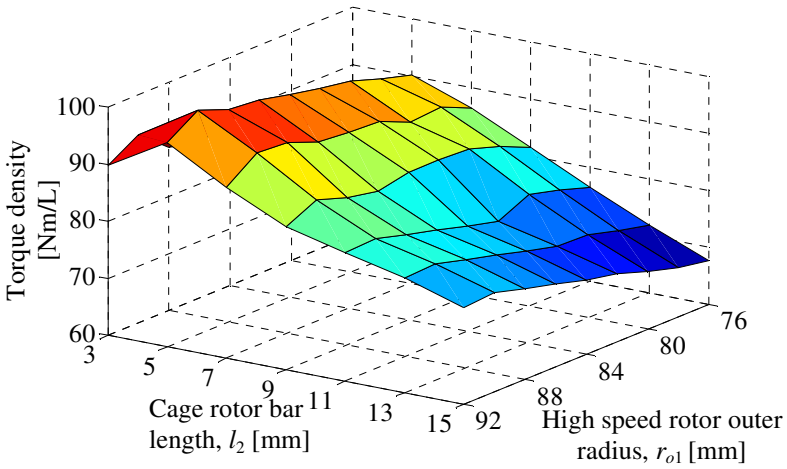

Figure 4-3: Volumetric torque density for changes in the cage rotor bar length, l_2 and high-speed outer rotor radius, r_{o1}, when using ferrite magnets (θ_{s2}=7°)

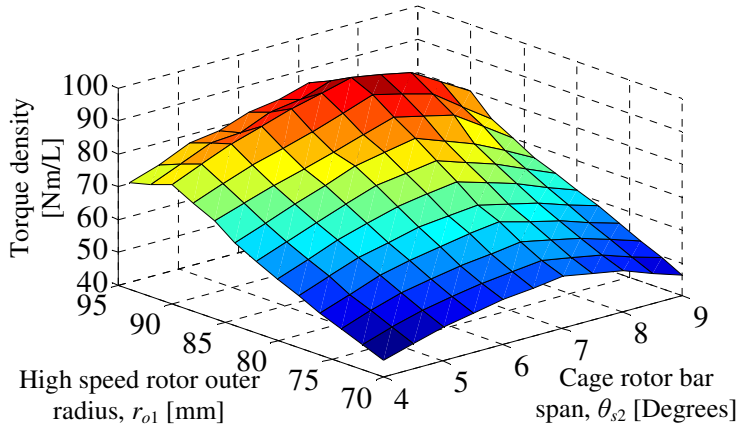

Figure 4-4: Volumetric torque density for cage rotor bar span, θ_{s2}, and high-speed outer rotor radius, r_{o1}, when using ferrite magnets (l_2=5mm)

The same parameter sweep analysis was conducted when using NdFeB magnets. Figure 4-5 and Figure 4-6 show the torque density values when the parameters r_{o1}, l_2, and θ_{s2} are varied. Surprisingly the peak torque density using NdFeB magnets occurred at the same geometric values as when using ferrite magnets, namely l_2=5 mm, r_{o1} = 90 mm, θ_{s2}=7°. The peak torque density was calculated to be 266.9 Nm/L. The final geometric parameters after the optimization are shown in Table 4-3.

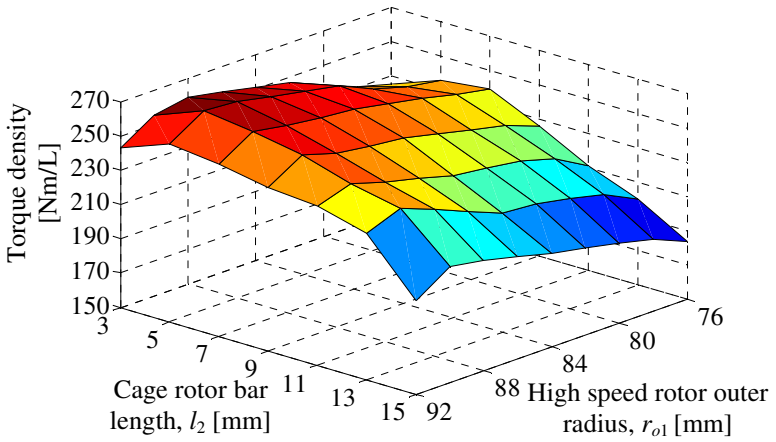

Figure 4-5: Volumetric torque density for changes in the cage rotor bar length, l_2 and high-speed outer rotor radius, r_{o1}, when using NdFeB magnets (θ_{s2}=7°)

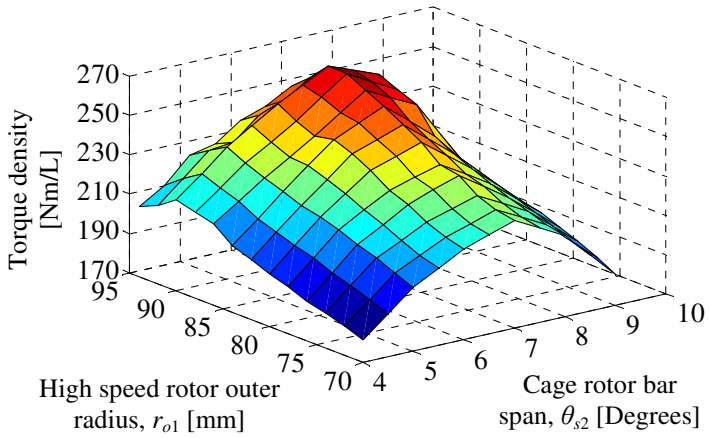

Figure 4-6: Volumetric torque density for cage rotor bar spans, θ_{s2}, and high-speed outer rotor radius, r_{o1}, when using NdFeB magnets (l_2=5mm)

As with the case for the sub-scale design the magnets have been made rectangular in order to reduce manufacturing cost and additional steel rotor pole lips have been added in order to retain the magnets in place, the addition of the lips increases the outer rotor radius to r_{o3} = 114 mm. The final model after making these adjustments is shown in Figure 4-7. Figure 4-8 shows the surface plot for the radial flux density of the design where the distribution of the field across the three rotors is shown. It can be seen that concentration of flux is higher on the lower edges of the outer rotor steel and inner edges of inner rotor steel. The calculated torque as a function of mechanical angle when only

one rotor is rotating (pole slipping) for both ferrite and NdFeB designs is shown in Figure 4-9 and Figure 4-10. A peak torque of 282.6 Nm and 750 Nm respectively was obtained. This results in a volumetric torque density of 92.3 Nm/L and 244.5 Nm/L for the ferrite and NdFeB magnet designs respectively.

Table 4-3: Final geometric sweep parameters

	Description	Value	Unit
Inner rotor (high speed)	Pole pairs, p_1	8	-
	Steel pole span, θ_{s1}	π/16	radians
	Air-gap, g	0.5	mm
Cage rotor	Steel poles, n_2	34	-
Outer rotor (stationary)	Pole pairs, p_3	26	-
	Inner radius, r_{i3}	99	mm
	Outer radius, r_{o3}	114	mm
	Steel pole span, θ_{s3}	π/52	radians
	Air-gap, g	0.5	mm
Material	Ferrite magnet, Hitachi NMF12F	0.46	T
	NdFeB magnet, N40H, B_r	1.25T	T
	416 steel resistivity (cage rotor)	57.0	μΩ-cm
	1018 steel resistivity (inner/outer rotor)	15.9	μΩ-cm
Active region stack length, d		75	mm

Table 4-4: Final geometric sweep parameters

	Description	Value	Unit
Inner rotor (high speed)	Inner radius, r_{i1}	26	mm
	Outer radius, r_{o1}	92	mm
Cage rotor	Cage bar length, l_2	5	mm
	Pole span, θ_{s2}	7	degrees

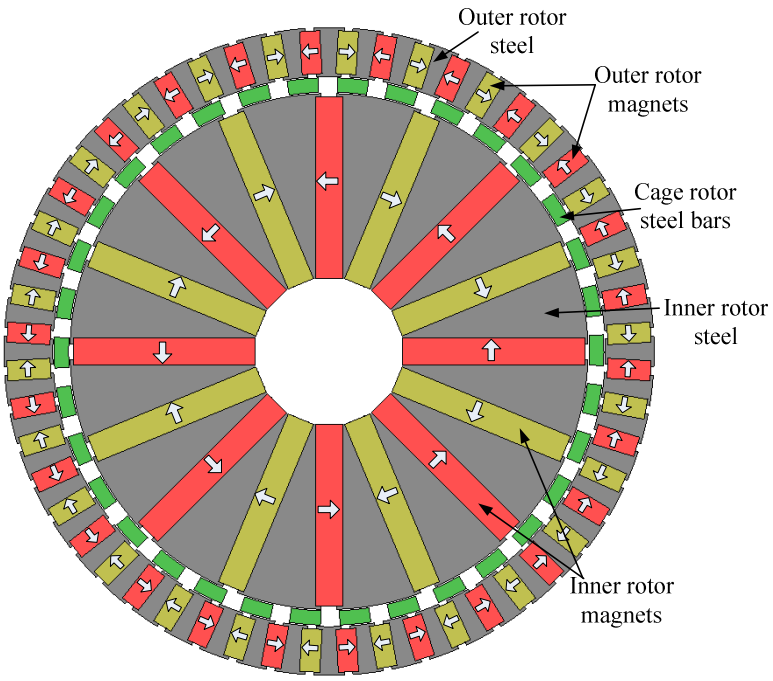

Figure 4-7: Final design for the scaled-up FFMG

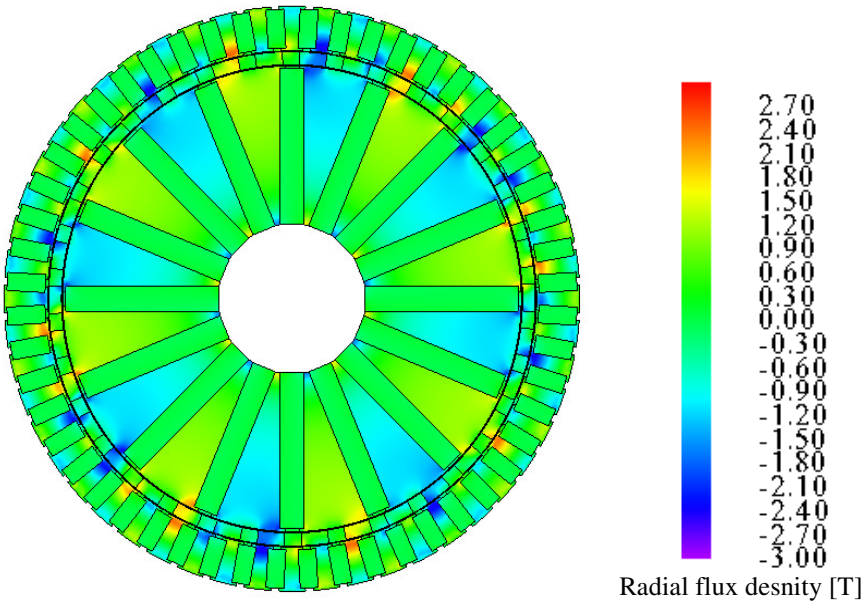

Figure 4-8: Surface plot of the radial flux density for the final design

Table 4-5: Key design parameters

Flux concentration ratio	$C_{\varphi 3}$	7.35
	$C_{\varphi 1}$	4.38
Angular span ratio	W_{s23}	2.02
Angular span [radians]	θ_{s1}	$\pi/(2p_1)$
	θ_{s2}	π/p_3
	θ_{s3}	$\pi/(2p_3)$

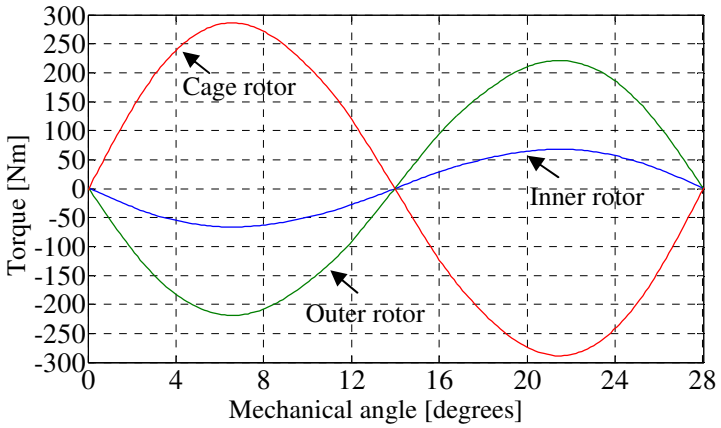

Figure 4-9: Torque on the three rotors when slipping when using ferrite magnets with an active region stack length of 75mm

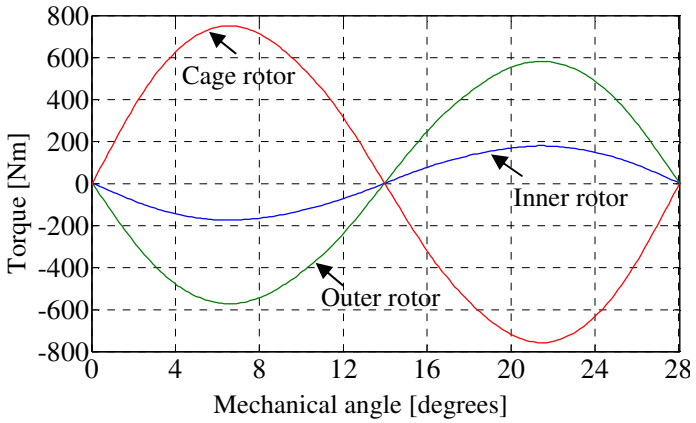

Figure 4-10: Torque on the three rotors when slipping when using NdFeB magnets, with an active region stack length of 75mm

The FEA calculated efficiency at various input speeds from 10 to 100 RPM with ferrite and NdFeB magnets is shown in Figure 4-11. An efficiency of 98.0% with ferrite magnets and 97.5% with NdFeB magnets was predicted at the 20 RPM input design speed. The calculated efficiency reduces significantly as speed increases due to the increased eddy current loss in the solid steel bars.

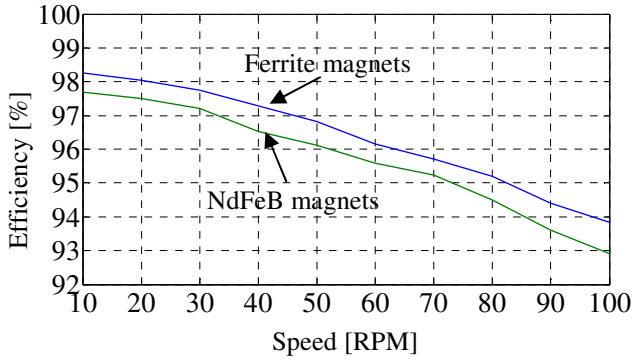

Figure 4-11: Calculated efficiency of the scaled-up FFMG with ferrite and NdFeB magnets

This design thus obtained was constructed and experimentally verified. However, it should be noted that this design is not a completely optimized design. For instance, Figure 4-12 shows the variation of torque due to variation of high speed rotor inner radius, r_{i1}. Figure 4-13 shows the variation of the volumetric and mass torque density of the scaled-up MG design and Figure 4-14 shows the variation of torque density-per-kg-of-magnets with variation in r_{i1}. It can be indicated from these figures that for this design there is a trade-off between the active region mass torque density and volumetric torque density. Figure 4-13 shows that selecting r_{i1}=25mm was not ideal as there would be no difference if r_{i1}=49mm was used. When the inner radius is increased beyond r_{i1}=49mm, the mass torque density increases but at the cost of a reduced volumetric torque density. If the mechanical assembly structure can be designed to be low mass, the mass torque density capability of this type of FFMG could therefore be substantial.

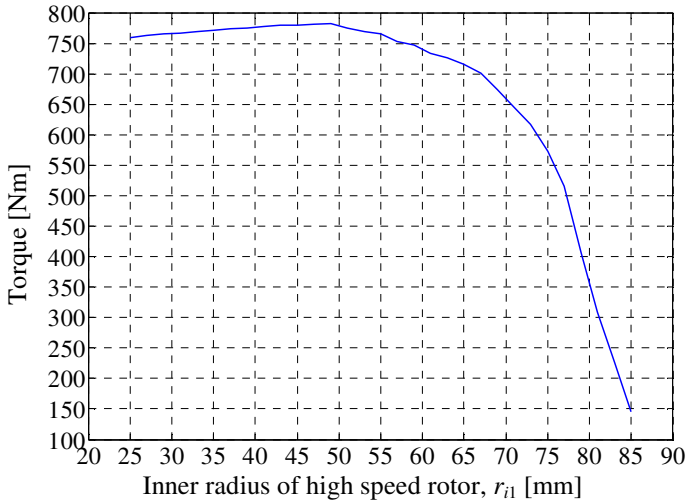

Figure 4-12: Torque variation when the inner radius of the high speed rotor is varied

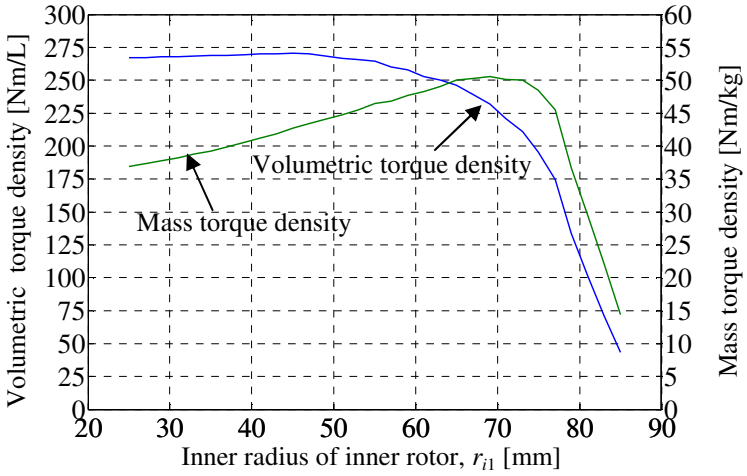

Figure 4-13: Active region torque density variation when the inner radius of the inner rotor is varied

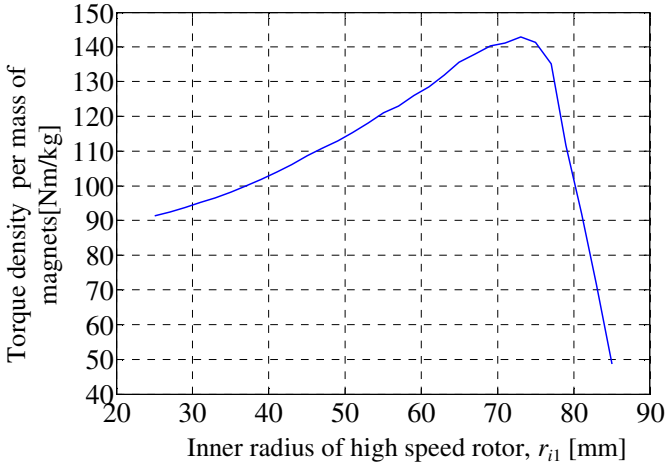

Figure 4-14: Active region torque density per kg of magnets, variation when the inner radius of the high speed rotor is varied

4.4. Harmonic Analysis

As seen in the previous chapter the dominant harmonics within the rotor air-gap play the primary torque transferring role between the rotors. In the scaled-up design the inner and outer rotor's dominant harmonics are the 8th and 26th while in the sub-scale design the 4th and 13th harmonics are dominant. Figure 4-15 through Figure 4-18 shows the calculated radial flux densities in the inner and outer air-gaps and their corresponding spatial harmonics for the scaled-up FFMG. It can be noticed that there is a significant increase in the harmonics between the sub-scale and scaled-up model resulting in the higher torques in the scaled-up model.

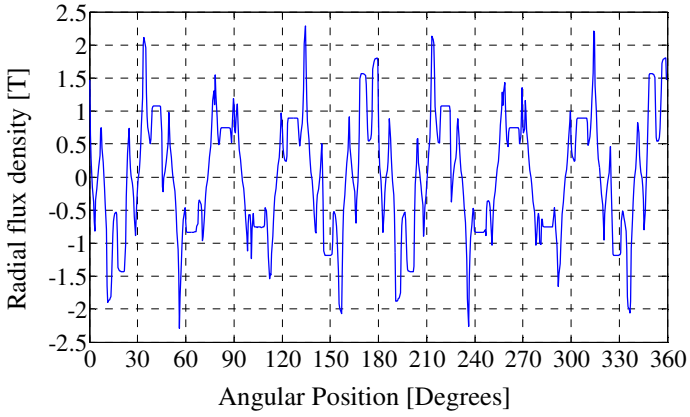

Figure 4-15: Radial flux density, B_r, in the inner rotor air-gap adjacent to inner cylinder when using NdFeB magnets

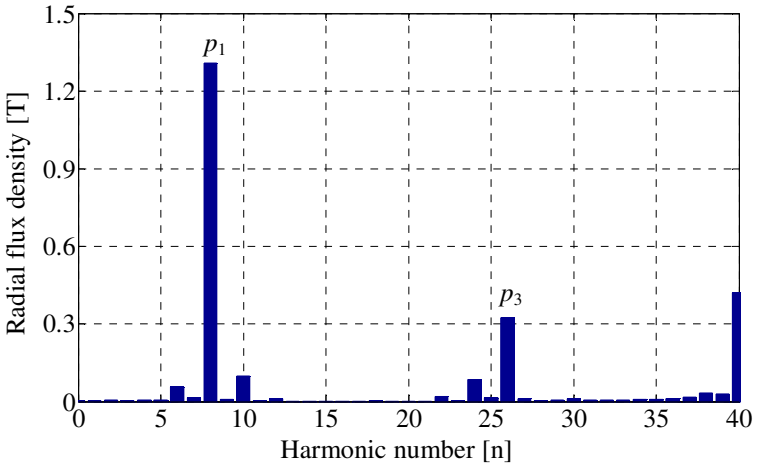

Figure 4-16: Spatial frequency analysis of radial flux density, B_r, in the inner rotor airgap adjacent to inner cylinder when using NdFeB magnets

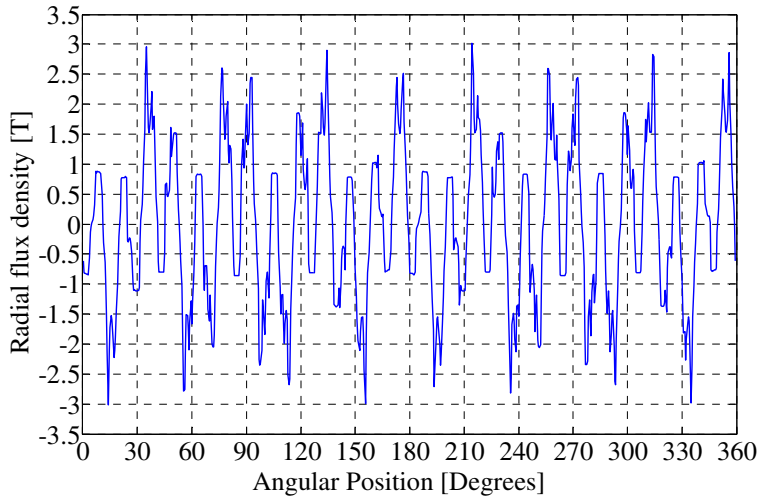

Figure 4-17: Radial flux density, B_r, in the outer rotor air-gap adjacent to outer cylinder when using NdFeB magnets

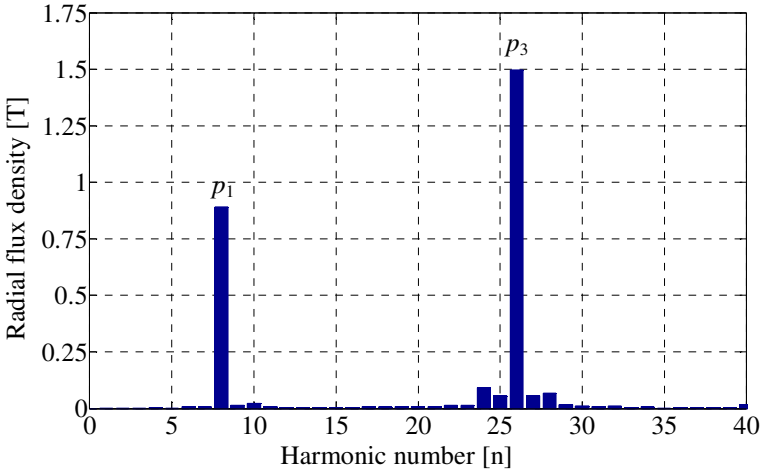

Figure 4-18: Spatial frequency analysis of radial flux density, B_r, in the outer rotor air-gap adjacent to outer cylinder when using NdFeB magnets

Figure 4-19 and Figure 4-20 compare the magnitudes of the radial, B_r, and azimuthal, B_θ, flux density dominant harmonics for the scaled-up and sub-scale designs within the inner and outer air-gaps respectively. It can be observed that for the scaled-up design the B_r harmonic in the inner and outer air-gap is increased by 32% and 24% respectively. While the dominant B_θ harmonic in the inner and outer air-gap is increased by 36% and 37% respectively.

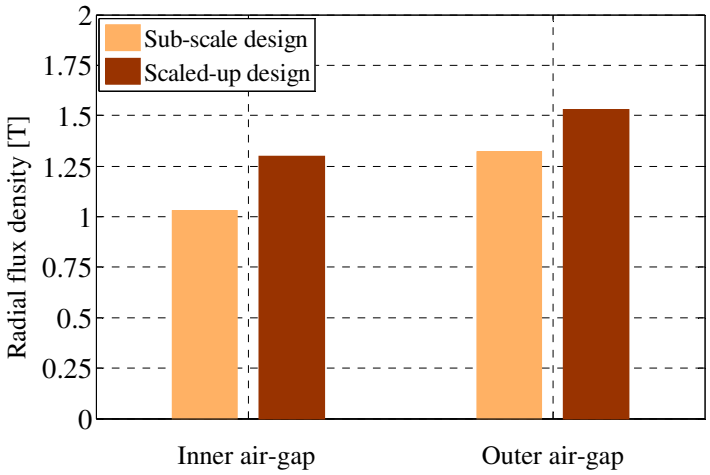

Figure 4-19: Comparison between the dominant harmonics for the radial flux density, B_r, for the sub-scale and scaled-up FFMG

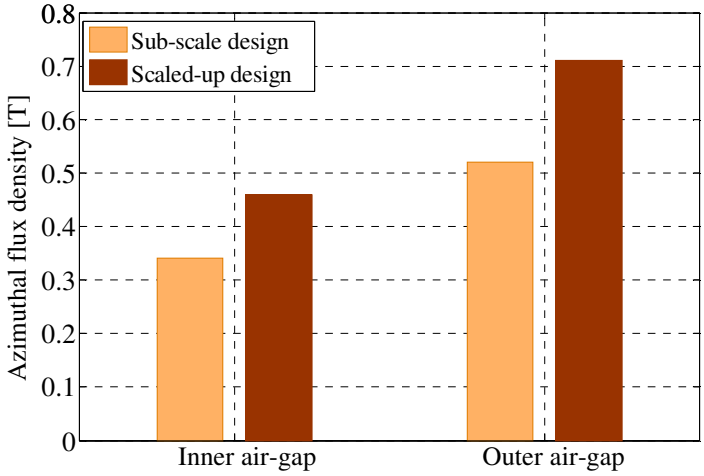

Figure 4-20: Comparison between the dominant harmonics for the azimuthal flux density, B_θ, for the sub-scale and scaled-up FFMG

4.5. Deflection Analysis

As presented in the previous chapter the large magnetic forces created by the inner and outer rotor magnets result in the deflection of the thin central cage rotor bars. The deflection will result in a reduction of the air-gap between the rotors and will affect the torque transmitted. The deflection of the cage rotor bars for the scaled-up model using the same iterative approach was determined. The radial and tangential deflection of the cage bars is shown in Figure 4-21 and Figure 4-23. The maximum radial and tangential deflection for the scaled-up FFMG with a 75 mm axial length was only 0.044 mm and 0.01 mm respectively when using NdFeB magnets. Figure 4-22 shows that the iteration converges after 5 iterations with a deflection of 0.044 mm. As the designed air-gap is 0.5 mm this amount of deflection was deemed acceptable.

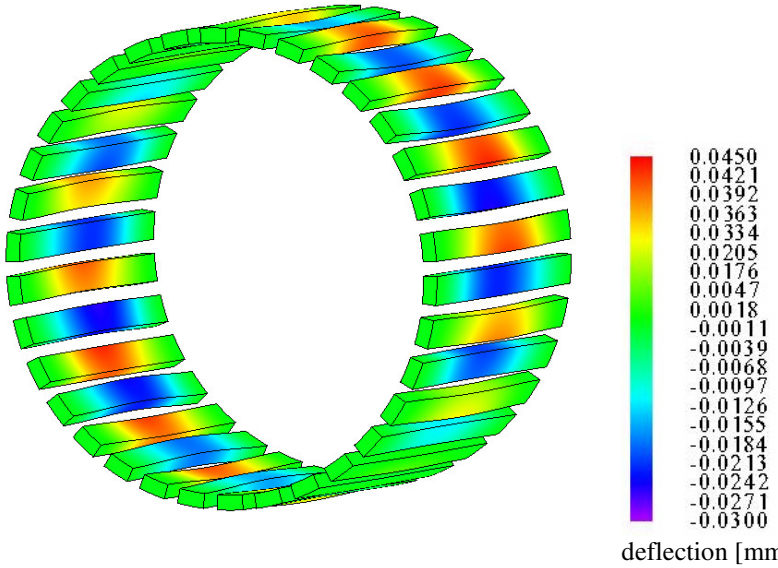

Figure 4-21: Peak cage bar radial deflection for a 75mm stack length when both the inner and outer rotors are present and are assumed to be held fixed.

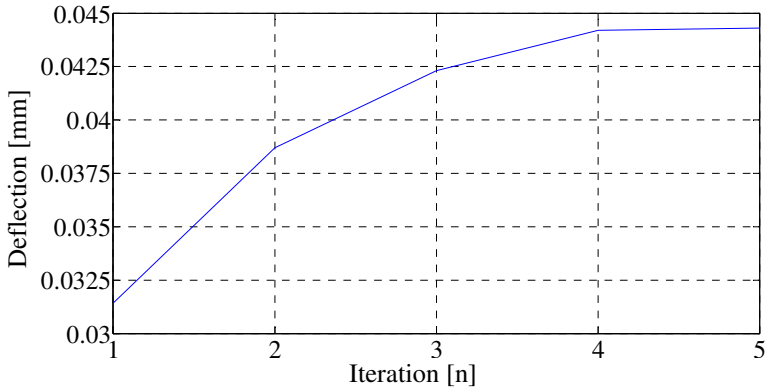

Figure 4-22: Iterations showing converging for radial deflection of cage rotor bars

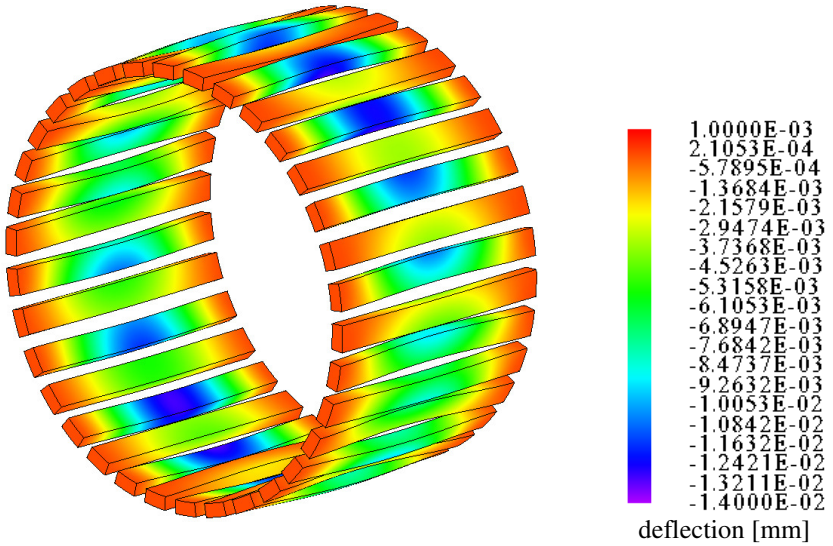

Figure 4-23: Peak cage bar tangential deflection for a 75mm stack length when both the inner and outer rotors are present and are assumed to be held fixed.

4.6. Experimental Validation

The mechanical assembly exploded view for the scaled-up FFMG when using NdFeB magnets is shown in Figure 4-24. Figure 4-25 through Figure 4-27 show the assembly of inner rotor, cage rotor and outer rotors. It can be seen in Figure 4-25 that a small layer of Kevlar thread was glued around the inner rotor in order to retain the magnets in their place. The fully assembled FFMG on the dynamometer test-stand is shown in Figure 4-28.

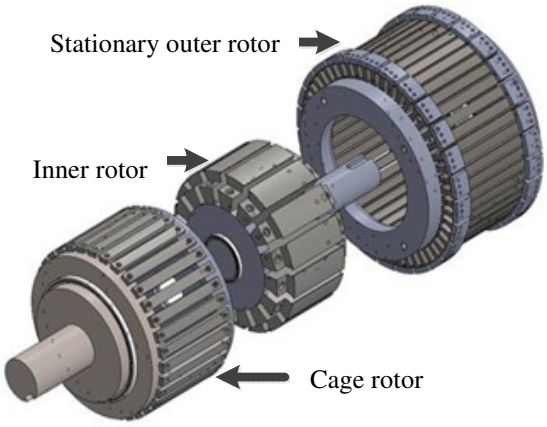

Figure 4-24: Exploded view of the mechanical assembly

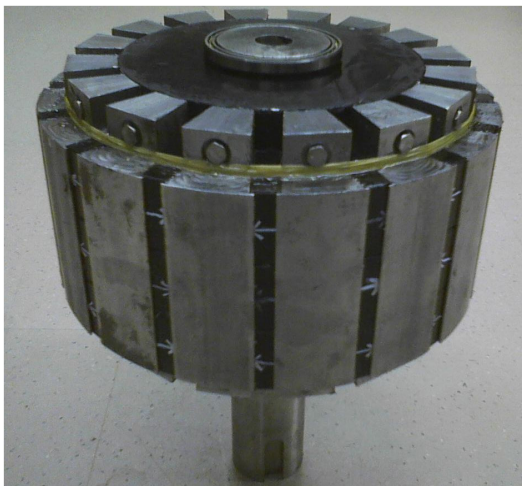

Figure 4-25: Assembly of inner rotor

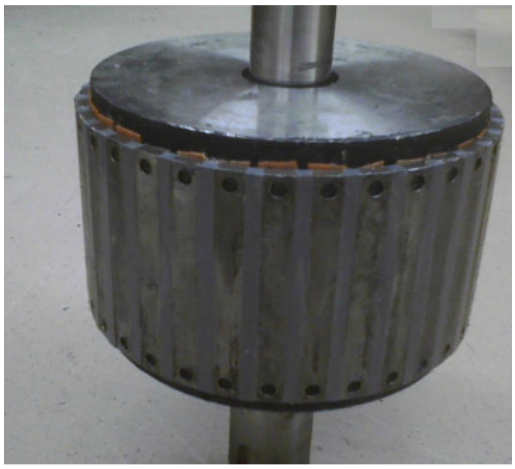

Figure 4-26: Assembly of cage rotor and inner rotor

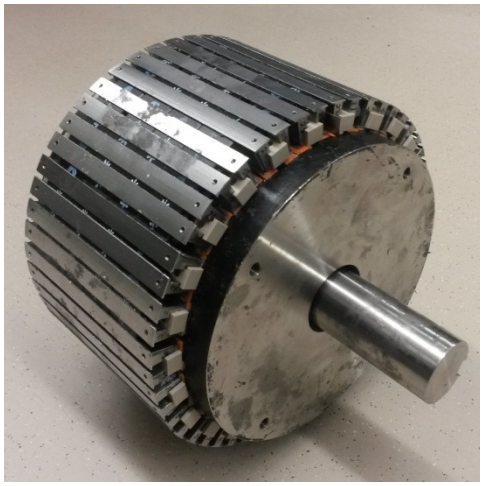

Figure 4-27: Completely assembled FFMG with all the three rotors

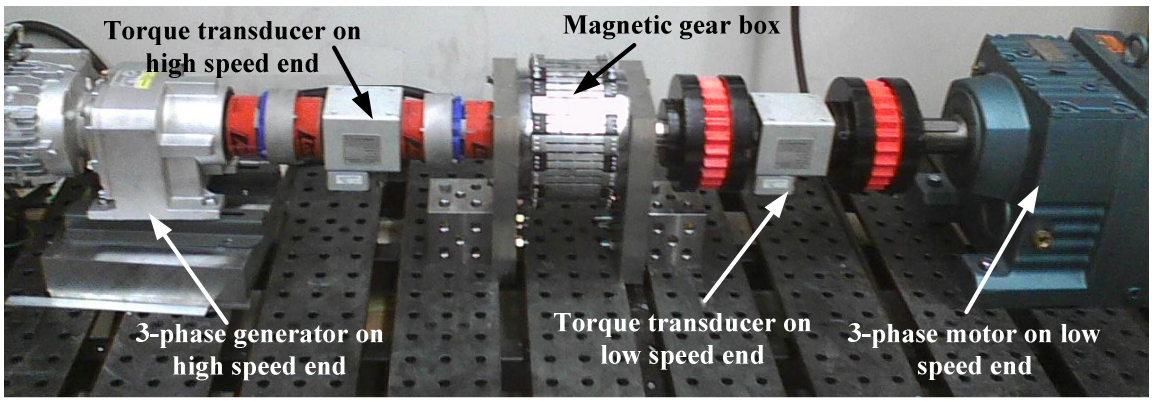

Figure 4-28: Complete test bench setup

A comparison of the radial flux density, B_r, created by the inner rotor when surrounded by air is shown in Figure 4-29 while Figure 4-30 shows the extracted dominant 8^{th} harmonic comparison for the inner rotor field. The experimental value was observed to be within 5% of the value obtained by using FEA.

Figure 4-31 and Figure 4-32 show the measured torque and torque ripple on the cage rotor when 15% of peak torque is applied. This is the minimum torque that is needed in order to start the MG rotating continuously. The average torque is 110.5 Nm with a torque ripple of 1.5 Nm (1.4% of the measured torque).

Figure 4-33 shows the measured torque under different load conditions at the 20 RPM design speed. A maximum torque of 731 Nm was measured beyond which the rotor slipped poles. This measured torque is 2.5 % (19 Nm) lower than the FEA calculated value of 750 Nm. This gives an active region volumetric torque density of 238.7 Nm/L. The corresponding torque ripple on the low-speed cage and high-speed inner rotor is shown in Figure 4-34. A torque ripple of 2 Nm on the inner rotor and 1.6 Nm on cage rotor was measured at the peak torque condition.

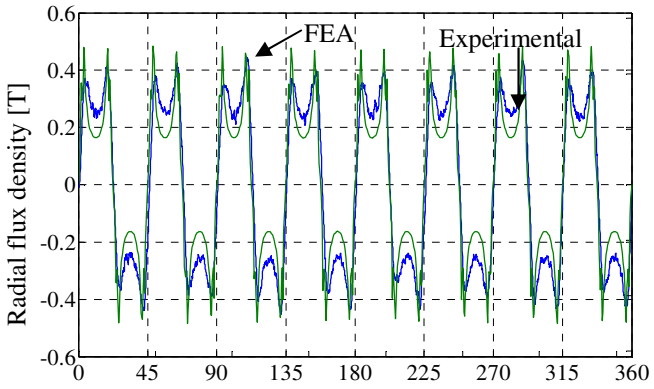

Figure 4-29: Experimental and FEA comparison of radial flux density at r=90.25mm created by the inner rotor when surrounded by air.

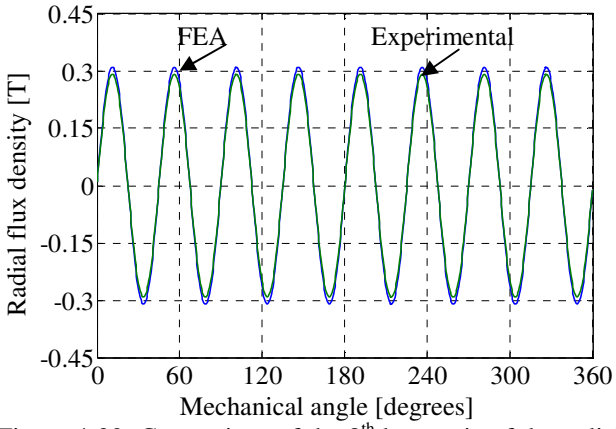

Figure 4-30: Comparison of the 8th harmonic of the radial flux density , B_r, of the inner rotor field

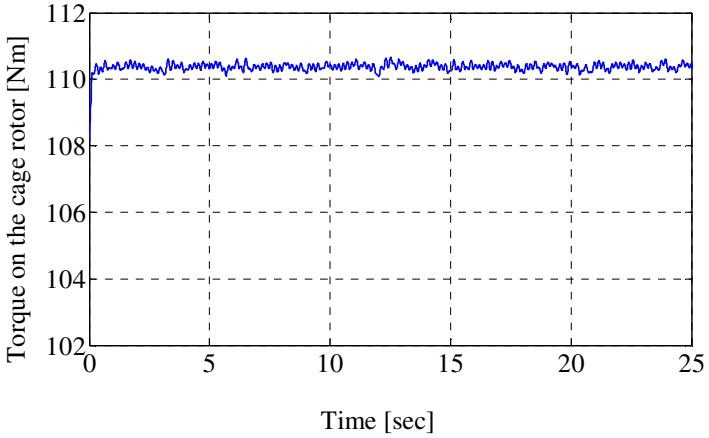

Figure 4-31: Experimental torque on the cage rotor under 15% load

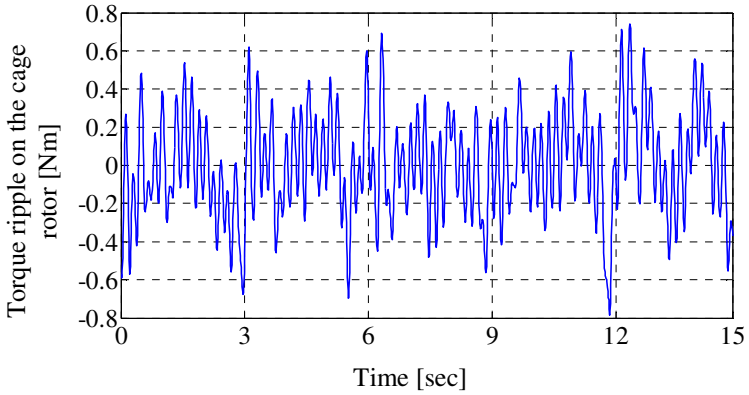

Figure 4-32: Experimental torque ripple on the cage rotor under 15% load

Figure 4-35 shows the measured FFMG efficiency at different load and speed conditions. It can be observed that the efficiency comes down as the load and speed increase. An efficiency of 96.5% was measured at the 20 RPM full load design speed.

Figure 4-36 shows a comparison between the FEA calculated and measured efficiency at the maximum load condition, a relatively good match was achieved. The main discrepancy in the results is believed to be due to the FEA model not accounting for the bearing and the friction losses.

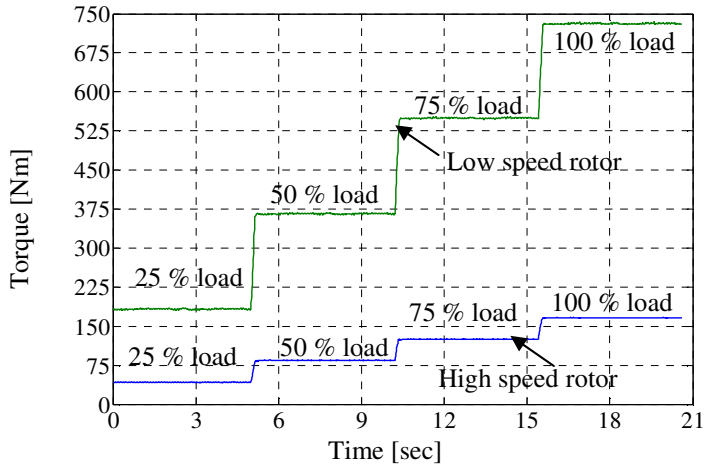

Figure 4-33: Experimental measured torque on the low speed and high speed rotors under various load conditions

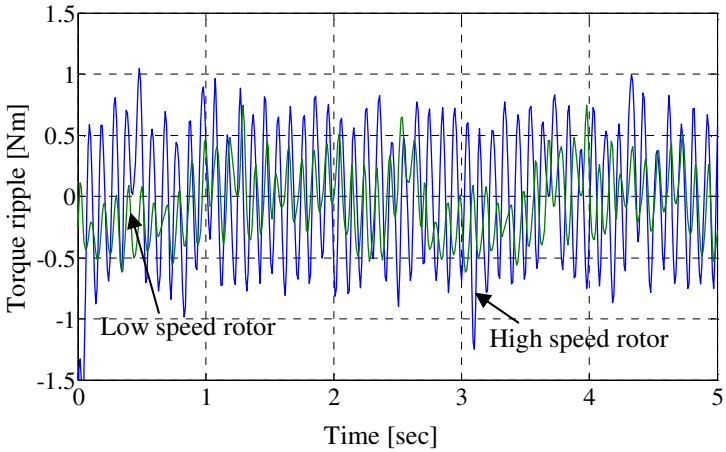

Figure 4-34: Experimental measured torque ripple on the low speed and high speed rotors

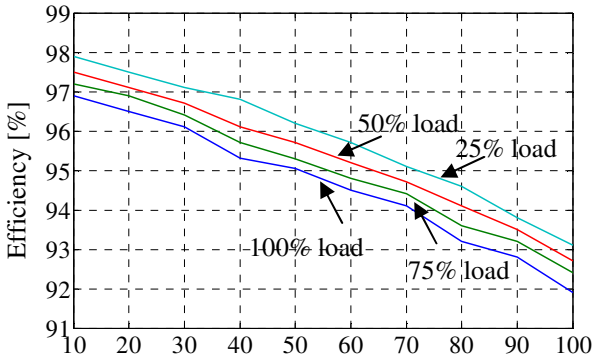

Figure 4-35: Measured efficiency for different input speeds at different load conditions

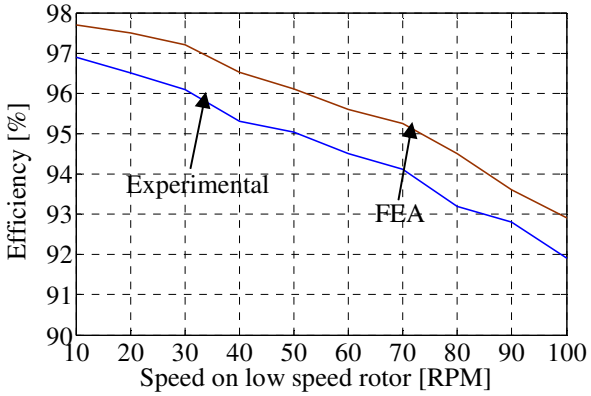

Figure 4-36: Comparison of measured and predicted efficiency for different input speeds at maximum load

In order to further improve the volumetric torque density of the design the radius of the inner rotor, r_{i1}, is changed to 49 mm and the parametric sweep discussed in section 4.3 is again conducted to improve the torque density. The procedure is shown in

Figure 4-37. Maximum torque density is calculated for the change in the l_2 and $r_{o1.}$ With the new values of l_2 and $r_{o1,}$ the inner radius of the inner rotor r_{i1}, is again varied till a maximum torque density is obtained. This procedure is continued until there is no further change in the torque density.

Figure 4-38 shows the change in volumetric torque density due to changes in the cage rotor steel pole length l_2, and the high speed rotor outer radius, r_{o1}, when using ferrite magnets and the inner radius r_{i1}=49mm. A maximum torque density is obtained when l_2 = 7mm and r_{o1} = 88 mm. Figure 4-39 shows the change in torque density when the angular span of cage rotor bars, θ_{s2} and r_{o1} are varied.

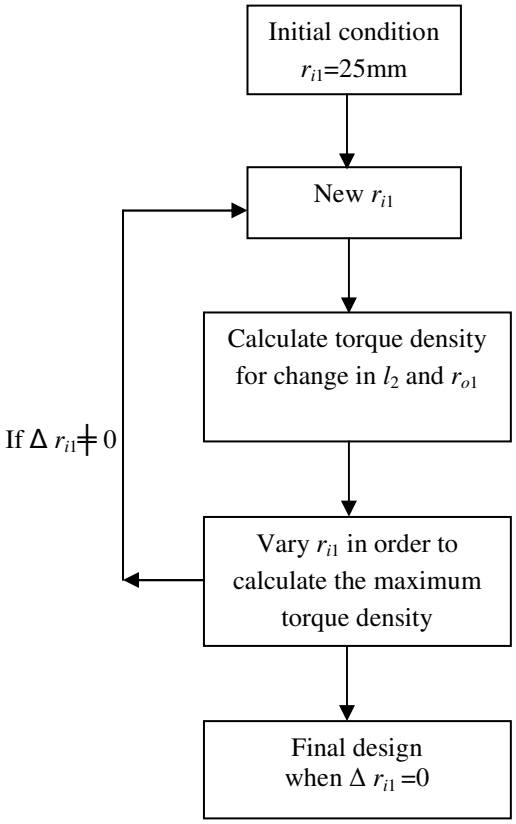

Figure 4-37: Procedure for further optimizing the MG design

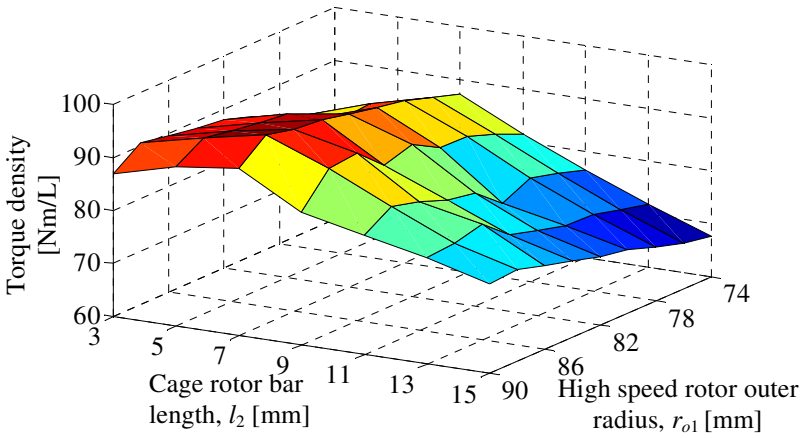

Figure 4-38: Volumetric torque density for changes in the cage rotor bar length, l_2 and high-speed outer rotor radius, r_{o1}, when using ferrite magnets (θ_{s2}=7°) and r_{i1}=49mm

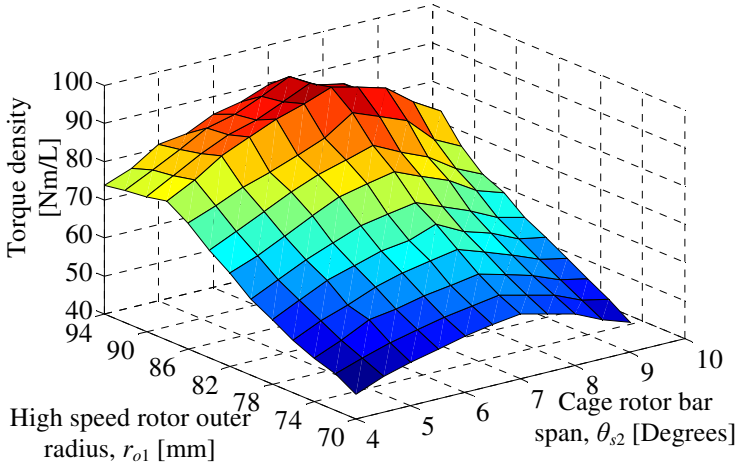

Figure 4-39: Volumetric torque density for cage rotor bar span, θ_{s2}, and high-speed outer rotor radius, r_{o1}, when using ferrite magnets (l_2=7mm) and r_{i1}=49mm

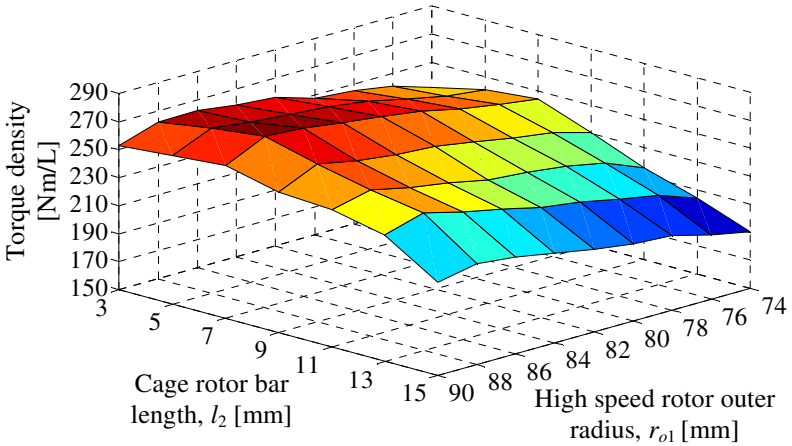

Figure 4-40: Volumetric torque density for changes in the cage rotor bar length, l_2 and high-speed outer rotor radius, r_{o1}, when using NdFeB magnets (θ_{s2}=7°) and r_{i1}=49mm

It is observed that there is no change in the angular span of the cage rotor bars even when other parameters are changed. A maximum torque is obtained at an angular span of 7°. Similarly, Figure 4-40 and Figure 4-41 shows the corresponding volumetric torque densities changes when using NdFeB magnets. The peak torque density occurs at the same geometric values. With the new parameters obtained i.e. l_2=7mm, θ_{s2}=7° and r_{o1}=88mm, the high speed rotor inner radius, r_{i1}, is changed again.

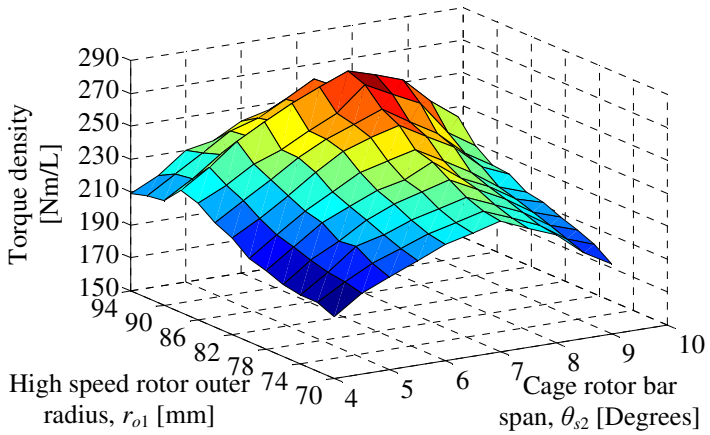

Figure 4-41: Volumetric torque density for cage rotor bar spans, θ_{s2}, and high-speed outer rotor radius, r_{o1}, when using NdFeB magnets (l_2=7mm) and r_{i1}=49mm

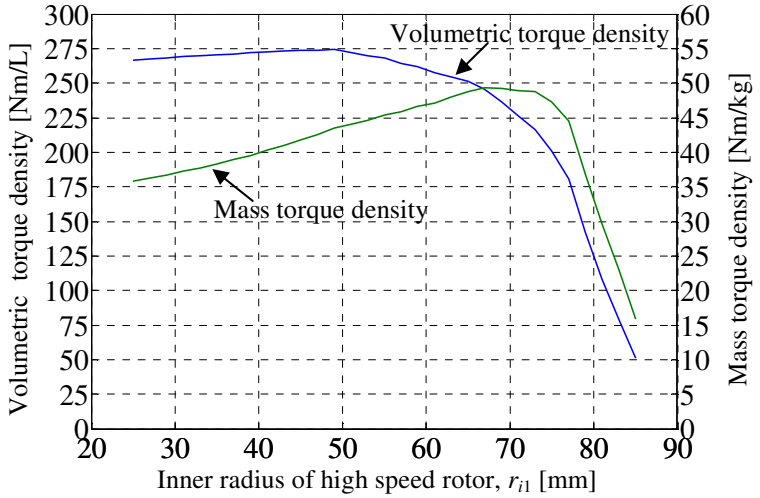

Figure 4-42: Active region torque density variation when the inner radius of the high speed rotor is varied and r_{i1}=49mm

Figure 4-42 shows the variation in the volumetric and mass torque densities and Figure 4-43 shows the torque density per kg of magnets when changing in the inner radius of the high speed rotor. It can be seen that the peak volumetric torque density occurs at r_{i1}=49mm. After including the lips for retaining magnets on the inner and outer rotors the peak torques calculated when using ferrite and NdFeB magnets were 292.6 Nm and 761.2 Nm. This corresponds to a torque density of 95.5 Nm/L and 248.6 Nm/L respectively. The final design after the parametric sweep is shown in Figure 4-44, Table 4-6 and Table 4-7.

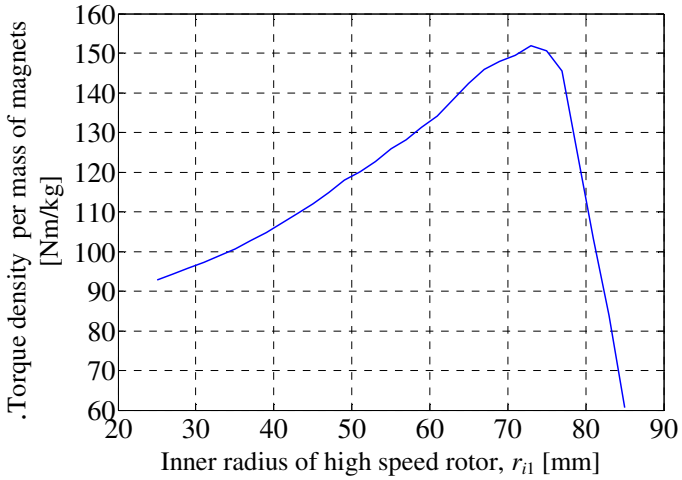

Figure 4-43: Active region torque density per kg of magnets, variation when the inner radius of the high speed rotor is varied and r_{i1}=49mm

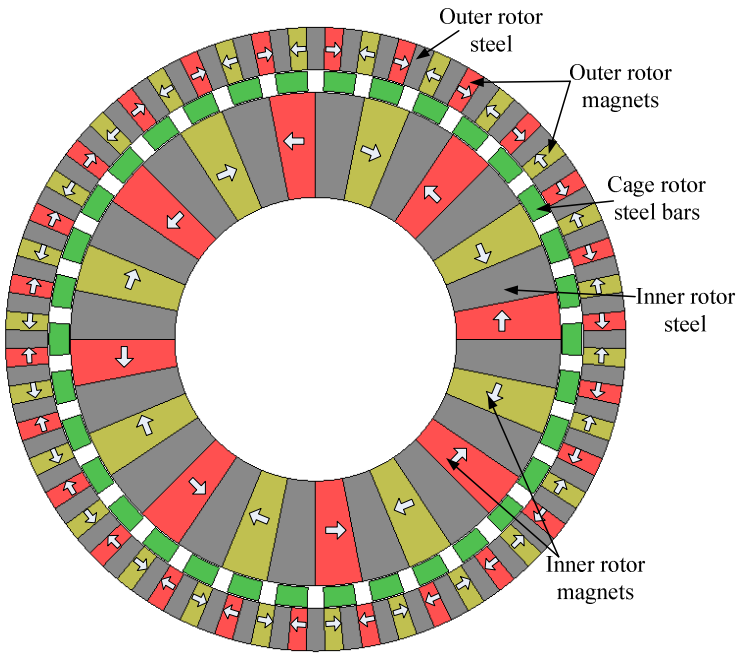

Figure 4-44: Improved design of scaled-up FFMG

Table 4-6: Final geometric sweep parameters of improved scaled-up FFMG

	Description	Value	Unit
Inner rotor (high speed)	Pole pairs, p_1	8	-
	Steel pole span, θ_{s1}	π/16	radians
	Air-gap, g	0.5	mm
Cage rotor	Steel poles, n_2	34	-
Outer rotor (stationary)	Pole pairs, p_3	26	-
	Inner radius, r_{i3}	77	mm
	Outer radius, r_{o3}	110	mm
	Steel pole span, θ_{s3}	π/52	radians
	Air-gap, g	0.5	mm
Material	Ferrite magnet, Hitachi NMF12F	0.46	T
	NdFeB magnet, N40H, B_r	1.25T	T
	416 steel resistivity (cage rotor)	57.0	μΩ-cm
	1018 steel resistivity (inner/outer rotor)	15.9	μΩ-cm
Active region stack length, d		75	mm

Table 4-7: Final geometric sweep parameters of improved scaled-up FFMG

	Description	Value	Unit
Inner rotor (high speed)	Inner radius, r_{i1}	49	mm
	Outer radius, r_{o1}	88	mm
Cage rotor	Cage bar length, l_2	7	mm
	Pole span, θ_{s2}	7	degrees

Table 4-8 and Table 4-9 summarize the active region and full assembly volumetric, mass torque density and shear stress values. It can be noted that the full assembly and active region volumetric torque density values are relatively close, however the active region and measured mass torque density values are significantly different. This is mainly due to the fact that the measured mass included the shafts and additional assembly fixtures some of which do not change the volumetric size. These parts were not significantly optimized. Figure 4-45 shows the comparison of the volumetric torque density values for FFMG designs constructed and experimentally verified in prior research (2003-2014) and this research. The active volumetric torque densities achieved in this research are significantly higher than any other design in the literature. Table 4-10 summarizes the flux concentration ratios of the sub-scale, scaled-up and improved scaled-up designs.

Table 4-8: Active region torque and torque density values

	Scaled-up design			**Sub-scale design**				
	FEA		**Experimental**	**FEA**		**Experimental**		
Magnet type	**Ferrite**	**NdFeB**	**NdFeB**	**Ferrite**	**NdFeB**	**Ferrite**	**NdFeB**	**Units**
Torque	282.6	750.0	731.0	41	115.7	25	113.5	Nm
Volumetric torque density	92.3	244.5	238.7	56	154	33	151.2	Nm/L
Mass torque density	16.6	36.2	35.2	7.4	17.7	4.5	17.4	Nm/kg
Torque-per-kilogram of magnet	51.2	90.1	87.8	23.9	45.5	14.6	44.6	Nm/kg
Shear stress on inner rotor	34.65	92	89.6	17.9	50.5	10.9	50.4	kN/m^2
Shear stress on outer rotor	100	265.5	258.7	41.4	116.9	25.3	114.7	kN/m^2

Table 4-9: Full assembly torque density values

	FEA		Experimental	
Magnet type	**Ferrite**	**NdFeB**	**NdFeB**	**Units**
Volumetric torque density	82	214.9	209.4	Nm/L
Mass torque density	-	-	15.77	Nm/kg

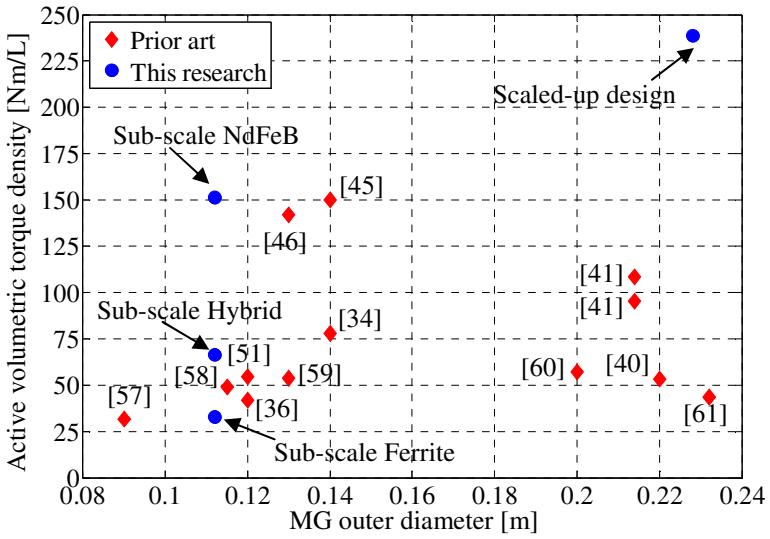

Figure 4-45: Torque density comparison with experimental MG research

Table 4-10: Summary of flux concentration ratios for sub-scale and scaled up designs

Description		Sub-scale design	Scaled-up design	Improved scaled-up design
Flux concentration ratio	$C_{\varphi 3}$	5.28	4.83	4.83
	$C_{\varphi 1}$	3.08	7.3	4.51
Angular span ratio	W_{s23}	2.02	2.02	2.02
Angular span [radians]	θ_{s1}	$\pi/(2p_1)$	$\pi/(2p_1)$	$\pi/(2p_1)$
	θ_{s2}	π/p_3	π/p_3	π/p_3
	θ_{s3}	$\pi/(2p_3)$	$\pi/(2p_3)$	$\pi/(2p_3)$

CHAPTER 5 : ANALYTICAL MODELING OF THE FLUX - FOCUSING MAGNETIC GEAR

5.1. Introduction

The FFMG designs presented in the previous chapters have been obtained after the judicious parameter sweep of various parameters. As the parameters are coupled there is still a lot of scope for further optimization of the parameters to obtain optimum performance from the designs. Further, the scaling of the FFMG is necessary in order to obtain higher torque densities and power transfer capabilities with low torque ripple. Although numerical methods like FEA are an effective tool for optimizing the designs, the computational time and memory required for complete optimization are very high, especially for large diameter designs. FEA designs have the advantage of taking into account the actual geometry and also the non-linear characteristics of the steel parts. However, they don't provide the designer with as much physical insight into the modeling of the design.

An alternative method for optimization is to develop an analytical model based on some simplified assumptions such as simplified boundary conditions and the ideal characterization of the steel parts. These simplifications can greatly reduce the computational time and aid in the design of an optimized FFMG.

Many analytical methods for field prediction in the air-gaps of PM machines have been developed in the literature [60, 75-80]. In most of the designs Maxwell's equations are solved by using the separation of variables method in the low permeability regions by

applying boundary conditions on the interface of these regions. Many of the analytic methods described in the literature focus on the determination of the cogging torque in PM motors that have a radial field topology [81-86]. The analytical modeling of the MG is complicated by the presence of the modulating steel poles in the cage rotor. This field modulation phenomenon is similar to the slotting effects in PM machines.

A number of analytical models for MGs with surface mounted magnets have previously been presented in the literature. For instance Jian [87] developed an analytical model by solving Maxwell's equations by using the magnetic scalar potential. The magnetic field excited in the two air-gaps was separately calculated. The final magnetic field obtained was a superposition of the fields excited by the individual rotors. Penzkofer [88] developed an analytical model for MG equipped with Halbach magnets. Lubin developed a comparable analytical model for determining the field distribution in a MG with surface mounted PMs for a radial [89-90] and an axial-field MG [91]. In Lubin's analysis the Laplace and Poisson's equations were solved in each region and the solution was obtained by using the applicable boundary and interface conditions.

In 2012 Belguerras [92] developed an analytical model for a flux concentration PM machine with a single rotor.

This research takes a similar approach to that adopted in [90] and [92] for developing the analytical model for the FFMG. The method proposed in these papers is adopted and improved upon to attain an accurate field prediction in the air-gaps of the FFMG.

The problem description and assumptions made during the derivation of the FFMG analytic model are given in section 5.2. The governing equations for each region are defined in section 5.3. The boundary conditions are defined in section 5.4. The derivation

of the solution considering homogenous boundary conditions is presented in section 5.5. The modified solutions when considering the non-homogenous boundary conditions is presented in section 5.6. The Fourier coefficient derivation is presented in section 5.7 and the analytical field and force calculations are validated in section 5.8.

5.2. Problem Description

The schematic representation of the FFMG studied is shown in Figure 5-1. The geometric parameters of the model are given as

- R_1 and R_2 are the inner and outer radii of the inner rotor respectively
- R_3 and R_4 are the inner and outer radii of the cage rotor respectively
- R_5 and R_6 are the inner and outer radii of the outer rotor respectively

The model is divided into 5 regions. For clarity the FFMG schematic is represented as a linear model, as shown in Figure 5-2.

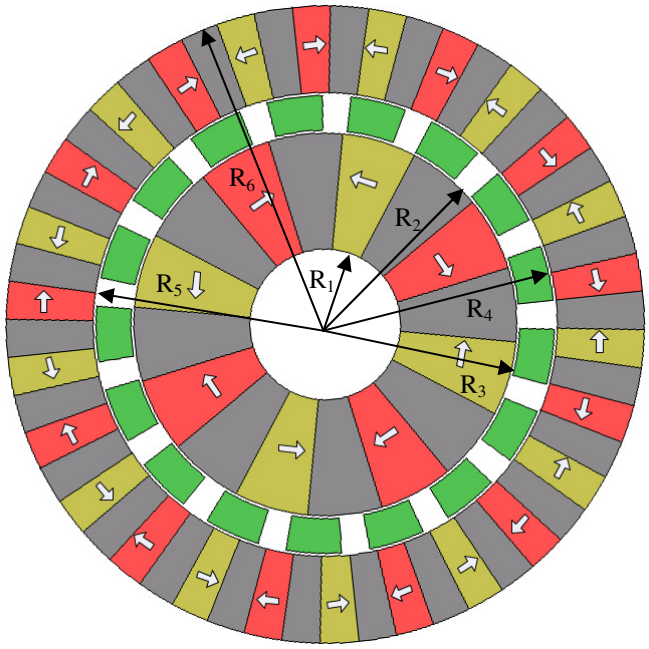

Figure 5-1: Schematic of a FFMG

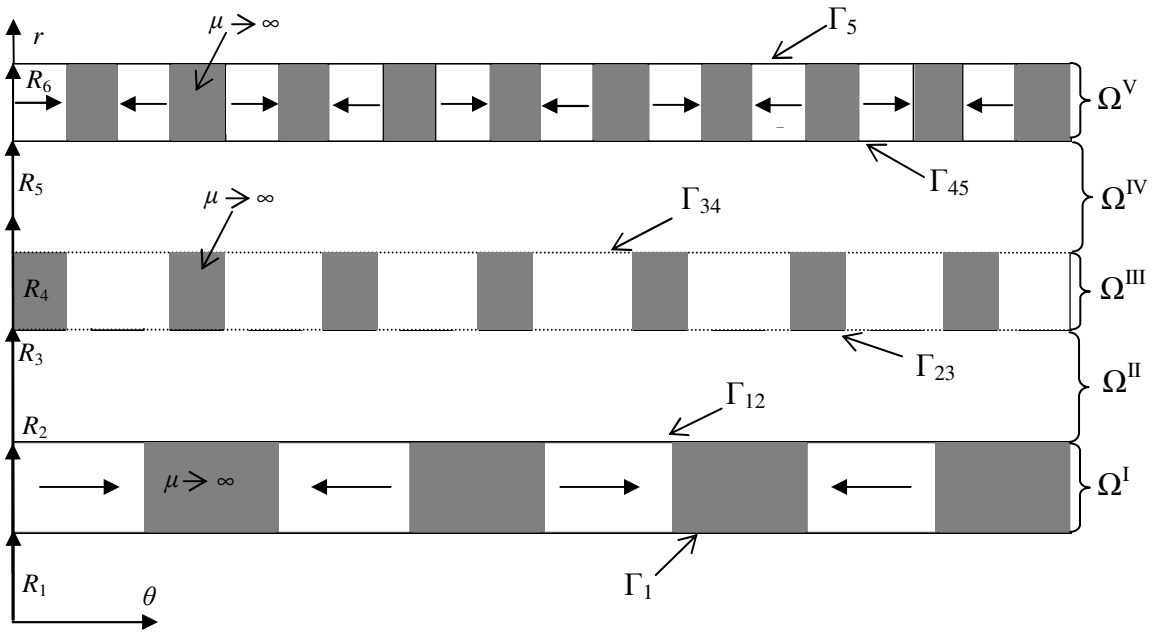

Figure 5-2: Linear schematic of the FFMG with regions and boundary conditions

The following basic assumptions are adopted in the formulation of the analytical model

- The relative permeability of the steel cores of the two rotors are infinite
- The relative permeability of the steel poles of the cage rotor is infinite
- The PMs have the same permeability as air which is equal to one.
- End effects along the *z*-axis direction are neglected
- Magnets are assumed to be azimuthally magnetized

The 2-D analytical model is developed by using the magnetic vector potential formulation in polar coordinates. As shown in Figure 5-2 the FFMG is sub-divided into five regions. The inner and outer air-gap continuous regions are represented by Ω^{II} and Ω^{IV} respectively. The inner and outer rotor magnet piecewise regions are represented by Ω^{I} and Ω^{V} respectively. The cage rotor's non-magnetic piecewise region is given by Ω^{III}. The field solution will involve determining the governing equations in the continuous and

piecewise regions and then by utilizing the Fourier series the fields within the piecewise and continuous regions will be connected together at the boundary interfaces.

5.3. Governing Equations

The magnetic flux density $\mathbf{B}$ in regions Ω^{I} and Ω^{V} is equal to the externally applied magnetic field intensity $\mathbf{H}$ and magnetization vector **M** by [93]

$$\mathbf{B}=\mu_0\mu_r\mathbf{H}+\mu_0\mathbf{M} \tag{5.1}$$

where μ_r is the relative permeability and **M** is the residual magnetization vector. In this analysis it is assumed that within Ω^{I} and Ω^{V}, there is no applied source field **H** and thus (5.1) becomes

$$\mathbf{B}=\mu_0\mathbf{M} \tag{5.2}$$

In the air regions within regions Ω^{II}, Ω^{III} and Ω^{IV}:

$$\mathbf{B}=\mu_0\mathbf{H} \tag{5.3}$$

The governing Maxwell's equations in the non-conducting region are defined as [93]

$$\nabla\cdot\mathbf{B}=0 \tag{5.4}$$

$$\nabla\times\mathbf{B}=0 \tag{5.5}$$

In terms of the magnetic vector potential **A** the magnetic flux density can be represented as

$$\mathbf{B}=\nabla\times\mathbf{A} \tag{5.6}$$

Now applying the cross product on both sides of (5.6) we get

$$\nabla\times\mathbf{B}=\nabla\times\left(\nabla\times\mathbf{A}\right) \tag{5.7}$$

substituting the vector identity defined by

$$\nabla\times\left(\nabla\times\mathbf{A}\right)=\nabla\left(\nabla\cdot\mathbf{A}\right)-\nabla^2\mathbf{A} \tag{5.8}$$

into (5.7) gives

$$\nabla\times\mathbf{B}=\nabla\left(\nabla\cdot\mathbf{A}\right)-\nabla^2\mathbf{A} \tag{5.9}$$

The Coulomb gauge law is given by

$$\nabla\cdot\mathbf{A}=0 \tag{5.10}$$

substituting (5.5) and (5.10) into (5.9) results in Laplace's equation as

$$\nabla^2\mathbf{A}=0 \tag{5.11}$$

Equation (5.11) forms the governing partial differential equation in the region Ω^{II}, Ω^{III} and Ω^{IV}.

Similarly, the governing partial differential equation for the PM region Ω^{I} and Ω^{V} is obtained by substituting (5.2) into (5.9) and utilizing (5.10). This gives

$$\mu_o\nabla\times\mathbf{M}=-\nabla^2\mathbf{A} \tag{5.12}$$

The partial differential equations are solved using the separation of variables method and the Sturm-Liouville method in cylindrical coordinates [94].

The general solution for each region is represented by using Laplace and Poisson's equations in terms of the magnetic vector potential. The fields within each of the air regions between the cage rotor steel poles represented by Ω^{III}, must be determined.

In this 2-D model only the A_z field component of **A** is needed. This is because the magnetic vector potential and magnetic flux density are related by (5.6). When only the A_z term is present we have

$$\mathbf{B}=\nabla\times\mathbf{A}=\frac{1}{r}\begin{vmatrix}\hat{\mathbf{r}} & \hat{\boldsymbol{\theta}}\,r & \hat{\mathbf{z}}\\ \dfrac{\partial}{\partial r} & \dfrac{\partial}{\partial\theta} & \dfrac{\partial}{\partial z}\\ 0 & 0 & A_z\end{vmatrix} \tag{5.13}$$

Evaluating (5.13) gives

$$\mathbf{B}=\nabla\times\mathbf{A}=\hat{\mathbf{r}}\frac{\partial A_z}{\partial\theta}\frac{1}{r}-\hat{\boldsymbol{\theta}}\frac{\partial A_z}{\partial r} \tag{5.14}$$

From (5.14) we get

$$B_r=\frac{\partial A_z}{\partial\theta}\frac{1}{r} \tag{5.15}$$

$$B_\theta=-\frac{\partial A_z}{\partial r} \tag{5.16}$$

For clarity in the following sections the subscript z will be dropped.

The governing Laplacian equation in the region Ω^{III} for the cage rotor air regions is

$$\frac{\partial^2 A_i^{III}}{\partial r^2}+\frac{1}{r}\frac{\partial A_i^{III}}{\partial r}+\frac{1}{r^2}\frac{\partial^2 A_i^{III}}{\partial\theta^2}=0,\ \text{ for } \theta_i\le\theta\le\theta_i+\beta_c \text{ and } R_3\le r\le R_4 \tag{5.17}$$

where A_i^{III} is the magnetic potential in the i^{th} air-gap slot between the steel poles, θ_i is the angular position of the i^{th} slot and β_c is the angular span length between two respective steel poles. Figure 5-3 provides a simplified view of a cage rotor and each of the air regions are consecutively labeled.

The angular position of the i^{th} air-gap slot between steel poles is defined as

$$\theta_i=\frac{2i\pi}{n_2}-\frac{\beta_c}{2}+\theta_0,\ \text{ for } 1\le i\le n_2 \tag{5.18}$$

where θ_0 is the initial angular position of the cage rotor and n_2 is the number of steel poles.

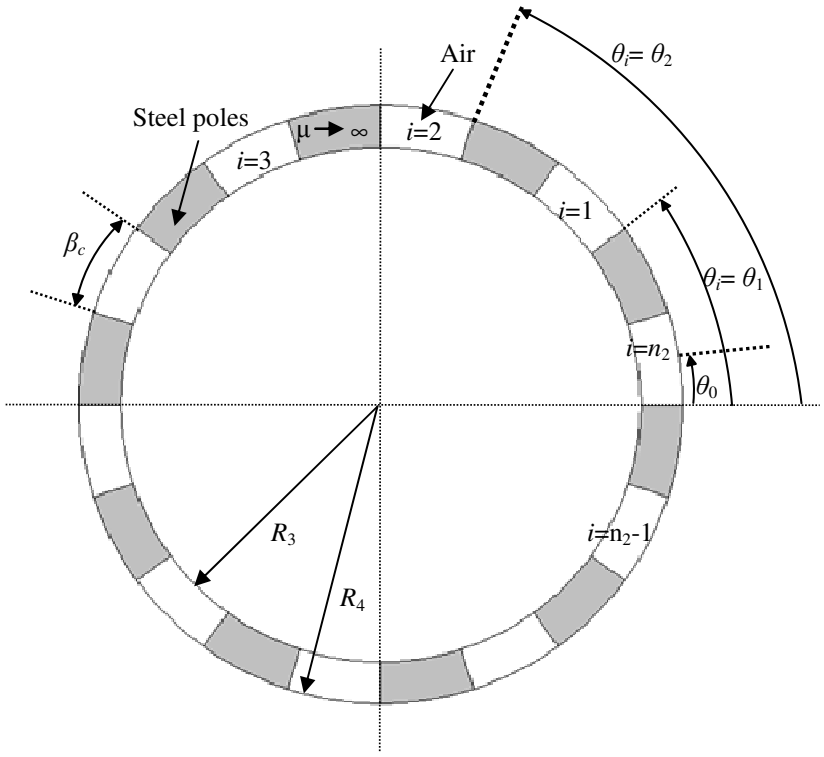

Figure 5-3: Cage rotor steel poles in Ω^{III} shown for $\theta_0 = \beta_c/2$

The governing equation to be solved in the inner rotor air-gap represented by region Ω^{II} has the same form as that derived for region Ω^{III}. It is given by

$$\frac{\partial^2 A^{II}}{\partial r^2} + \frac{1}{r}\frac{\partial A^{II}}{\partial r} + \frac{1}{r^2}\frac{\partial^2 A^{II}}{\partial \theta^2} = 0, \text{ for } R_2 \le r \le R_3 \tag{5.19}$$

and similarly the field in the outer air-gap region, Ω^{IV} is

$$\frac{\partial^2 A^{IV}}{\partial r^2} + \frac{1}{r}\frac{\partial A^{IV}}{\partial r} + \frac{1}{r^2}\frac{\partial^2 A^{IV}}{\partial \theta^2} = 0, \text{ for } R_4 \le r \le R_5 \tag{5.20}$$

The inner rotor represented by region Ω^{I} consists of $2p_1$ magnets where p_1 is the number of inner rotor pole-pairs. The initial angular position of the magnet is assumed to be θ_j and the angular span of magnets is assumed to be β_h as shown in Figure 5-4.

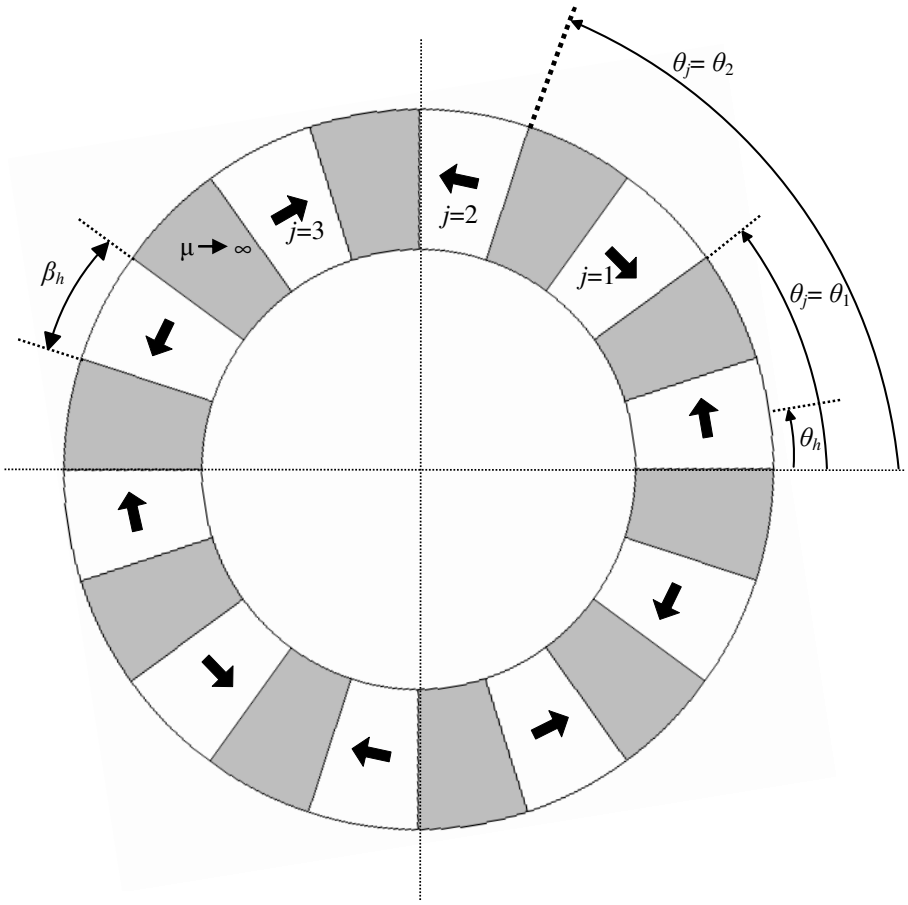

Figure 5-4: Inner rotor, Ω^{I} with $\theta_j=\theta_1$ and $\theta_j= \theta_2$ shown when $\theta_0 =\beta_h/2$

The angular position of the j^{th} magnet is defined as

$$\theta_j = \frac{j\pi}{p_1} - \frac{\beta_h}{2} + \theta_h, \text{ for } 1 \le j \le 2\,p_1 \tag{5.21}$$

The governing equation within region Ω^{I} is obtained from (5.12) and is given by

$$\frac{\partial^2 A_j^{\mathrm{I}}}{\partial r^2} + \frac{1}{r}\frac{\partial A_j^{\mathrm{I}}}{\partial r} + \frac{1}{r^2}\frac{\partial^2 A_j^{\mathrm{I}}}{\partial \theta^2} = -\mu_{\mathrm{o}} \nabla \times \mathbf{M} \tag{5.22}$$

where A_j^{I} is the magnetic potential of the j^{th} magnet of the inner rotor. The magnets are assumed to be azimuthally magnetized and the j^{th} magnet $\mathbf{M}$ is defined as

$$\mathbf{M} = (-1)^j \frac{B_m}{\mu_o} \hat{\boldsymbol{\theta}} \tag{5.23}$$

where B_m is the residual magnetic flux density. The curl of the magnetization vector **M** is given by

$$\nabla \times \mathbf{M} = \frac{1}{r} \begin{vmatrix} \hat{\mathbf{r}} & \hat{\boldsymbol{\theta}} r & \hat{\mathbf{z}} \\ \frac{\partial}{\partial \mathrm{r}} & \frac{\partial}{\partial \theta} & \frac{\partial}{\partial z} \\ 0 & r(-1)^j \frac{B_m}{\mu_o} & 0 \end{vmatrix} = \frac{1}{r}(-1)^j \frac{B_m}{\mu_o} \hat{\mathbf{z}} \tag{5.24}$$

Substituting (5.24) into (5.22) we get

$$\frac{\partial^2 A_j^{\mathrm{I}}}{\partial r^2} + \frac{1}{r}\frac{\partial A_j^{\mathrm{I}}}{\partial r} + \frac{1}{r^2}\frac{\partial^2 A_j^{\mathrm{I}}}{\partial \theta^2} = -(-1)^j \frac{B_m}{r}, \text{ for } R_1 \le r \le R_2 \text{ and } \theta_j \le \theta \le \theta_j + \beta_h \tag{5.25}$$

The outer rotor represented by region, Ω^{V} consists of $2p_3$ magnets where p_3 is the number of pole pairs. The initial angular position of the magnet is assumed to be θ_k and the angular span of magnets is assumed to be β_l as shown in Figure 5-5. The angular position of the k^{th} magnet is defined as

$$\theta_k = \frac{k\pi}{p_3} - \frac{\beta_l}{2} + \theta_l \quad \text{for } 1 \le k \le 2p_3 \tag{5.26}$$

The Laplace equation governing the field in the outer rotor magnets has the same form as that derived in (5.25). It is given by

$$\frac{\partial^2 A_k^{\mathrm{V}}}{\partial r^2} + \frac{1}{r}\frac{\partial A_k^{\mathrm{V}}}{\partial r} + \frac{1}{r^2}\frac{\partial^2 A_k^{\mathrm{V}}}{\partial \theta^2} = -(-1)^k \frac{B_m}{r}, \text{ for } R_5 \le r \le R_6 \text{ and } \theta_k \le \theta \le \theta_k + \beta_l \tag{5.27}$$

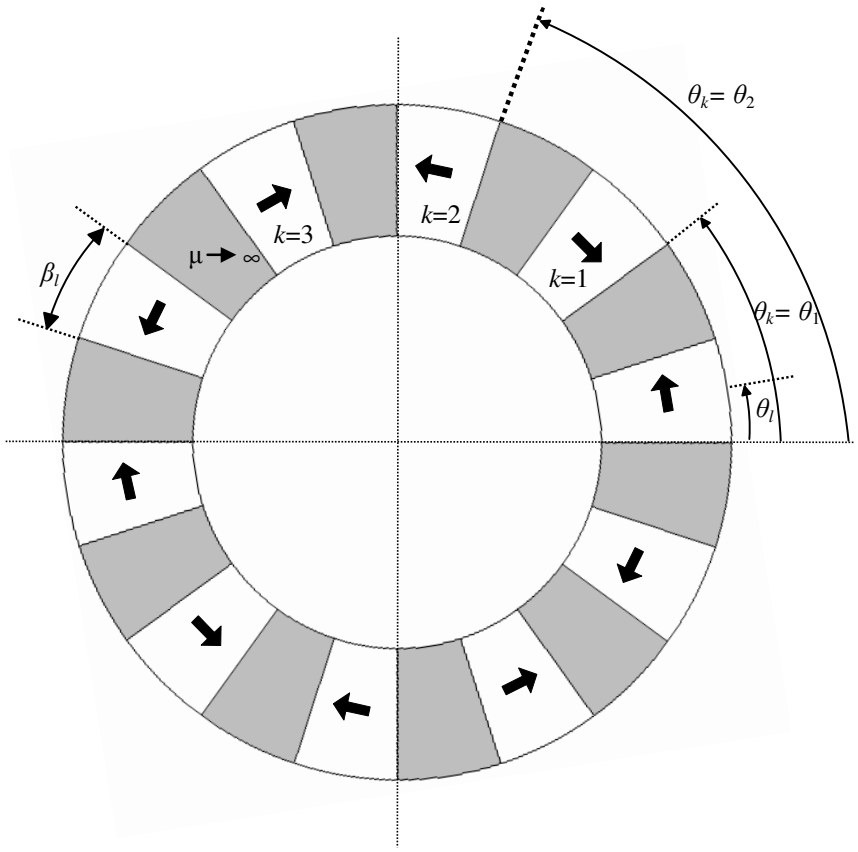

Figure 5-5: Outer rotor, Ω^V with $\theta_k=\theta_1$ and $\theta_k= \theta_2$ shown when $\theta_0 =\beta_l/2$

5.4. Boundary Conditions

The boundary conditions on the inner, cage and outer rotor of the MG are presented in the following three sections.

5.4.1. Inner Rotor Boundary Conditions

The Neumann boundary conditions for a single j^{th} magnet and iron segment in the inner rotor, Ω^I, is shown in Figure 5-6. The PMs are assumed to be azimuthally magnetized and therefore the boundary conditions of the PMs on the inner rotor are

$$\left.\frac{\partial A_j^I}{\partial \theta}\right|_{\theta_j+\beta_h} = 0 \tag{5.28}$$

$$\left.\frac{\partial A_j^{\mathrm{I}}}{\partial \theta}\right|_{\theta_j} = 0 \tag{5.29}$$

The vector potential continuity equations on the outer and inner radii are

$$A_j^{\mathrm{I}}(R_2,\theta) = A^{\mathrm{II}}(R_2,\theta), \text{for } \theta_j \le \theta \le \theta_j + \beta_h, \text{on } \Gamma_{12} \tag{5.30}$$

$$A_j^{\mathrm{I}}(R_1,\theta) = 0 \text{ , on } \Gamma_1 \tag{5.31}$$

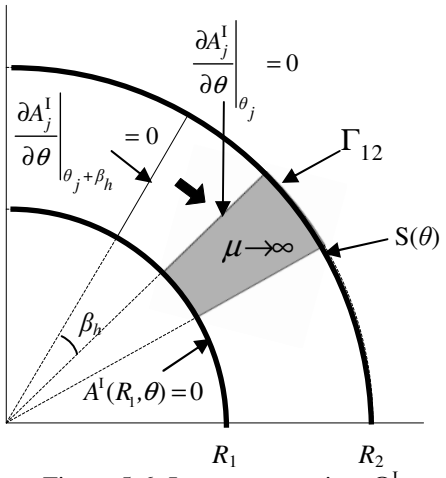

Figure 5-6: Inner rotor region, Ω^{I}

The continuity of the tangential magnetic field at the outer radius, R_2, of the inner rotor is given by

$$\left.\frac{\partial A^{\mathrm{II}}}{\partial r}\right|_{r=R_2} = \mathrm{S}(\theta) \text{ , on } \Gamma_{12} \tag{5.32}$$

where

$$\mathrm{S}(\theta) = \begin{cases} \left.\dfrac{\partial A_j^{\mathrm{I}}}{\partial r}\right|_{r=R_2} + (-1)^j B_m, \text{ for } \theta_j \le \theta \le \theta_j + \beta_h \\ 0 \qquad\qquad\qquad\qquad \text{, elsewhere} \end{cases} \tag{5.33}$$

S(θ) is a piecewise function. The use of the piecewise function, S(θ), enables the continuous function $A^{\mathrm{II}}(r,\theta)$ to be connected to the discontinuous function A_j^{I} at the

boundary interface. The field due to the magnet is assumed to be present at the boundary interface and therefore (5.33) includes B_m at the Γ_{12} boundary interface.

5.4.2. Cage Rotor Boundary Conditions

The boundary conditions for a single cage rotor steel pole in region Ω^{III}, is shown in Figure 5-7.

The radial component of the magnetic field is assumed to be zero on the left and right angular sides of the steel pole, therefore:

$$\left.\frac{\partial A_i^{III}}{\partial \theta}\right|_{\theta=\theta_i} = 0 \tag{5.34}$$

$$\left.\frac{\partial A_i^{III}}{\partial \theta}\right|_{\theta=\theta_i+\beta_c} = 0 \tag{5.35}$$

Also at $r=R_3$ and $r=R_4$ the continuity boundary conditions are:

$$A_i^{III}(R_4,\theta) = A^{IV}(R_4,\theta)\ \text{, for}\ \ \theta_i \le \theta \le \theta_i + \beta_c\text{, on } \Gamma_{34} \tag{5.36}$$

$$A_i^{III}(R_3,\theta) = A^{II}(R_3,\theta)\text{, for } \theta_i \le \theta \le \theta_i + \beta_c\text{, on } \Gamma_{23} \tag{5.37}$$

The continuity of the tangential component of the magnetic field at radius $r = R_3$ is given by

$$\left.\frac{\partial A_i^{II}}{\partial r}\right|_{r=R_3} = \mathrm{F}(\theta)\ \text{, on } \Gamma_{23} \tag{5.38}$$

where F(θ) is a piecewise function given by:

$$\mathrm{F}(\theta) = \begin{cases} \left.\dfrac{\partial A_i^{III}}{\partial r}\right|_{r=R_3}\text{, for}\ \ \theta_i \le \theta \le \theta_i + \beta_c \\ 0 \qquad\quad \text{, elsewhere} \end{cases} \tag{5.39}$$

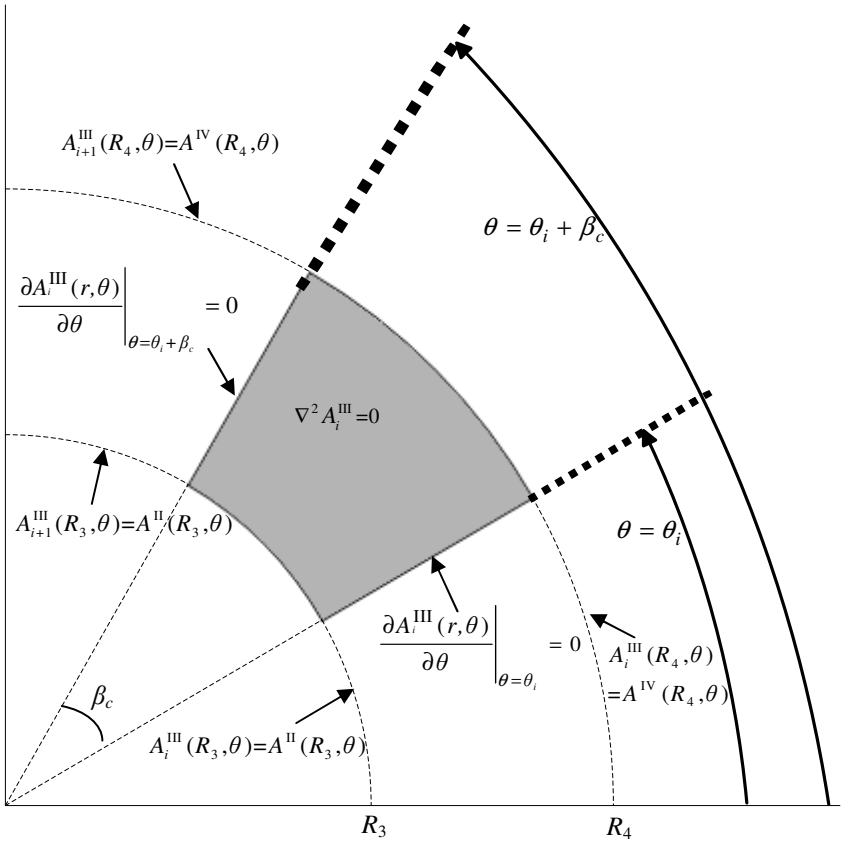

Figure 5-7: Single i^{th} slot of cage rotor steel pole in Ω^{III}

The continuity of the tangential component of the magnetic field at $r = R_4$ leads to

$$\left.\frac{\partial A^{\mathrm{IV}}}{\partial r}\right|_{r=R_4} = \mathrm{H}(\theta)\ , \text{on } \Gamma_{34} \tag{5.40}$$

where $\mathrm{H}(\theta)$ is the piecewise function given by:

$$\mathrm{H}(\theta) = \begin{cases} \left.\frac{\partial A_i^{\mathrm{III}}}{\partial r}\right|_{r=R_4} & \text{, for } \theta_i \le \theta \le \theta_i + \beta_c \\ 0 & \text{, elsewhere} \end{cases} \tag{5.41}$$

5.4.3. Outer Rotor Boundary Conditions

The Neumann boundary conditions for a single magnet and iron segment in the outer rotor, Ω^{V}, is shown in Figure 5-8. The boundary conditions are:

$$\left.\frac{\partial A_k^{\mathrm{V}}}{\partial \theta}\right|_{\theta_k+\beta_l} = 0 \tag{5.42}$$

$$\left.\frac{\partial A_k^{\mathrm{V}}}{\partial \theta}\right|_{\theta_k} = 0 \tag{5.43}$$

The magnetic vector potential continuity equation at $r=R_5$ is

$$A_k^{\mathrm{V}}(R_5,\theta) = A^{\mathrm{IV}}(R_5,\theta)\text{ , for }\ \theta_k \le \theta \le \theta_k+\beta_l\text{, on }\Gamma_{45} \tag{5.44}$$

$$A_k^{\mathrm{V}}(R_6,\theta) = 0\text{ , on }\Gamma_5 \tag{5.45}$$

$$\left.\frac{\partial A^{\mathrm{IV}}}{\partial r}\right|_{r=R_5} = \mathrm{L}(\theta)\text{ , on }\Gamma_{45} \tag{5.46}$$

where

$$\mathrm{L}(\theta) = \begin{cases} \left.\dfrac{\partial A^{\mathrm{V}}}{\partial r}\right|_{r=R_5} + (-1)^k B_m\text{ , for }\ \theta_k \le \theta \le \theta_k+\beta_l \\ 0 \qquad\qquad\qquad\qquad\text{, elsewhere} \end{cases} \tag{5.47}$$

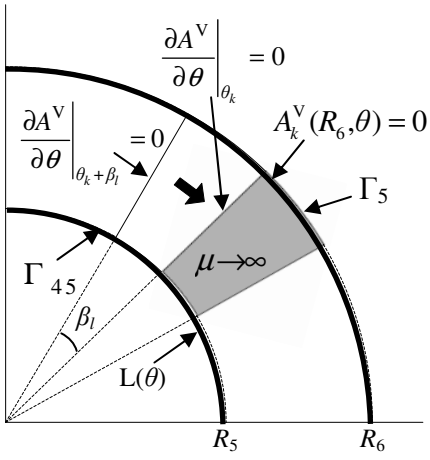

Figure 5-8: Outer rotor region, Ω^{V}

5.5. General Solutions when Accounting for Homogeneous Boundary Conditions

In this section the general solution for each region is derived when accounting of the homogeneous boundary conditions. The solution derivation of air regions Ω^{II}, Ω^{IV}, Ω^{III} and magnet regions Ω^{I} and Ω^{V} are discussed in the following two sections.

5.5.1. General Solution in the Air Regions, Ω^{II}, Ω^{III} and Ω^{IV}

The Laplace equation to be solved in the air-gap regions is given by equations (5.17), (5.19) and (5.20). By using the method of separation of variables we can obtain the solution of the partial differential equations. For the inner rotor air-gap region Ω^{II} we can define:

$$A^{II}(r,\theta) = \rho^{II}(r)\phi^{II}(\theta) \tag{5.48}$$

Substituting (5.48) into (5.19) we get

$$\frac{\partial^2 \rho^{II}(r)}{\partial r^2}\phi^{II}(\theta) + \frac{1}{r}\frac{\partial \rho^{II}(r)}{\partial r}\phi^{II}(\theta) + \frac{1}{r^2}\rho^{II}(r)\frac{\partial^2 \phi^{II}(\theta)}{\partial \theta^2} = 0 \tag{5.49}$$

Rearranging the terms in (5.49) we get

$$\frac{r^2\left(\frac{\partial^2 \rho^{II}(r)}{\partial r^2} + \frac{1}{r}\frac{\partial \rho^{II}(r)}{\partial r}\right)}{\rho^{II}(r)} = \frac{-\frac{\partial^2 \phi^{II}(\theta)}{\partial \theta^2}}{\phi^{II}(\theta)} \tag{5.50}$$

The left hand side of the equation depends only on r and the right hand side depends only on θ and both are independent of each other. Hence both sides of the equation have to be constants to be equal. Assuming that constant to be λ^2 we obtain the two ordinary differential equations (ODE's) shown in (5.51) and (5.52) which can then be easily solved.

$$\frac{d^2 \phi^{II}(\theta)}{d\theta^2} + \lambda^2 \phi^{II}(\theta) = 0 \tag{5.51}$$

$$r^2\frac{d^2\rho^{II}(r)}{dr^2}+r\frac{d\rho^{II}(r)}{dr}-\lambda^2\rho^{II}(r)=0 \tag{5.52}$$

Solving the differential equations will help us determine the value of the separation constant λ which will satisfy the new boundary conditions. Using Strum-Liouville method of solving the differential equations and solving (5.51) we get the general form as

$$\phi_\lambda^{II}(\theta)=C_\lambda^{II}\cos(\lambda\theta)+D_\lambda^{II}\sin(\lambda\theta) \tag{5.53}$$

where C_λ^{II} and D_λ^{II} are constants that need to be determined.

Equation (5.52) is Cauchy-Euler's equation [95] and can be solved to get a constant coefficient equation. Considering

$$\rho(r)=r^{\delta} \tag{5.54}$$

where δ is a constant.

Then substituting (5.54) into (5.52) gives

$$r^2\delta(\delta-1)r^{\delta-2}+\delta r r^{\delta-1}-\lambda^2 r^{\delta}=0 \tag{5.55}$$

Canceling out the radial variable (5.55) becomes

$$\delta^2-\lambda^2=0 \tag{5.56}$$

Equation (5.56) is called the Cauchy-Euler characteristic equation. Thus we have

$$\delta=\pm\lambda \tag{5.57}$$

equation (5.54) can then be written as

$$\rho_\lambda^{II}(r)=A_\lambda^{II}r^{\lambda}+B_\lambda^{II}r^{-\lambda} \tag{5.58}$$

where A_λ^{II} and B_λ^{II} are unknown constants. Substituting (5.58) and (5.53) into (5.48) we get

$$A^{II}(r,\theta)=\left(A_\lambda^{II}r^{\lambda}+B_\lambda^{II}r^{-\lambda}\right)\left(C_\lambda^{II}\cos(\lambda\theta)+D_\lambda^{II}\sin(\lambda\theta)\right) \tag{5.59}$$

Since the angular boundary conditions must be periodic such that

$$A^{II}(r,0) = A^{II}(r,2\pi) \tag{5.60}$$

we require that $\lambda=n$, where n is an integer in the region Ω^{II}. Equation (5.59) can then be expressed as a Fourier series as

$$A^{II}(r,\theta) = \sum_{n=1}^{\infty}\left(A_n^{II} r^n + B_n^{II} r^{-n}\right)\left(C_n^{II}\cos(n\theta) + D_n^{II}\sin(n\theta)\right) \tag{5.61}$$

For n=0 however, λ=0 and therefore (5.52) reduces to

$$\frac{\partial}{\partial r}\left(r\frac{\partial \rho_0^{II}}{\partial r}\right) = 0 \tag{5.62}$$

Integrating both sides of (5.62) gives

$$r\frac{\partial \rho_0^{II}}{\partial r} = B_0^{II} \tag{5.63}$$

where B_0^{II} is a constant. Rearranging and integrating again (5.63) gives

$$\rho_0^{II}(r) = \int \frac{B_0^{II}}{r} dr = A_0^{II} + B_0^{II}\ln(r) \tag{5.64}$$

The general solution is the superposition of all λ values. Therefore for all $\lambda \geq 0$ the solution to (5.19) is then [94]

$$A^{II}(r,\theta) = A_0^{II} + B_0^{II}\ln(r) + \sum_{n=1}^{\infty}\left(A_n^{II} r^n + B_n^{II} r^{-n}\right)\left(C_n^{II}\cos(n\theta) + D_n^{II}\sin(n\theta)\right) \tag{5.65}$$

The total flux, Φ, through a closed surface must be zero. By integrating (5.4) on both sides one obtains

$$\Phi = \int_0^{2\pi}\int_0^{d} \mathbf{B}\cdot d\mathbf{S} = 0 \tag{5.66}$$

where d is the axial length of MG and:

$$d\mathbf{S} = r\,d\theta\,dz\,\hat{r} \tag{5.67}$$

Therefore

$$\mathbf{B}.d\mathbf{S} = B_r r d\theta dz \tag{5.68}$$

Assuming no field travels along the z-axis and utilizing (5.15) equation (5.66) can be written as:

$$\Phi = d\int_0^{2\pi} \frac{\partial A^{\mathrm{II}}}{\partial \theta} d\theta = 0 \tag{5.69}$$

where d is the axial length of the MGG.

Substituting (5.65) into (5.69) we get

$$\Phi = d\int_0^{2\pi} \frac{\partial}{\partial \theta}\left(A_0^{\mathrm{II}} + B_0^{\mathrm{II}} \ln(r) + \sum_{n=1}^{\infty}\left(A_n^{\mathrm{II}} r^n + B_n^{\mathrm{II}} r^{-n}\right)\left(C_n^{\mathrm{II}} \cos(n\theta) + D_n^{\mathrm{II}} \sin(n\theta)\right)\right) d\theta = 0 \tag{5.70}$$

Evaluating (5.70) we get

$$\Phi = \left[\frac{1}{n}\left(A_n^{\mathrm{II}} r^n + B_n^{\mathrm{II}} r^{-n}\right)\left(C_n^{\mathrm{II}} \sin(n\theta) - D_n^{\mathrm{II}} \cos(n\theta)\right) + A_0^{\mathrm{II}} + B_0^{\mathrm{II}} \ln(r)\right]_0^{2\pi} = 0 \tag{5.71}$$

One can see that for (5.71) to be zero the constant terms must be

$$A_0^{\mathrm{II}} = B_0^{\mathrm{II}} = 0 \tag{5.72}$$

Substituting (5.72) into (5.65) gives:

$$A^{\mathrm{II}}(r,\theta) = \sum_{n=1}^{\infty}\left(A_n^{\mathrm{II}} r^n + B_n^{\mathrm{II}} r^{-n}\right)\left(C_n^{\mathrm{II}} \cos(n\theta) + D_n^{\mathrm{II}} \sin(n\theta)\right) \tag{5.73}$$

The general solution of (5.20) in the outer air-gap region Ω^{IV} is similarly derived and is given by

$$A^{\mathrm{IV}}(r,\theta) = \sum_{n=1}^{\infty}\left(A_n^{\mathrm{IV}} r^n + B_n^{\mathrm{IV}} r^{-n}\right)\left(C_n^{\mathrm{IV}} \cos(n\theta) + D_n^{\mathrm{IV}} \sin(n\theta)\right) \tag{5.74}$$

The index n will be used to denote the harmonic field term within the inner and outer air-gap regions.

The general solution of (5.17) for the i^{th} cage rotor air-gap in region Ω^{III} has the same form as (5.59) and is given by

$$A_i^{\text{III}}(r,\theta) = \left(A_\lambda^{\text{III}} r^{\lambda} + B_\lambda^{\text{III}} r^{-\lambda}\right)\left(C_\lambda^{\text{III}} \cos(\lambda\theta) + D_\lambda^{\text{III}} \sin(\lambda\theta)\right) \tag{5.75}$$

However, the azimuthal boundary conditions given by (5.34) and (5.35) must also be accounted for. Substituting (5.75) into (5.34) we get

$$\left.\frac{\partial A_i^{\text{III}}}{\partial\theta}\right|_{\theta=\theta_i} = 0 = \left(A_\lambda^{\text{III}} r^{\lambda} + B_\lambda^{\text{III}} r^{-\lambda}\right)\left(-\lambda C_\lambda^{\text{III}} \sin(\lambda\theta_i) + \lambda D_\lambda^{\text{III}} \cos(\lambda\theta_i)\right) \tag{5.76}$$

and substituting (5.75) into (5.35) we get

$$\left.\frac{\partial A_i^{\text{III}}}{\partial\theta}\right|_{\theta=\theta_i+\beta_c} = 0 = \left(A_\lambda^{\text{III}} r^{\lambda} + B_\lambda^{\text{III}} r^{-\lambda}\right)\left(-\lambda C_\lambda^{\text{III}} \sin(\lambda(\theta_i+\beta_c)) + \lambda D_\lambda^{\text{III}} \cos(\lambda(\theta_i+\beta_c))\right) \tag{5.77}$$

Equation (5.76) and (5.77) can result in a non-trivial solution only if

$$D_\lambda^{\text{III}} = 0 \tag{5.78}$$

and

$$\lambda = uk_c \tag{5.79}$$

where u is an integer and $k_c = \dfrac{\pi}{\beta_c}$

The corresponding solutions for the Eigenvalues given by λ are called Eigenfunctions.

Substituting (5.78) and (5.79) into (5.75) the general solution for $u \geq 0$ will be:

$$A_i^{\text{III}}(r,\theta) = A_{0,i}^{\text{III}} + B_{0,i}^{\text{III}} \ln(r) + \sum_{u=1}^{\infty}\left(A_{u,i}^{\text{III}} r^{uk_c} + B_{u,i}^{\text{III}} r^{-uk_c}\right)\cos(uk_c(\theta-\theta_i)) \tag{5.80}$$

where in (5.80) the u=0 term has been added. Since the net flux in each individual i^{th} air space does not have to be zero. The index u and not n will be used to denote harmonic terms within the cage rotor air-gap region as well as magnet regions. Different spatial harmonic index names need to be used within the continuous and piecewise regions.

5.5.2. General Solution in the Inner and Outer Magnet Regions, Ω^{I} and Ω^{V}

The general solution for the j^{th} inner rotor magnet in region Ω^{I} is obtained by solving (5.25). Equation (5.25) is a non-homogeneous Poisson equation. The general solution is obtained by calculating the superposition of the complementary solution, $A_j^{Ic}(r,\theta)$ and a particular solution, $A_j^{Ip}(r,\theta)$ such that:

$$A_j^{I}(r,\theta) = A_j^{Ic}(r,\theta) + A_j^{Ip}(r,\theta) \tag{5.81}$$

The complementary equation is determining by solving (5.25) with the right side equal to zero such that

$$\frac{\partial^2 A_j^{Ic}}{\partial r^2} + \frac{1}{r}\frac{\partial A_j^{Ic}}{\partial r} + \frac{1}{r^2}\frac{\partial^2 A_j^{Ic}}{\partial \theta^2} = 0, \text{ for } R_1 \le r \le R_2 \text{ and } \theta_j \le \theta \le \theta_j + \beta_h \tag{5.82}$$

The complementary solution to (5.82) is obtained in the same way as for the cage rotor region Ω^{III}. The homogeneous boundary conditions given in (5.28) and (5.29) are applied and the solution is obtained as

$$A_j^{Ic}(r,\theta) = A_{0,j}^{Ic} + B_{0,j}^{Ic}\ln(r) + \sum_{u=1}^{\infty}\left(A_{u,j}^{Ic} r^{\frac{u\pi}{\beta_h}} + B_{u,j}^{Ic} r^{\frac{-u\pi}{\beta_h}}\right)\cos\left(\frac{u\pi}{\beta_h}(\theta-\theta_j)\right) \tag{5.83}$$

where $A_{0,j}^{Ic}$, $B_{0,j}^{Ic}$, $A_{u,j}^{Ic}$ and $B_{u,j}^{Ic}$ are unknowns for the j^{th} magnet and need to be determined.

The particular solution is obtained by solving (5.25) with all boundary conditions taken as zero [96]. The boundary condition (5.30) is modified as

$$A_j^{\mathrm{I}}(R_2,\theta)=0 \tag{5.84}$$

The field at $r=R_1$ is already assumed to be zero (by (5.31)).

The right hand side of (5.25) is independent of θ and is only a function of r. Therefore, the $A_j^{\mathrm{I}p}$ field should not change with angular position. Equation (5.25) can then be modified into an ODE as

$$\frac{d^2A_j^{\mathrm{I}p}}{dr^2}+\frac{1}{r}\frac{dA_j^{\mathrm{I}p}}{dr}=-(-1)^j\frac{B_m}{r},\ \text{for } R_1\le r\le R_2 \tag{5.85}$$

Solving (5.85) gives the particular solution as

$$A_j^{\mathrm{I}p}=-r(-1)^jB_m+C_1+C_2\ln(r) \tag{5.86}$$

where C_1 and C_2 are arbitrary constants.

Equation (5.86) must satisfy the boundary conditions given in (5.28), (5.29) and (5.84), the coefficients C_1 and C_2 in (5.86) then must be zero. Hence (5.86) reduces to

$$A_j^{\mathrm{I}p}(r,\theta)=-r(-1)^jB_m \tag{5.87}$$

The general solution is thus obtained by substituting (5.83) and (5.87) into (5.81)

$$A_j^{\mathrm{I}}(r,\theta)=A_{0,j}^{\mathrm{I}}+B_{0,j}^{\mathrm{I}}\ln(r)-r(-1)^jB_m+\sum_{u=1}^{\infty}\left(A_{u,j}^{\mathrm{I}}r^{\frac{u\pi}{\beta_h}}+B_{u,j}^{\mathrm{I}}r^{\frac{-u\pi}{\beta_h}}\right)\cos\left(\frac{u\pi}{\beta_h}(\theta-\theta_j)\right) \tag{5.88}$$

But, since from equation (5.31) $A^{\mathrm{I}}(R_1,\theta)=0$ equation (5.88) must satisfy:

$$\begin{aligned}A_j^{\mathrm{I}}(R_1,\theta)=0=A_{0,j}^{\mathrm{I}}+B_{0,j}^{\mathrm{I}}\ln(R_1)-R_1(-1)^jB_m\\+\sum_{u=1}^{\infty}\left(A_{u,j}^{\mathrm{I}}R_1^{\frac{u\pi}{\beta_h}}+B_{u,j}^{\mathrm{I}}R_1^{\frac{-u\pi}{\beta_h}}\right)\cos\left(\frac{u\pi}{\beta_h}(\theta-\theta_j)\right)\end{aligned} \tag{5.89}$$

Therefore,

$$A_{0,j}^{\mathrm{I}}=-B_{0,j}^{\mathrm{I}}\ln(R_1)+R_1(-1)^jB_m \tag{5.90}$$

and

$$A^{\mathrm{I}}_{u,j} R_1^{\frac{u\pi}{\beta_h}} + B^{\mathrm{I}}_{u,j} R_1^{\frac{-u\pi}{\beta_h}} = 0 \tag{5.91}$$

Rearranging (5.91) and eliminating $B^{\mathrm{I}}_{u,j}$ we get:

$$B^{\mathrm{I}}_{u,j} = -A^{\mathrm{I}}_{u,j} R_1^{2uk_h} \tag{5.92}$$

where k_h is defined as

$$k_h = \frac{\pi}{\beta_h} \tag{5.93}$$

Substituting (5.90) and (5.92) into (5.88) and rearranging we get

$$\begin{aligned} A^{\mathrm{I}}_j(r,\theta) = B^{\mathrm{I}}_{0,j} \ln\left(\frac{r}{R_1}\right) + (R_1 - r)(-1)^j B_m \\ + \sum_{u=1}^{\infty} A^{\mathrm{I}}_{u,j} R_1^{uk_h} \left(\left(\frac{r}{R_1}\right)^{uk_h} - \left(\frac{R_1}{r}\right)^{uk_h} \right) \cos(uk_h(\theta - \theta_j)) \end{aligned} \tag{5.94}$$

The general solution for the field in the outer rotor magnet region Ω^{V} is obtained in an analogous way as for Ω^{I}. Utilizing the boundary conditions (5.42), (5.43) and (5.45) the solution of (5.27) for the k^{th} magnet in the outer rotor is

$$\begin{aligned} A^{\mathrm{V}}_k(r,\theta) = B^{\mathrm{V}}_{0,k} \ln\left(\frac{r}{R_6}\right) + (R_6 - r)(-1)^k B_m \\ + \sum_{u=1}^{\infty} A^{\mathrm{V}}_{u,k} R_6^{uk_l} \left(\left(\frac{r}{R_6}\right)^{uk_l} - \left(\frac{R_6}{r}\right)^{uk_l} \right) \cos(uk_l(\theta - \theta_k)) \end{aligned} \tag{5.95}$$

where

$$k_l = \frac{\pi}{\beta_l} \tag{5.96}$$

5.6. General Solutions Considering the Radial Boundary Conditions

The general solutions derived in section 5.5 do not take into account the radial field boundary conditions between each region. In this section the derived general solutions are re-written to account for the radial boundary conditions. The field equation unknowns are expressed in terms of Fourier series terms so as to enable the continuous field distribution in the region Ω^{II} and Ω^{IV} to be connected to the discontinuous field solution with regions Ω^{I}, Ω^{III} and Ω^{V}. The general solution obtained in section 5.5 for each region is summarized below.

$$A_j^{\mathrm{I}}(r,\theta) = \rho_{0,j}^{\mathrm{I}}(r) - (R_1 - r)(-1)^j B_m + \sum_{u=1}^{\infty} \rho_{u,j}^{\mathrm{I}}(r)\cos(uk_h(\theta - \theta_j)) \tag{5.97}$$

where

$$\rho_{0,j}^{\mathrm{I}}(r) = B_{0,j}^{\mathrm{I}} \ln\left(\frac{r}{R_1}\right) \tag{5.98}$$

$$\rho_{u,j}^{\mathrm{I}}(r) = A_{u,j}^{\mathrm{I}} R_1^{uk_h}\left(\left(\frac{r}{R_1}\right)^{uk_h} - \left(\frac{R_1}{r}\right)^{uk_h}\right) \tag{5.99}$$

$$A^{\mathrm{II}}(r,\theta) = \sum_{n=1}^{\infty} \rho_n^{\mathrm{II}}(r)\left(C_n^{\mathrm{II}}\cos(n\theta) + D_n^{\mathrm{II}}\sin(n\theta)\right) \tag{5.100}$$

where

$$\rho_n^{\mathrm{II}}(r) = A_n^{\mathrm{II}} r^n + B_n^{\mathrm{II}} r^{-n} \tag{5.101}$$

$$A_i^{\mathrm{III}}(r,\theta) = \rho_{0,i}^{\mathrm{III}}(r) + \sum_{u=1}^{\infty} \rho_{u,i}^{\mathrm{III}}(r,\theta)\cos(uk_c(\theta - \theta_i)) \tag{5.102}$$

where

$$\rho_{0,i}^{\mathrm{III}}(r) = A_{0,i}^{\mathrm{III}} + B_{0,i}^{\mathrm{III}} \ln(r) \tag{5.103}$$

$$\rho_{u,i}^{\mathrm{III}}(r) = A_{u,i}^{\mathrm{III}} r^{uk_c} + B_{u,i}^{\mathrm{III}} r^{-uk_c} \tag{5.104}$$

$$A^{\mathrm{IV}}(r,\theta) = \sum_{n=1}^{\infty} \rho_n^{\mathrm{IV}}(r)\left(C_n^{\mathrm{IV}} \cos(n\theta) + D_n^{\mathrm{IV}} \sin(n\theta)\right) \tag{5.105}$$

where

$$\rho_n^{\mathrm{IV}}(r) = A_n^{\mathrm{IV}} r^n + B_n^{\mathrm{IV}} r^{-n} \tag{5.106}$$

$$A_k^{\mathrm{V}}(r,\theta) = \rho_{0,k}^{\mathrm{V}}(r) - (R_6 - r)(-1)^k B_m + \sum_{u=1}^{\infty} \rho_{u,k}^{\mathrm{V}}(r) \cos(uk_l(\theta - \theta_k)) \tag{5.107}$$

where

$$\rho_{0,k}^{\mathrm{V}}(r) = B_{0,k}^{\mathrm{V}} \ln\left(\frac{r}{R_6}\right) \tag{5.108}$$

$$\rho_{u,k}^{\mathrm{V}}(r) = A_{u,k}^{\mathrm{V}} R_6^{uk_l} \left(\left(\frac{r}{R_6}\right)^{uk_l} - \left(\frac{R_6}{r}\right)^{uk_l}\right) \tag{5.109}$$

In (5.97) - (5.109) there is a total of 16 unknowns. Therefore to solve for the 16 unknowns we must utilize 16 boundary conditions. But we have only 8 boundary conditions given by (5.30), (5.32), (5.36), (5.37), (5.38), (5.40), (5.44) and (5.46). However, by expressing the boundary conditions in terms of the Fourier series we can obtain 16 boundary conditions.

5.6.1. Cage Rotor, Region Ω^{III}

In this section the solution (5.102) is modified so as to account for the continuity conditions given in (5.36) and (5.37). This is achieved by using a Fourier series expansion along θ_i and $\theta_i+\beta_c$.

The principle of superposition [97] is used to connect the radial boundary conditions at $r=R_3$ and $r=R_4$. We consider the field superposition of the two boundary condition cases as illustrated in Figure 5-9.

For case (a), the boundary conditions are

$$A_i^{\mathrm{III}}(R_4,\theta)=0 \tag{5.110}$$

$$A_i^{\mathrm{III}}(R_3,\theta)=A^{\mathrm{II}}(R_3,\theta), \text{ for } \theta_i \le \theta \le \theta_i+\beta_c \tag{5.37}$$

For case (b), the boundary conditions are

$$A_i^{\mathrm{III}}(R_4,\theta)=A^{\mathrm{IV}}(R_4,\theta) \text{ , for } \theta_k \le \theta \le \theta_k+\beta_l \tag{5.36}$$

$$A_i^{\mathrm{III}}(R_3,\theta)=0 \tag{5.111}$$

Therefore using superposition we have

$$A_i^{\mathrm{III}}(r,\theta)=A_i^{\mathrm{IIIa}}(r,\theta)+A_i^{\mathrm{IIIb}}(r,\theta) \tag{5.112}$$

where the superscript ‘a’ and ‘b’ are used to denote the field solution for the two boundary condition cases.

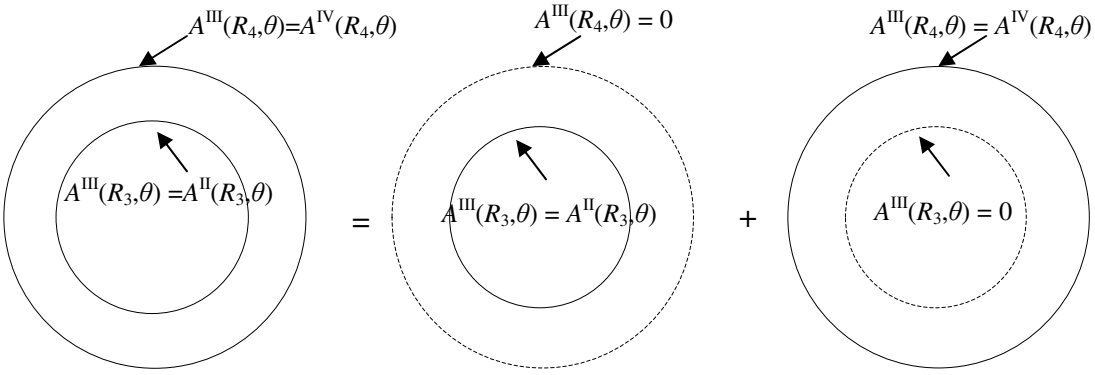

Figure 5-9: Superposition principle used to applying the two boundary conditions

The Fourier coefficients in (5.102) must satisfy the boundary conditions for case (a) and case (b). The equations that satisfy the two cases will be derived in the next two sections. It should be noted that the left side of (5.36) and (5.37) are written using

A_i^{III} that is only valid within each i^{th} cage rotor air space, but the right side is written with A^{II} which is valid for any angle. In order to connect the unknowns in each region the unknown in A_i^{III} must be written in terms of a Fourier series with respect to A^{II}.

5.6.1.1. Case (a)

In order to satisfy boundary condition (5.110) the Fourier coefficients (5.103) and (5.104) must be

$$\rho_{0,\text{i}}^{\text{III}}(R_4)=0 \tag{5.113}$$

$$\rho_{u,i}^{\text{III}}(R_4)=0 \tag{5.114}$$

Given condition (5.113) we can solve (5.103) to give

$$A_{0,i}^{\text{III}}=-B_{0,i}^{\text{III}}\ln(R_4) \tag{5.115}$$

By substituting (5.115) back into (5.103) we can eliminate $A_{0,i}^{\text{III}}$ to get

$$\rho_{0,i}^{\text{III}}(r)=B_{0,i}^{\text{III}}\ln\left(\frac{r}{R_4}\right) \tag{5.116}$$

Substituting (5.116) into (5.102) the solution for that satisfies boundary condition (5.113) is then:

$$A_i^{\text{IIIa}}(r,\theta)=B_{0,i}^{\text{III}}\ln\left(\frac{r}{R_4}\right)+\sum_{u=1}^{\infty}\rho_{u,i}^{\text{III}}(r)\cos(uk_c(\theta-\theta_i)) \tag{5.117}$$

Given boundary condition (5.114) we can solve (5.104) to get

$$A_{u,i}^{\text{III}}=-B_{u,i}^{\text{III}}\frac{R_4^{-uk_c}}{R_4^{uk_c}} \tag{5.118}$$

Substituting (5.118) into (5.104) and evaluating we have

$$\rho_{u,i}^{\mathrm{III}}(r) = c_{u,i}^{\mathrm{III}}\left(\left(\frac{r}{R_4}\right)^{uk_c} - \left(\frac{r}{R_4}\right)^{-uk_c}\right), \quad u=1,2,3..... \tag{5.119}$$

where $c_{u,i}^{\mathrm{III}} = B_{u,i}^{\mathrm{III}} R_4^{-uk_c}$ is a constant. Substituting (5.119) into (5.117) we have:

$$A_i^{\mathrm{IIIa}}(r,\theta) = B_{0,i}^{\mathrm{III}} \ln\left(\frac{r}{R_4}\right) + \sum_{u=1}^{\infty} c_{u,i}^{\mathrm{III}}\left(\left(\frac{r}{R_4}\right)^{uk_c} - \left(\frac{r}{R_4}\right)^{-uk_c}\right)\cos(uk_c(\theta-\theta_i)) \tag{5.120}$$

Equation (5.120) now satisfies the first boundary condition for case (a). In order to satisfy the second boundary condition for case (a) we must substituting (5.120) into the boundary condition (5.37). This gives:

$$B_{0,i}^{\mathrm{III}} \ln\left(\frac{R_3}{R_4}\right) + \sum_{u=1}^{\infty} c_{u,i}^{\mathrm{III}}\left(\left(\frac{R_3}{R_4}\right)^{uk_c} - \left(\frac{R_3}{R_4}\right)^{-uk_c}\right)\cos(uk_c(\theta-\theta_i)) = A^{\mathrm{II}}(R_3,\theta), \text{ for } \theta_i \le \theta \le \theta_i + \beta_c \tag{5.121}$$

The left hand side is a Fourier series and from the definition of a Fourier series we can redefine $A_i^{\mathrm{IIIa}}(R_3,\theta)$ as:

$$A_i^{\mathrm{IIIa}}(R_3,\theta) = a_{0,i}^{\mathrm{III}} + \sum_{u=1}^{\infty} a_{u,i}^{\mathrm{III}}\cos(uk_c(\theta-\theta_i)) \text{ , for } \theta_i \le \theta \le \theta_i + \beta_c \tag{5.122}$$

where in order to satisfy (5.121) the Fourier coefficients must be:

$$a_{0,i}^{\mathrm{III}} = \frac{1}{\beta_c}\int_{\theta_i}^{\theta_i+\beta_c} A^{\mathrm{II}}(R_3,\theta)d\theta \tag{5.123}$$

$$a_{u,i}^{\mathrm{III}} = \frac{2}{\beta_c}\int_{\theta_i}^{\theta_i+\beta_c} A^{\mathrm{II}}(R_3,\theta)\cos(uk_c(\theta-\theta_i))d\theta \text{ , } u=1,2..... \tag{5.124}$$

Comparing the left side of (5.121) with (5.122) we can see that (5.121) is satisfied when:

$$B_{0,i}^{\mathrm{III}} = \frac{a_{0,i}^{\mathrm{III}}}{\ln\left(\frac{R_3}{R_4}\right)} \tag{5.125}$$

$$c_{u,i}^{\mathrm{III}} = \frac{a_{u,i}^{\mathrm{III}}}{\left(\frac{R_3}{R_4}\right)^{\frac{u\pi}{\beta_c}} - \left(\frac{R_3}{R_4}\right)^{-\frac{u\pi}{\beta_c}}} \tag{5.126}$$

By substituting (5.125) and (5.126) into (5.120) we get

$$A_i^{\mathrm{IIIa}}(r,\theta) = a_{0,i}^{\mathrm{III}} \frac{\ln\left(\frac{R_4}{r}\right)}{\ln\left(\frac{R_4}{R_3}\right)} + \sum_{u=1}^{\infty} a_{u,i}^{\mathrm{III}} \left(\frac{\left(\frac{r}{R_4}\right)^{uk_c} - \left(\frac{R_4}{r}\right)^{uk_c}}{\left(\frac{R_3}{R_4}\right)^{uk_c} - \left(\frac{R_4}{R_3}\right)^{uk_c}} \right) \cos(uk_c(\theta - \theta_i)) \tag{5.127}$$

In (5.127) the unknowns are now written in a form that satisfies the field solution of $A^{\mathrm{II}}(r,\theta)$ at $r=R_3$.

5.6.1.2. Case (b)

In order to satisfy boundary condition (5.111) the Fourier coefficients (5.103) and (5.104) must be

$$\rho_{0,i}^{\mathrm{III}}(R_3) = 0 \tag{5.128}$$

$$\rho_{n,i}^{\mathrm{III}}(R_3,\theta) = 0 \tag{5.129}$$

The general solution for this case is obtained in an analogous way to case (a) and the final result is obtained as

$$A_i^{\mathrm{IIIb}}(r,\theta) = -b_{0,i}^{\mathrm{III}} \frac{\ln\left(\frac{R_3}{r}\right)}{\ln\left(\frac{R_4}{R_3}\right)} - \sum_{u=1}^{\infty} b_{u,i}^{\mathrm{III}} \left(\frac{\left(\frac{r}{R_3}\right)^{uk_c} - \left(\frac{R_3}{r}\right)^{uk_c}}{\left(\frac{R_3}{R_4}\right)^{uk_c} - \left(\frac{R_4}{R_3}\right)^{uk_c}} \right) \cos(uk_c(\theta - \theta_i)) \tag{5.130}$$

where

$$b_{0,i}^{\mathrm{III}} = \frac{1}{\beta_c} \int_{\theta_i}^{\theta_i+\beta_c} A^{\mathrm{IV}}(R_4, \theta) d\theta \tag{5.131}$$

$$b_{u,i}^{\mathrm{III}} = \frac{2}{\beta_c} \int_{\theta_i}^{\theta_i+\beta_c} A^{\mathrm{IV}}(R_4, \theta) \cos\left(uk_c(\theta - \theta_i)\right) d\theta \tag{5.132}$$

Now substituting (5.130) and (5.127) into (5.112) we get

$$\begin{aligned} A_i^{\mathrm{III}}(r,\theta) &= a_{0,i}^{\mathrm{III}} \frac{\ln\left(\frac{R_4}{r}\right)}{\ln\left(\frac{R_4}{R_3}\right)} - b_{0,i}^{\mathrm{III}} \frac{\ln\left(\frac{R_3}{r}\right)}{\ln\left(\frac{R_4}{R_3}\right)} \\ &+ \sum_{u=1}^{\infty} \left(a_{u,i}^{\mathrm{III}} \frac{\left(\frac{r}{R_4}\right)^{uk_c} - \left(\frac{R_4}{r}\right)^{uk_c}}{\left(\frac{R_3}{R_4}\right)^{uk_c} - \left(\frac{R_4}{R_3}\right)^{uk_c}} - b_{u,i}^{\mathrm{III}} \frac{\left(\frac{r}{R_3}\right)^{uk_c} - \left(\frac{R_3}{r}\right)^{uk_c}}{\left(\frac{R_3}{R_4}\right)^{uk_c} - \left(\frac{R_4}{R_3}\right)^{uk_c}} \right) \cos(uk_c(\theta - \theta_i)) \end{aligned} \tag{5.133}$$

Defining:

$$U_z(a,b) = \left(\frac{a}{b}\right)^z + \left(\frac{b}{a}\right)^z \tag{5.134}$$

$$V_z(a,b) = \left(\frac{a}{b}\right)^z - \left(\frac{b}{a}\right)^z \tag{5.135}$$

allows (5.133) to be written more succinctly as

$$\begin{aligned} A_i^{\mathrm{III}}(r,\theta) &= a_{0,i}^{\mathrm{III}} \frac{\ln\left(\frac{R_4}{r}\right)}{\ln\left(\frac{R_4}{R_3}\right)} - b_{0,i}^{\mathrm{III}} \frac{\ln\left(\frac{R_3}{r}\right)}{\ln\left(\frac{R_4}{R_3}\right)} \\ &+ \sum_{u=1}^{\infty} \left(a_{u,i}^{\mathrm{III}} \frac{V_{uk_c}(r, R_4)}{V_{uk_c}(R_3, R_4)} - b_{u,i}^{\mathrm{III}} \frac{V_{uk_c}(r, R_3)}{V_{uk_c}(R_3, R_4)} \right) \cos(uk_c(\theta - \theta_i)) \end{aligned} \tag{5.136}$$

5.6.2. Inner Rotor, Region Ω^{I}

The boundary conditions that apply for region Ω^{I} are given by (5.30) and (5.31). They are rewritten below:

$$A_j^{\mathrm{I}}(R_2,\theta) = A^{\mathrm{II}}(R_2,\theta), \text{for } \theta_j \le \theta \le \theta_j + \beta_h \tag{5.30}$$

$$A_j^{\mathrm{I}}(R_1,\theta) = 0 \text{ , on } \Gamma_1 \tag{5.31}$$

Figure 5-10 shows the boundary conditions that need to be satisfied.

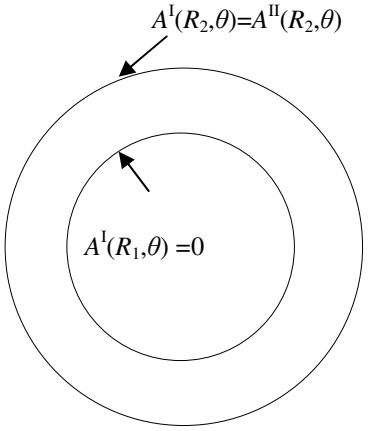

Figure 5-10: Boundary conditions on the inner rotor for region Ω^1

From (5.94) we have:

$$\begin{aligned} A_j^{\mathrm{I}}(r,\theta) = {} & B_{0,j}^{\mathrm{I}} \ln\left(\frac{r}{R_1}\right) + (R_1 - r)(-1)^j B_m \\ & + \sum_{u=1}^{\infty} A_{u,j}^{\mathrm{I}} R_1^{uk_h} \left(\left(\frac{r}{R_1}\right)^{uk_h} - \left(\frac{R_1}{r}\right)^{uk_h} \right) \cos(uk_h(\theta - \theta_j)) \end{aligned} \tag{5.94}$$

Substituting (5.94) into the boundary condition (5.30) we get after rearranging

$$\begin{aligned} & B_{0,j}^{I} \ln\left(\frac{R_2}{R_1}\right) + \sum_{u=1}^{\infty} A_{u,j}^{I} R_1^{uk_h} \left(\left(\frac{R_2}{R_1}\right)^{uk_h} - \left(\frac{R_1}{R_2}\right)^{uk_h} \right) \cos(uk_h(\theta - \theta_j)) \\ & \qquad = A^{\mathrm{II}}(R_2,\theta) - (R_1 - R_2)(-1)^j B_m, \text{ for } \theta_j \le \theta \le \theta_j + \beta_h \end{aligned} \tag{5.137}$$

The left hand side is a Fourier series and from the definition of the Fourier series [97] we can redefine $A_j^{\mathrm{I}}(R_2,\theta)$ as:

$$A_j^{\mathrm{I}}(R_2,\theta) - (R_1 - R_2)(-1)^j B_m = a_{0,j}^{\mathrm{I}} + \sum_{u=1}^{\infty} a_{u,j}^{\mathrm{I}} \cos(uk_h(\theta - \theta_j)) \text{ , for } \theta_j \le \theta \le \theta_j + \beta_h \tag{5.138}$$

where the Fourier coefficients are:

$$a_{0,j}^{\mathrm{I}} = \frac{1}{\beta_h} \int_{\theta_j}^{\theta_j+\beta_h} [(R_2 - R_1)(-1)^j B_m + A^{\mathrm{II}}(R_2, \theta)] d\theta \tag{5.139}$$

$$a_{u,j}^{\mathrm{I}} = \frac{2}{\beta_h} \int_{\theta_j}^{\theta_j+\beta_h} [(R_2 - R_1)(-1)^j B_m + A^{\mathrm{II}}(R_2, \theta)) \cos(uk_h(\theta - \theta_j)] d\theta \tag{5.140}$$

Comparing the left side of (5.137) with (5.138) we can see that:

$$B_{0,j}^{\mathrm{I}} = \frac{a_{0,j}^{\mathrm{I}}}{\ln\left(\frac{R_2}{R_1}\right)} \tag{5.141}$$

$$A_{u,j}^{\mathrm{I}} R_1^{uk_h} = \frac{a_{u,j}^{\mathrm{I}}}{\left(\frac{R_2}{R_1}\right)^{uk_h} - \left(\frac{R_2}{R_1}\right)^{-uk_h}} \tag{5.142}$$

Substituting (5.141) and (5.142) into (5.94) we obtain

$$\begin{aligned} A_j^{\mathrm{I}}(r, \theta) = a_{0,j}^{\mathrm{I}} & \frac{\ln\left(\frac{r}{R_1}\right)}{\ln\left(\frac{R_2}{R_1}\right)} + (R_1 - r)(-1)^j B_m \\ & + \sum_{u=1}^{\infty} a_{u,j}^{\mathrm{I}} \frac{\left(\frac{r}{R_1}\right)^{uk_h} - \left(\frac{R_1}{r}\right)^{uk_h}}{\left(\frac{R_2}{R_1}\right)^{uk_h} - \left(\frac{R_1}{R_2}\right)^{uk_h}} \cos(uk_h(\theta - \theta_j)) \end{aligned} \tag{5.143}$$

Using the notation shown in (5.134) and (5.135) equation (5.143) can be simplified to

$$A_j^{\mathrm{I}}(r, \theta) = a_{0,j}^{\mathrm{I}} \frac{\ln\left(\frac{r}{R_1}\right)}{\ln\left(\frac{R_2}{R_1}\right)} + (R_1 - r)(-1)^j B_m + \sum_{u=1}^{\infty} a_{u,j}^{\mathrm{I}} \frac{V_{uk_h}(r, R_1)}{V_{uk_h}(R_1, R_2)} \cos(uk_h(\theta - \theta_j)) \tag{5.144}$$

5.6.3. Outer Rotor, Region Ω^{V}

The solution in the outer rotor region is given in equation (5.107). The applicable Dirichlet boundary conditions are given by (5.44) and (5.45). They are rewritten as:

$$A_k^{V}(R_5,\theta) = A^{IV}(R_5,\theta) \text{ , for } \theta_k \le \theta \le \theta_k + \beta_l \tag{5.44}$$

$$A_k^{V}(R_6,\theta) = 0 \tag{5.45}$$

The boundary conditions are shown in Figure 5-11.

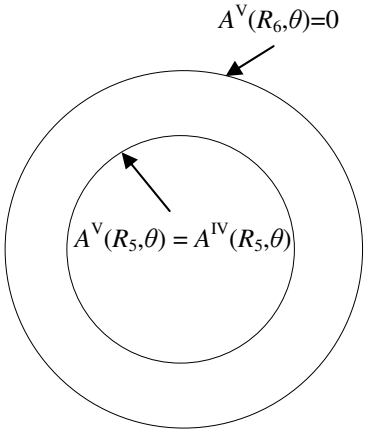

Figure 5-11: Boundary conditions on outer rotor

A similar approach is taken for the derivation of the field within the magnets of the outer rotor as was undertaken in section 5.6.2 for the inner rotor. After significant manipulation the following field solution is obtained.

$$\begin{aligned} A_k^{V}(r,\theta) = a_{0,k}^{V} \frac{\ln\left(\frac{R_6}{r}\right)}{\ln\left(\frac{R_6}{R_5}\right)} + \left(R_6 - r\right)(-1)^k B_m \\ + \sum_{u=1}^{\infty} a_{u,k}^{V} \frac{\left(\frac{r}{R_6}\right)^{uk_l} - \left(\frac{R_6}{r}\right)^{uk_l}}{\left(\frac{R_5}{R_6}\right)^{uk_l} - \left(\frac{R_6}{R_5}\right)^{uk_l}} \cos(uk_l(\theta - \theta_k)) \end{aligned} \tag{5.145}$$

where

$$a_{0,k}^{\mathrm{V}} = \frac{1}{\beta_l} \int_{\theta_l}^{\theta_k+\beta_l} \left(\left(R_6 - R_5 \right) (-1)^k B_m + A^{\mathrm{IV}}(R_5, \theta) \right) d\theta \tag{5.146}$$

$$a_{u,k}^{\mathrm{V}} = \frac{2}{\beta_l} \int_{\theta_k}^{\theta_k+\beta_l} \left(\left(R_6 - R_5 \right) (-1)^k B_m + A^{\mathrm{IV}}(R_5, \theta) \right) \cos(uk_l(\theta - \theta_k)) d\theta \tag{5.147}$$

Using the notations shown in (5.134) and (5.135) equation (5.145) can be simplified to

$$A_k^{\mathrm{V}}(r,\theta) = a_{0,k}^{\mathrm{V}} \frac{\ln\left(\frac{R_6}{r}\right)}{\ln\left(\frac{R_6}{R_5}\right)} + \left(R_6 - r\right)(-1)^k B_m + \sum_{u=1}^{\infty} \left(a_{u,k}^{\mathrm{V}} \frac{V_{uk_l}(r, R_6)}{V_{uk_l}(R_5, R_6)} \right) \cos(uk_l(\theta - \theta_k)) \tag{5.148}$$

5.6.4. Inner Air-gap, Region Ω^{II}

The solution given in (5.100) is

$$A^{\mathrm{II}}(r,\theta) = \sum_{n=1}^{\infty} \rho_n^{\mathrm{II}}(r) \left(C_n^{\mathrm{II}} \cos(n\theta) + D_n^{\mathrm{II}} \sin(n\theta) \right) \tag{5.100}$$

where $\rho_n^{\mathrm{II}}(r)$ is given by (5.101). Equation (5.100) can be rewritten as

$$A^{\mathrm{II}}(r,\theta) = \sum_{n=1}^{\infty} \rho_n^{\mathrm{II}}(r) \phi_n^{\mathrm{II}}(\theta) \tag{5.149}$$

where

$$\phi_n^{\mathrm{II}}(\theta) = C_n^{\mathrm{II}} \cos(n\theta) + D_n^{\mathrm{II}} \sin(n\theta) \tag{5.150}$$

In this region the periodic Neumann boundary conditions are used to obtain the solution. The Neumann rather than the Dirchlet boundary conditions are used as the Neumann boundary conditions includes the presence of the magnet terms. The boundary conditions are given by (5.32) and (5.38).

The principle of superposition is again used to connect the radial boundary conditions at $r=R_2$ and $r=R_3$. This is illustrated in Figure 5-12. We use the superposition of two boundary condition cases. For case (a), the boundary conditions are

$$\left.\frac{\partial A^{\mathrm{II}}}{\partial r}\right|_{r=R_2} = \mathrm{S}(\theta) \tag{5.32}$$

$$\left.\frac{\partial A^{\mathrm{II}}}{\partial r}\right|_{r=R_3} = 0 \tag{5.151}$$

For case (b), the boundary conditions are

$$\left.\frac{\partial A^{\mathrm{II}}}{\partial r}\right|_{r=R_2} = 0 \tag{5.152}$$

$$\left.\frac{\partial A^{\mathrm{II}}}{\partial r}\right|_{r=R_3} = \mathrm{F}(\theta) \tag{5.38}$$

Therefore, using superposition

$$A^{\mathrm{II}}(r,\theta) = A^{\mathrm{IIa}}(r,\theta) + A^{\mathrm{IIb}}(r,\theta) \tag{5.153}$$

The superscript ‘a’ and ‘b’ are used to denote the field solution for the two boundary condition cases as shown in Figure 5-12.

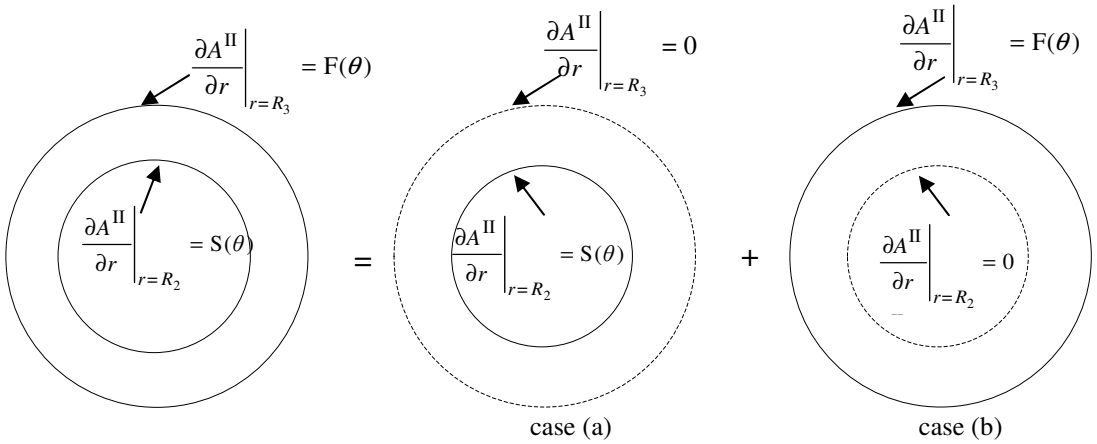

Figure 5-12: Superposition principle used to applying the two boundary conditions

5.6.4.1. Case (a)

The boundary conditions given are periodic with a period 2π. Hence we have

$$\phi^{\mathrm{II}}(0)=\phi^{\mathrm{II}}(2\pi) \tag{5.154}$$

In order to satisfy (5.151) we must have [97]:

$$\frac{d\rho_n^{\mathrm{II}}(R_3)}{dr}=0 \tag{5.155}$$

Substituting (5.101) into (5.155) we get

$$nA_n^{\mathrm{II}}R_3^{\,n-1}-nB_n^{\mathrm{II}}R_3^{\,-n-1}=0 \tag{5.156}$$

Rearranging (5.156) we get

$$B_n^{\mathrm{II}}=A_n^{\mathrm{II}}\frac{R_3^{\,n-1}}{R_3^{\,-n-1}} \tag{5.157}$$

Substituting (5.157) into (5.100) and solving we get

$$A^{\mathrm{IIa}}(r,\theta)=\sum_{n=1}^{\infty}h_n^{\mathrm{II}}\left(\left(\frac{r}{R_3}\right)^n+\left(\frac{R_3}{r}\right)^n\right)\cos(n\theta)+\sum_{n=1}^{\infty}v_n^{\mathrm{II}}\left(\left(\frac{r}{R_3}\right)^n+\left(\frac{R_3}{r}\right)^n\right)\sin(n\theta) \tag{5.158}$$

where $h_n^{\mathrm{II}}=A_n^{\mathrm{II}}R_3^{\,n}C_n^{\mathrm{II}}$ and $v_n^{\mathrm{II}}=A_n^{\mathrm{II}}R_3^{\,n}D_n^{\mathrm{II}}$ are constants. Now substituting (5.158) into the Neumann boundary condition given by (5.32) we get after rearranging:

$$\begin{aligned}\mathrm{S}(\theta)=&\sum_{n=1}^{\infty}h_n^{\mathrm{II}}\frac{n}{R_2}\left(\left(\frac{R_2}{R_3}\right)^n-\left(\frac{R_3}{R_2}\right)^n\right)\cos(n\theta)\\&+\sum_{n=1}^{\infty}v_n^{\mathrm{II}}\frac{n}{R_2}\left(\left(\frac{R_2}{R_3}\right)^n-\left(\frac{R_3}{R_2}\right)^n\right)\sin(n\theta)\end{aligned} \tag{5.159}$$

The right hand side is a Fourier series and from the definition of the Fourier series we can rewrite (5.159) as:

$$\mathrm{S}(\theta)=\sum_{n=1}^{\infty}a_n^{\mathrm{II}}\cos(n\theta)+\sum_{n=1}^{\infty}c_n^{\mathrm{II}}\sin(n\theta) \tag{5.160}$$

The Fourier coefficients must satisfy:

$$a_n^{\mathrm{II}} = \frac{1}{\pi}\int_0^{2\pi} \mathrm{S}(\theta)\cos(n\theta)d\theta \text{ , at } \Gamma_{12} \tag{5.161}$$

$$c_n^{\mathrm{II}} = \frac{1}{\pi}\int_0^{2\pi} \mathrm{S}(\theta)\sin(n\theta)d\theta \text{ , at } \Gamma_{12} \tag{5.162}$$

Comparing (5.160) with the right side of (5.159) we can note that:

$$h_n^{\mathrm{II}} = \frac{R_2}{n}\frac{a_n^{\mathrm{II}}}{\left(\frac{R_2}{R_3}\right)^n - \left(\frac{R_3}{R_2}\right)^n} \tag{5.163}$$

$$v_n^{\mathrm{II}} = \frac{R_2}{n}\frac{c_n^{\mathrm{II}}}{\left(\frac{R_2}{R_3}\right)^n - \left(\frac{R_3}{R_2}\right)^n} \tag{5.164}$$

Substituting (5.163) and (5.164) back into (5.158) we get

$$\begin{aligned} A^{\mathrm{IIa}}(r,\theta) = &\sum_{n=1}^{\infty} a_n^{\mathrm{II}}\frac{R_2}{n}\frac{\left(\frac{r}{R_3}\right)^n + \left(\frac{R_3}{r}\right)^n}{\left(\frac{R_2}{R_3}\right)^n - \left(\frac{R_3}{R_2}\right)^n}\cos(n\theta) \\ &+ \sum_{n=1}^{\infty} c_n^{\mathrm{II}}\frac{R_2}{n}\frac{\left(\frac{r}{R_3}\right)^n + \left(\frac{R_3}{r}\right)^n}{\left(\frac{R_2}{R_3}\right)^n - \left(\frac{R_3}{R_2}\right)^n}\sin(n\theta) \end{aligned} \tag{5.165}$$

Using the notion given in (5.134) and (5.135) the final solution is obtained as

$$A^{\mathrm{II}a}(r,\theta) = a_n^{\mathrm{II}}\frac{R_2}{n}\left(\frac{U_n(r,R_3)}{V_n(R_2,R_3)}\right)\cos(n\theta) + \sum_{n=1}^{\infty} c_n^{\mathrm{II}}\frac{R_2}{n}\left(\frac{U_n(r,R_3)}{V_n(R_2,R_3)}\right)\sin(n\theta) \tag{5.166}$$

5.6.4.2. Case (b)

For case (b) the same procedure as followed in case (a) is used and the solution is obtained as

$$A^{\mathrm{II}b}(r,\theta)=b_n^{\mathrm{II}}\frac{R_3}{n}\left(\frac{U_n(r,R_2)}{V_n(R_3,R_2)}\right)\cos(n\theta)+\sum_{n=1}^{\infty}d_n^{\mathrm{II}}\frac{R_3}{n}\left(\frac{U_n(r,R_2)}{V_n(R_3,R_2)}\right)\sin(n\theta) \tag{5.167}$$

where

$$b_n^{\mathrm{II}}=\frac{1}{\pi}\int_0^{2\pi}\mathrm{F}(\theta)\cos(n\theta)d\theta \text{ , at } \Gamma_{23} \tag{5.168}$$

$$d_n^{\mathrm{II}}=\frac{1}{\pi}\int_0^{2\pi}\mathrm{F}(\theta)\sin(n\theta)d\theta \text{ , at } \Gamma_{23} \tag{5.169}$$

F(θ) is defined by equation (5.39).

Finally substituting (5.166) and (5.167) into (5.153) we get

$$\begin{aligned}A^{\mathrm{II}}(r,\theta)=&\sum_{n=1}^{\infty}\left(a_n^{\mathrm{II}}\frac{R_2}{n}\left(\frac{U_n(r,R_3)}{V_n(R_2,R_3)}\right)+b_n^{\mathrm{II}}\frac{R_3}{n}\left(\frac{U_n(r,R_2)}{V_n(R_3,R_2)}\right)\right)\cos(n\theta)\\&+\sum_{n=1}^{\infty}\left(c_n^{\mathrm{II}}\frac{R_2}{n}\left(\frac{U_n(r,R_3)}{V_n(R_2,R_3)}\right)+d_n^{\mathrm{II}}\frac{R_3}{n}\left(\frac{U_n(r,R_2)}{V_n(R_3,R_2)}\right)\right)\sin(n\theta)\end{aligned} \tag{5.170}$$

5.6.5. Outer Air-gap, Region Ω^{IV}

Following the same procedure as shown for the inner air gap region Ω^{II} in section 5.6.4, we obtain the solution by using the Neumann boundary conditions given in equation (5.40) and (5.46) as

$$\begin{aligned}A^{\mathrm{IV}}(r,\theta)=&\sum_{n=1}^{\infty}\left(a_n^{\mathrm{IV}}\frac{R_4}{n}\left(\frac{U_n(r,R_5)}{V_n(R_4,R_5)}\right)+b_n^{\mathrm{IV}}\frac{R_5}{n}\left(\frac{U_n(r,R_4)}{V_n(R_5,R_4)}\right)\right)\cos(n\theta)\\&+\sum_{n=1}^{\infty}\left(c_n^{\mathrm{IV}}\frac{R_4}{n}\left(\frac{U_n(r,R_5)}{V_n(R_4,R_5)}\right)+d_n^{\mathrm{IV}}\frac{R_5}{n}\left(\frac{U_n(r,R_4)}{V_n(R_5,R_4)}\right)\right)\sin(n\theta)\end{aligned} \tag{5.171}$$

where

$$a_n^{\mathrm{IV}} = \frac{1}{\pi}\int_0^{2\pi} \mathrm{H}(\theta)\cos(n\theta)d\theta \text{ , at } \Gamma_{34} \tag{5.172}$$

$$b_n^{\mathrm{IV}} = \frac{1}{\pi}\int_0^{2\pi} \mathrm{L}(\theta)\cos(n\theta)d\theta \text{ , at } \Gamma_{45} \tag{5.173}$$

$$c_n^{\mathrm{IV}} = \frac{1}{\pi}\int_0^{2\pi} \mathrm{H}(\theta)\sin(n\theta)d\theta \text{ , at } \Gamma_{34} \tag{5.174}$$

$$d_n^{\mathrm{IV}} = \frac{1}{\pi}\int_0^{2\pi} \mathrm{L}(\theta)\sin(n\theta)d\theta \text{ , at } \Gamma_{45} \tag{5.175}$$

5.6.6. Summary of the General Solutions

Inner rotor region, Ω^{I}

$$A_j^{\mathrm{I}}(r,\theta) = a_{0,j}^{\mathrm{I}}\frac{\ln\left(\frac{r}{R_1}\right)}{\ln\left(\frac{R_2}{R_1}\right)} - (R_1 - r)(-1)^j B_m + \sum_{u=1}^{\infty}\left(a_{u,j}^{\mathrm{I}}\frac{V_{uk_h}(r,R_1)}{V_{uk_h}(R_1,R_2)}\right)\cos(uk_h(\theta-\theta_j)) \tag{5.144}$$

Inner air-gap region, Ω^{II}

$$\begin{aligned} A^{\mathrm{II}}(r,\theta) = &\sum_{n=1}^{\infty}\left(a_n^{\mathrm{II}}\frac{R_2}{n}\left(\frac{U_n(r,R_3)}{V_n(R_2,R_3)}\right) + b_n^{\mathrm{II}}\frac{R_3}{n}\left(\frac{U_n(r,R_2)}{V_n(R_3,R_2)}\right)\right)\cos(n\theta) \\ &+ \sum_{n=1}^{\infty}\left(c_n^{\mathrm{II}}\frac{R_2}{n}\left(\frac{U_n(r,R_3)}{V_n(R_2,R_3)}\right) + d_n^{\mathrm{II}}\frac{R_3}{n}\left(\frac{U_n(r,R_2)}{V_n(R_3,R_2)}\right)\right)\sin(n\theta) \end{aligned} \tag{5.170}$$

Cage rotor region, Ω^{III}

$$\begin{aligned} A_i^{\mathrm{III}}(r,\theta) = &a_{0,i}^{\mathrm{III}}\frac{\ln\left(\frac{R_4}{r}\right)}{\ln\left(\frac{R_4}{R_3}\right)} - b_{0,i}^{\mathrm{III}}\frac{\ln\left(\frac{R_3}{r}\right)}{\ln\left(\frac{R_4}{R_3}\right)} \\ &+ \sum_{u=1}^{\infty}\left(a_{u,i}^{\mathrm{III}}\frac{V_{uk_c}(r,R_4)}{V_{uk_c}(R_3,R_4)} - b_{u,i}^{\mathrm{III}}\frac{V_{uk_c}(r,R_3)}{V_{uk_c}(R_3,R_4)}\right)\cos(uk_c(\theta-\theta_i)) \end{aligned} \tag{5.136}$$

Outer air-gap region, Ω^{IV}

$$A^{IV}(r,\theta)=\sum_{n=1}^{\infty}\left(a_n^{IV}\frac{R_4}{n}\left(\frac{U_n(r,R_5)}{V_n(R_4,R_5)}\right)+b_n^{IV}\frac{R_5}{n}\left(\frac{U_n(r,R_4)}{V_n(R_5,R_4)}\right)\right)\cos(n\theta)+\sum_{n=1}^{\infty}\left(c_n^{IV}\frac{R_4}{n}\left(\frac{U_n(r,R_5)}{V_n(R_4,R_5)}\right)+d_n^{IV}\frac{R_5}{n}\left(\frac{U_n(r,R_4)}{V_n(R_5,R_4)}\right)\right)\sin(n\theta) \tag{5.171}$$

Outer rotor region, Ω^{V}

$$A_k^{V}(r,\theta)=a_{0,k}^{V}\frac{\ln\left(\frac{R_6}{r}\right)}{\ln\left(\frac{R_6}{R_5}\right)}-(R_6-r)(-1)^k B_m+\sum_{u=1}^{\infty}\left(a_{u,k}^{V}\frac{V_{uk_l}(r,R_5)}{V_{uk_l}(R_5,R_6)}\right)\cos(uk_l(\theta-\theta_k)) \tag{5.148}$$

5.7. Fourier Coefficient Expressions

In order to determine the Fourier coefficients obtained at each region the following integral forms will be used

$$f(n,u,\tau,\beta)=\int_{\theta_\tau}^{\theta_\tau+\beta}\cos(n\theta)\cos(\frac{u\pi}{\beta}(\theta-\theta_\tau))d\theta \tag{5.176}$$

$$g(n,u,\tau,\beta)=\int_{\theta_\tau}^{\theta_\tau+\beta}\sin(n\theta)\cos(\frac{u\pi}{\beta}(\theta-\theta_\tau))d\theta \tag{5.177}$$

$$r(n,\tau,\beta)=\int_{\theta_\tau}^{\theta_\tau+\beta}\cos(n\theta)d\theta \tag{5.178}$$

$$s(n,\tau,\beta)=\int_{\theta_\tau}^{\theta_\tau+\beta}\sin(n\theta)d\theta \tag{5.179}$$

where n is the harmonic number in the inner and outer rotor air-gap and u is the harmonic number in the cage rotor air-gaps and magnets. Here τ is replaced with i for cage rotor, j for inner rotor and k for inner and outer rotors respectively and β is replaced with β_c for the cage rotor, β_h for the inner rotor and β_l for the outer rotor.

Evaluating (5.176) we get

$$f(n,u,\tau,\beta)=\begin{cases}\dfrac{-n\beta^2\left((-1)^u\sin n(\beta+\theta_\tau)-\sin(n\theta_\tau)\right)}{u^2\pi^2-n^2\beta^2} & \text{, for } u\pi\neq n\beta\\ \dfrac{\beta}{2}\left(\cos(n\theta_\tau)+\dfrac{1}{2k\pi}(\sin n(2\beta+\theta_\tau)-\sin(n\theta_\tau))\right) & \text{, for } u\pi=n\beta\end{cases} \tag{5.180}$$

Evaluating (5.177) we get

$$g(n,u,\tau,\beta)=\begin{cases}\dfrac{n\beta^2\left((-1)^k\cos n(\beta+\theta_\tau)-\cos(n\theta_\tau)\right)}{u^2\pi^2-n^2\beta^2} & \text{, for } u\pi\neq n\beta\\ \dfrac{\beta}{2}\left(\sin(n\theta_\tau)-\dfrac{1}{2k\pi}(\cos n(2\beta+\theta_\tau)-\cos(n\theta_\tau))\right) & \text{, for } u\pi=n\beta\end{cases} \tag{5.181}$$

Evaluating (5.178) we get

$$r(n,\tau,\beta)=\frac{1}{n}\left(\sin(n\theta_\tau+n\beta)-\sin(n\theta_\tau)\right) \tag{5.182}$$

Evaluating (5.179)

$$s(n,\tau,\beta)=\frac{1}{n}\left(-\cos(n\theta_\tau+n\beta)+\cos(n\theta_\tau)\right) \tag{5.183}$$

5.7.1. Fourier Coefficients for the Inner Air-gap, Region Ω^{II}

The Fourier coefficients for the inner air-gap region are given by (5.161), (5.162), (5.168) and (5.169). Development of these equations will give linear equations which can be easily solved to obtain the coefficients.

The integral equations defined in (5.161) and (5.162) can be written as a summation of field values between θ_j to $\theta_j+\beta_h$ with the summation from j= 1 to $2p_1$. This gives:

$$a_n^{II}=\frac{1}{\pi}\sum_{j=1}^{2p_1}\int_{\theta_j}^{\theta_j+\beta_h}\mathrm{S}(\theta)\cos(n\theta)d\theta \text{ , at } \Gamma_{12} \tag{5.184}$$

$$c_n^{II}=\frac{1}{\pi}\sum_{j=1}^{2p_1}\int_{\theta_j}^{\theta_j+\beta_h}\mathrm{S}(\theta)\sin(n\theta)d\theta, \text{ at } \Gamma_{12} \tag{5.185}$$

Substituting S(θ), defined in (5.33), into (5.184) we obtain:

$$a_n^{\mathrm{II}} = \frac{1}{\pi}\sum_{j=1}^{2p_1}\int_{\theta_j}^{\theta_j+\beta_h}\left(\left.\frac{\partial A_j^{\mathrm{I}}}{\partial r}\right|_{r=R_2} + (-1)^j B_m\right)\cos(n\theta)d\theta \tag{5.186}$$

A_j^{I} is defined in (5.144) and the derivative of (5.144) at r=R_2 is obtained as:

$$\left.\frac{\partial A_j^{I}}{\partial r}\right|_{r=R_2} = \frac{a_{0,j}^{\mathrm{I}}}{R_2\ln(R_2)} - (-1)^j B_m + \sum_{u=1}^{\infty} a_{u,j}^{\mathrm{I}}\frac{uk_h}{R_2}\frac{U_{uk_h}(R_1,R_2)}{V_{uk_h}(R_1,R_2)}\cos(uk_h(\theta-\theta_j)) \tag{5.187}$$

Substituting (5.187) into (5.186) we get

$$a_n^{\mathrm{II}} = \frac{1}{\pi}\sum_{j=1}^{2p_1}\int_{\theta_j}^{\theta_j+\beta_h}\left(\frac{a_{0,j}^{\mathrm{I}}}{R_2\ln(R_2)} + \sum_{u=1}^{\infty} a_{u,j}^{\mathrm{I}}\frac{uk_h}{R_2}\frac{U_{uk_h}(R_1,R_2)}{V_{uk_h}(R_1,R_2)}\cos(uk_h(\theta-\theta_j))\right)\cos(n\theta)d\theta \tag{5.188}$$

Utilizing (5.178) and (5.176), equation (5.188) can be modified as

$$a_n^{\mathrm{II}} = \sum_{j=1}^{2p_1}\frac{a_{0,j}^{\mathrm{I}}}{\pi R_2\ln(R_2)}r(n,j,\beta_h) + \sum_{j=1}^{2p_1}\sum_{u=1}^{\infty} a_{u,j}^{\mathrm{I}}\frac{uk_h}{\pi R_2}\frac{U_{uk_h}(R_1,R_2)}{V_{uk_h}(R_1,R_2)}f(n,u,j,\beta_h) \tag{5.189}$$

The solution of (5.185) is similar to (5.188) except that the cosine term is replaced with a sine term. The solution of (5.185) can thus be written as

$$c_n^{\mathrm{II}} = \sum_{j=1}^{2p_1}\frac{a_{0,j}^{\mathrm{I}}}{\pi R_2\ln(R_2)}s(n,j,\beta_h) + \sum_{j=1}^{2p_1}\sum_{u=1}^{\infty} a_{u,j}^{\mathrm{I}}\frac{uk_h}{\pi R_2}\frac{U_{uk_h}(R_1,R_2)}{V_{uk_h}(R_1,R_2)}g(n,u,j,\beta_h) \tag{5.190}$$

where $s(n, j, \beta_h)$ and $g(n, u, j, \beta_h)$ are defined in (5.179) and (5.177) respectively.

Substituting F(θ) as defined in (5.39) into (5.168) we get

$$b_n^{\mathrm{II}} = \frac{1}{\pi}\sum_{i=1}^{n_2}\int_{\theta_i}^{\theta_i+\beta_c}\left.\frac{\partial A_i^{\mathrm{III}}}{\partial r}\right|_{r=R_3}\cos(n\theta)d\theta \tag{5.191}$$

A_i^{III} is defined in (5.136) and the derivative of (5.136) at r=R_3 is obtained as:

$$\frac{\partial A_i^{\mathrm{III}}}{\partial r} = \frac{-a_{0,i}^{\mathrm{III}}}{R_3 \ln(R_3)} + \frac{b_{0,i}^{\mathrm{III}}}{R_3 \ln(R_4)} + \sum_{u=1}^{\infty} \left(a_{u,i}^{\mathrm{III}} \frac{uk_c}{R_3} \frac{U_{uk_c}(R_3, R_4)}{V_{uk_c}(R_3, R_4)} - b_{u,i}^{\mathrm{III}} \frac{uk_c}{R_3} \frac{U_{uk_c}(R_3, R_4)}{V_{uk_c}(R_3, R_4)} \right) \cos(uk_c(\theta - \theta_i)) \tag{5.192}$$

Substituting (5.192) into (5.191) we get

$$b_n^{\mathrm{II}} = \frac{1}{\pi R_3} \sum_{i=1}^{n_2} \int_{\theta_i}^{\theta_i + \beta_c} \left(\frac{-a_{0,i}^{\mathrm{III}}}{\ln(R_3)} + \frac{b_{0,i}^{\mathrm{III}}}{\ln(R_4)} + \sum_{u=1}^{\infty} (a_{u,i}^{\mathrm{III}} - b_{u,i}^{\mathrm{III}}) uk_c \frac{U_{uk_c}(R_3, R_4)}{V_{uk_c}(R_3, R_4)} \cos(uk_c(\theta - \theta_i)) \right) \cos(n\theta) d\theta \tag{5.193}$$

Further by utilizing (5.178) and (5.176) equation (5.193) can be simplified as:

$$b_n^{\mathrm{II}} = \sum_{i=1}^{n_2} \frac{1}{\pi R_3} \left(\frac{-a_{0,i}^{\mathrm{III}}}{\ln(R_3)} + \frac{b_{0,i}^{\mathrm{III}}}{\ln(R_4)} \right) r(n, i, \beta_c) + \sum_{i=1}^{n_2} \sum_{u=1}^{\infty} (a_{u,i}^{\mathrm{III}} - b_{u,i}^{\mathrm{III}}) \frac{uk_c}{R_3} \frac{U_{uk_c}(R_3, R_4)}{V_{uk_c}(R_3, R_4)} f(n, u, i, \beta_c) \tag{5.194}$$

The derivation process used to solve (5.169) is similar to that used to solve(5.191). By substituting F(θ) defined in (5.39) into (5.169) and evaluating one obtains:

$$d_n^{\mathrm{II}} = \sum_{i=1}^{n_2} \frac{1}{\pi R_3} \left(\frac{-a_{0,i}^{\mathrm{III}}}{\ln(R_3)} + \frac{b_{0,i}^{\mathrm{III}}}{\ln(R_4)} \right) s(n, i, \beta_c) + \sum_{i=1}^{n_2} \sum_{u=1}^{\infty} (a_{u,i}^{\mathrm{III}} - b_{u,i}^{\mathrm{III}}) \frac{uk_c}{R_3} \frac{U_{uk_c}(R_3, R_4)}{V_{uk_c}(R_3, R_4)} g(n, u, i, \beta_c) \tag{5.195}$$

where $s(n, i, \beta_c)$ and $g(n, u, i, \beta_c)$ are defined in (5.179) and (5.177) respectively.

5.7.2. Fourier Coefficients for Outer Air-gap, Region Ω^{IV}

The Fourier coefficients for the outer air-gap region are given by equations (5.172) through (5.175). Development of these equations will give linear equations which can be easily solved to obtain the coefficients. The Fourier coefficients in the air-gaps need to be connected to the piecewise Fourier coefficients in the magnet and cage rotor

air regions. Therefore, (5.172) can be expressed as a summation of integral terms over each cage rotor air region and we can write:

$$a_n^{\mathrm{IV}} = \frac{1}{\pi}\sum_{i=1}^{n_2}\int_{\theta_i}^{\theta_i+\beta_c} \mathrm{H}(\theta)\cos(n\theta)d\theta \text{ , at } \Gamma_{34} \tag{5.196}$$

Similarly by substituting (5.41) into (5.174) equation (5.174) can be written as:

$$c_n^{\mathrm{IV}} = \frac{1}{\pi}\sum_{i=1}^{n_2}\int_{\theta_i}^{\theta_i+\beta_c} \mathrm{H}(\theta)\sin(n\theta)d\theta, \text{at } \Gamma_{34} \tag{5.197}$$

Substituting H(θ), defined in (5.41) into (5.196) the equation becomes

$$a_n^{\mathrm{IV}} = \frac{1}{\pi}\sum_{i=1}^{n_2}\int_{\theta_i}^{\theta_i+\beta_c} \left.\frac{\partial A_i^{\mathrm{III}}}{\partial r}\right|_{r=R_4} \cos(n\theta)d\theta \tag{5.198}$$

Substituting (5.136) into (5.198) and solving the equation we get

$$a_n^{\mathrm{IV}} = \frac{1}{\pi}\sum_{i=1}^{n_2}\int_{\theta_i}^{\theta_i+\beta_c} \left(\begin{array}{l} \dfrac{-a_{0,i}^{\mathrm{III}}}{R_4\ln(R_4)} + \dfrac{b_{0,i}^{\mathrm{III}}}{R_4\ln(R_3)} \\ +\displaystyle\sum_{u=1}^{\infty}(a_{u,i}^{\mathrm{III}} - b_{u,i}^{\mathrm{III}})\frac{uk_c}{R_4}\frac{2}{V_{uk_c}(R_3,R_4)}\cos(uk_c(\theta-\theta_i)) \end{array} \right)\cos(n\theta)d\theta \tag{5.199}$$

By using (5.178) and (5.176) Equation (5.199) can further be reduced to

$$\begin{aligned} a_n^{\mathrm{IV}} = &\sum_{i=1}^{n_2}\frac{1}{\pi R_4}\left(\frac{-a_{0,i}^{\mathrm{III}}}{\ln(R_4)} + \frac{b_{0,i}^{\mathrm{III}}}{\ln(R_3)}\right) r(n,i,\beta_c) \\ &+\sum_{i=1}^{n_2}\sum_{u=1}^{\infty}(a_{u,i}^{\mathrm{III}} - b_{u,i}^{\mathrm{III}})\frac{uk_c}{R_4}\frac{2}{V_{uk_c}(R_3,R_4)} f(n,u,i,\beta_c) \end{aligned} \tag{5.200}$$

The solution of (5.197) is similar to (5.200) except that the cosine term is replaced with a sine term. The solution of (5.197) can thus be written as

$$c_n^{\mathrm{IV}} = \sum_{i=1}^{n_2} \frac{1}{\pi R_4} \left(\frac{-a_{0,i}^{\mathrm{III}}}{\ln(R_4)} + \frac{b_{0,i}^{\mathrm{III}}}{\ln(R_3)} \right) s(n,i,\beta_c) + \sum_{i=1}^{n_2} \sum_{u=1}^{\infty} (a_{u,i}^{\mathrm{III}} - b_{u,i}^{\mathrm{III}}) \frac{uk_c}{R_4} \frac{2}{V_{uk_c}(R_3,R_4)} g(n,u,i,\beta_c) \tag{5.201}$$

where $s(n, i, \beta_c)$ and $g(n, u, i, \beta_c)$ are defined in (5.179) and (5.177) respectively.

Substituting L(θ) as defined in (5.47) into (5.173) and writing as a piecewise integral we get

$$b_n^{\mathrm{IV}} = \frac{1}{\pi} \sum_{k=1}^{2p_3} \int_{\theta_k}^{\theta_k+\beta_l} \left(\left. \frac{\partial A_k^{\mathrm{V}}}{\partial r} \right|_{r=R_5} + (-1)^k B_m \right) \cos(n\theta) d\theta, \text{ at } \Gamma_{45} \tag{5.202}$$

Similarly by substituting L(θ) as defined in (5.47) into (5.175) we get

$$d_n^{\mathrm{IV}} = \frac{1}{\pi} \sum_{k=1}^{2p_3} \int_{\theta_k}^{\theta_k+\beta_l} \left(\left. \frac{\partial A_k^{\mathrm{V}}}{\partial r} \right|_{r=R_5} + (-1)^k B_m \right) \sin(n\theta) d\theta \text{ , at } \Gamma_{45} \tag{5.203}$$

A_k^{V} is given by (5.148) and the derivative of (5.148) is obtained as

$$\left. \frac{\partial A^{\mathrm{V}}}{\partial r} \right|_{r=R_5} = \frac{-a_{0,k}^{\mathrm{V}}}{R_5 \ln(R_5)} - (-1)^k B_m + \sum_{u=1}^{\infty} \left(a_{u,k}^{\mathrm{V}} \frac{uk_l}{R_5} \frac{2}{V_{uk_c}(R_5,R_6)} \right) \cos(uk_l(\theta - \theta_k)) \tag{5.204}$$

Substituting (5.204) into (5.202) we get

$$b_n^{\mathrm{IV}} = \frac{1}{\pi} \sum_{k=1}^{2p_3} \int_{\theta_k}^{\theta_k+\beta_l} \left(\frac{-a_{0,k}^{\mathrm{V}}}{R_5 \ln(R_5)} + \sum_{u=1}^{\infty} \left(a_{u,k}^{\mathrm{V}} \frac{uk_l}{R_5} \frac{2}{V_{uk_c}(R_5,R_6)} \right) \cos(uk_l(\theta - \theta_k)) \right) \cos(n\theta) d\theta \tag{5.205}$$

Utilizing (5.178) and (5.176) equation (5.205) can be written as:

$$b_n^{\mathrm{IV}} = \sum_{k=1}^{2p_3} \frac{-a_{0,k}^{\mathrm{V}}}{\pi R_5 \ln(R_5)} r(n,k,\beta_l) + \sum_{k=1}^{2p_3} \sum_{u=1}^{\infty} \left(a_{u,k}^{\mathrm{V}} \frac{uk_l}{\pi R_5} \frac{2}{V_{uk_c}(R_5,R_6)} \right) f(n,u,k,\beta_l) \tag{5.206}$$

The solution of (5.203) is similar to (5.205) except that the cosine terms are replaced with sine terms. The solution of (5.203) can thus be written as:

$$d_n^{\mathrm{IV}} = \sum_{k=1}^{2p_3} \frac{-a_{0,k}^{\mathrm{V}}}{\pi R_5 \ln(R_5)} s(n,k,\beta_l) + \sum_{k=1}^{2p_3}\sum_{u=1}^{\infty}\left(a_{u,k}^{\mathrm{V}} \frac{uk_l}{\pi R_5} \frac{2}{V_{uk_c}(R_5,R_6)} \right) g(n,u,k,\beta_l) \tag{5.207}$$

where $s(n, k, \beta_l)$ and $g(n, u, k, \beta_l)$ are defined in (5.179) and (5.177) respectively.

5.7.3. Fourier Coefficients for the Inner Rotor, Region Ω^{I}

The Fourier coefficients for the inner rotor region are given in equations (5.139) and (5.140). Development of these equations will give linear equations which can be solved to obtain the coefficients.

Substituting $r=R_2$ into (5.170) we get

$$\begin{aligned} A^{\mathrm{II}}(R_2,\theta) = &\sum_{n=1}^{\infty}\left(a_n^{\mathrm{II}} \frac{R_2}{n}\left(\frac{U_n(R_2,R_3)}{V_n(R_2,R_3)} \right) + b_n^{\mathrm{II}} \frac{R_3}{n}\left(\frac{2}{V_n(R_3,R_2)} \right) \right)\cos(n\theta) \\ &+\sum_{n=1}^{\infty}\left(c_n^{\mathrm{II}} \frac{R_2}{n}\left(\frac{U_n(R_2,R_3)}{V_n(R_2,R_3)} \right) + d_n^{\mathrm{II}} \frac{R_3}{n}\left(\frac{2}{V_n(R_3,R_2)} \right) \right)\sin(n\theta) \end{aligned} \tag{5.208}$$

Substituting (5.208) into (5.139) and evaluating we get

$$\begin{aligned} a_{0,j}^{\mathrm{I}} = (R_2 - R_1)(-1)^j B_m + \frac{1}{\beta_h}\sum_{n=1}^{\infty}\frac{1}{n}&\left(a_n^{\mathrm{II}} R_2 \left(\frac{U_n(R_2,R_3)}{V_n(R_2,R_3)} \right) + b_n^{\mathrm{II}} \left(\frac{2R_3}{V_n(R_3,R_2)} \right) \right) r(n,j,\beta_h) \\ &+ \frac{1}{\beta_h}\sum_{n=1}^{\infty}\frac{1}{n}\left(c_n^{\mathrm{II}} R_2 \left(\frac{U_n(R_2,R_3)}{V_n(R_2,R_3)} \right) + d_n^{\mathrm{II}} \left(\frac{2R_3}{V_n(R_3,R_2)} \right) \right) s(n,j,\beta_h) \end{aligned} \tag{5.209}$$

Similarly substituting (5.208) into (5.140) and evaluating we get

$$\begin{aligned} a_{u,j}^{\mathrm{I}} = &\frac{2}{\beta_h}\sum_{n=1}^{\infty}\left(a_n^{\mathrm{II}} \frac{R_2}{n}\left(\frac{U_n(R_2,R_3)}{V_n(R_2,R_3)} \right) + b_n^{\mathrm{II}} \frac{R_3}{n}\left(\frac{2}{V_n(R_3,R_2)} \right) \right) f(n,u,j,\beta_h) \\ &+ \frac{2}{\beta_h}\sum_{n=1}^{\infty}\left(c_n^{\mathrm{II}} \frac{R_2}{n}\left(\frac{U_n(R_2,R_3)}{V_n(R_2,R_3)} \right) + d_n^{\mathrm{II}} \frac{R_3}{n}\left(\frac{2}{V_n(R_3,R_2)} \right) \right) g(n,u,j,\beta_h) \end{aligned} \tag{5.210}$$

5.7.4. Fourier Coefficients for the Outer Rotor, Region Ω^{V}

The Fourier coefficients for outer rotor region are given in (5.146) and (5.147). Substituting $r=R_5$ into (5.171) we get

$$A^{\mathrm{IV}}(R_5,\theta)=\sum_{n=1}^{\infty}\left(a_n^{\mathrm{IV}}\frac{R_4}{n}\left(\frac{2}{V_n(R_4,R_5)}\right)+b_n^{\mathrm{IV}}\frac{R_5}{n}\left(\frac{U_n(R_5,R_4)}{V_n(R_5,R_4)}\right)\right)\cos(n\theta)$$
$$+\sum_{n=1}^{\infty}\left(c_n^{\mathrm{IV}}\frac{R_4}{n}\left(\frac{2}{V_n(R_4,R_5)}\right)+d_n^{\mathrm{IV}}\frac{R_5}{n}\left(\frac{U_n(R_5,R_4)}{V_n(R_5,R_4)}\right)\right)\sin(n\theta) \tag{5.211}$$

Substituting (5.211) into (5.146) and evaluating we get

$$a_{0,k}^{\mathrm{V}}=(R_6-R_5)(-1)^k B_m+\frac{1}{\beta_l}\sum_{n=1}^{\infty}\left(a_n^{\mathrm{IV}}\frac{R_4}{n}\left(\frac{2}{V_n(R_4,R_5)}\right)+b_n^{\mathrm{IV}}\frac{R_5}{n}\left(\frac{U_n(R_5,R_4)}{V_n(R_5,R_4)}\right)\right)r(n,k,\beta_l)$$
$$+\frac{1}{\beta_l}\sum_{n=1}^{\infty}\left(c_n^{\mathrm{IV}}\frac{R_4}{n}\left(\frac{2}{V_n(R_4,R_5)}\right)+d_n^{\mathrm{IV}}\frac{R_5}{n}\left(\frac{U_n(R_5,R_4)}{V_n(R_5,R_4)}\right)\right)s(n,k,\beta_l) \tag{5.212}$$

Similarly substituting (5.211) into (5.147) and evaluating we get

$$a_{u,k}^{\mathrm{V}}=\frac{2}{\beta_l}\sum_{n=1}^{\infty}\left(a_n^{\mathrm{IV}}\frac{R_4}{n}\left(\frac{2}{V_n(R_4,R_5)}\right)+b_n^{\mathrm{IV}}\frac{R_5}{n}\left(\frac{U_n(R_5,R_4)}{V_n(R_5,R_4)}\right)\right)f(n,u,k,\beta_l)$$
$$+\frac{2}{\beta_l}\sum_{n=1}^{\infty}\left(c_n^{\mathrm{IV}}\frac{R_4}{n}\left(\frac{2}{V_n(R_4,R_5)}\right)+d_n^{\mathrm{IV}}\frac{R_5}{n}\left(\frac{U_n(R_5,R_4)}{V_n(R_5,R_4)}\right)\right)g(n,u,k,\beta_l) \tag{5.213}$$

5.7.5. Fourier Coefficients for the Cage Rotor, Ω^{III}

The Fourier coefficients for the cage rotor are given in (5.123), (5.124), (5.131) and (5.132). Substituting $r=R_3$ into (5.170) gives

$$A^{\mathrm{II}}(R_3,\theta)=\sum_{n=1}^{\infty}\left(a_n^{\mathrm{II}}\frac{R_2}{n}\left(\frac{2}{V_n(R_2,R_3)}\right)+b_n^{\mathrm{II}}\frac{R_3}{n}\left(\frac{U_n(R_3,R_2)}{V_n(R_3,R_2)}\right)\right)\cos(n\theta)$$
$$+\sum_{n=1}^{\infty}\left(c_n^{\mathrm{II}}\frac{R_2}{n}\left(\frac{2}{V_n(R_2,R_3)}\right)+d_n^{\mathrm{II}}\frac{R_3}{n}\left(\frac{U_n(R_3,R_2)}{V_n(R_3,R_2)}\right)\right)\sin(n\theta) \tag{5.214}$$

Substituting (5.214) into (5.123) gives

$$a_{0,i}^{\mathrm{III}}=\sum_{n=1}^{\infty}\frac{1}{n\beta_c}\left(a_n^{\mathrm{II}}\frac{2R_2}{V_n(R_2,R_3)}+b_n^{\mathrm{II}}R_3\frac{U_n(R_3,R_2)}{V_n(R_3,R_2)}\right)r(n,i,\beta_c)$$
$$+\sum_{n=1}^{\infty}\frac{1}{n\beta_c}\left(c_n^{\mathrm{II}}\frac{2R_2}{V_n(R_2,R_3)}+d_n^{\mathrm{II}}R_3\frac{U_n(R_3,R_2)}{V_n(R_3,R_2)}\right)s(n,i,\beta_c) \tag{5.215}$$

Similarly substituting (5.214) into (5.124) and evaluating we get

$$a_{u,i}^{\mathrm{III}} = \sum_{n=1}^{\infty} \frac{2}{n\beta_c} \left(a_n^{\mathrm{II}} \frac{2R_2}{V_n(R_2,R_3)} + b_n^{\mathrm{II}} R_3 \frac{U_n(R_3,R_2)}{V_n(R_3,R_2)} \right) f(n,u,i,\beta_c) + \sum_{n=1}^{\infty} \frac{2}{n\beta_c} \left(c_n^{\mathrm{II}} \frac{2R_2}{V_n(R_2,R_3)} + d_n^{\mathrm{II}} R_3 \frac{U_n(R_3,R_2)}{V_n(R_3,R_2)} \right) g(n,u,i,\beta_c) \tag{5.216}$$

Substituting r=R_4 into (5.171) we get

$$A^{\mathrm{IV}}(R_4,\theta) = \sum_{n=1}^{\infty} \left(a_n^{\mathrm{IV}} \frac{R_4}{n} \left(\frac{U_n(R_4,R_5)}{V_n(R_4,R_5)} \right) + b_n^{\mathrm{IV}} \frac{R_5}{n} \left(\frac{2}{V_n(R_5,R_4)} \right) \right) \cos(n\theta) + \sum_{n=1}^{\infty} \left(c_n^{\mathrm{IV}} \frac{R_4}{n} \left(\frac{U_n(R_4,R_5)}{V_n(R_4,R_5)} \right) + d_n^{\mathrm{IV}} \frac{R_5}{n} \left(\frac{2}{V_n(R_5,R_4)} \right) \right) \sin(n\theta) \tag{5.217}$$

Substituting (5.217) into (5.131) and evaluating we get

$$b_{0,i}^{\mathrm{III}} = \sum_{n=1}^{\infty} \frac{1}{n\beta_c} \left(a_n^{\mathrm{IV}} R_4 \frac{U_n(R_4,R_5)}{V_n(R_4,R_5)} + b_n^{\mathrm{IV}} \frac{2R_5}{V_n(R_5,R_4)} \right) r(n,i,\beta_c) + \sum_{n=1}^{\infty} \frac{1}{n\beta_c} \left(c_n^{\mathrm{IV}} R_4 \frac{U_n(R_4,R_5)}{V_n(R_4,R_5)} + d_n^{\mathrm{IV}} \frac{2R_5}{V_n(R_5,R_4)} \right) s(n,i,\beta_c) \tag{5.218}$$

Similarly substituting (5.217) into (5.132) and evaluating we get

$$b_{u,i}^{\mathrm{III}} = \sum_{n=1}^{\infty} \frac{2}{n\beta_c} \left(a_n^{\mathrm{IV}} R_4 \frac{U_n(R_4,R_5)}{V_n(R_4,R_5)} + b_n^{\mathrm{IV}} \frac{2R_5}{V_n(R_5,R_4)} \right) f(n,u,i,\beta_c) + \sum_{n=1}^{\infty} \frac{2}{n\beta_c} \left(c_n^{\mathrm{IV}} R_4 \frac{U_n(R_4,R_5)}{V_n(R_4,R_5)} + d_n^{\mathrm{IV}} \frac{2R_5}{V_n(R_5,R_4)} \right) g(n,u,i,\beta_c) \tag{5.219}$$

Equations (5.189), (5.190), (5.194), (5.195), (5.200), (5.201), (5.206), (5.207), (5.209), (5.210), (5.212), (5.213), (5.215), (5.216), (5.218) and (5.219) are a set of 16 linear equations which can be solved to calculate the 16 unknown coefficients for n=1,2….N and u=1,2…..U where N and U equal total number of harmonics that are considered in the summation and n_2 is the number of cage rotor steel poles. The matrix defined as given in equation (5.220) is used to calculate the coefficient values.

$$\bar{A}\bar{B} = \bar{M} \tag{5.220}$$

where $\bar{M}$ and $\bar{B}$ are given by

$$\bar{B} = \begin{bmatrix} a^{\mathrm{I}}_{0,j}\big|_{2p_1,1} \\ a^{\mathrm{I}}_{u,j}\big|_{2p_1.U,1} \\ a^{\mathrm{II}}_{n}\big|_{N,1} \\ b^{\mathrm{II}}_{n}\big|_{N,1} \\ c^{\mathrm{II}}_{n}\big|_{N,1} \\ d^{\mathrm{II}}_{n}\big|_{N,1} \\ a^{\mathrm{III}}_{0,i}\big|_{n_2,1} \\ b^{\mathrm{III}}_{0,i}\big|_{n_2,1} \\ a^{\mathrm{III}}_{u,i}\big|_{n_2.U,1} \\ b^{\mathrm{III}}_{u,i}\big|_{n_2.U,1} \\ a^{\mathrm{IV}}_{n}\big|_{N,1} \\ b^{\mathrm{IV}}_{n}\big|_{N,1} \\ c^{\mathrm{IV}}_{n}\big|_{N,1} \\ d^{\mathrm{IV}}_{n}\big|_{N,1} \\ a^{\mathrm{V}}_{0,k}\big|_{2p_3,1} \\ a^{\mathrm{V}}_{u,k}\big|_{2p_3.U,1} \end{bmatrix} \qquad \bar{M} = \begin{bmatrix} -(R_2 - R_1)(-1)^j B_m\big|_{2p_1,1} \\ 0\big|_{2p_1.U,1} \\ 0\big|_{N,1} \\ 0\big|_{N,1} \\ 0\big|_{N,1} \\ 0\big|_{N,1} \\ 0\big|_{n_2,1} \\ 0\big|_{n_2,1} \\ 0\big|_{n_2.U,1} \\ 0\big|_{n_2.U,1} \\ 0\big|_{N,1} \\ 0\big|_{N,1} \\ 0\big|_{N,1} \\ 0\big|_{N,1} \\ -(R_6 - R_5)(-1)^k B_m\big|_{2p_3,1} \\ 0\big|_{2p_3.U,1} \end{bmatrix} \tag{5.221}$$

The source terms in matrix $\bar{M}$ are from (5.209) and (5.212). The subscripts after the bar in the elements of matrix $\bar{M}$ and $\bar{B}$ represents the size of the matrix. For example, $a^{\mathrm{I}}_{0,j}\big|_{2\mathrm{p}_1,1}$ is a matrix with $2p_1$ rows and 1 column and the elements of the matrix are written as $a^{\mathrm{I}}_{0,j}\big|_{2p_1,1} = \begin{bmatrix} a^{\mathrm{I}}_{0,1} \\ a^{\mathrm{I}}_{0,2} \\ \vdots \\ a^{\mathrm{I}}_{0,2p_1} \end{bmatrix}$.

For clarity the matrix A is represented as

$$\overline{A} = \begin{bmatrix} A_1 & A_2 & A_3 \\ A_4 & A_5 & A_6 \\ A_7 & A_8 & A_9 \end{bmatrix} \tag{5.222}$$

where

$$A_1 = \begin{bmatrix} -\mathrm{I}_{2p_1,2p_1} & 0_{2p_1,2p_1.U} & \mathrm{M}^{1}_{2p_1,N} & \mathrm{M}^{2}_{2p_1,N} & \mathrm{M}^{3}_{2p_1,N} & \mathrm{M}^{4}_{2p_1,N} \\ 0_{2p_1.U,2p_1} & -\mathrm{I}_{2p_1.U,2p_1.U} & \mathrm{M}^{5}_{2p_1.U,N} & \mathrm{M}^{6}_{2p_1.U,N} & \mathrm{M}^{7}_{2p_1.U,N} & \mathrm{M}^{8}_{2p_1.U,N} \\ \mathrm{M}^{9}_{N,2p_1} & \mathrm{M}^{10}_{N,2p_1.U} & -\mathrm{I}_{N,N} & 0_{N,N} & 0_{N,N} & 0_{N,N} \\ 0_{N,2p_1} & 0_{N,2p_1.U} & 0_{N,N} & -\mathrm{I}_{N,N} & 0_{N,N} & 0_{N,N} \\ \mathrm{M}^{15}_{N,2p_1} & \mathrm{M}^{16}_{N,2p_1.U} & 0_{N,N} & 0_{N,N} & -\mathrm{I}_{N,N} & 0_{N,N} \\ 0_{N,2p_1} & 0_{N,2p_1.U} & 0_{N,N} & 0_{N,N} & 0_{N,N} & -\mathrm{I}_{N,N} \end{bmatrix} \tag{5.223}$$

$$A_2 = \begin{bmatrix} 0_{2p_1,n_2} & 0_{2p_1,n_2} & 0_{2p_1,n_2.U} & 0_{2p_1,n_2.U} & 0_{2p_1,N} & 0_{2p_1,N} \\ 0_{2p_1.U,n_2} & 0_{2p_1.U,n_2} & 0_{2p_1.U,n_2.U} & 0_{2p_1.U,n_2.U} & 0_{2p_1.U,N} & 0_{2p_1.U,N} \\ 0_{N,n_2} & 0_{N,n_2} & 0_{N,n_2.U} & 0_{N,n_2.U} & 0_{N,N} & 0_{N,N} \\ -\mathrm{M}^{11}_{N,n_2} & \mathrm{M}^{12}_{N,n_2} & \mathrm{M}^{13}_{N,n_2.U} & -\mathrm{M}^{14}_{N,n_2.U} & 0_{N,N} & 0_{N,N} \\ 0_{N,n_2} & 0_{N,n_2} & 0_{N,n_2.U} & 0_{N,n_2.U} & 0_{N,N} & 0_{N,N} \\ -\mathrm{M}^{17}_{N,n_2} & \mathrm{M}^{18}_{N,n_2} & \mathrm{M}^{19}_{N,n_2.U} & -\mathrm{M}^{20}_{N,n_2.U} & 0_{N,N} & 0_{N,N} \end{bmatrix} \tag{5.224}$$

$$A_3 = \begin{bmatrix} 0_{2p_1,N} & 0_{2p_1,N} & 0_{2p_1,2p_3} & 0_{2p_1,2p_3.U} \\ 0_{2p_1.U,N} & 0_{2p_1.U,N} & 0_{2p_1.U,2p_3} & 0_{2p_1.U,2p_3.U} \\ 0_{N,N} & 0_{N,N} & 0_{N,2p_3} & 0_{N,2p_3.U} \\ 0_{N,N} & 0_{N,N} & 0_{N,2p_3} & 0_{N,2p_3.U} \\ 0_{N,N} & 0_{N,N} & 0_{N,2p_3} & 0_{N,2p_3.U} \\ 0_{N,N} & 0_{N,N} & 0_{N,2p_3} & 0_{N,2p_3.U} \end{bmatrix} \tag{5.225}$$

$$A_4 = \begin{bmatrix} 0_{n_2,2p_1} & 0_{n_2,2p_1.U} & \mathrm{M}^{21}_{n_2,N} & \mathrm{M}^{22}_{n_2,N} & \mathrm{M}^{23}_{n_2,N} & \mathrm{M}^{24}_{n_2,N} \\ 0_{n_2,2p_1} & 0_{n_2,2p_1.U} & 0_{n_2,N} & 0_{n_2,N} & 0_{n_2,N} & 0_{n_2,N} \\ 0_{n_2.U,2p_1} & 0_{n_2.U,2p_1.U} & \mathrm{M}^{29}_{n_2.U,N} & \mathrm{M}^{30}_{n_2.U,N} & \mathrm{M}^{31}_{n_2.U,N} & \mathrm{M}^{32}_{n_2.U,N} \\ 0_{n_2.U,2p_1} & 0_{n_2.U,2p_1.U} & 0_{n_2.U,N} & 0_{n_2.U,N} & 0_{n_2.U,N} & 0_{n_2.U,N} \\ 0_{N,2p_1} & 0_{N,2p_1.U} & 0_{N,N} & 0_{N,N} & 0_{N,N} & 0_{N,N} \\ 0_{N,2p_1} & 0_{N,2p_1.U} & 0_{N,N} & 0_{N,N} & 0_{N,N} & 0_{N,N} \end{bmatrix} \tag{5.226}$$

$$A_5 = \begin{bmatrix} -\mathrm{I}_{n_2,n_2} & 0_{n_2,n_2} & 0_{n_2,n_2.U} & 0_{n_2,n_2.U} & 0_{n_2,N} & 0_{n_2,N} \\ 0_{n_2,n_2} & -\mathrm{I}_{n_2,n_2} & 0_{n_2,n_2.U} & 0_{n_2,n_2.U} & \mathrm{M}^{25}_{n_2,N} & \mathrm{M}^{26}_{n_2,N} \\ 0_{n_2.U,n_2} & 0_{n_2.U,n_2} & -\mathrm{I}_{n_2.U,n_2.U} & 0_{n_2.U,n_2.U} & 0_{n_2.U,N} & 0_{n_2.U,N} \\ 0_{n_2.U,n_2} & 0_{n_2.U,n_2} & 0_{n_2.U,n_2.U} & -\mathrm{I}_{n_2.U,n_2.U} & \mathrm{M}^{33}_{n_2.U,N} & \mathrm{M}^{34}_{n_2.U,N} \\ -\mathrm{M}^{37}_{N,n_2} & \mathrm{M}^{38}_{N,n_2} & \mathrm{M}^{39}_{N,n_2.U} & -\mathrm{M}^{40}_{N,n_2.U} & -\mathrm{I}_{N,N} & 0_{N,N} \\ 0_{N,n_2} & 0_{N,n_2} & 0_{N,n_2.U} & 0_{N,n_2.U} & 0_{N,N} & -\mathrm{I}_{N,N} \end{bmatrix} \tag{5.227}$$

$$A_6 = \begin{bmatrix} 0_{n_2,N} & 0_{n_2,N} & 0_{n_2,2p_3} & 0_{n_2,2p_3.U} \\ \mathrm{M}^{27}_{n_2,N} & \mathrm{M}^{28}_{n_2,N} & 0_{n_2,2p_3} & 0_{n_2,2p_3.U} \\ 0_{n_2.U,N} & 0_{n_2.U,N} & 0_{n_2.U,2p_3} & 0_{n_2.U,2p_3.U} \\ \mathrm{M}^{35}_{n_2.U,N} & \mathrm{M}^{36}_{n_2.U,N} & 0_{n_2.U,2p_3} & 0_{n_2.U,2p_3.U} \\ 0_{N,N} & 0_{N,N} & 0_{N,2p_3} & 0_{N,2p_3.U} \\ 0_{N,N} & 0_{N,N} & -\mathrm{M}^{41}_{N,2p_3} & \mathrm{M}^{42}_{N,2p_3.U} \end{bmatrix} \tag{5.228}$$

$$A_7 = \begin{bmatrix} 0_{N,2p_1} & 0_{N,2p_1.U} & 0_{N,N} & 0_{N,N} & 0_{N,N} & 0_{N,N} \\ 0_{N,2p_1} & 0_{N,2p_1.U} & 0_{N,N} & 0_{N,N} & 0_{N,N} & 0_{N,N} \\ 0_{2p_3,2p_1} & 0_{2p_3,2p_1.U} & 0_{2p_3,N} & 0_{2p_3,N} & 0_{2p_3,N} & 0_{2p_3,N} \\ 0_{2p_3.U,2p_1} & 0_{2p_3.U,2p_1.U} & 0_{2p_3.U,N} & 0_{2p_3.U,N} & 0_{2p_3.U,N} & 0_{2p_3.U,N} \end{bmatrix} \tag{5.229}$$

$$A_8 = \begin{bmatrix} -\mathrm{M}^{43}_{N,n_2} & \mathrm{M}^{44}_{N,n_2} & \mathrm{M}^{45}_{N,n_2.U} & -\mathrm{M}^{46}_{N,n_2.U} & 0_{N,N} & 0_{N,N} \\ 0_{N,n_2} & 0_{N,n_2} & 0_{N,n_2.U} & 0_{N,n_2.U} & 0_{N,N} & 0_{N,N} \\ 0_{2p_3,n_2} & 0_{2p_3,n_2} & 0_{2p_3,n_2.U} & 0_{2p_3,n_2.U} & \mathrm{M}^{49}_{2p_3,N} & \mathrm{M}^{50}_{2p_3,N} \\ 0_{2p_3.U,n_2} & 0_{2p_3.U,n_2} & 0_{2p_3.U,n_2.U} & 0_{2p_3.U,n_2.U} & \mathrm{M}^{53}_{2p_3.U,N} & \mathrm{M}^{54}_{2p_3.U,N} \end{bmatrix} \tag{5.230}$$

$$A_9 = \begin{bmatrix} -\mathrm{I}_{N,N} & 0_{N,N} & 0_{N,2p_3} & 0_{N,2p_3.U} \\ 0_{N,N} & -\mathrm{I}_{N,N} & -\mathrm{M}^{47}_{N,2p_3} & \mathrm{M}^{48}_{N,2p_3.U} \\ \mathrm{M}^{51}_{2p_3,N} & \mathrm{M}^{52}_{2p_3,N} & -\mathrm{I}_{2p_3,2p_3} & 0_{2p_3,2p_3.U} \\ \mathrm{M}^{55}_{2p_3.U,N} & \mathrm{M}^{56}_{2p_3.U,N} & 0_{2p_3.U,2p_3} & -\mathrm{I}_{2p_3.U,2p_3.U} \end{bmatrix} \tag{5.231}$$

The elements of the matrix are defined below. $\mathrm{I}_{N,N}$ is an identity matrix with N rows and N columns. For example $\mathrm{I}_{2,2} = \begin{bmatrix} 1 & 0 \\ 0 & 1 \end{bmatrix}$. The subscripts define the size of the element in

the matrix, where the first subscript denotes row length and second subscript column length. For example $\mathrm{M}_{2,3} = \begin{bmatrix} M_{11} & M_{12} & M_{13} \\ M_{21} & M_{22} & M_{23} \end{bmatrix}$

The superscripts define the number of the matrix. There are a total of 56 matrices in $\overline{A}$.

$$\mathrm{M}^{1}_{2p_1,N} = \frac{R_2}{n\beta_h}\left(\frac{U_n(R_2,R_3)}{V_n(R_2,R_3)}\right) r(n,j,\beta_h) \tag{5.232}$$

$$\mathrm{M}^{2}_{2p_1,N} = \frac{R_3}{n\beta_h}\left(\frac{2}{V_n(R_3,R_2)}\right) r(n,j,\beta_h) \tag{5.233}$$

$$\mathrm{M}^{3}_{2p_1,N} = \frac{R_2}{n\beta_h}\left(\frac{U_n(R_2,R_3)}{V_n(R_2,R_3)}\right) s(n,j,\beta_h) \tag{5.234}$$

$$\mathrm{M}^{4}_{2p_1,N} = \frac{R_3}{n\beta_h}\left(\frac{2}{V_n(R_3,R_2)}\right) s(n,j,\beta_h) \tag{5.235}$$

$$\mathrm{M}^{5}_{2p_1.U,N} = \frac{R_2}{n\beta_h}\left(\frac{U_n(R_2,R_3)}{V_n(R_2,R_3)}\right) f(n,u,j,\beta_h) \tag{5.236}$$

$$\mathrm{M}^{6}_{2p_1.U,N} = \frac{R_3}{n\beta_h}\left(\frac{2}{V_n(R_3,R_2)}\right) f(n,u,j,\beta_h) \tag{5.237}$$

$$\mathrm{M}^{7}_{2p_1.U,N} = \frac{2R_2}{n\beta_h}\left(\frac{U_n(R_2,R_3)}{V_n(R_2,R_3)}\right) g(n,u,j,\beta_h) \tag{5.238}$$

$$\mathrm{M}^{8}_{2p_1.U,N} = \frac{2R_3}{n\beta_h}\left(\frac{2}{V_n(R_3,R_2)}\right) g(n,u,j,\beta_h) \tag{5.239}$$

$$\mathrm{M}^{9}_{N,2p_1} = \frac{1}{\pi R_2 \ln(R_2)} r(n,j,\beta_h) \tag{5.240}$$

$$\mathrm{M}^{10}_{N,2p_1.U} = \frac{uk_h}{\pi R_2}\frac{U_{uk_h}(R_1,R_2)}{V_{uk_h}(R_1,R_2)} f(n,u,j,\beta_h) \tag{5.241}$$

$$\mathrm{M}_{N,n_2}^{11} = \frac{-1}{\pi R_3 \ln(R_3)} r(n,i,\beta_c) \tag{5.242}$$

$$\mathrm{M}_{N,n_2}^{12} = \frac{1}{\pi R_3 \ln(R_4)} r(n,i,\beta_c) \tag{5.243}$$

$$\mathrm{M}_{N,n_2.U}^{13} = \frac{uk_c}{R_3} \frac{U_{uk_c}(R_3,R_4)}{V_{uk_c}(R_3,R_4)} f(n,u,i,\beta_c) \tag{5.244}$$

$$\mathrm{M}_{N,n_2.U}^{14} = \frac{-uk_c}{R_3} \frac{U_{uk_c}(R_3,R_4)}{V_{uk_c}(R_3,R_4)} f(n,u,i,\beta_c) \tag{5.245}$$

$$\mathrm{M}_{N,2p_1}^{15} = \frac{1}{\pi R_2 \ln(R_2)} s(n,j,\beta_h) \tag{5.246}$$

$$\mathrm{M}_{N,2p_1.U}^{16} = \frac{uk_h}{\pi R_2} \frac{U_{uk_h}(R_1,R_2)}{V_{uk_h}(R_1,R_2)} g(n,u,j,\beta_h) \tag{5.247}$$

$$\mathrm{M}_{N,n_2}^{17} = \frac{-1}{\pi R_3 \ln(R_3)} s(n,i,\beta_c) \tag{5.248}$$

$$\mathrm{M}_{N,n_2}^{18} = \frac{1}{\pi R_3 \ln(R_4)} s(n,i,\beta_c) \tag{5.249}$$

$$\mathrm{M}_{N,n_2.U}^{19} = \frac{uk_c}{R_3} \frac{U_{uk_c}(R_3,R_4)}{V_{uk_c}(R_3,R_4)} g(n,u,i,\beta_c) \tag{5.250}$$

$$\mathrm{M}_{N,n_2.U}^{20} = \frac{-uk_c}{R_3} \frac{U_{uk_c}(R_3,R_4)}{V_{uk_c}(R_3,R_4)} g(n,u,i,\beta_c) \tag{5.251}$$

$$\mathrm{M}_{n_2,N}^{21} = \frac{R_2}{n\beta_c} \frac{2}{V_n(R_2,R_3)} r(n,i,\beta_c) \tag{5.252}$$

$$\mathrm{M}_{n_2,N}^{22} = \frac{R_3}{n\beta_c} \frac{U_n(R_3,R_2)}{V_n(R_3,R_2)} r(n,i,\beta_c) \tag{5.253}$$

$$\mathrm{M}_{n_2,N}^{23} = \frac{R_2}{n\beta_c} \frac{2}{V_n(R_2,R_3)} s(n,i,\beta_c) \tag{5.254}$$

$$\mathrm{M}_{n_2,N}^{24} = \frac{R_3}{n\beta_c}\frac{U_n(R_3,R_2)}{V_n(R_3,R_2)}s(n,i,\beta_c) \tag{5.255}$$

$$\mathrm{M}_{n_2,N}^{25} = \frac{R_4}{n\beta_c}\frac{U_n(R_4,R_5)}{V_n(R_4,R_5)}r(n,i,\beta_c) \tag{5.256}$$

$$\mathrm{M}_{n_2,N}^{26} = \frac{R_5}{n\beta_c}\frac{2}{V_n(R_5,R_4)}r(n,i,\beta_c) \tag{5.257}$$

$$\mathrm{M}_{n_2,N}^{27} = \frac{R_4}{n\beta_c}\frac{U_n(R_4,R_5)}{V_n(R_4,R_5)}s(n,i,\beta_c) \tag{5.258}$$

$$\mathrm{M}_{n_2,N}^{28} = \frac{R_5}{n\beta_c}\frac{2}{V_n(R_5,R_4)}s(n,i,\beta_c) \tag{5.259}$$

$$\mathrm{M}_{n_2.U,N}^{29} = \frac{2R_2}{n\beta_c}\frac{2}{V_n(R_2,R_3)}f(n,u,i,\beta_c) \tag{5.260}$$

$$\mathrm{M}_{n_2.U,N}^{30} = \frac{2R_3}{n\beta_c}\frac{U_n(R_3,R_2)}{V_n(R_3,R_2)}f(n,u,i,\beta_c) \tag{5.261}$$

$$\mathrm{M}_{n_2.U,N}^{31} = \frac{2R_2}{n\beta_c}\frac{2}{V_n(R_2,R_3)}g(n,u,i,\beta_c) \tag{5.262}$$

$$\mathrm{M}_{n_2.U,N}^{32} = \frac{2R_3}{n\beta_c}\frac{U_n(R_3,R_2)}{V_n(R_3,R_2)}g(n,u,i,\beta_c) \tag{5.263}$$

$$\mathrm{M}_{n_2.U,N}^{33} = \frac{2R_4}{n\beta_c}\frac{U_n(R_4,R_5)}{V_n(R_4,R_5)}f(n,u,i,\beta_c) \tag{5.264}$$

$$\mathrm{M}_{n_2.U,N}^{34} = \frac{2R_5}{n\beta_c}\frac{2}{V_n(R_5,R_4)}f(n,u,i,\beta_c) \tag{5.265}$$

$$\mathrm{M}_{n_2.U,N}^{35} = \frac{2R_4}{n\beta_c}\frac{U_n(R_4,R_5)}{V_n(R_4,R_5)}g(n,u,i,\beta_c) \tag{5.266}$$

$$\mathrm{M}_{n_2.U,N}^{36} = \frac{2R_5}{n\beta_c}\frac{2}{V_n(R_5,R_4)}g(n,u,i,\beta_c) \tag{5.267}$$

$$\mathrm{M}_{N,n_2}^{37} = \frac{1}{\pi R_4 \ln(R_4)}r(n,i,\beta_c) \tag{5.268}$$

$$\mathrm{M}_{N,n_2}^{38} = \frac{1}{\pi R_4 \ln(R_3)} r(n,i,\beta_c) \tag{5.269}$$

$$\mathrm{M}_{N,n_2.U}^{39} = \frac{uk_c}{R_4} \frac{2}{V_{uk_c}(R_3,R_4)} f(n,u,i,\beta_c) \tag{5.270}$$

$$\mathrm{M}_{N,n_2.U}^{40} = \frac{uk_c}{R_4} \frac{2}{V_{uk_c}(R_3,R_4)} f(n,u,i,\beta_c) \tag{5.271}$$

$$\mathrm{M}_{N,2p_3}^{41} = \frac{1}{\pi R_5 \ln(R_5)} r(n,k,\beta_l) \tag{5.272}$$

$$\mathrm{M}_{N,2p_3.U}^{42} = \frac{uk_l}{\pi R_5} \frac{2}{V_{uk_c}(R_5,R_6)} f(n,u,k,\beta_l) \tag{5.273}$$

$$\mathrm{M}_{N,n_2}^{43} = \frac{1}{\pi R_4 \ln(R_4)} s(n,i,\beta_c) \tag{5.274}$$

$$\mathrm{M}_{N,n_2}^{44} = \frac{1}{\pi R_4 \ln(R_3)} s(n,i,\beta_c) \tag{5.275}$$

$$\mathrm{M}_{N,n_2.U}^{45} = \frac{uk_c}{R_4} \frac{2}{V_{uk_c}(R_3,R_4)} g(n,u,i,\beta_c) \tag{5.276}$$

$$\mathrm{M}_{N,n_2.U}^{46} = \frac{uk_c}{R_4} \frac{2}{V_{uk_c}(R_3,R_4)} g(n,u,i,\beta_c) \tag{5.277}$$

$$\mathrm{M}_{N,2p_3}^{47} = \frac{1}{\pi R_5 \ln(R_5)} s(n,k,\beta_l) \tag{5.278}$$

$$\mathrm{M}_{N,2p_3.U}^{48} = \frac{uk_l}{\pi R_5} \frac{2}{V_{uk_c}(R_5,R_6)} g(n,u,k,\beta_l) \tag{5.279}$$

$$\mathrm{M}_{2p_3,N}^{49} = \frac{R_4}{n\beta_l} \frac{2}{V_n(R_4,R_5)} r(n,k,\beta_l) \tag{5.280}$$

$$\mathrm{M}_{2p_3,N}^{50} = \frac{R_5}{n\beta_l} \frac{U_n(R_5,R_4)}{V_n(R_5,R_4)} r(n,k,\beta_l) \tag{5.281}$$

$$\mathrm{M}_{2p_3,N}^{51} = \frac{R_4}{n\beta_l} \frac{2}{V_n(R_4,R_5)} s(n,k,\beta_l) \tag{5.282}$$

$$\mathrm{M}^{52}_{2p_3,N} = \frac{R_5}{n\beta_l}\frac{U_n(R_5,R_4)}{V_n(R_5,R_4)}s(n,k,\beta_l) \tag{5.283}$$

$$\mathrm{M}^{53}_{2p_3.U,N} = \frac{2R_4}{n\beta_l}\frac{2}{V_n(R_4,R_5)}f(n,u,k,\beta_l) \tag{5.284}$$

$$\mathrm{M}^{54}_{2p_3.U,N} = \frac{2R_5}{n\beta_l}\frac{U_n(R_5,R_4)}{V_n(R_5,R_4)}f(n,u,k,\beta_l) \tag{5.285}$$

$$\mathrm{M}^{55}_{2p_3.U,N} = \frac{2R_4}{n\beta_l}\frac{2}{V_n(R_4,R_5)}g(n,u,k,\beta_l) \tag{5.286}$$

$$\mathrm{M}^{56}_{2p_3.U,N} = \frac{2R_5}{n\beta_l}\frac{U_n(R_5,R_4)}{V_n(R_5,R_4)}g(n,u,k,\beta_l) \tag{5.287}$$

5.7.6. Flux Density Equation in the Inner Rotor Air-gap, Region Ω^{II}

The magnetic flux density distribution in the inner air-gap can be determined from the magnetic vector potential by using (5.15) and (5.16). In region Ω^{II} we get:

$$B_r^{II}(r,\theta) = \frac{1}{r}\frac{\partial A^{II}}{\partial \theta} \tag{5.288}$$

$$B_\theta^{II}(r,\theta) = -\frac{\partial A^{II}}{\partial r} \tag{5.289}$$

Substituting (5.170) into (5.288) the radial magnetic flux density component is then given by

$$\begin{aligned} B_r^{II}(r,\theta) = &\sum_{n=1}^{\infty} -\left(a_n^{II}\frac{R_2}{r}\frac{\left(\frac{r}{R_3}\right)^n + \left(\frac{R_3}{r}\right)^n}{\left(\frac{R_2}{R_3}\right)^n - \left(\frac{R_3}{R_2}\right)^n} + b_n^{II}\frac{R_3}{r}\frac{\left(\frac{r}{R_2}\right)^n + \left(\frac{R_2}{r}\right)^n}{\left(\frac{R_3}{R_2}\right)^n - \left(\frac{R_2}{R_3}\right)^n}\right)\sin(n\theta) \\ &+\sum_{n=1}^{\infty}\left(c_n^{II}\frac{R_2}{r}\frac{\left(\frac{r}{R_3}\right)^n + \left(\frac{R_3}{r}\right)^n}{\left(\frac{R_2}{R_3}\right)^n - \left(\frac{R_3}{R_2}\right)^n} + d_n^{II}\frac{R_3}{r}\frac{\left(\frac{r}{R_2}\right)^n + \left(\frac{R_2}{r}\right)^n}{\left(\frac{R_3}{R_2}\right)^n - \left(\frac{R_2}{R_3}\right)^n}\right)\cos(n\theta) \end{aligned} \tag{5.290}$$

While substituting (5.170) into (5.289) gives the tangential component of magnetic flux density as:

$$B_\theta^{\mathrm{II}}(r,\theta)=\sum_{n=1}^{\infty}-\left(a_n^{\mathrm{II}}\frac{R_2}{r}\frac{\left(\frac{r}{R_3}\right)^n-\left(\frac{R_3}{r}\right)^n}{\left(\frac{R_2}{R_3}\right)^n-\left(\frac{R_3}{R_2}\right)^n}+b_n^{\mathrm{II}}\frac{R_3}{r}\frac{\left(\frac{r}{R_2}\right)^n-\left(\frac{R_2}{r}\right)^n}{\left(\frac{R_3}{R_2}\right)^n-\left(\frac{R_2}{R_3}\right)^n}\right)\cos(n\theta)$$
$$+\sum_{n=1}^{\infty}-\left(c_n^{\mathrm{II}}\frac{R_2}{r}\frac{\left(\frac{r}{R_3}\right)^n-\left(\frac{R_3}{r}\right)^n}{\left(\frac{R_2}{R_3}\right)^n-\left(\frac{R_3}{R_2}\right)^n}+d_n^{\mathrm{II}}\frac{R_3}{r}\frac{\left(\frac{r}{R_2}\right)^n-\left(\frac{R_2}{r}\right)^n}{\left(\frac{R_3}{R_2}\right)^n-\left(\frac{R_2}{R_3}\right)^n}\right)\sin(n\theta) \tag{5.291}$$

5.7.7. Flux Density Equation in the Outer Rotor Air-gap, Region Ω^{IV}

The magnetic flux density distribution in the outer air-gap can be determined from the magnetic vector potential by

$$B_r^{\mathrm{IV}}(r,\theta)=\frac{1}{r}\frac{\partial A^{\mathrm{IV}}}{\partial\theta} \tag{5.292}$$

$$B_\theta^{\mathrm{IV}}(r,\theta)=-\frac{\partial A^{\mathrm{IV}}}{\partial r} \tag{5.293}$$

Substituting (5.171) into (5.292) gives the radial component of magnetic flux density as:

$$B_r^{\mathrm{IV}}(r,\theta)=\sum_{n=1}^{\infty}-\left(a_n^{\mathrm{IV}}\frac{R_4}{r}\frac{\left(\frac{r}{R_5}\right)^n+\left(\frac{R_5}{r}\right)^n}{\left(\frac{R_4}{R_5}\right)^n-\left(\frac{R_5}{R_4}\right)^n}+b_n^{\mathrm{IV}}\frac{R_5}{r}\frac{\left(\frac{r}{R_4}\right)^n+\left(\frac{R_4}{r}\right)^n}{\left(\frac{R_5}{R_4}\right)^n-\left(\frac{R_4}{R_5}\right)^n}\right)\sin(n\theta)$$
$$+\sum_{n=1}^{\infty}\left(c_n^{\mathrm{IV}}\frac{R_4}{r}\frac{\left(\frac{r}{R_5}\right)^n+\left(\frac{R_5}{r}\right)^n}{\left(\frac{R_4}{R_5}\right)^n-\left(\frac{R_5}{R_4}\right)^n}+d_n^{\mathrm{IV}}\frac{R_5}{r}\frac{\left(\frac{r}{R_4}\right)^n+\left(\frac{R_4}{r}\right)^n}{\left(\frac{R_5}{R_4}\right)^n-\left(\frac{R_4}{R_5}\right)^n}\right)\cos(n\theta) \tag{5.294}$$

While substituting (5.171) into (5.293) gives the tangential component of magnetic flux density as:

$$B_\theta^{\mathrm{IV}}(r,\theta)=\sum_{n=1}^{\infty}-\left(a_n^{\mathrm{IV}}\frac{R_4}{r}\frac{\left(\frac{r}{R_5}\right)^n-\left(\frac{R_5}{r}\right)^n}{\left(\frac{R_4}{R_5}\right)^n-\left(\frac{R_5}{R_4}\right)^n}+b_n^{\mathrm{IV}}\frac{R_5}{r}\frac{\left(\frac{r}{R_4}\right)^n-\left(\frac{R_4}{r}\right)^n}{\left(\frac{R_5}{R_4}\right)^n-\left(\frac{R_4}{R_5}\right)^n}\right)\cos(n\theta)$$
$$+\sum_{n=1}^{\infty}-\left(c_n^{\mathrm{IV}}\frac{R_4}{r}\frac{\left(\frac{r}{R_5}\right)^n-\left(\frac{R_5}{r}\right)^n}{\left(\frac{R_4}{R_5}\right)^n-\left(\frac{R_5}{R_4}\right)^n}+d_n^{\mathrm{IV}}\frac{R_5}{r}\frac{\left(\frac{r}{R_4}\right)^n-\left(\frac{R_4}{r}\right)^n}{\left(\frac{R_5}{R_4}\right)^n-\left(\frac{R_4}{R_5}\right)^n}\right)\sin(n\theta) \tag{5.295}$$

5.7.8. Electromagnetic Torque

The electromagnetic torque is obtained using the Maxwell's stress tensor equation. The magnetic fields calculated in (5.290), (5.291), (5.294) and (5.295) are used to calculate the torque. A circle at radius r=R_e in the inner air-gap is taken as the path for calculating torque and the torque equation is expressed as

$$T_e=\frac{dR_e^2}{\mu_o}\int_0^{2\pi}B_r^{\mathrm{IV}}(R_e,\theta)B_\theta^{\mathrm{IV}}(R_e,\theta)d\theta \tag{5.296}$$

where d is the axial length of the MG.

Similarly the torque in the outer air-gap is computed from

$$T_e=\frac{dR_e^2}{\mu_o}\int_0^{2\pi}B_r^{\mathrm{IV}}(R_e,\theta)B_\theta^{\mathrm{IV}}(R_e,\theta)d\theta \tag{5.297}$$

5.8. Model Validation

In order to validate the developed analytical model, the flux density values in the inner and outer rotor air-gap for the scaled-up FFMG are compared. A FEA study for the scaled-up design with ideal steel properties was performed in order to compare with the

analytical model. The ideal FEA model was simulated by using μ_r=100,000 in the steel regions. This approximated the ideal condition in which μ_r tends to ∞. The non-linear FEA model used the non-linear BH steel properties shown in Figure 5.13.

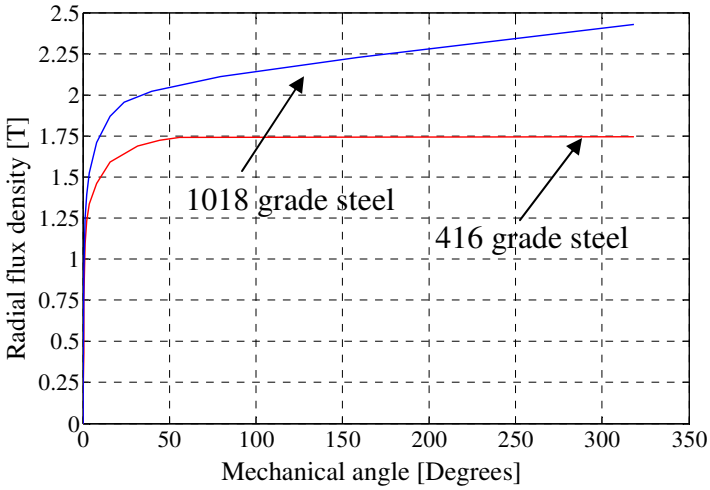

Figure 5-13: BH curves of steel used in non-linear FEA

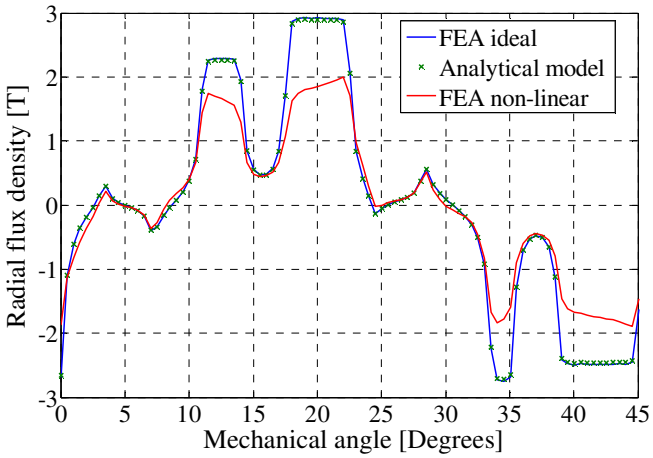

Figure 5-14: Comparison of the radial flux densities in the inner air-gap with the analytical, ideal and non-linear FEA models

Figure 5-14 shows the comparison of the radial flux density in the inner rotor air-gap between the FEA ideal and non-linear models and the analytical model. It can be seen that the FEA linear and analytical models are very close thereby validating the accuracy of the analytical model. Figure 5-15 shows the dominant harmonic comparison of the inner air-gap field. The dominant harmonic is the 8th harmonic due to the 8 inner

rotor pole-pairs. The accuracy of the analytic model can be verified by noting the close dominant harmonic values for the ideal FEA and analytical model.

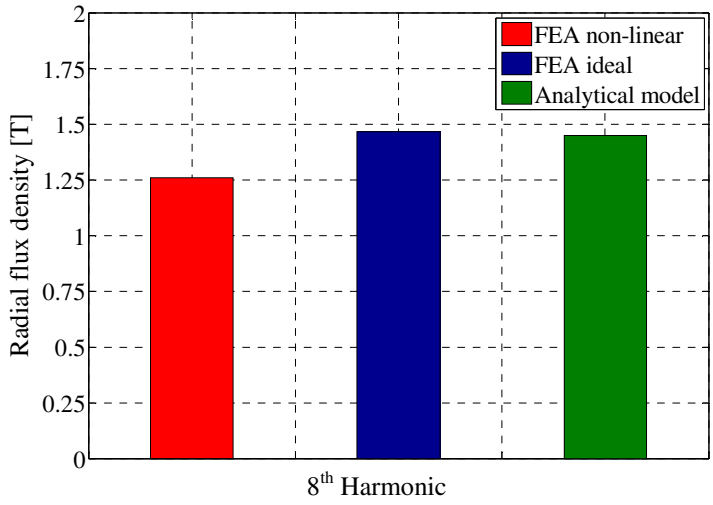

Figure 5-15: Comparison of the the 8th harmonic of the radial flux density in the inner air-gap with the analytical, FEA ideal and non-linear models

Figure 5-16 shows the comparison of the azimuthal flux density in the inner rotor air-gap and shows the corresponding dominant harmonic comparison. Again close agreement is achieved between the ideal FEA and analytical model.

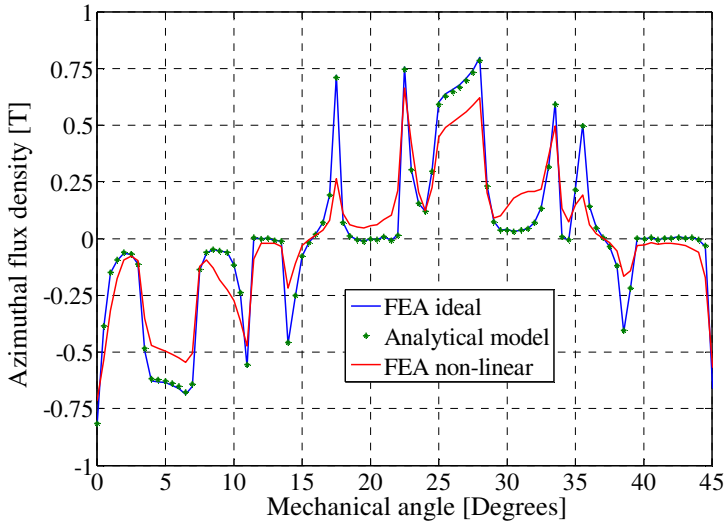

Figure 5-16: Comparison of the azimuthal flux densities in the inner air-gap with the analytical, FEA ideal and non-linear models

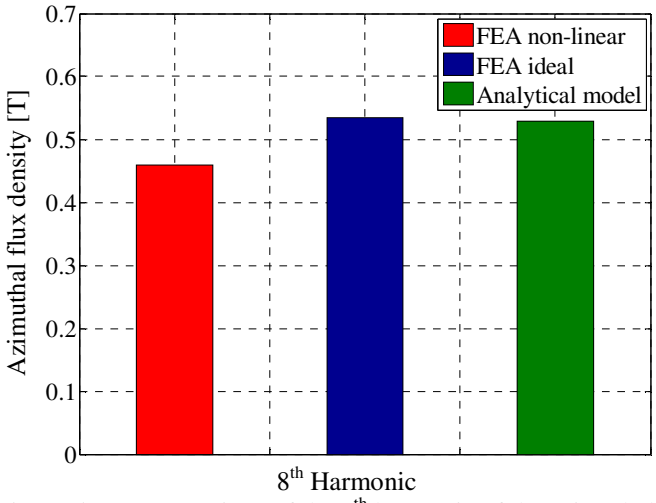

Figure 5-17: Comparison of the 8th harmonic of the azimuthal flux density in the inner air-gap with the analytical, FEA ideal and non-linear models

Figure 5-18 and Figure 5-19 shows the comparison of the radial flux density and the corresponding dominant harmonic in the outer air-gap between the three models.

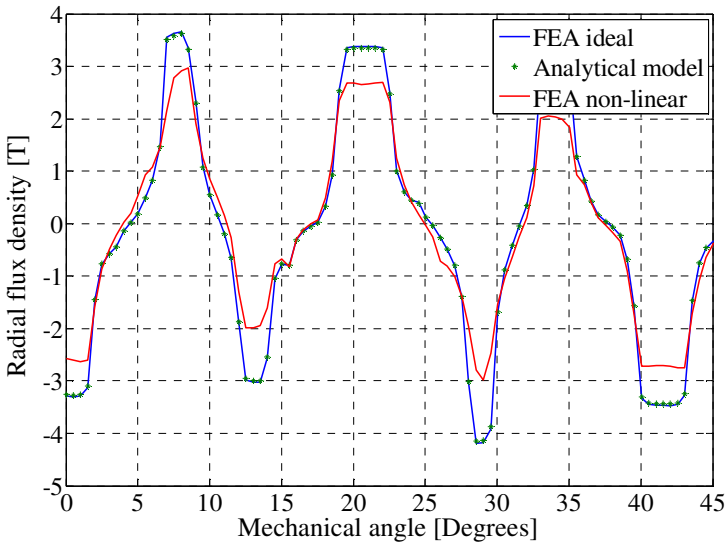

Figure 5-18: Comparison of the radial flux densities in the outer air-gap with the analytical, FEA ideal and non-linear models

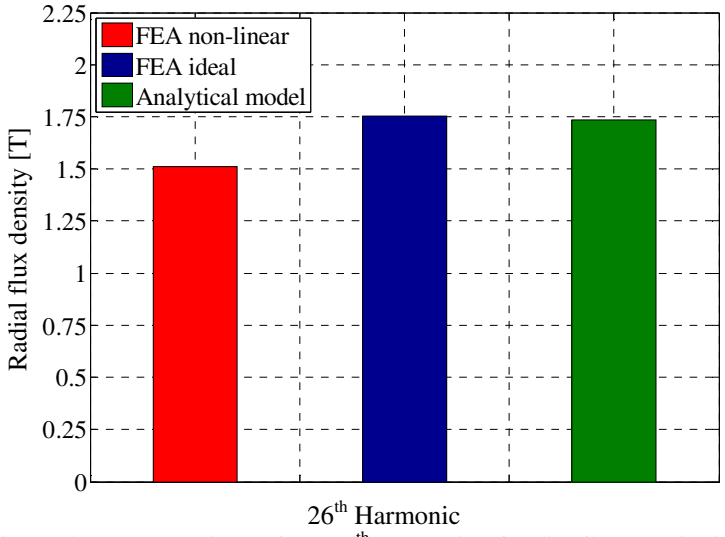

Figure 5-19: Comparison of the 26th harmonic of radial flux density in the outer air-gap with the analytical, FEA ideal and non-linear models

Figure 5-20 and Figure 5-21 shows the comparison of the azimuthal flux density and their corresponding dominant harmonics in the outer rotor air-gap.

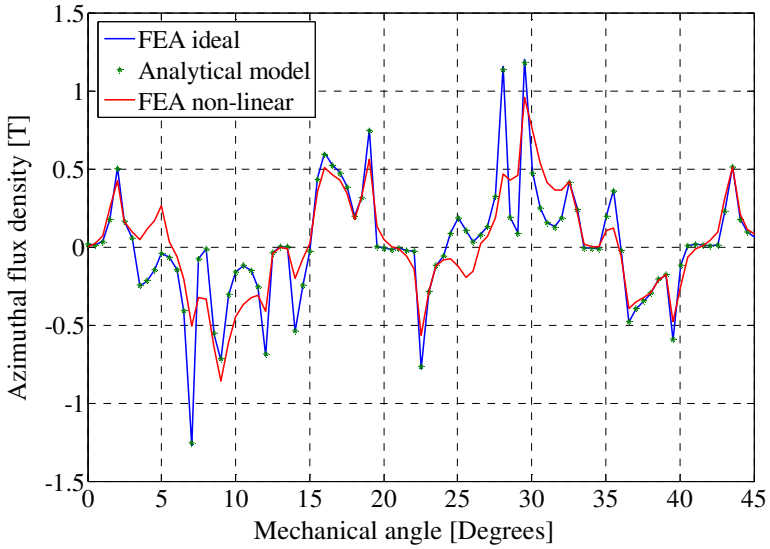

Figure 5-20: Comparison of the azimuthal flux densities in the outer air-gap with the analytical, FEA ideal and non-linear models

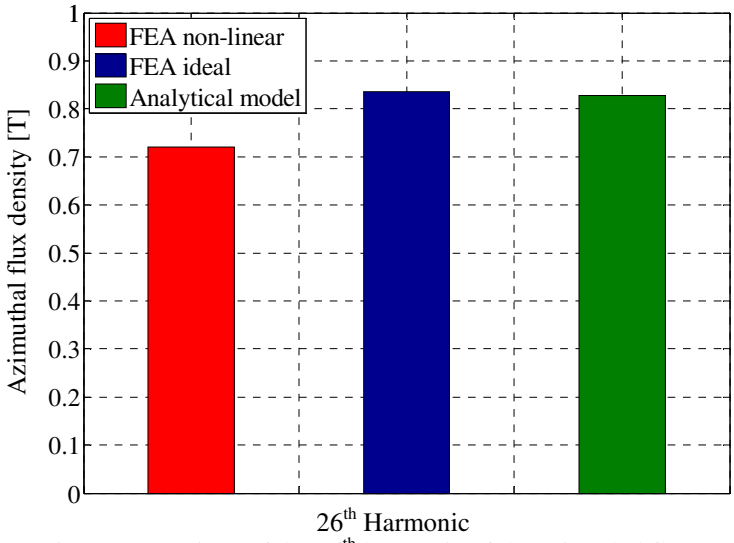

Figure 5-21: Comparison of the 26th harmonic of the azimuthal flux density in the outer air-gap with the analytical, FEA ideal and non-linear models

The analytical model field prediction is very accurate and close to the ideal FEA model. However when compared to the non-linear FEA model the values are higher by around 16% due to the ideal model not accounting for the saturation within the steel.

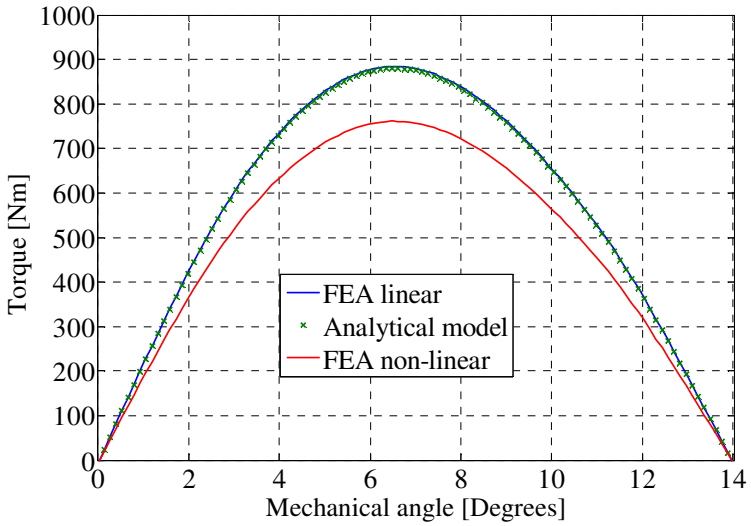

Figure 5-22: Comparison of torque on the cage rotor for analytical, FEA ideal and non-linear models

Figure 5-22 shows the torque comparison on the cage rotor between the three models. The torque calculated by the non-linear FEA model was 761 Nm which corresponds to a torque density of 266.9 Nm/L. With the ideal FEA model the calculated torque was 884 Nm which gives a torque density of 310 Nm/L. The torque obtained through the analytical model was 879 Nm which gives a torque density of 308.3 Nm/L.

The computational time taken for ideal FEA model was 75 minutes where as the analytical model took 3 minutes and 10 seconds to complete the analysis. It is observed that the computational time can be significantly reduced by using the analytical model. Although the results vary significantly between the ideal and non-linear models the analytical model can be used for scaling and parametric sweep of the FFMG designs as it significantly reduces the computational time and resources required. The analytic model is particularly useful for conducting scaling analysis.

5.8.1. Parametric Sweep Validation

In order to see if a parametric sweep analysis using the analytic based model follows the same trend as the non-linear FEA model, in this section the same parametric sweep analysis performed for the scaled-up design is repeated with analytical model.

Figure 5-23 shows the variation of volumetric torque density when the cage rotor steel pole length l_2, was varied along with the high speed rotor outer radius r_{o1}. A maximum volumetric torque density 304 Nm/L is obtained when the cage bar length of 5.5 mm which is 0.5 mm more than the non-linear FEA model. Figure 5-24 shows the variation of the cage rotor steel pole span θ_{s2}. It can be seen that maximum torque density is obtained always when $\theta_{s2}=7^{o}$. This is consistent with the non-linear FEA model.

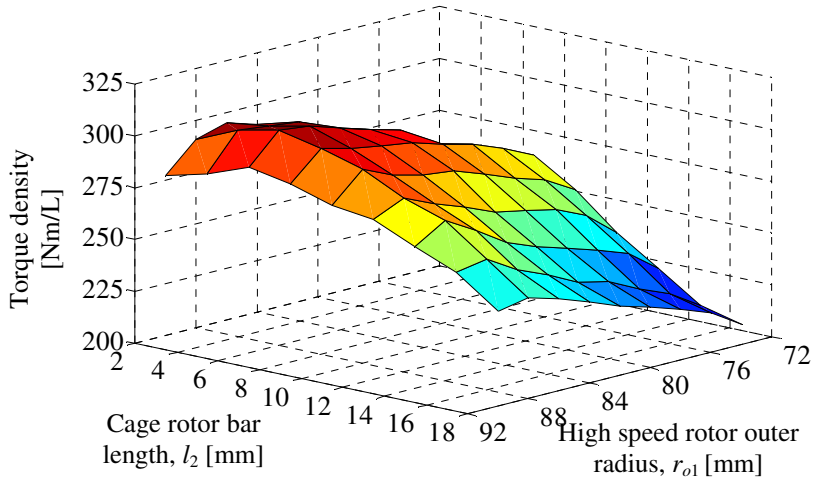

Figure 5-23: Volumetric torque density for changes in the cage rotor bar length, l_2 and high-speed outer rotor radius, r_{o1}, when using NdFeB magnets (θ_{s2}=7°)

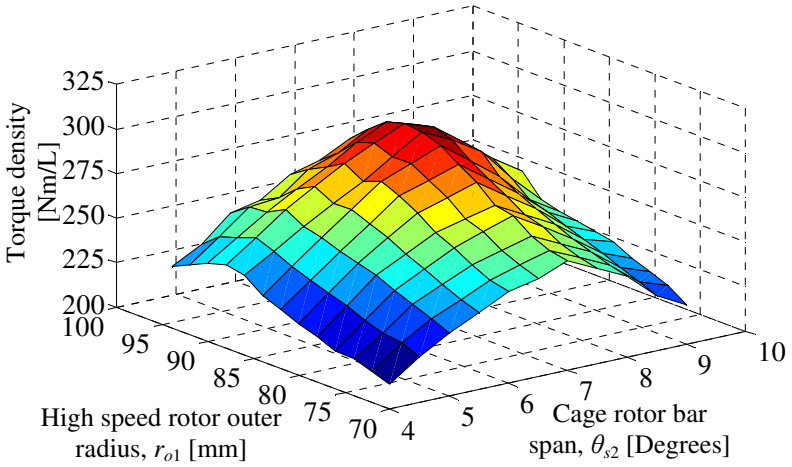

Figure 5-24: Volumetric torque density for cage rotor bar spans, θ_{s2}, and high-speed outer rotor radius, r_{o1}, when using NdFeB magnets (l_2=5.5mm)

Figure 5-25 shows the variation of the volumetric and mass torque densities as the inner radius of inner rotor is varied. It is observed that at an inner radius of r_{i1}=50 mm maximum torque density is obtained. With the new inner radius r_{i1} of 50 mm, the analysis is repeated till a maximum torque density is obtained. Figure 5-26 shows the variation of torque density with changes in cage rotor steel pole length l_2 and outer radius of inner rotor r_{o1}. It is observed that a peak torque density is obtained when the length of the cage rotor bar length is 7.5 mm. This value is 0.5 mm more than the non-linear FEA model.

Figure 5-27 shows that there is no change in the width of the cage rotor bars with changes in length. The final torque after the parametric sweep is 879 Nm which corresponds to a volumetric torque density of 287 Nm/L.

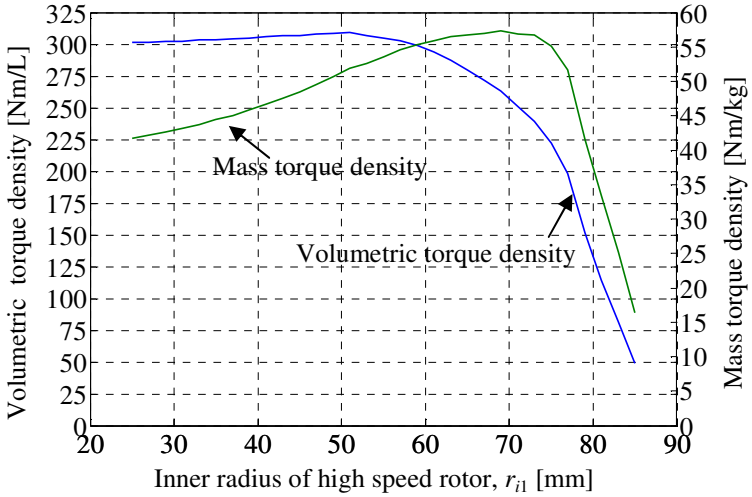

Figure 5-25: Active region torque density variation when the inner radius of the high speed rotor is varied

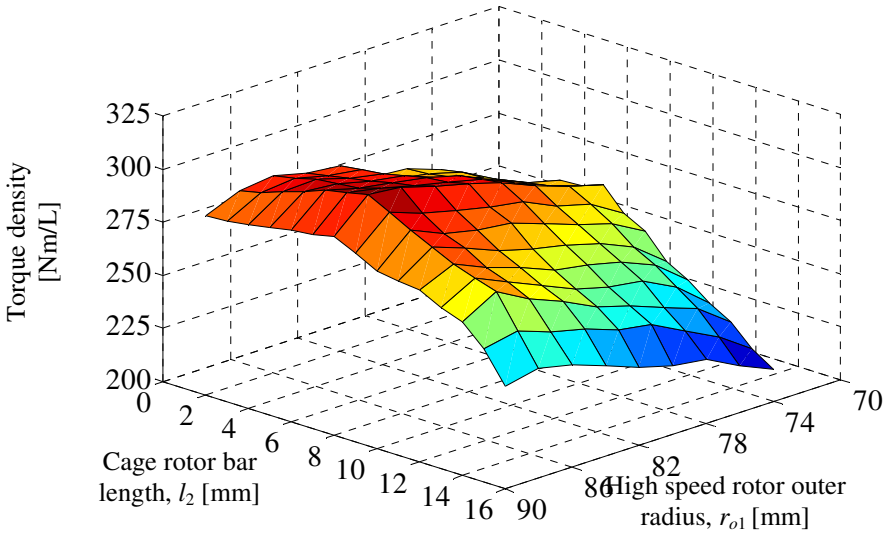

Figure 5-26: Volumetric torque density for changes in the cage rotor bar length, l_2 and high-speed outer rotor radius, r_{o1}, when using NdFeB magnets (θ_{s2}=7°) and r_{i1}=50 mm

The comparison of the parameters after the final parametric sweep between the non-linear FEA and analytical model is shown in Table 5-1. It can be seen that the final

parameters are very close to each other. The only difference being that the cage rotor bar length l_2 and inner radius of the inner rotor r_{i1}. Figure 5-28 shows the percentage difference between the volumetric torque densities calculated using the analytical model and the FEA model. A maximum difference of 20.5% and a minimum difference of 17% was observed between the analytical and FEA models.

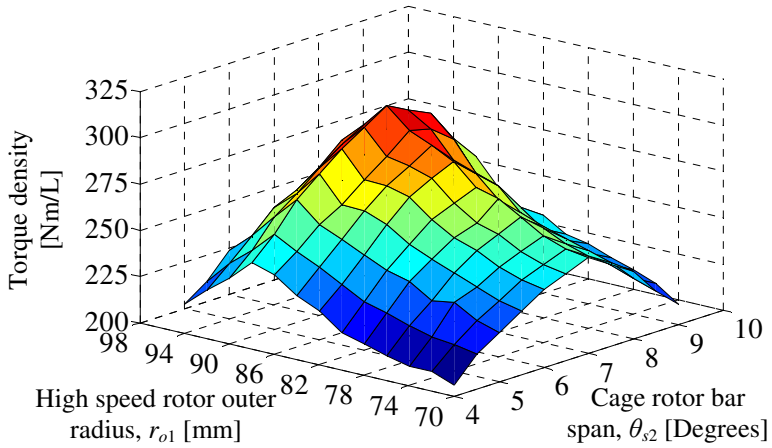

Figure 5-27: Volumetric torque density for cage rotor bar spans, θ_{s2}, and high-speed outer rotor radius, r_{o1}, when using NdFeB magnets (l_2=7mm) and r_{i1}=50 mm

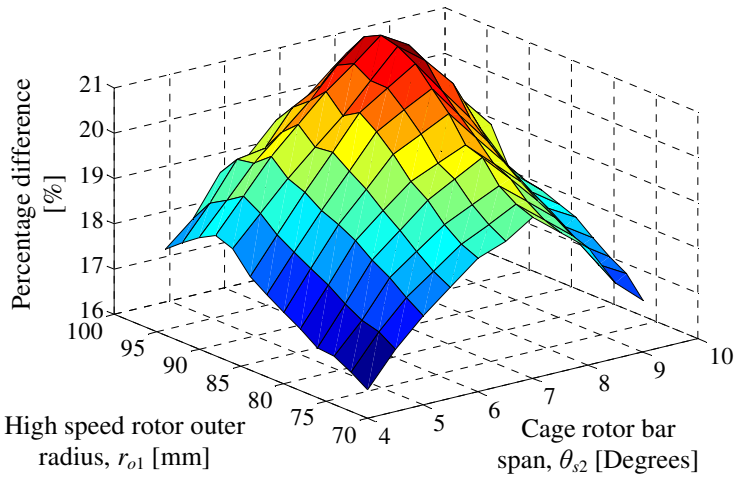

Figure 5-28: The percentage difference in torque density between the analytical and non-linear FEA calculations for cage rotor bar spans, θ_{s2}, and high-speed outer rotor radius, r_{o1}, when using NdFeB magnets (l_2=7mm) and r_{i1}=50 mm

Table 5-1: Final geometric sweep parameters after optimization

	Description	Non-linear FEA	Analytical model	Unit
Inner rotor (high speed)	Pole pairs, p_1	8	8	-
	Steel pole span, θ_{s1}	π/16	π/16	radians
	Air-gap, g	0.5	0.5	mm
	Inner radius, r_{i1}	49	50	
	Outer radius, r_{o1}	88	87.5	
Cage rotor	Steel poles, n_2	34	34	-
	Cage bar length, l_2	7	7.5	mm
	Pole span, θ_{s2}	7	7	degrees
Outer rotor (stationary)	Pole pairs, p_3	26	26	-
	Inner radius, r_{i3}	96	96	mm
	Outer radius, r_{o3}	110	110	mm
	Steel pole span, θ_{s3}	π/52	π/52	radians
	Air-gap, g	0.5	0.5	mm
Material	Ferrite magnet, Hitachi NMF12F	0.46	0.46	T
	NdFeB magnet, N40H, B_r	1.25	1.25	T
	416 steel resistivity (cage rotor)	57.0	57.0	μΩ-cm
	1018 steel resistivity (inner/outer rotor)	15.9	15.9	μΩ-cm
Active region stack length, d		75	75	mm

It is inferred from the parametric sweep that though the analytical model predicts a higher torque density value when compared to the non-linear FEA calculated values, it follows a similar trend during parametric analysis as the non-linear FEA model. Hence, it can be concluded that the analytical model can be useful for conducting initial parametric sweep for scaling up FFMG models.

The comparison of the computational time for the analytical model and ideal FEA is shown in Table 5-2. The computational time for the analytical model is very low compared to the FEA analysis and hence is a very useful tool for scaling and initial parametric sweep of FFMG.

Table 5-2: Computational time comparison for FEA and analytical models

	Time (sec)
Ideal FEA	4520
Analytical model	190

CHAPTER 6 : SCALING ANALYSIS OF FLUX FOCUSING MAGNETIC GEAR

6.1. Introduction

This chapter provides the scaling analysis of a FFMG. The analytical model developed in chapter 5 is used for scaling of the FFMG. The performance of FFMG at various outer diameters [OD] will be analyzed and the effects of changing the pole-pairs on the inner and outer rotors will be analyzed.

6.2. Scaling analysis

The scaling analysis of the MG is accomplished by varying the outer diameter of the MG along with the number of PM pole-pairs on the inner and outer rotors. In this analysis the OD of 230 mm, 300 mm, 350 mm and 400 mm are taken into consideration. The inner rotor pole-pairs, p_1, are first varied from 2 to 16 for a given OD and outer rotor pole-pairs. This procedure is continued for different outer rotor pole-pairs, p_3. The number of steel poles on the cage rotor is obtained as $n_2=p_1+p_3$. The parameters used for this analysis with OD=230 mm are shown in Figure 6-1 and Figure 6-2 show the variation of the volumetric mass torque density with the variation of inner and outer rotor pole-pairs for an OD of 230 mm. A combination of outer rotor pole-pairs of $p_3=25$ and inner rotor pole-pairs of $p_1=8$ gives a maximum volumetric and mass torque density at this diameter. The maximum value of mass torque density occurs at the same point as the volumetric torque density as the radii of all the rotors have been kept constant. It should

be noted that the peak mass torque density could occur at a different location if the radial parametric sweep was performed.

The parameters given in Table 6-1 are taken as reference for the other OD's. The radii of the rotors for other OD's are taken in such a way that the ratio of inner and outer radii of each rotor in the FFMG remains constant for all the OD's. The ratio constants used in the analysis are given in Table 6-2. The parameters for all the OD's are given in Table 6-3 through Table 6-5.

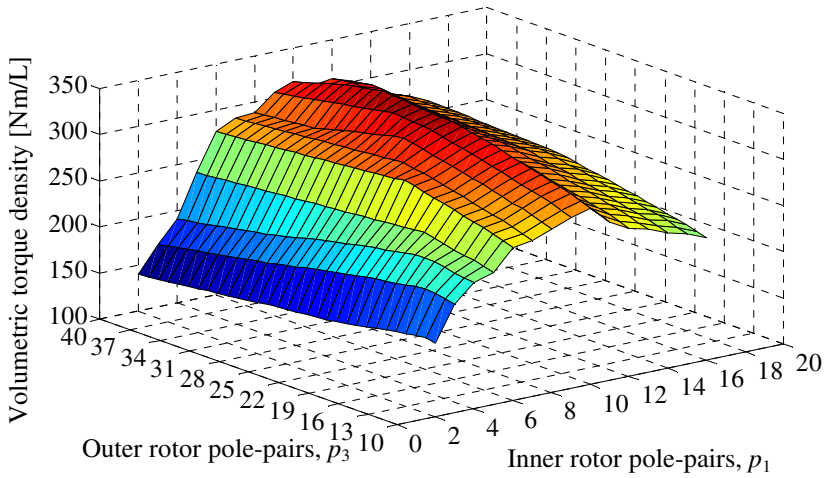

Figure 6-1: Comparison of volumetric torque density of FFMG for different inner and outer pole-pair combinations with an OD of 230 mm

Table 6-1: Geometric parameters for OD=230 mm

	Description	Value	Unit
Inner rotor (high speed)	Inner radius, r_{i1}	49	mm
	Outer radius, r_{o1}	88	mm
Cage rotor	Inner radius, r_{i2}	88.5	mm
	Outer radius, r_{o2}	95.5	mm
Outer rotor	Inner radius, r_{i3}	96	mm
	Outer radius, r_{o3}	115	mm
Material	NdFeB magnet, N40H, density	7600	kg/m^3
	416 steel density (cage rotor)	7750	kg/m^3
	1018 steel resistivity (inner/outer rotor)	7850	kg/m^3
Active region stack length, d		75	mm

Table 6-2: Ratio constants used for scaling analysis

	Description	Value
Inner rotor	r_{o1}/r_{i1}	1.8
Cage rotor	r_{o2}/r_{i2}	1.08
Outer rotor	r_{o3}/r_{i3}	1.2

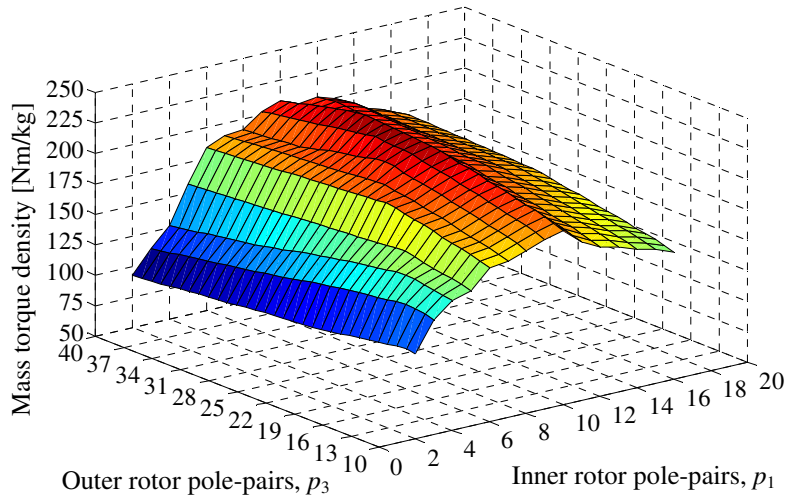

Figure 6-2: Comparison of mass torque density of FFMG for different inner and outer pole-pair combinations with an OD of 230 mm

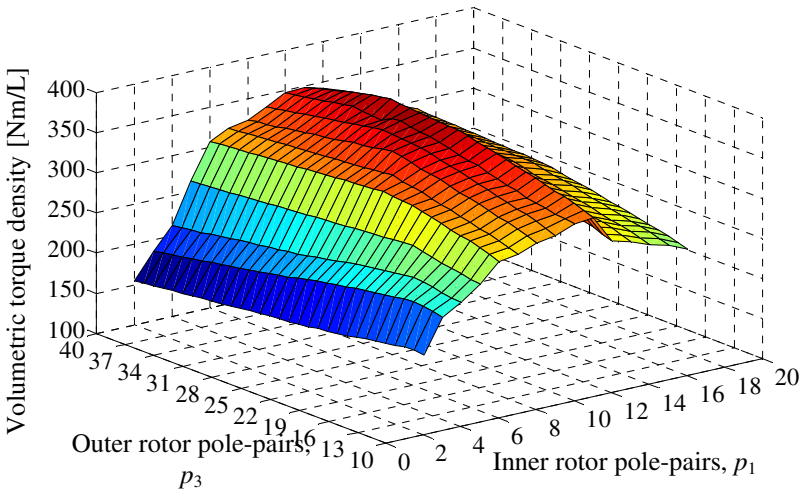

Figure 6-3: Comparison of volumetric torque density of FFMG for different inner and outer pole-pair combinations with an OD of 300 mm

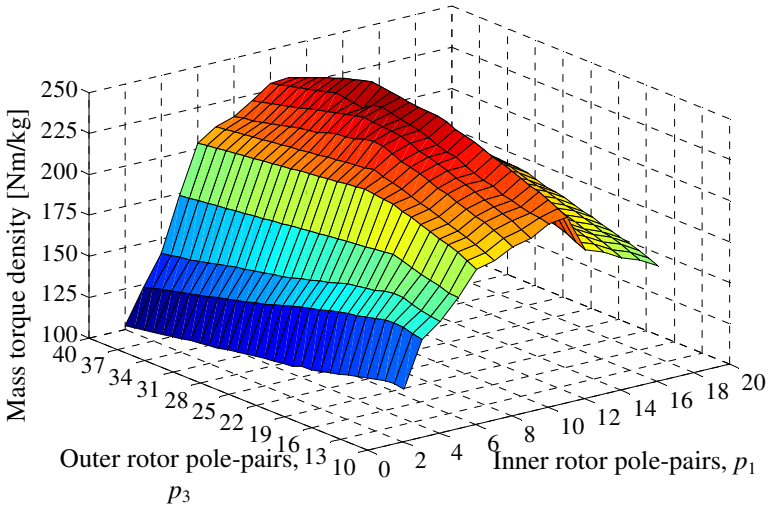

Figure 6-4: Comparison of mass torque density of FFMG for different inner and outer pole-pair combinations with an OD of 300 mm

Table 6-3: Geometric parameters for OD=300 mm

	Description	Value	Unit
Inner rotor (high speed)	Inner radius, r_{i1}	64	mm
	Outer radius, r_{o1}	115	mm
Cage rotor	Inner radius, r_{i2}	115.5	mm
	Outer radius, r_{o2}	124.5	mm
Outer rotor	Inner radius, r_{i3}	125	mm
	Outer radius, r_{o3}	150	mm
Material	NdFeB magnet, N40H, density	7600	kg/m^3
	416 steel density (cage rotor)	7750	kg/m^3
	1018 steel resistivity (inner/outer rotor)	7850	kg/m^3
Active region stack length, d		75	mm

A similar analysis for an OD = 300 mm, 350 mm and 400 mm is shown in Figure 6-3, Figure 6-5 and Figure 6-7 respectively. It is observed for an OD of 300 mm that the maximum volumetric torque density occurs at p_3= 33 and p_1=10. For an OD=350 mm the maximum torque density is obtained at p_3= 39 and p_1=12. Similarly for an OD=400 mm the maximum torque density is obtained at p_3= 41 and p_1=12. The volumetric torque density increases as the OD is increased. Also, the number of magnets on the inner and outer magnets plays a significant role in determining the maximum volumetric density. As we increase the number of magnets on the two rotors the

volumetric torque density increased. But, after a certain point the magnets became too thin and therefore the volumetric torque density decreased. The magnets may also experience demagnetization if the size of the magnets becomes thinner; however this is not considered in the analytical model. An optimum number of pole-pair combinations exist for a different OD resulting in a different optimum gear ratio for each OD.

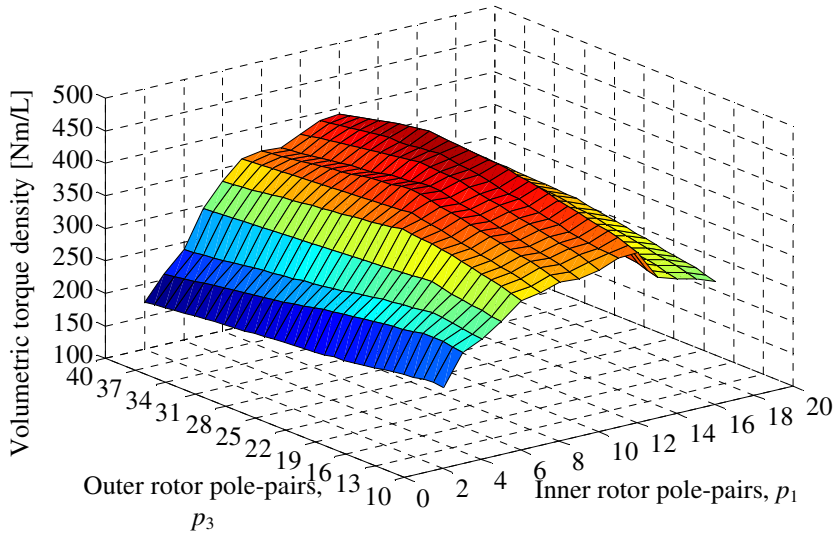

Figure 6-5: Comparison of volumetric torque density of FFMG for different inner and outer pole-pair combinations with an OD of 350 mm

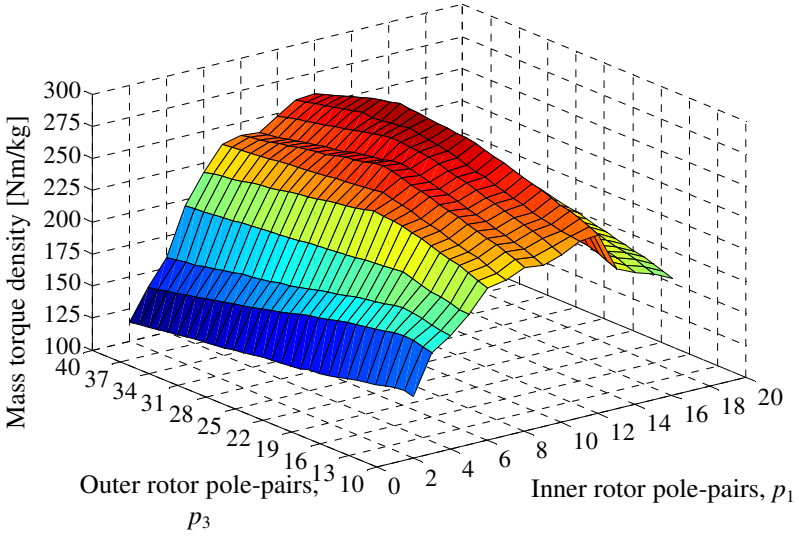

Figure 6-6: Comparison of mass torque density of FFMG for different inner and outer pole-pair combinations with an OD of 350 mm

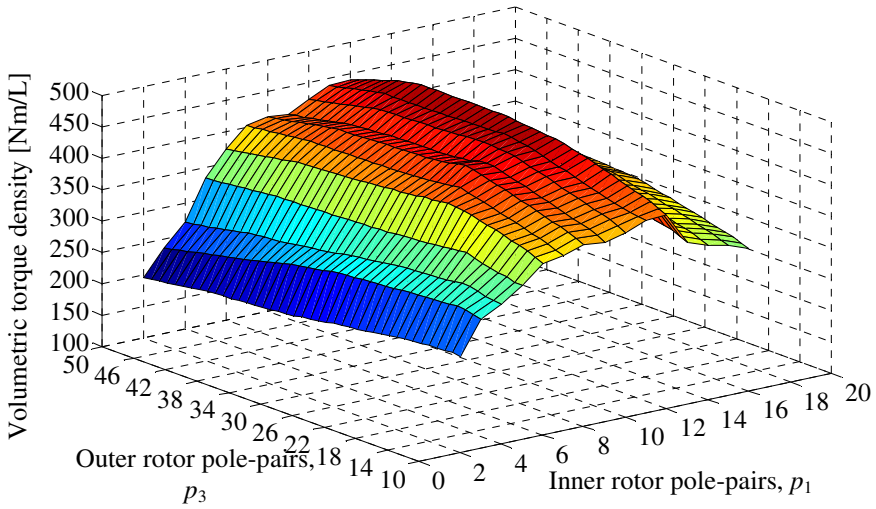

Figure 6-7: Comparison of volumetric torque density of FFMG for different inner and outer pole-pair combinations with an OD of 400 mm

Table 6-4: Geometric parameters for OD=350 mm

	Description	Value	Unit
Inner rotor (high speed)	Inner radius	75	mm
	Outer radius	134	mm
Cage rotor	Inner radius	134.5	mm
	Outer radius	145.5	mm
Outer rotor	Inner radius, r_{i3}	146	mm
	Outer radius, r_{o3}	175	mm
Material	NdFeB magnet, N40H, density	7600	kg/m^3
	416 steel density (cage rotor)	7750	kg/m^3
	1018 steel resistivity (inner/outer rotor)	7850	kg/m^3
Active region stack length, d		75	mm

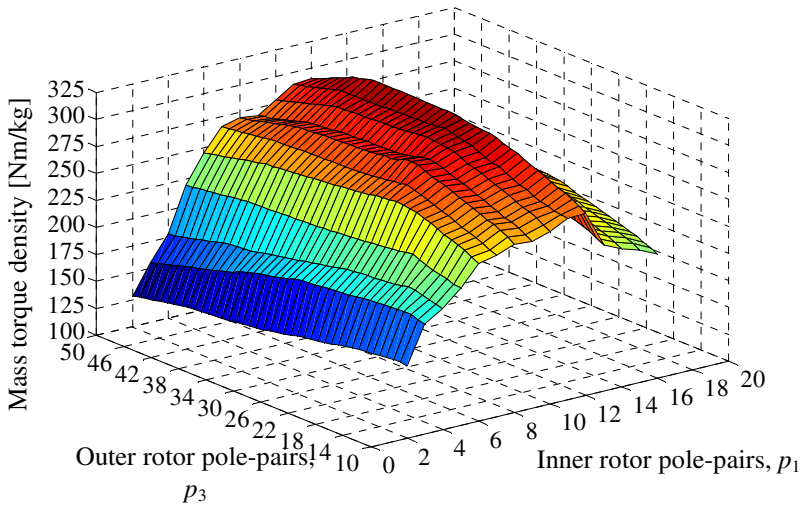

Figure 6-8: Comparison of mass torque density of FFMG for different inner and outer pole-pair combinations with an OD of 400 mm

Table 6-5: Geometric parameters for OD=400 mm

	Description	Value	Unit
Inner rotor (high speed)	Inner radius, r_{i1}	85	mm
	Outer radius, r_{o1}	153.5	mm
Cage rotor	Inner radius, r_{i2}	154	mm
	Outer radius, r_{o2}	166.5	mm
Outer rotor	Inner radius, r_{i3}	167	mm
	Outer radius, r_{o3}	200	mm
Material	NdFeB magnet, N40H, density	7600	kg/m^3
	416 steel density (cage rotor)	7750	kg/m^3
	1018 steel resistivity (inner/outer rotor)	7850	kg/m^3
Active region stack length, d		75	mm

Figure 6-9 shows the variation of the volumetric torque density with the variation of the gear ratio for each OD. The different pole-pairs on the inner and outer rotor give rise to a large combination of gear ratios. The volumetric torque density for all combinations of gear ratios for each OD is shown in Figure 6-9 through Figure 6-12. It can be observed that the maximum torque density for all the four outer ODs occurs between the gear ratio of 4 and 4.5. A summary of the peak volumetric and mass torque density values for different OD values is shown in Table 6-5.

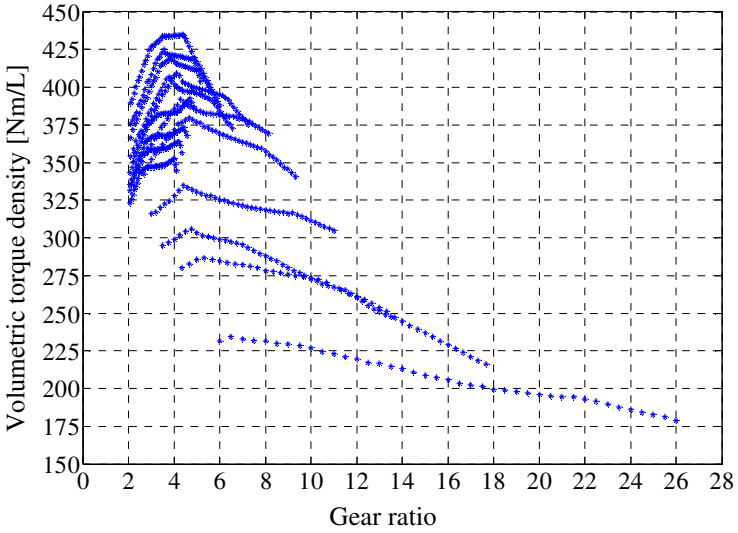

Figure 6-9: Comparison of the volumetric torque density of FFMG at different gear ratios and 400 mm OD

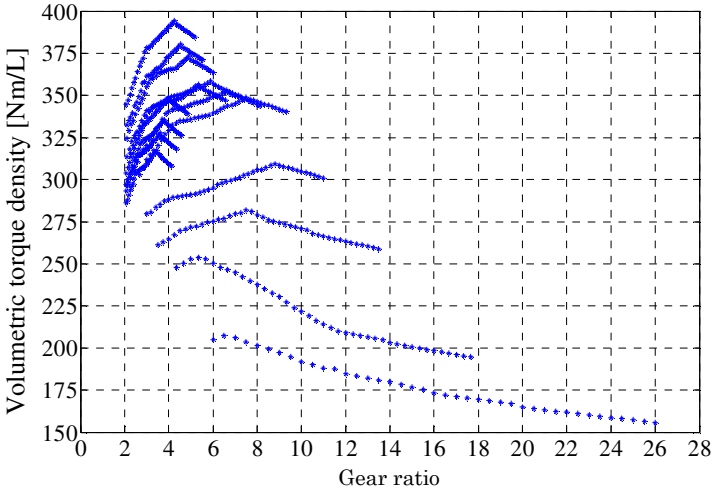

Figure 6-10: Comparison of the volumetric torque density of the FFMG at different gear ratios and 350 mm OD

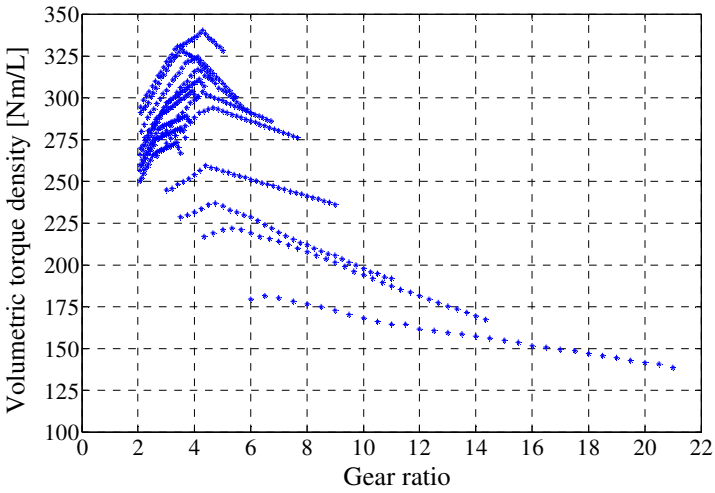

Figure 6-11: Comparison of the volumetric torque density of the FFMG at different gear ratios and 300 mm OD

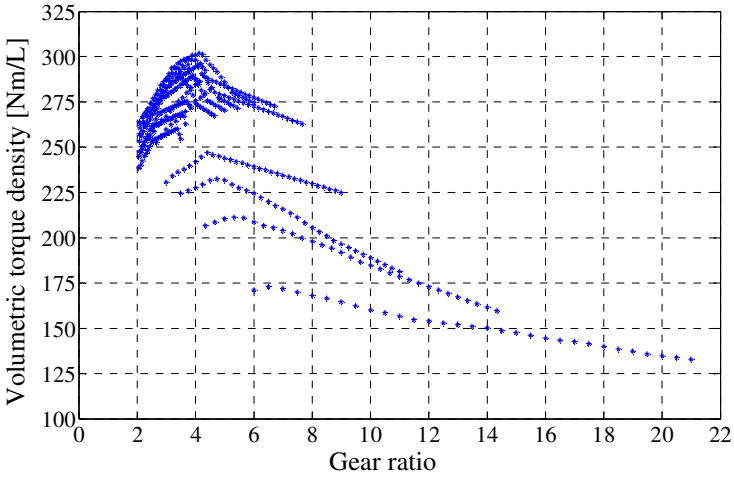

Figure 6-12: Comparison of the volumetric torque density of the FFMG at different gear ratios and 230 mm OD

Table 6-6: Summary of scaling of the FFMG using the analytic model

OD (mm)	Outer rotor pole-pairs, p_3	Inner rotor pole-pairs, p_1	Gear ratio	Volumetric torque-density (Nm/L)	Mass torque-density (Nm/kg)
230	25	8	4.125	302	220
300	33	10	4.3	340	245
350	39	12	4.25	394	276
400	42	12	4.41	435	310

This analysis can be continued for any radii of the OD and the appropriate number of pole-pairs on the inner and outer rotors can be easily determined. The scaling of this magnitude would take huge amount of time and memory if it was performed using FEA. The analytical model is hence a very valuable tool for conducting a scaling analysis. Once an appropriate design is developed using the analytical model, FEA can be performed to take the non-linear properties of the steel into account. Table 6-7 through Table 6-12 show look-up tables for the volumetric torque density values at each pole-pair combination and the corresponding gear ratio.

Table 6-7: Summary of volumetric torque density values for different inner and outer rotor magnet pole-pair combinations for OD=230 mm

Inner rotor pole-pairs, p_1

Outer rotor pole pairs, p_3	2	3	4	5	6	7	8	9	10	11	12	13	14	15	16
10	171.0	206.8	224.6	230.8	252.6	255.3	263.2	260.5	-	-	-	-	-	-	-
11	172.9	208.8	226.0	234.1	256.3	258.9	267.0	264.3	262.9	-	-	-	-	-	-
12	172.0	210.7	227.5	236.5	259.9	262.6	270.8	268.0	266.7	264.0	-	-	-	-	-
13	169.9	211.5	229.7	238.0	262.7	265.4	273.6	270.9	269.5	266.8	257.2	-	-	-	-
14	168.2	210.8	231.8	239.7	264.5	267.2	275.5	272.7	271.4	268.6	259.0	253.5	-	-	-
15	166.4	208.8	232.6	242.2	267.2	270.0	278.4	275.6	274.2	271.4	261.6	256.1	247.7	-	-
16	164.7	206.8	231.9	244.6	270.0	272.8	281.2	278.4	277.0	274.2	264.3	258.7	250.3	244.6	-
17	162.5	205.5	229.7	247.1	272.7	275.5	284.1	281.2	279.8	276.9	267.0	261.3	252.8	247.1	238.6
18	160.2	204.2	227.5	246.1	274.5	277.4	286.0	283.1	281.7	278.8	268.8	263.1	254.5	248.8	240.2
19	158.5	202.2	226.0	245.1	277.2	280.1	288.8	286.9	284.5	281.6	271.5	265.7	257.0	251.3	242.6
20	156.8	200.2	224.6	244.2	280.0	282.9	291.7	288.7	287.3	284.4	274.2	268.3	259.6	253.7	245.0
21	154.9	198.2	222.4	243.2	281.8	284.7	293.6	290.6	289.1	286.2	275.9	270.1	261.3	255.4	246.6
22	153.9	196.2	220.2	242.3	280.3	286.6	295.5	293.4	291.0	288.1	277.7	271.8	263.0	257.0	248.2
23	153.0	194.2	218.0	241.3	279.3	289.4	298.3	295.3	293.8	290.8	280.4	274.4	265.5	259.5	250.6
24	152.0	192.2	215.8	240.4	278.4	287.9	301.1	298.0	296.5	293.5	283.0	277.0	267.9	261.9	252.9
25	151.1	189.5	213.6	239.4	277.4	286.9	302.1	299.1	297.6	294.5	284.0	277.9	268.9	262.8	253.8
26	150.1	186.9	211.4	238.5	276.5	286.0	301.2	301.0	298.5	293.6	285.0	278.4	269.8	263.2	254.6
27	148.9	184.9	208.5	237.5	275.5	285.0	298.3	298.2	299.2	290.8	286.0	279.3	270.3	263.6	255.1
28	147.4	182.9	205.6	236.6	274.6	284.1	295.5	294.4	292.9	288.1	286.9	280.3	270.8	264.1	255.6
29	146.2	180.5	203.4	235.6	273.6	283.1	293.6	290.6	289.1	286.2	287.9	281.2	271.2	264.6	256.0
30	144.5	178.6	201.2	234.7	272.7	282.2	291.7	288.7	287.3	284.4	288.8	282.2	271.7	265.1	256.5
31	143.5	176.7	198.6	233.7	271.7	281.2	288.8	285.9	284.5	281.6	289.8	283.1	272.2	265.5	257.0
32	142.5	174.8	196.7	232.8	270.8	280.3	286.0	283.1	281.7	278.8	290.7	284.1	272.7	266.0	257.5
33	141.6	172.9	194.8	231.8	269.8	279.3	283.1	280.3	278.9	276.0	291.7	285.0	273.1	266.5	257.9
34	139.9	171.0	192.9	230.9	268.9	278.4	280.3	277.4	276.0	273.2	292.6	286.0	273.6	267.0	258.4
35	138.7	169.1	191.0	229.9	267.9	277.4	279.3	276.5	275.1	272.3	293.6	286.9	274.1	267.4	258.9
36	137.6	167.2	189.1	229.0	267.0	276.5	278.4	275.6	274.2	271.4	294.5	287.9	274.6	267.9	259.4
37	136.0	165.3	187.2	228.0	266.0	275.5	277.4	274.6	273.2	270.5	295.5	288.8	275.0	268.4	259.8
38	134.9	163.4	185.3	227.1	265.1	274.6	276.5	273.7	272.3	269.5	296.4	289.8	275.5	268.9	260.3
39	134.0	161.5	183.4	226.1	264.1	273.6	275.5	272.7	271.4	268.6	294.5	287.9	273.6	267.0	257.5
40	133.0	159.6	181.5	225.2	263.2	272.7	274.6	271.8	270.4	267.7	292.6	286.0	271.7	263.2	254.6

Table 6-8: Summary of gear ratios for different inner and outer rotor magnet pole-pair combinations for OD=230 and 300 mm

Outer rotor pole-pairs, p_3	Inner rotor pole-pairs, p_1															
	2	3	4	5	6	7	8	9	10	11	12	13	14	15	16
10	6.0	4.3	3.5	3.0	2.7	2.4	2.3	2.1	-	-	-	-	-	-	-
11	6.5	4.7	3.8	3.2	2.8	2.6	2.4	2.2	2.1	-	-	-	-	-	-
12	7.0	5.0	4.0	3.4	3.0	2.7	2.5	2.3	2.2	2.1	-	-	-	-	-
13	7.5	5.3	4.3	3.6	3.2	2.9	2.6	2.4	2.3	2.2	2.1	-	-	-	-
14	8.0	5.7	4.5	3.8	3.3	3.0	2.8	2.6	2.4	2.3	2.2	2.1	-	-	-
15	8.5	6.0	4.8	4.0	3.5	3.1	2.9	2.7	2.5	2.4	2.3	2.2	2.1	-	-
16	9.0	6.3	5.0	4.2	3.7	3.3	3.0	2.8	2.6	2.5	2.3	2.2	2.1	2.1	-
17	9.5	6.7	5.3	4.4	3.8	3.4	3.1	2.9	2.7	2.5	2.4	2.3	2.2	2.1	2.1
18	10.0	7.0	5.5	4.6	4.0	3.6	3.3	3.0	2.8	2.6	2.5	2.4	2.3	2.2	2.1
19	10.5	7.3	5.8	4.8	4.2	3.7	3.4	3.1	2.9	2.7	2.6	2.5	2.4	2.3	2.2
20	11.0	7.7	6.0	5.0	4.3	3.9	3.5	3.2	3.0	2.8	2.7	2.5	2.4	2.3	2.3
21	11.5	8.0	6.3	5.2	4.5	4.0	3.6	3.3	3.1	2.9	2.8	2.6	2.5	2.4	2.3
22	12.0	8.3	6.5	5.4	4.7	4.1	3.8	3.4	3.2	3.0	2.8	2.7	2.6	2.5	2.4
23	12.5	8.7	6.8	5.6	4.8	4.3	3.9	3.6	3.3	3.1	2.9	2.8	2.6	2.5	2.4
24	13.0	9.0	7.0	5.8	5.0	4.4	4.0	3.7	3.4	3.2	3.0	2.8	2.7	2.6	2.5
25	13.5	9.3	7.3	6.0	5.2	4.6	4.1	3.8	3.5	3.3	3.1	2.9	2.8	2.7	2.6
26	14.0	9.7	7.5	6.2	5.3	4.7	4.3	3.9	3.6	3.4	3.2	3.0	2.9	2.7	2.6
27	14.5	10.0	7.8	6.4	5.5	4.9	4.4	4.0	3.7	3.5	3.3	3.1	2.9	2.8	2.7
28	15.0	10.3	8.0	6.6	5.7	5.0	4.5	4.1	3.8	3.5	3.3	3.2	3.0	2.9	2.8
29	15.5	10.7	8.3	6.8	5.8	5.1	4.6	4.2	3.9	3.6	3.4	3.2	3.1	2.9	2.8
30	16.0	11.0	8.5	7.0	6.0	5.3	4.8	4.3	4.0	3.7	3.5	3.3	3.1	3.0	2.9
31	16.5	11.3	8.8	7.2	6.2	5.4	4.9	4.4	4.1	3.8	3.6	3.4	3.2	3.1	2.9
32	17.0	11.7	9.0	7.4	6.3	5.6	5.0	4.6	4.2	3.9	3.7	3.5	3.3	3.1	3.0
33	17.5	12.0	9.3	7.6	6.5	5.7	5.1	4.7	4.3	4.0	3.8	3.5	3.4	3.2	3.1
34	18.0	12.3	9.5	7.8	6.7	5.9	5.3	4.8	4.4	4.1	3.8	3.6	3.4	3.3	3.1
35	18.5	12.7	9.8	8.0	6.8	6.0	5.4	4.9	4.5	4.2	3.9	3.7	3.5	3.3	3.2
36	19.0	13.0	10.0	8.2	7.0	6.1	5.5	5.0	4.6	4.3	4.0	3.8	3.6	3.4	3.3
37	19.5	13.3	10.3	8.4	7.2	6.3	5.6	5.1	4.7	4.4	4.1	3.8	3.6	3.5	3.3
38	20.0	13.7	10.5	8.6	7.3	6.4	5.8	5.2	4.8	4.5	4.2	3.9	3.7	3.5	3.4
39	20.5	14.0	10.8	8.8	7.5	6.6	5.9	5.3	4.9	4.5	4.3	4.0	3.8	3.6	3.4
40	21.0	14.3	11.0	9.0	7.7	6.7	6.0	5.4	5.0	4.6	4.3	4.1	3.9	3.7	3.5

Table 6-9: Summary of volumetric torque density values for different inner and outer rotor magnet pole-pair combinations for OD=300 mm

Outer rotor pole pairs, p_3 \ Inner rotor pole pairs, p_1	2	3	4	5	6	7	8	9	10	11	12	13	14	15	16
10	179.4	217.0	228.5	244.8	265.0	268.7	276.0	279.8	-	-	-	-	-	-	-
11	181.4	219.0	230.0	245.6	268.8	271.6	280.0	283.9	294.2	-	-	-	-	-	-
12	180.4	221.1	231.5	248.1	272.7	275.5	284.0	288.1	298.4	290.9	-	-	-	-	-
13	178.2	221.8	233.7	249.7	275.5	278.4	287.0	291.1	301.5	292.9	269.8		-	-	-
14	176.4	221.1	235.9	251.4	277.4	280.3	289.0	293.2	303.6	294.9	271.7	265.9	-	-	-
15	174.6	219.0	236.7	254.0	280.3	283.2	292.0	296.3	306.8	296.9	274.5	268.6	259.9	-	-
16	172.8	217.0	235.1	256.6	283.2	286.1	295.0	299.3	309.9	300.8	277.3	271.4	262.5	256.6	-
17	170.4	215.6	232.8	259.2	286.1	289.0	298.0	302.4	313.0	302.8	280.1	274.1	265.2	259.2	250.3
18	168.0	214.2	231.5	258.1	288.0	291.0	300.0	304.5	315.1	305.6	282.0	276.0	267.0	261.0	252.0
19	166.2	212.1	230.0	257.1	290.8	293.9	303.0	307.6	318.3	308.6	284.8	278.7	269.6	263.6	254.5
20	164.4	210.0	228.5	256.1	291.9	296.8	305.9	310.6	321.4	312.4	287.6	281.5	272.3	266.2	257.0
21	164.2	207.9	226.3	255.1	292.9	298.7	307.9	312.7	323.5	313.4	289.5	283.3	274.1	267.9	258.7
22	161.4	205.8	224.0	254.1	294.0	300.6	309.9	314.7	325.6	316.3	291.3	285.1	275.8	269.6	260.3
23	160.4	203.7	221.8	253.1	293.0	303.5	312.9	317.8	328.8	319.2	294.1	287.9	278.5	272.2	262.9
24	159.4	201.6	219.6	252.1	292.0	302.0	315.8	320.8	330.8	322.1	296.9	290.5	281.1	274.8	265.3
25	158.5	198.8	217.3	251.1	291.0	301.0	316.9	321.9	330.9	324.0	297.9	291.6	282.0	275.7	266.2
26	157.5	196.0	215.1	250.1	290.0	300.0	315.9	322.4	331.9	325.3	299.0	292.0	283.0	276.0	267.1
27	156.2	193.9	213.0	249.1	289.0	299.0	312.9	323.4	332.9	327.2	300.0	293.0	283.5	276.5	267.6
28	154.7	191.8	211.8	248.1	288.0	298.0	311.7	324.4	333.8	329.1	301.0	294.0	284.0	277.0	268.1
29	153.4	189.3	209.6	247.1	287.0	297.0	310.6	322.4	334.8	327.4	302.0	295.0	284.5	277.5	268.6
30	151.6	187.4	208.3	246.1	286.0	296.0	308.6	320.4	335.8	326.6	303.0	296.0	285.0	278.0	269.1
31	150.5	185.4	206.5	245.2	285.0	295.0	305.6	318.4	336.8	325.8	304.0	297.0	285.5	278.5	269.6
32	149.5	183.4	205.5	244.2	284.0	294.0	304.5	316.4	338.4	325.0	304.9	298.0	286.0	279.0	270.1
33	148.5	181.4	203.6	243.2	283.0	293.0	303.3	314.4	340.0	323.3	305.9	299.0	286.5	279.5	270.6
34	146.8	179.4	201.6	242.2	282.0	292.0	301.2	312.4	338.0	323.1	306.9	300.0	287.0	280.0	271.1
35	145.5	177.4	199.7	241.2	281.0	291.0	299.3	310.4	335.9	321.1	307.9	301.0	287.5	280.5	271.6
36	144.3	175.4	197.8	240.2	280.0	290.0	297.4	308.4	334.8	319.1	308.9	302.0	288.0	281.0	272.1
37	142.7	173.4	195.8	239.2	279.0	289.0	295.5	306.4	333.6	317.1	309.9	303.0	288.5	281.5	272.6
38	141.5	171.4	194.8	238.2	278.0	288.0	293.6	304.4	331.5	315.1	310.9	304.0	289.0	282.0	273.1
39	140.5	169.4	192.9	237.2	277.0	287.0	292.6	302.5	330.3	313.1	308.9	302.0	287.0	280.0	270.1
40	138.6	167.4	191.8	236.2	276.0	286.0	290.7	300.5	328.2	311.1	306.9	300.0	285.0	276.0	267.1

Table 6-10: Summary of volumetric torque density values for different inner and outer rotor magnet pole-pair combinations for OD=350 mm

Inner rotor pole pairs, p_1

Outer rotor pole-pairs, p_3	2	3	4	5	6	7	8	9	10	11	12	13	14	15	16
10	205.0	248.0	261.2	279.9	302.9	307.1	315.5	313.5							
11	207.3	250.4	262.9	280.8	307.3	310.5	320.1	318.0	324.6						
12	206.2	252.7	264.6	283.6	311.7	314.9	324.7	322.6	329.3	332.5					
13	203.7	253.6	267.2	285.4	315.0	318.2	328.1	326.0	332.8	334.9	344.7				
14	201.6	252.8	269.6	287.4	317.1	320.4	330.4	328.3	335.1	337.1	347.1	303.9			
15	199.6	250.4	270.6	288.4	320.4	323.8	333.8	331.7	338.7	339.4	350.7	307.1	297.1		
16	197.5	248.0	271.7	289.4	323.7	327.1	337.2	335.1	342.2	343.8	354.2	310.2	300.1	293.4	
17	194.8	246.4	272.2	289.9	327.0	330.4	340.6	338.6	345.7	346.1	357.8	313.4	303.1	296.3	286.1
18	192.1	244.8	273.6	290.3	329.2	332.6	342.9	340.8	348.0	349.4	360.2	315.5	305.2	298.3	288.0
19	190.0	242.4	274.9	290.9	332.4	335.9	343.3	341.2	351.6	352.7	363.8	318.6	308.2	301.3	290.9
20	188.0	240.0	275.2	291.3	333.7	339.2	344.7	342.7	355.1	357.1	367.4	321.7	311.2	304.3	293.8
21	187.7	237.6	276.7	291.8	334.8	340.4	346.0	343.9	357.4	358.3	369.8	323.8	313.3	306.2	295.7
22	184.5	235.2	277.1	292.5	335.0	341.6	346.3	344.2	359.8	361.6	372.2	325.9	315.3	308.2	297.6
23	183.4	232.8	278.5	293.3	335.5	342.0	347.7	344.6	360.3	361.9	375.8	329.1	318.3	311.2	300.5
24	182.3	230.4	280.0	294.2	335.9	342.2	349.0	344.9	361.7	362.1	378.1	332.1	321.3	314.1	303.2
25	181.1	227.3	280.4	295.1	336.6	342.5	349.2	345.2	363.0	363.4	378.3	333.3	322.4	315.2	304.3
26	180.0	224.1	281.9	296.9	336.9	343.0	349.5	345.8	363.5	364.8	379.3	333.8	323.5	315.5	305.3
27	178.5	221.7	281.2	297.8	337.4	343.7	350.1	346.2	364.1	366.0	380.5	334.9	324.1	316.1	305.9
28	176.8	219.3	279.2	298.6	337.7	344.6	350.4	346.6	364.6	366.2	381.6	336.0	324.7	316.7	306.4
29	175.3	216.4	277.6	299.5	338.3	345.5	351.1	347.0	364.9	367.2	382.8	337.2	325.2	317.3	307.0
30	173.3	214.2	276.1	300.4	339.5	345.9	351.8	347.4	365.2	368.7	383.9	338.3	325.8	317.8	307.6
31	172.0	211.9	275.1	301.2	340.5	346.2	352.1	347.9	365.6	370.2	385.0	339.5	326.4	318.4	308.1
32	171.2	210.0	274.2	302.4	341.6	346.9	352.5	348.5	365.9	372.3	386.2	340.6	327.5	319.5	309.3
33	170.3	209.2	273.4	303.5	342.8	347.5	353.0	349.6	366.3	373.5	387.3	341.8	328.7	320.7	310.4
34	169.5	208.3	272.5	304.7	343.9	348.7	353.8	350.8	367.4	374.6	388.5	342.9	329.8	321.9	311.6
35	168.6	207.5	271.7	305.8	344.1	349.2	355.0	351.9	368.6	375.8	389.6	344.1	331.0	323.0	312.8
36	167.8	206.7	270.8	306.0	345.2	350.0	355.2	353.1	369.7	376.9	390.8	345.2	332.1	324.2	313.9
37	166.9	205.8	270.0	307.2	346.4	350.3	356.3	354.3	370.9	378.1	392.0	346.4	333.3	325.3	315.1
38	165.1	205.0	268.2	308.3	347.5	351.3	357.5	355.4	372.0	379.2	393.1	347.5	334.4	326.5	316.2
39	164.2	203.1	267.3	309.5	348.7	352.4	358.6	356.6	373.2	380.4	394.3	348.7	335.6	327.6	317.4
40	163.3	202.2	266.4	308.5	347.8	351.5	356.7	354.6	371.3	378.5	392.3	346.8	333.7	325.7	315.5
41	162.6	201.4	265.6	307.8	347.0	350.7	355.9	353.9	370.5	377.7	391.6	346.0	332.9	325.0	314.7
42	161.8	200.7	264.9	307.0	346.3	350.0	355.2	353.1	369.8	377.0	390.8	345.3	332.2	324.2	314.0
43	161.1	199.9	264.1	306.3	345.5	349.2	354.4	352.4	369.0	376.2	390.1	344.5	331.4	323.5	313.2
44	160.3	199.2	263.4	305.5	344.8	348.5	353.7	351.6	368.3	375.5	389.3	343.8	330.7	322.7	312.5
45	159.6	198.4	262.6	304.8	344.0	347.7	352.9	350.9	367.5	374.7	388.6	343.0	329.9	322.0	311.7
46	158.8	197.7	261.9	304.0	343.3	347.0	352.2	350.1	366.8	374.0	387.8	342.3	329.2	321.2	311.0
47	158.1	196.9	261.1	303.3	342.5	346.2	351.4	349.4	366.0	373.2	387.1	341.5	328.4	320.5	310.2
48	157.3	196.2	260.4	302.5	341.8	345.5	350.7	348.6	365.3	372.5	386.3	340.8	327.7	319.7	309.5
49	156.6	195.4	259.6	301.8	341.0	344.7	349.9	347.9	364.5	371.7	385.6	340.0	326.9	319.0	308.7
50	155.8	194.7	258.9	301.0	340.3	344.0	349.2	347.1	363.8	371.0	384.8	339.3	326.2	318.2	308.0

Table 6-11: Summary of volumetric torque density values for different inner and outer rotor magnet pole-pair combinations for OD=400 mm

Inner rotor pole pairs, p_1

Outer rotor pole-pairs, p_3	Inner rotor pole pairs, p_1														
	2	3	4	5	6	7	8	9	10	11	12	13	14	15	16
10	231.7	280.2	295.1	316.2	342.3	347.0	356.5	354.2	-	-	-	-	-	-	-
11	234.3	282.9	297.1	317.2	347.2	350.8	361.7	359.4	366.7	-	-	-	-	-	-
12	233.0	285.5	299.0	320.4	352.1	355.8	366.8	364.5	372.0	375.7	-	-	-	-	-
13	232.0	286.5	301.9	322.5	355.9	359.6	370.7	368.4	376.0	378.3	389.4	-	-	-	-
14	231.5	285.6	304.6	324.7	358.3	362.1	373.3	370.9	378.7	380.9	392.1	343.4	-	-	-
15	230.1	284.7	305.7	328.1	362.0	365.8	377.1	374.8	382.6	383.5	396.2	346.9	335.6	-	-
16	229.6	283.9	303.6	331.5	365.7	369.5	381.0	378.7	386.6	388.4	400.3	350.5	339.1	331.5	-
17	228.3	283.0	301.6	334.8	369.4	373.3	384.8	382.5	390.6	391.1	404.3	354.1	342.5	334.8	323.3
18	227.1	282.1	300.8	333.4	371.9	375.8	387.4	385.1	393.2	394.7	407.0	356.4	344.8	337.1	325.4
19	224.8	281.2	299.8	332.1	375.6	379.5	391.3	389.0	397.2	398.5	411.1	360.0	348.2	340.4	328.7
20	223.4	280.4	298.8	330.8	377.0	383.3	395.1	392.8	401.2	403.5	415.1	363.5	351.7	343.8	331.9
21	221.3	278.6	298.7	329.5	378.3	385.8	397.7	395.4	403.8	404.8	417.8	365.9	354.0	346.0	334.1
22	219.5	277.7	297.6	328.2	379.7	388.3	400.3	398.0	406.5	408.5	420.5	368.3	356.3	348.2	336.2
23	217.3	276.8	296.6	327.8	378.2	392.0	404.1	401.8	410.5	412.3	424.6	371.8	359.7	351.6	339.5
24	216.9	276.0	295.5	326.6	376.8	390.0	407.9	405.6	414.3	416.0	427.2	375.2	363.0	354.9	342.6
25	214.7	275.1	293.5	325.3	376.3	388.7	409.3	407.0	415.8	418.5	427.4	376.6	364.3	356.1	343.8
26	213.4	274.2	291.6	324.9	374.1	387.4	408.0	405.7	416.4	420.1	428.6	377.1	365.5	356.5	344.9
27	210.8	273.4	289.8	323.6	372.7	386.1	404.1	401.8	417.7	422.6	429.9	378.4	366.2	357.2	345.6
28	208.9	272.5	288.3	323.2	371.3	384.8	402.6	400.3	418.9	425.0	431.2	379.7	366.8	357.8	346.2
29	207.2	270.2	286.3	321.9	370.8	384.5	402.1	398.9	418.2	422.8	432.5	381.0	367.5	358.5	346.9
30	205.8	267.5	284.6	321.6	369.5	383.2	400.4	398.1	417.5	422.2	433.8	382.3	367.7	358.5	347.1
31	203.4	265.7	282.2	320.7	368.3	383.0	399.9	397.6	416.0	421.9	433.8	382.3	367.7	358.6	347.2
32	202.5	262.9	280.4	320.2	367.4	382.5	399.5	397.4	415.0	421.6	433.9	382.4	367.8	358.7	347.3
33	201.6	261.1	278.5	319.8	366.5	382.3	399.0	397.2	414.6	421.4	434.0	382.5	367.9	358.8	347.4
34	199.7	259.3	276.7	319.3	365.6	382.1	398.5	396.8	414.1	421.1	434.1	382.6	367.9	358.9	347.5
35	198.8	256.5	274.9	318.8	364.6	381.9	398.1	396.5	413.7	420.8	434.2	382.7	368.0	359.0	347.6
36	197.9	253.8	273.0	318.4	363.7	381.6	397.6	396.2	413.2	420.5	434.3	382.9	368.1	359.1	347.7
37	197.0	251.0	271.2	317.9	362.8	381.1	397.2	395.8	412.7	420.2	434.4	383.0	368.2	359.2	347.8
38	196.1	247.4	269.4	317.0	361.9	381.0	396.7	394.9	412.3	419.8	434.5	383.2	368.3	359.3	347.9
39	195.2	244.6	268.4	317.5	361.0	380.6	395.8	394.0	411.8	419.6	434.6	383.2	368.4	359.4	348.0
40	194.7	241.9	267.5	316.1	360.1	380.2	394.9	393.0	411.4	419.4	434.7	383.3	367.6	359.6	348.1
41	194.4	239.4	266.7	316.6	359.8	379.3	394.8	392.4	411.2	418.9	435.0	383.6	368.8	359.7	348.2
42	193.1	236.8	265.4	315.3	357.5	379.7	393.2	390.9	408.6	418.6	432.5	384.8	369.4	360.4	348.8
43	191.8	234.3	262.9	314.1	355.2	378.4	391.7	389.4	406.1	419.9	429.9	386.1	370.0	361.0	349.4
44	189.6	231.7	260.4	312.8	353.9	377.1	389.0	386.6	403.5	417.3	427.3	387.4	370.7	361.7	350.1
45	187.9	229.1	257.9	311.5	351.6	375.8	386.5	384.2	400.9	414.7	423.5	388.7	371.3	362.3	350.7
46	186.4	226.5	255.4	310.2	349.2	374.5	384.1	381.8	398.3	412.1	419.6	390.0	372.0	363.0	351.4
47	184.3	224.0	252.9	308.9	346.9	373.3	381.6	379.3	395.8	409.6	415.7	391.3	372.6	363.6	352.0
48	182.8	221.4	251.6	307.6	345.6	372.0	379.2	376.9	393.2	407.0	411.9	392.6	373.3	364.2	352.7
49	181.5	218.8	249.1	306.3	343.3	370.7	377.9	375.6	390.6	404.4	408.0	390.0	370.7	361.7	348.8
50	179.0	216.2	247.7	305.0	341.0	369.4	375.4	373.1	388.1	401.8	404.1	387.4	368.1	356.5	344.9

Table 6-12: Summary of gear ratios for different inner and outer rotor magnet pole-pair combinations for OD=350 and 400 mm

	Inner rotor pole-pairs, p_1															
		2	3	4	5	6	7	8	9	10	11	12	13	14	15	16
Outer rotor pole-pairs, p_3	10	6.00	4.33	3.50	3.00	2.67	2.43	2.25	2.11	-	-	-	-	-	-	-
	11	6.50	4.67	3.75	3.20	2.83	2.57	2.38	2.22	2.10	-	-	-	-	-	-
	12	7.00	5.00	4.00	3.40	3.00	2.71	2.50	2.33	2.20	2.09	-	-	-	-	-
	13	7.50	5.33	4.25	3.60	3.17	2.86	2.63	2.44	2.30	2.18	2.08	-	-	-	-
	14	8.00	5.67	4.50	3.80	3.33	3.00	2.75	2.56	2.40	2.27	2.17	2.08	-	-	-
	15	8.50	6.00	4.75	4.00	3.50	3.14	2.88	2.67	2.50	2.36	2.25	2.15	2.07	-	-
	16	9.00	6.33	5.00	4.20	3.67	3.29	3.00	2.78	2.60	2.45	2.33	2.23	2.14	2.07	-
	17	9.50	6.67	5.25	4.40	3.83	3.43	3.13	2.89	2.70	2.55	2.42	2.31	2.21	2.13	2.06
	18	10.00	7.00	5.50	4.60	4.00	3.57	3.25	3.00	2.80	2.64	2.50	2.38	2.29	2.20	2.13
	19	10.50	7.33	5.75	4.80	4.17	3.71	3.38	3.11	2.90	2.73	2.58	2.46	2.36	2.27	2.19
	20	11.00	7.67	6.00	5.00	4.33	3.86	3.50	3.22	3.00	2.82	2.67	2.54	2.43	2.33	2.25
	21	11.50	8.00	6.25	5.20	4.50	4.00	3.63	3.33	3.10	2.91	2.75	2.62	2.50	2.40	2.31
	22	12.00	8.33	6.50	5.40	4.67	4.14	3.75	3.44	3.20	3.00	2.83	2.69	2.57	2.47	2.38
	23	12.50	8.67	6.75	5.60	4.83	4.29	3.88	3.56	3.30	3.09	2.92	2.77	2.64	2.53	2.44
	24	13.00	9.00	7.00	5.80	5.00	4.43	4.00	3.67	3.40	3.18	3.00	2.85	2.71	2.60	2.50
	25	13.50	9.33	7.25	6.00	5.17	4.57	4.13	3.78	3.50	3.27	3.08	2.92	2.79	2.67	2.56
	26	14.00	9.67	7.50	6.20	5.33	4.71	4.25	3.89	3.60	3.36	3.17	3.00	2.86	2.73	2.63
	27	14.50	10.00	7.75	6.40	5.50	4.86	4.38	4.00	3.70	3.45	3.25	3.08	2.93	2.80	2.69
	28	15.00	10.33	8.00	6.60	5.67	5.00	4.50	4.11	3.80	3.55	3.33	3.15	3.00	2.87	2.75
	29	15.50	10.67	8.25	6.80	5.83	5.14	4.63	4.22	3.90	3.64	3.42	3.23	3.07	2.93	2.81
	30	16.00	11.00	8.50	7.00	6.00	5.29	4.75	4.33	4.00	3.73	3.50	3.31	3.14	3.00	2.88
	31	16.50	11.33	8.75	7.20	6.17	5.43	4.88	4.44	4.10	3.82	3.58	3.38	3.21	3.07	2.94
	32	17.00	11.67	9.00	7.40	6.33	5.57	5.00	4.56	4.20	3.91	3.67	3.46	3.29	3.13	3.00
	33	17.50	12.00	9.25	7.60	6.50	5.71	5.13	4.67	4.30	4.00	3.75	3.54	3.36	3.20	3.06
	34	18.00	12.33	9.50	7.80	6.67	5.86	5.25	4.78	4.40	4.09	3.83	3.62	3.43	3.27	3.13
	35	18.50	12.67	9.75	8.00	6.83	6.00	5.38	4.89	4.50	4.18	3.92	3.69	3.50	3.33	3.19
	36	19.00	13.00	10.00	8.20	7.00	6.14	5.50	5.00	4.60	4.27	4.00	3.77	3.57	3.40	3.25
	37	19.50	13.33	10.25	8.40	7.17	6.29	5.63	5.11	4.70	4.36	4.08	3.85	3.64	3.47	3.31
	38	20.00	13.67	10.50	8.60	7.33	6.43	5.75	5.22	4.80	4.45	4.17	3.92	3.71	3.53	3.38
	39	20.50	14.00	10.75	8.80	7.50	6.57	5.88	5.33	4.90	4.55	4.25	4.00	3.79	3.60	3.44
	40	21.00	14.33	11.00	9.00	7.67	6.71	6.00	5.44	5.00	4.64	4.33	4.08	3.86	3.67	3.50
	41	21.50	14.67	11.25	9.20	7.83	6.86	6.13	5.56	5.10	4.73	4.42	4.15	3.93	3.73	3.56
	42	22.00	15.00	11.50	9.40	8.00	7.00	6.25	5.67	5.20	4.82	4.50	4.23	4.00	3.80	3.63
	43	22.50	15.33	11.75	9.60	8.17	7.14	6.38	5.78	5.30	4.91	4.58	4.31	4.07	3.87	3.69
	44	23.00	15.67	12.00	9.80	8.33	7.29	6.50	5.89	5.40	5.00	4.67	4.38	4.14	3.93	3.75
	45	23.50	16.00	12.25	10.00	8.50	7.43	6.63	6.00	5.50	5.09	4.75	4.46	4.21	4.00	3.81
	46	24.00	16.33	12.50	10.20	8.67	7.57	6.75	6.11	5.60	5.18	4.83	4.54	4.29	4.07	3.88
	47	24.50	16.67	12.75	10.40	8.83	7.71	6.88	6.22	5.70	5.27	4.92	4.62	4.36	4.13	3.94
	48	25.00	17.00	13.00	10.60	9.00	7.86	7.00	6.33	5.80	5.36	5.00	4.69	4.43	4.20	4.00
	49	25.50	17.33	13.25	10.80	9.17	8.00	7.13	6.44	5.90	5.45	5.08	4.77	4.50	4.27	4.06
	50	26.00	17.67	13.50	11.00	9.33	8.14	7.25	6.56	6.00	5.55	5.17	4.85	4.57	4.33	4.13

CHAPTER 7 : CONCLUSIONS AND FUTURE SCOPE

7.1. Conclusions

The operating principle of a MG has been analyzed in detail. The field distribution in the air-gaps of the FFMG have been derived and analyzed to study the effects of the spatial harmonics and modulation effect of the cage rotor steel poles. A Flux-focusing rotor design approach was adopted wherein the magnets in the inner and outer rotors are arranged in a flux-concentrating position also called spoke-type arrangement. This gives a natural flux concentration capability because two circumferentially magnetized PMs are buried between the steel cores.

The software package JMAG was used to conduct the 2-D and 3-D static and transient FEA models. Design, construction and experimental evaluation of a sub-scale coaxial FFMG with an outer diameter of 110 mm was performed when using ferrite and NdFeB magnets. The magnetic forces on the cage rotor steel poles resulting from the magnets on the inner and outer rotors has a bending effect on the steel poles of the cage rotor. To study this deflection an iterative magnetomechanical analysis technique was proposed that used the structural analysis component of the JMAG software. The power losses resulting from the induced eddy-currents was studied using transient FEA and the efficiencies were calculated at various speeds. These calculations were experimentally verified. It was shown that when using ferrite magnets, the magnets would experience cyclic demagnetization due to the rotating magnetic fields. This effect was studied using

FEA. It was however observed that the demagnetization was limited to the corners of the magnets nearest to the air-gap.

A scaled-up FFMG with a diameter of 228 mm was designed, constructed and tested. The size of the sub-scale FFMG was doubled along with the number of pole-pairs on the inner and outer rotor in order to study how the torque density values would vary as the diameter of the FFMG increased. Analysis analogous to the sub-scale model was performed to study the deflection of the cage rotor steel poles, the power loss, efficiency and torque ripple at various loads and speeds was measured.

An analytical FFMG model was developed using the magnetic vector potential. The separation of variables method was utilized. The applicable Laplace and Poisson's equations were solved in each region by using the applicable boundary and interface conditions. The results of the analytical model were then compared with ideal and non-linear FEA models. The results obtained were very close to the ideal FEA model. However, the computational time for the analytical model was very low compared to the FEA model. It is demonstrated that the derived analytic based model is a valuable tool for the initial parameter selection and scaling analysis of the FFMG.

7.1.1. Key Research Achievements

The key achievements of this research are:

- The design, construction and experimental evaluation of a sub-scale FFMG with an active volumetric torque density of 151.4 Nm/L. Three sub-scale designs with ferrite, NdFeB and a combination of ferrite and NdFeB magnets were constructed and verified.

- A magnetomechanical analysis technique was developed that was used to study the deflection effects of the cage rotor steel poles due to the magnetic forces created by the inner and outer rotor magnets.
- A scaled-up FFMG was designed, constructed and experimentally evaluated. A design with ferrite and NdFeB magnets was studied. The NdFeB magnet FFMG design was experimentally demonstrated to operate with an active volumetric torque density of 238.7 Nm/L. A summary of the sub-scale and scaled-up FFMG performance metrics is given in Table 7-1.
- An accurate analytical based model using a Fourier harmonic approach was developed for the FFMG. The models calculated values were shown to be in agreement with the ideal FEA model results and will be a useful tool for scaling and initial parameter variation analysis of the FFMG.

Table 7-1: Summary of experimental performance metrics

	Type	**Torque [Nm]**	**Volume torque-density [Nm/L]**	**Mass torque density [Nm/kg]**	**Torque-per-kg of magnet [Nm/kg]**
Sub-scale design	Ferrite	25	33	4.5	14.6
	Hybrid	48	66.3	8	24.2
	NdFeB	113.5	151.2	17.4	44.6
Scaled up design	Ferrite (FEA)	282.6	92.3	16.6	51.2
	NdFeB	731	238.7	35.2	87.8

7.2. Recommendations for Future Work

Although MG research has picked up over the last decade, more research has to be conducted before MGs can be adopted by industry. Some recommendations for further research are:

- Thermal analysis has to be conducted in order to study the effect of the increasing temperatures on the magnets due to continuous operation. Although there is no current flowing in the rotors, the losses created by the induced eddy currents will result in the FFMG heating up and this could result in the demagnetization of the magnets.
- Multi-stage MGs have to be studied in order to achieve a higher gear-ratio while maintaining a high torque density.
- Control systems need to be developed to prevent the rotors from slipping when over-loaded, and if slippage occurs, the control technique must be robust so as to enable the MG to recover from the pole slippage condition.

BIBLIOGRAPHY

[1] OECD/IEA. (2013) Medium-term renewable energy market report 2013.

[2] R. Wiser and M. Bolinger, "2013 Wind Technologies Market Report," U.S. Department of Energy2014.

[3] M. Moyeed, "Wind Energy-The Worlds Fastest Growing Renewable Energy Resource-An Overview," *International Journal of Scientific & Engineering Research,* vol. 5, 2014.

[4] F. Rasmussen*, et al.*, "The Gearbox Problem Revisited," in *Riso fact Sheet AED-RB-17(EN), Riso National Laboratory*, Roskilde, DK, 2004.

[5] W. Musial*, et al.*, "Improving Wind Turbine Gearbox Reliability," *National Renewable Energy Laboratory,* vol. NREL/CP-500-41548, 2007.

[6] M. R. Adam M. Ragheb, *Wind Turbine Gearbox Technologies, Fundamental and Advanced Topics in Wind Power*, 2011.

[7] J. V. Rensselar, "The elephant in the wind turbine," *Tribology Lubrication Technology,* pp. 2-12, 2010.

[8] J. Puigcorbe and A. Beaumont. (2010, June 03, 2010) Wind Turbine Gearbox Reliability : The impact of rotor support. *RenewableEnergyWorld*.

[9] I. D. Margaris, "Direct Drive Synchronous Generator Wind Turbine Models for Power System Studies " presented at the 7th Mediterranean Conference and Exhibition on Power Generation, Transmission, Distribution and Energy Conversion, Agia Napa, Cyprus, 2010.

[10] *http://www.mtorres.es/en/energia-eolica/historia*.

[11] C. Bratiloveanu and I. Boldea, "A comparative investigation of three PM-less MW power range wind generator topologies," in *Optimization of Electrical and Electronic Equipment (OPTIM), 2012 13th International Conference on*, 2012, pp. 535-543.

[12] D. Bang*, et al.*, "Review of Generator Systems for Direct-Drive Wind Turbines," in *European Wind Energy Conference and Exhibition*, Brussels, 2008.

[13] R.Henderson, "Design, simulation testing of a novel hydraulic power take-off system for the pelamis wave energy converter," *Renew. Energy,* vol. 31, pp. 271-283, 2006.

[14] H. Polinder and F. Gardner, "Linear PM Generator System for Wave Energy Conversion in the AWS," *IEEE Trans. on Energy conv.,* vol. 19, pp. 583-586, 2004.

[15] *www.marineturbines.com/Seagen-Technology*.

[16] *http://www.oceanlinx.com/technology/products/ogwave-2*.

[17] *https://www.awsocean.com*.

[18] W. Kappel*, et al.*, "High Energy Density Magnetic Materials for Electronic Packaging," in *1st Electronics Systemintegration Technology COnference*, 2006, pp. 337-342.

[19] D. Smith*, et al.*, "Shear stress concentrations in permanent magnet rotor sleeves," in *XIX Inter. Conf. on Elec.Machines (ICEM)*, 2010, pp. 1-6.

[20] C. Armstrong, "Power transmitting device," US Patent 687,292, 1901.

[21] H.Faus, "Magnet gearing," US Patent 2,243,555, May 27, 1941.

[22] S. Kikuchi and K. Tsurumoto, "Design and characteristics of a new magnetic worm gear using permanent magnet," *IEEE Trans. on Magnetics,* vol. 29, pp. 2923-2925, 1993.

[23] S. Kikuchi and K. Tsurumoto, "A new magentic gear using permanent magnet," *IEEE Trans. on Magnetics,* vol. 23, pp. 3622-3624, 1987.

[24] K. Tsurumoto, "Power transmission of magnetic gear using common meshing and insensibility to center distance," *IEEE Trans. on Magnetics, Japan,* vol. 3, pp. 588-589, 1988.

[25] K. Tsurumoto, "Some consideration on the improvement of performance characteristics of magnetic gear," *IEEE Trans. on Magnetics, Japan,* vol. 4, pp. 576-582, 1989.

[26] K. Tsurumoto*, et al.*, "Characteristics of the magnetic gear using a bulk high-Tc superconductor," *IEEE Trans. on Applied superconductivity,* vol. 12, pp. 979-983, March 2002.

[27] C. Huang*, et al.*, "Development of a magnetic planetary gearbox," *IEEE Trans. on Magnetics,* vol. 44, pp. 403-412, 2008.

[28] A. Neuland, "Apparatus for transmitting power," US Patent 1,717,351, 1916.

[29] G. Reese, "Magentic gearing arrangement " US Patent 3,301,091, 1967.

[30] J. Martin, "Magnetic transmission," US Patent 3,378,710, 1968.

[31] B. Ackermann and L. Honds, "Magnetic drive arrangement comprising a plurality of magnetically cooperating parts which are movable relative to one another," US Patent 5,633,555, 1997.

[32] B. Ackermann, "Magnetic drive arrangement " US Patent 5,994,809, 1999.

[33] K. Atallah and D. Howe, "A Novel High-Performance Magnetic Gear," *IEEE Trans. on Magnetics,* vol. 37, pp. 2844-2846, 2002.

[34] K. Atallah*, et al.*, "Design, analysis and realisation of a high-performance magnetic gear," *IEEE Proc.-Electr. Power Appl.,* vol. 151, pp. 135-143, 2004.

[35] P. O. Rasmussen*, et al.*, "Development of a high-performance magnetic gear," *IEEE Trans. on Ind. Appl.,* vol. 41, pp. 764-770, 2005.

[36] N. Frank and H. Toliyat, "Analysis of the Concentric Planetary Magnetic Gear With Strengthened Stator and Interior Permanent Magnet Inner Rotor," *IEEE Trans. on Ind. Appl.,* vol. 47, pp. 1652-1660, July 2011.

[37] N. Frank and H. Toliyat, "Gearing ratios of a magnetic gear for marine applications," in *IEEE Electric Ship Technologies Symposium, ESTS*, 2009, pp. 477-481.

[38] N. Frank and H. Toliyat, "Gearing ratios of a magnetic gear for wind turbines," in *IEEE International Electric Machines and Drives conference, IEMDC* 2009, pp. 1224-1230.

[39] K. Nakamura*, et al.*, "Performance improvement of magnetic gear and efficiency comparison with conventional mechanical gear," *Journal of Applied Physics,* vol. 115, 2014.

[40] X. Liu*, et al.*, "Design and analysis of interior-magnet outer-rotor concentric magnetic gears," *Journal of Appl. Physics* vol. 105, 07F101 2009.

[41] J. Linni*, et al.*, "Comparison of Coaxial Magnetic Gears With Different Topologies," *Magnetics, IEEE Transactions on,* vol. 45, pp. 4526-4529, 2009.

[42] K. Atallah and R. Holehouse, "Design and Realization of a Linear Magnetic Gear," *IEEE Trans. on Magnetics* vol. 47, 2011.

[43] S. Mezani*, et al.*, "A high-performance axial-field magnetic gear," *Journal of Appl. Physics 99,* vol. 08R303, 2006.

[44] V. M. Acharya*, et al.*, "A low torque ripple flux focusing axial magnetic gear," in *Power Electronics, Machines and Drives (PEMD 2014), 7th IET International Conference on* 2014, pp. 1-6.

[45] J. Rens*, et al.*, "A Novel Magnetic Harmonic Gear " *IEEE Trans. on Ind. Appl.,* vol. 46, pp. 206-212, 2010.

[46] F. Jorgensen*, et al.*, "The Cycloidal Permanent Magnetic Gear," *IEEE Trans. on Ind. Appl.,* vol. 44, 2008.

[47] K. Davey*, et al.*, "Axial Flux Cycloidal Magnetic Gears," *IEEE Trans. on Magnetics,* vol. 50, pp. 1-7, 2014.

[48] K. Atallah and J. Rens, "Electrical machines," WO Patent 125,284A1, 2007.

[49] K. Atallah*, et al.*, "A New PM Machine Topology for Low-Speed, High-Torque Drives," in *Proceedings of the 18th International Conference on Electrical Machines*, 2008, pp. 1-4.

[50] K. Atallah*, et al.*, "A Novel “Pseudo” Direct-Drive Brushless Permanent Magnet Machine," *IEEE Trans. on Magnetics,* vol. 44, pp. 4349-4352, 2008.

[51] P. O. Rasmussen*, et al.*, "Motor integrated permanent magnet gear with a wide torque-speed range," in *IEEE Energy Conversion Congress and Exposition, ECCE*, 2009, pp. 1510-1518.

[52] T. Frandsen*, et al.*, "Improved Motor Integrated Permanent Magnet Gear for Traction Applications," in *IEEE Energy Conversion Congress and Exposition (ECCE)*, 2012, pp. 3332-3339.

[53] T. Chau*, et al.*, "Transient analysis of coaxial magnetic gears using finite element comodeling," *Journal of Appl. Physics* vol. 103, 07F101 2008.

[54] T. Chau*, et al.*, "Design of a Magnetic-Geared Outer-Rotor Permanent-Magnet Brushless Motor for Electric Vehicles " *IEEE Trans. on Magnetics,* vol. 43, pp. 2504-2506, 2007.

[55] S. Du*, et al.*, "Research on a novel combined permanent magnet electrical machine," in *Electrical Machines and Systems (ICEMS), International Conference on*, 2008, pp. 3564-3567.

[56] P. Padmanathan and J. Bird, "A Continuously Variable Magnetic Gear," presented at the 9th IEEE International Machines and Drives Conference, Chicago, IL, 2013.

[57] N. Niguchi and K. Hirata, "Cogging Torque Analysis of Magnetic Gear," *IEEE Trans. on Ind. Elec.,* vol. 59, pp. 2189-2197, 2012.

[58] L. Bronn*, et al.*, "Development of a shutter type magnetic gear," in *Proceedings of the19th Southern African Univ. Power Eng. Conf., SAUPEC*, Johannesburg, 2010.

[59] L. Shah*, et al.*, "A Variable Speed Magnetic Gear Box Using Contra-Rotating Input Shafts," *IEEE Trans. on Magnetics,* vol. 47, pp. 431-438, 2011.

[60] L.Jing*, et al.*, "Parameters Analysis and Optimization Design for a Concentric Magnetic Gear Based on Sinusoidal Magnetizations," *IEEE Trans. on Appl. Superconductivity* vol. 24, 2014.

[61] O. Molokanov*, et al.*, "Analyses and experimental validation of coaxial magnetic planetary gear," in *18th International Symposium on Electrical Appa. and Tech (SIELA)*, 2014, pp. 1-4.

[62] L. Bronn, "Design and Performance Evaluation of a Magnetically Geared Axial-Flux Permanent Magnet Generator," Master of Science Thesis, Electrical Engg, Stellenbosch University, 2012.

[63] K. Hwang*, et al.*, "A Study on Optimal Pole Design of Spoke-Type IPMSM With Concentrated Winding for Reducing the Torque Ripple by Experiment Design Method," *IEEE Trans. on Magnetics,* vol. 45, pp. 4712-4715, 2009.

[64] D. Ionel*, et al.*, "Spoke permanent magnet rotors for electrical machines and methods of manufacturing same," US Patent 7,148,598 B2, 2006.

[65] D. Jones, "A new buried magnet brushless PM motor for a traction application," in *Proc. of the Elec. Insu. conf. and Elect. Man. and Coil Wind. Tech. Conf.* , 2003, pp. 421-429.

[66] D. Lin*, et al.*, "Analytical prediction of cogging torque in spoke type permanent magnet motors," in *Proceedings of the 18th International Conference on Electrical Machines*, 2008, pp. 1-5.

[67] I. Chabu*, et al.*, "Axial flux concentration technique applied to the design of permanent magnet motors: theoretical aspects and their numerical and experimental validation," in *IEEE Inter. Conf. on Elec. Mach. and Drives*, 2005, pp. 1988-1994.

[68] E. Gouda*, et al.*, "Comparative Study Between Mechanical and Magnetic Planetary Gears," *IEEE Trans. on Magnetics,* vol. 47, pp. 439-450, 2011.

[69] Z. Zhu and D. Howe, "Influence of design parameters on cogging torque in permanent magnet machines," *IEEE Trans. on Energy conv.,* vol. 15, pp. 407-412, 2000.

[70] F. C. Moon, "The Mechanics of Ferroelastic Plates in a Uniform Magnetic Field," *Journal of Appl. Mech.,* vol. 37, pp. 153-158, 1970.

[71] F. C. Moon and Y. Pao, "Magnetoelastic Buckling of a Thin Plate," *Journal of Appl. Mech.,* vol. 35, pp. 53-58, 1968.

[72] K. Fonteyn*, et al.*, "FEM for Directly Coupled Magneto-Mechanical Phenomena in Electrical Machines," *IEEE Trans. on Magnetics,* vol. 46, pp. 2923-2926, 2010.

[73] Z. Ren*, et al.*, "Calculation of mechanical deformation of magnetic materials in electromagnetic devices," *IEEE Trans. on Magnetics,* vol. 31, pp. 1873-1876, 1995.

[74] A. Belahcen, "Magnetoelastic coupling in rotating electrical machines," *IEEE Trans. on Magnetics,* vol. 41, pp. 1624-1627, 2005.

[75] D. Zarko, "Analytical calculation of magnetic field distribution in the slotted air gap of a surface permanent-magnet rotor using complex relative air-gap permeance," *IEEE Trans. on Magnetics,* vol. 42, pp. 1828-1837, 2006.

[76] L. Jian and K.Chau, "Analytical calculation of magnetic field distribution in coaxial magnetic gears," *Prog. Electrom. Res.,* vol. 92, pp. 1-16, 2009.

[77] A. Proca, "Analytical model for permanent magnet motors with surface mounted magnets," *IEEE Trans. Energy Conv.,* vol. 18, pp. 386-391, Sept. 2003.

[78] Z. Liu and J. Li, "Accurate prediction of magntic field and magnetic forces in permanent magnet motors using an analytical solution," *IEEE Trans. Energy Conv.,* vol. 23, pp. 717-726, 2008.

[79] Z. Liu*, et al.*, "Prediction and analysis of magnetic forces in permanent magnet brushless dc motor with rotor eccentricity," *Journal of Appl. Physics,* vol. 99, pp. O8R321:1-3, 2006.

[80] Z. Liu*, et al.*, "An improved analytical solution for predicting magnetic forces in permanent magnet motors," *Journal of Appl. Physics,* vol. 103, p. 07F135, 2008.

[81] B. L. J. Gysen*, et al.*, "Modeling of Flux Switching Permanent Magnet Machines With Fourier Analysis," *IEEE Trans. on Magnetics,* vol. 46, pp. 1499-1502, 2010.

[82] Z. Zhu, *et al.*, "Influence of Pole and Slot Number Combinations on Cogging Torque in Permanent-Magnet Machines With Static and Rotating Eccentricities," *IEEE Trans. on Industry Appl.,* vol. 50, pp. 3265-3277, 2014.

[83] L. Zhu, *et al.*, "Analytical Methods for Minimizing Cogging Torque in Permanent-Magnet Machines," *IEEE Trans. on Magnetics,* vol. 45, pp. 2023-2031, 2009.

[84] L. Dosiek and P. Pillay, "Cogging Torque Reduction in Permanent Magnet Machines," *IEEE Trans. on Industry Appl.,* vol. 43, pp. 1565-1571, 2007.

[85] Y. Zhou, *et al.*, "Analytical Calculation of Magnetic Field and Cogging Torque in Surface-Mounted Permanent-Magnet Machines Accounting for any Eccentric Rotor Shape," *IEEE Trans. on Industry Appl.*

[86] D. Wang, *et al.*, "Reduction on Cogging Torque in Flux-Switching Permanent Magnet Machine by Teeth Notching Schemes," *IEEE Trans. on Magnetics,* vol. 48, pp. 4228-4231, 2012.

[87] L. Jian, "Analytical Method for Magnetic Field Calculation in a Low-Speed Permanent-Magnet Harmonic Machine," *IEEE Trans. on Energy Conv.,* vol. 26, pp. 862-870, 2011.

[88] A. Penzkofer and K. Atallah, "Magnetic Gears for High Torque Applications," *IEEE Trans. on Magnetics,* vol. 50, 2014.

[89] T. Lubin, *et al.*, "Exact Analytical Method for Magnetic Field Computation in the Air Gap of Cylindrical Electrical Machines Considering Slotting Effects," *IEEE Trans. on Magnetics,* vol. 46, pp. 1092-1099, 2010.

[90] T. Lubin, *et al.*, "Analytical Computation of the Magnetic Field Distribution in a Magnetic Gear," *IEEE Trans. on Magnetics,* vol. 46, p. 2611, 2010.

[91] T. Lubin, *et al.*, "Development of a 2-D Analytical Model for the Electromagnetic Computation of Axial-Field Magnetic Gears," *IEEE Trans. on Magnetics,* vol. 49, pp. 5507-5521, 2013.

[92] L. Belguerras, *et al.*, "Analytical computation of Flux Concentration PM Machines: Study of the influence of the magnets shape," presented at the XXth Internatioal Conference on Electrical Machines (ICEM), 2012.

[93] D.K.Cheng, *Field and Wave Electromagnetics*: Addison-Wesley Publishing, 1989.

[94] S. Farlow, *Partial Differential Equations for Scientists and Engineers*: John Wiley & Sons, 1982.

[95] M. Sadiku, *Numerical Techniques in Electromagnetics*: CRC press LLC, 2001.

[96] D. Griffiths, *Introduction to Electrdynamics*, 3rd ed.: Prentice Hall publications.

[97] E. Kreyszig, *Advanced Engineering Mathematics*, 9th ed.: John Wiley & Sons, 2006.